

Lei Wang

Strand Corrosion in Prestressed Concrete Structures

OPEN ACCESS

 Springer

Strand Corrosion in Prestressed Concrete Structures

Lei Wang

Strand Corrosion in Prestressed Concrete Structures

 Springer

Lei Wang
Changsha University of Science
and Technology
Changsha, China



ISBN 978-981-99-2056-3 ISBN 978-981-99-2054-9 (eBook)
<https://doi.org/10.1007/978-981-99-2054-9>

© The Editor(s) (if applicable) and The Author(s) 2023. This book is an open access publication.

Open Access This book is licensed under the terms of the Creative Commons Attribution 4.0 International License (<http://creativecommons.org/licenses/by/4.0/>), which permits use, sharing, adaptation, distribution and reproduction in any medium or format, as long as you give appropriate credit to the original author(s) and the source, provide a link to the Creative Commons license and indicate if changes were made.

The images or other third party material in this book are included in the book's Creative Commons license, unless indicated otherwise in a credit line to the material. If material is not included in the book's Creative Commons license and your intended use is not permitted by statutory regulation or exceeds the permitted use, you will need to obtain permission directly from the copyright holder.

The use of general descriptive names, registered names, trademarks, service marks, etc. in this publication does not imply, even in the absence of a specific statement, that such names are exempt from the relevant protective laws and regulations and therefore free for general use.

The publisher, the authors, and the editors are safe to assume that the advice and information in this book are believed to be true and accurate at the date of publication. Neither the publisher nor the authors or the editors give a warranty, expressed or implied, with respect to the material contained herein or for any errors or omissions that may have been made. The publisher remains neutral with regard to jurisdictional claims in published maps and institutional affiliations.

This Springer imprint is published by the registered company Springer Nature Singapore Pte Ltd. The registered company address is: 152 Beach Road, #21-01/04 Gateway East, Singapore 189721, Singapore

Preface

Prestressed concrete (PC) has been widely used in structure construction because of its high strength, good compactness, small cracks, and superior spanning ability. However, the durability degradation of these structures, caused by the bad construction quality, environmental erosion, and material deterioration, has been gradually found during the serviceability period. Strand corrosion is one of the main reasons for the performance deterioration of PC structures. Corrosion can induce mechanical performance of strand, cause concrete cracking, degrade bond performance at the strand–concrete interface, lead to prestress loss, and deteriorate the bearing capacity of PC structures. Therefore, it has an important economic and academic values to study the durability and remaining service life of corroded PC bridges for ensuring their normal operation and safety utilization.

This book introduces the research results on the performance deterioration of existing PC structures, clarifies the mechanical behavior of corroded prestressing strands, corrosion-induced cracking, bond degradation, prestress loss and structural performance deterioration of PC structures, and proposes the corresponding prediction models, which is an important guidance for the durability and maintenance design of PC structures.

Chapter 1 introduces the history and development of PC structures, practical application of PC structures, and corrosion of strand in prestressed concrete.

Chapter 2 is organized as follows. First, corroded prestressing strands are obtained by the artificial climate conditions. Then, the number and shape of corrosion pits are measured to investigate its probability distribution. Furthermore, static tensile tests are carried out to study the mechanical property of corroded prestressing strands.

Chapter 3 designs an experimental study on corrosion-induced cracking in PC structures at first. Next, it proposes theoretical models for predicting the corrosion-induced cracking. Following this, it establishes the numerical model to simulate the concrete cracking induced by helical strand corrosion.

Chapter 4 studies the bond behavior between prestressing strands and concrete. First, the effect of corrosion on residual bond stress of strand is clarified based on the pull-out test. Next, the bond behaviors of corroded strand in pretensioned concrete beams are investigated by the bending test.

Chapter 5 aims to develop an analytical model for predicting the bond strength of strand considering rotation effect at first. Then, the effect of corrosion-induced concrete cracking on the ultimate bond strength of corroded strand is discussed. Following this, a simplified model is proposed to predict bond stress–slip relationship between corroded strand and concrete.

Chapter 6 proposes an analytical model to evaluate the prestress loss in corroded pretensioned concrete structures, incorporating the coupling effects of concrete cracking and bond degradation. A model, combining the coupling effect of the Hoyer effect and corrosion, is also proposed to predict the transfer length of pretensioned concrete beams.

Chapter 7 designs an experimental study with five specimens to explore the secondary anchorage, secondary transfer length, and residual prestress in locally corroded post-tensioned concrete beams after strand fracture. A numerical model is established to reproduce the process of strand fracture and the secondary anchorage of fractured strand.

Chapter 8 designs an experimental study with twenty post-tensioned concrete beams to study the influence of grouting defects, strand corrosion in insufficient grouting, and strand corrosion in full grouting on the flexural performance of post-tensioned concrete beams.

Chapter 9 proposes an analytical model to predict the flexural behavior of locally ungrouted PC beams at first. Then, a model is proposed to predict the bearing capacity of corroded PC beams considering bond degradation.

Changsha, China

Lei Wang

Acknowledgements

The book was written by Prof. Lei Wang. During the writing process, I got the support of data and materials provided by Jianren Zhang, Yafei Ma, Lizhao Dai, Hanbing Bian, Ke Huang, Wen Chen, Yongming Liu, Xuhui Zhang, Ju Yi, Shanchang Yi, Tang Li, Dixuan Long, Hong Chen, Yang Chen, Wengang Xu, Floyd Royce W., and Potier-Ferry Michel. In addition, the book also cites a large number of relevant documents of experts, and I would like to express my heartfelt thanks!

This work was supported by the National Key Research and Development Program of China (Grant No. 2019YFC1511000, 2021YFB2600900), the Science Fund for Creative Research Groups of Hunan Province (Grant No. 2020JJ1006), the Science and Technology Innovation Program of Hunan Province (Grant No. 2020RC4024), the Special Funds for the Construction of Innovative Provinces in Hunan Province (2019SK2171). Their supports are gratefully acknowledged.

I am sure that this publication is a useful tool for all people interested in the field of strand corrosion in PC structures, and hope that all readers will receive new information, insights, and ideas.

Contents

1	Brief Description of Prestressed Concrete Structures	1
1.1	History and Development of PC Structures	1
1.1.1	Reinforced Concrete Structures	1
1.1.2	Prestressed Concrete Structures	2
1.1.3	Main Methods of Prestressing	3
1.1.4	Characteristics of PC Structures	4
1.2	Practical Application of PC Structures	4
1.2.1	Application of Prestressing Technology in Bridges	4
1.2.2	Examples of Prestressing in Bridges	6
1.3	Corrosion of Strand in Prestressed Concrete	8
1.3.1	Mechanisms of Electrochemical Corrosion	9
1.3.2	Mechanisms of Stress Corrosion	11
1.3.3	Influence Factors of Strand Corrosion	12
1.4	Contents of This Book	14
	References	15
2	Mechanical Behaviors of Corroded Prestressing Strands	17
2.1	Introduction	17
2.2	Corrosion Morphology and Microscopic Damage of Strands	18
2.2.1	Corrosion Morphology of Prestressing Strands	18
2.2.2	Microscopic Damage of Corroded Strands	21
2.3	Corrosion Pits of Prestressing Strands	22
2.4	Probability Distribution of Corrosion Pits	24
2.4.1	Frequency Distribution of Corrosion Pits	24
2.4.2	K–S Test of Pit Size Parameters	27
2.5	Mechanical Behavior of Corroded Prestressing Strands	29
2.5.1	Relation Between Load and Displacement	29
2.5.2	Ultimate Strength, Strain, and Elastic Modulus	29
2.6	Constitutive Model of Prestressing Corroded Strands	31
2.7	Conclusions	33
	References	34

3	Corrosion-Induced Cracking of Prestressed Concrete	37
3.1	Introduction	37
3.2	Experimental Study on Corrosion-Induced Cracking	39
3.2.1	Filling of Strand Corrosion Products	39
3.2.2	Concrete Cracking Under Combined Prestress and Strand Corrosion	46
3.3	Prediction of Corrosion-Induced Cracking in PC Beams	52
3.3.1	Model for Corrosion-Induced Cracking	52
3.3.2	Model Validation	58
3.4	Meso-scale Modeling of Strand Corrosion-Induced Concrete Cracking	59
3.4.1	3D Corrosion Expansion Model of Helical Strand	59
3.4.2	Meso-scale Model of Heterogeneous Concrete	62
3.4.3	Model Validation	65
3.4.4	Influencing Parameters for Corrosion-Induced Cracking	67
3.5	Conclusions	72
	References	72
4	Bond Behavior Between Strand and Concrete with Corrosive Cracking	75
4.1	Introduction	75
4.2	Bond Behavior of Strand with Corrosive Cracking in Pull-Out Specimens	76
4.2.1	Corrosion-Induced Concrete Cracking	76
4.2.2	Concrete Strain	80
4.2.3	Twisting of Strands	82
4.2.4	Pull-Out Force and Slip	82
4.2.5	Distribution of Bond Stress	84
4.2.6	Bond Strength of Corroded Strand	88
4.3	Bond Behavior of Corroded Strand in PC Beams	90
4.3.1	Corrosion Loss and Corrosion-Induced Crack	90
4.3.2	Effect of Corrosion on Force–Slip Response of Strand	92
4.3.3	Failure Mode and Bond Strength	97
4.3.4	Degradation of Strand Bond and Tensile Strengths	100
4.4	Conclusions	102
	References	102
5	Bond–Slip Model of Corroded Strand Considering Rotation Effect	105
5.1	Introduction	105
5.2	Bond Strength of Strand Considering Rotation Effect	106
5.2.1	Theoretical Expressions for Bond Strength	107
5.2.2	Model Verification	113
5.3	Model for Bond Strength of Corroded Strand	115
5.3.1	Ultimate Bond Strength of Corroded Strand	115

- 5.3.2 Corrosion-Induced Pressure at Bond Interface 117
- 5.3.3 Confining Stress at Bond Failure 121
- 5.3.4 Model Validation 124
- 5.4 Model for Bond–Slip Between Corroded Strand and Concrete 128
 - 5.4.1 Method for the Local Bond Characteristics 128
 - 5.4.2 Local Bond–Slip Between Corroded Strand and Concrete 129
- 5.5 Conclusions 134
- References 135
- 6 Prestress Loss and Transfer Length Prediction in Pretensioned Concrete Structures with Corrosive Cracking 139**
 - 6.1 Introduction 139
 - 6.2 Calculation of Corrosion-Induced Expansive Pressure 140
 - 6.2.1 Prediction Model of Prestress Loss Under Corrosive Cracking 143
 - 6.2.2 Bond Degradation Due to Strand Corrosion 143
 - 6.2.3 Calculation Flow Chart of Prestress Loss 144
 - 6.2.4 Evaluation of Effective Prestress 147
 - 6.2.5 Effective Prestress Evaluation 149
 - 6.2.6 Validation on Prestress Loss Model 150
 - 6.2.7 Prediction of Transfer Length Under Corrosive Cracking 153
 - 6.2.8 Calculation of Transfer Length 155
 - 6.3 Evaluation of the Transfer Length in Corroded PC Beams 157
 - 6.3.1 Specimen Design and Data Analysis 157
 - 6.3.2 Evaluation of Transfer Length Under Corrosive Cracking 159
 - 6.4 Model Validation and Parameter Sensitivity Analysis 161
 - 6.4.1 Verification of Proposed Model 161
 - 6.4.2 Effect of Material Parameters on Expansive Pressure 161
 - 6.4.3 Effect of Material Parameters on Transfer Length 163
 - 6.5 Conclusions 163
 - References 164
- 7 Secondary Anchorage and Prestress Loss of Fractured Strand in PT Beams 167**
 - 7.1 Introduction 167
 - 7.2 Literature Review 168
 - 7.2.1 Bonding Properties of Fractured Strand 168
 - 7.2.2 Prestress Loss of Fractured Strand 169
 - 7.3 Secondary Anchorage of Fractured Strand 170
 - 7.3.1 Strand Fracture Test 170
 - 7.3.2 Mechanism of Secondary Anchorage 171
 - 7.3.3 Secondary Transfer Length After Strand Fracture 173

- 7.3.4 Residual Prestress in Secondary Anchorage of Fractured Strand 175
- 7.4 Residual Prestress in PT Beams After Strand Fracture 176
 - 7.4.1 Calculation of Residual Prestress 176
 - 7.4.2 Relation Between Residual Prestress and Strand Fracture Position 179
- 7.5 Numerical Model for Secondary Anchorage of Fractured Strand 180
 - 7.5.1 Numerical Model Generation 180
 - 7.5.2 Interfacial Bond-Slip Simulation 181
 - 7.5.3 Strand Fracture Simulation 183
 - 7.5.4 Model Validation 184
- 7.6 Evaluation of Damage Control Section and Flexural Capacity After Strand Fracture 187
- 7.7 Conclusions 189
- References 190
- 8 Flexural Behaviors of Corroded Post-tensioned Concrete Beams 193**
 - 8.1 Introduction 193
 - 8.2 Design of Specimens with Different Defects 194
 - 8.3 Effect of Insufficient Grouting on Flexural Behaviors 196
 - 8.3.1 Design of Insufficient Grouting 196
 - 8.3.2 Cracking Behavior 198
 - 8.3.3 Load–Deflection Response 200
 - 8.3.4 Ultimate Strength and Failure Mode 202
 - 8.4 Effect of Strand Corrosion in Insufficient Grouting on Flexural Behaviors 203
 - 8.4.1 Corrosion Characteristic of Strand 203
 - 8.4.2 Cracking Behavior 205
 - 8.4.3 Load–Deflection Response 207
 - 8.4.4 Failure Mode and Ultimate Strength 210
 - 8.5 Effect of Strand Corrosion in Full Grouting on Flexural Behaviors 211
 - 8.5.1 Corrosion of Prestressed Concrete Beams 211
 - 8.5.2 Cracking Patterns at the Ultimate State 213
 - 8.5.3 Load–Deflection Response 214
 - 8.5.4 Failure Mode and Ultimate Strength 217
 - 8.6 Conclusions 222
 - References 222
- 9 Bearing Capacity Prediction of Corroded PT Beams Incorporating Grouting Defects and Bond Degradation 225**
 - 9.1 Introduction 225
 - 9.2 Analytical Model for Flexural Capacity of PT Beams 227
 - 9.2.1 Simplified Calculation Method 227
 - 9.2.2 Calculation Procedure 230

9.3	Model Validation	233
9.4	Quantification of Corrosion-Induced Uncoordinated Deformation in Bond–Slip Zone	236
9.4.1	Quantification Principle of Bond–Slip Zone	236
9.4.2	A Quantitative Method for Uncoordinated Deformation	238
9.5	Bearing Capacity Assessment Considering Bond Degradation	243
9.5.1	Bonding Degradation Model	243
9.5.2	Calculation of Bearing Capacity	245
9.5.3	Model Verification	247
9.5.4	Effect of Corrosion on Uncoordinated Deformation	249
9.6	Conclusions	251
	References	252

About the Author

Prof. Lei Wang is the Dean of the School of Civil Engineering, Changsha University of Science and Technology, China. He got the Ph.D., M.S. and B.S. in 2008, 2005, and 2002, respectively.

He is a Young Yangtze Scholar of Ministry of Education, Young and Middle-age Science and Technology Leader of the Ministry of Transport, Science and Technology Leader of Hunan Province, and Excellent Youth Talents in Traffic Science and Technology, etc.

He is a member of American Society of Civil Engineers (ASCE) and International Association for Bridge and Structural Engineering (IABSE). He was the Executive director of TEFC, the committee member of Structural Vibration Control and Health Monitoring and China Journal of Highway and Transportation Society.

His research interests are in the intelligent operation and maintenance of bridges, the disease diagnosis and treatment of bridges, engineering safety risk prevention and control, and engineering uncertainty quantification.

He got more than 20 scientific projects supported by the National Key R&D Program of China, National Natural Science Foundation of China, the Foundation for Innovative Research Groups of Hunan Province, and the Outstanding Youth Fund in Hunan Province. He has gotten 25 Chinese invention patents, 7 national standards, published 3 books, and more than 150 journal papers, indexed in the SCI with 95.

He was awarded the second prize of the National Science and Technology, three first prizes of provincial and ministerial award, the National Excellent Doctoral Dissertations Award, and Young Science and Technology Award of China Highway Society.

Chapter 1

Brief Description of Prestressed Concrete Structures



1.1 History and Development of PC Structures

The creation of reinforced concrete (RC) occurred in contemporary times. It is widely recognized that French gardener Joseph Monier devised and patented it in 1849 and 1867 respectively, featuring reinforced concrete flower pots and highway guardrails with reinforced concrete beams and columns [7]. The world's first reinforced concrete edifice was built in 1872, located in New York, USA, signaling the start of a new era in human architecture. Reinforced concrete constructions became popular in the engineering profession after 1900. Prestressed concrete (PC), a new type of reinforced concrete construction, was introduced in 1928 and was widely used in engineering practice after World War II.

Concrete is made up of aggregates (stone as coarse aggregate and sand as fine aggregate) and cement (typically Portland cement). When water is added into the cement, it hydrates and forms a small opaque lattice structure that wraps and seals the aggregate into a solid structure. Concrete constructions typically have high compressive strength (about 28 MPa), but poor tensile strength (such as beam bending). Any significant tensile stress will break the microscopic hard lattice of concrete, resulting in cracking and separation. However, since most structural components require tensile stress, unreinforced concrete is rarely employed in engineering without reinforcement.

1.1.1 Reinforced Concrete Structures

Compared to concrete, the tensile strength of steel is generally above 200 MPa. People usually add steel and other tensile reinforcing materials in concrete to work together, which makes up a reinforced concrete structure. The tensile force is borne by the steel, the concrete bears the compressive stress part. According to the force of

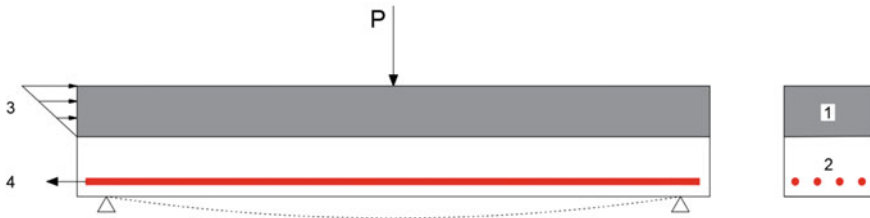


Fig. 1.1 Reinforced concrete force characteristics

the structure, the reasonable configuration of the reinforcing steel can form a higher load-bearing capacity and a greater stiffness of the structure.

For example, a simply supported beam under bending is shown in Fig. 1.1. When the load P is applied, the beam cross-section is subjected to compression at the top and tension at the bottom. At this point, the reinforcement configured at the bottom of the beam bears the tension, while the concrete shown in the upper shaded area bears the compression.

1.1.2 Prestressed Concrete Structures

Although reinforced concrete structures make reasonable use of the force performance characteristics of both steel and concrete, forming a structure with better integrity and durability, reinforced concrete needs to face two main problems in actual use.

- (a) Concrete structures generally work with cracks. When a reinforced concrete structure is loaded, it will inevitably deform, resulting in cracking. The existence of cracks not only reduces the stiffness of the structure but also renders it impossible to apply the reinforced concrete structure in situations where cracking is not allowed.
- (b) Concrete structures cannot make full use of high-strength materials. As the load increases, it is not economic to increase the cross-sectional size of reinforced concrete structures or the amount of reinforcement to control the cracks and deformation of the structures. Additionally, the self-weight of concrete structures has also been increased, especially for bridge structures, with the increase in span, the proportion of the role of self-weight also increases, which will obviously limit the application of reinforced concrete structures in bridge engineering.

The emergence of prestressed concrete structures is a good solution to these problems. Prestressed concrete structures use steel cables to provide pressure at the ends of the concrete structure to establish a state of stress within it, the magnitude and distribution of which are used to resist or eliminate tensile stresses generated by the application of loads. This type of concrete structures, in which prestressing

steel is configured and then established by tensioning or other methods, is called prestressed concrete structures [17].

1.1.3 Main Methods of Prestressing

Pretensioning method: The pretensioning method is the method of tensioning the reinforcement first and then pouring the concrete of the structure afterward. As shown in Fig. 1.2a, after the concrete reaches the required strength (generally not less than 75% of the design strength), the temporary anchorage is released and the tension is slowly relaxed, allowing the retraction of prestressing reinforcement. The retraction force of the reinforcement is transferred to the concrete through the bond between the prestressing reinforcement and concrete, so that the concrete can obtain precompression stress. This kind of concrete structure in which the prestressing tendons are tensioned on the pedestal and the concrete is poured and the prestressing force is transferred through the bond is called pretensioned concrete structures.

Post-tensioning method: The post-tensioning method is a method of casting concrete elements first, and then tensioning and anchoring prestressing steels after the concrete has hardened. As shown in the Fig. 1.2b, concrete structures are poured first and holes are reserved in it. After the concrete strength reaches the required strength, the prestressing steels are threaded into the reserved holes, the jacks are supported at both the ends of the concrete structures, and the prestressing steels are tensioned and anchored to the concrete structures so that the concrete obtains and maintains its precompressive stress. Finally, cement slurry is injected into the reserved orifice to protect the prestressing steel from rusting and to make the prestressing steel bonded to the concrete as a whole. This kind of structure is called post-tensioned concrete structures after the concrete is hardened by tensioning the prestressing tendons and anchoring them to establish prestressing.

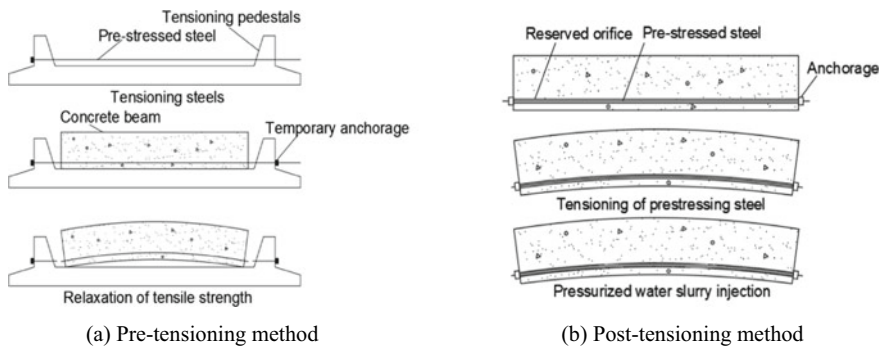


Fig. 1.2 Types of prestressed concrete structures

1.1.4 Characteristics of PC Structures

Compared with reinforced concrete structures, PC structures have the following main advantages.

- (1) It can improve the crack resistance and stiffness of concrete structures. After applying prestressing to the structures, the cracks may not appear or may be greatly delayed under the service load, thus effectively improving the serviceability of the structures, increasing the stiffness of the structures, and improving the durability of the structures.
- (2) It can save materials and reduce the self-weight of structures. Since prestressed concrete can reasonably use high-strength materials, it can reduce the cross-sectional size of the structures and reduce the dead load of the structure. This is a significant advantage for large span bridges where dead load is the main effect.
- (3) The vertical shear and principal tensile stresses in concrete beams can be reduced. The curved reinforcement of prestressed concrete beams can reduce the vertical shear force near the support in the beam; due to the presence of precompressive stresses in the concrete cross-section, the main tensile stresses in the concrete under load will be reduced accordingly.
- (4) Prestressing can be used as a means of connecting structures, promoting the development of new systems and construction methods for bridge structures.
- (5) The fatigue resistance of the structure can be improved, which is beneficial for bridge structures subjected to dynamic loads.

PC structures have the following main disadvantages.

- (1) The upper arch degree of structures induced by prestressing is not easy to control. The prestressing effect may make a large upper arch degree, resulting in unevenness of the bridge deck.
- (2) The construction cost of prestressed concrete structures is large for the projects with a small spans and small number of structures.

1.2 Practical Application of PC Structures

1.2.1 Application of Prestressing Technology in Bridges

The use of prestressing technology in engineering can greatly reduce the amount of concrete and steel, effectively reduce the self-weight of reinforced concrete components, and thus improve the crack resistance of concrete. The application of prestressing technology not only improves the quality of the bridge project but also improves the economic benefits of the project. It can further improve the aesthetic effect of the bridge project and prolong the service life of the bridge.

In bridge construction, the concrete structure is very important, which will directly carry most of the carrying load of the bridge. Therefore, applying prestressing technology to the concrete structure is to strengthen the main structure of the bridge, thereby improving the overall quality and stability. The implementation of prestressing technology in the concrete structures of bridge construction can solve the common problems, such as easy cracking and deformation of concrete to a certain extent. So that the stability and service life of the concrete structure can be greatly improved, thereby improving the overall quality of the bridge.

The selection of steel strands is directly related to the quality and performance of bridge construction. There are four main types of prestressing steel strands used in bridge engineering in China, namely prestressed steel bars, ordinary prestressing steel strands, low-relaxation steel strands, and prestressing steel strands with straightening and tempering properties. The low-relaxation steel strands are widely used in bridge engineering due to their characteristics of durability and low cost. Scientific and reasonable selection of steel strands can greatly reduce the use of steel on the basis of ensuring the quality of the project, thereby improving the economic effect of the project [2].

The choice of anchorage for prestressing technology is based on both friction anchorage and mechanical anchorage. Friction anchorage is the formation of prestressing steel anchor rotating effect and fixing the steel tightly. The advantage of this technology is easy to wear the cable, the defect is not enough convenient connection, and the loss is large. Mechanical anchorage is the use of mechanical processing to form the anchor working conditions suitable for the use of prestressing steel end and the construction method of anchorage [29].

In bridge construction, the construction quality of flexural components is a key factor affecting the construction quality and service life of the entire bridge [14]. Therefore, improving the construction quality of the flexural members can effectively improve the overall quality and service life of the bridge. To ensure the bridge's stability and safety during actual operation, it is essential to construct the components in accordance with the construction specification.

In bridge construction projects, the positive and negative bending moment area of multi-span continuous beams is a very important but easily neglected part. Prestressing technology is applied in the construction of this structure to improve the stability and resistance of positive and negative bending moment structures. The pressure capacity of the bridge will also have a significant improvement effect on the overall quality of the bridge. Usually, multi-span continuous bridges have the characteristics of large span and high strength. The quality of the bridge is very strict, and the large deformation and cracking cannot occur. Therefore, prestressing technology can be used in the construction of key positive and negative bending moments to improve the stability of critical instability, and then combined with prestressed concrete cast-in-place construction, to greatly improve the quality level of multi-span continuous bridges.

The prefabricated board is a common template in engineering construction, and the quality of the prefabricated boards affects the quality of the bridge construction [16]. Prestressed technology is applied in preplate production projects, and people

choose high-strength and relaxed steel strands as prestretched bands to increase seismic performance and stability of the prefabricated plates.

With the increase in traffic, the bearing capacity of some bridges designed and constructed in the early stage has been difficult to meet the current traffic requirements. Therefore, many bridge constructions are buried with many dangerous factors, and bridges need to be reinforced in time. The prestressing technique reinforcement method is a fairly mature and widely practical method. In recent years, with the continuous progress of bridge construction technology, prestressing technology has also been developed rapidly, which is able to carry out reinforcement construction in key areas such as bridge main structure, bridge deck layer, bridge structure, etc. By reinforcing different areas of the bridge, it can play a great role in repairing and improving the overall quality of the bridge and extending the service life of the bridge.

1.2.2 Examples of Prestressing in Bridges

Modern prestressed bridge structures have been widely used in the field of highway and railway bridge construction due to their good performance and superior spanning capacity. In the USA from the 1950s to the 1990s, compared with steel bridges, reinforced concrete bridges, and other types of bridges, the application of prestressed concrete bridges was increasing, and traditional steel bridges in the range of large and medium span are being gradually replaced by modern prestressed concrete bridges [15].

Prestressed concrete is ideally suited for long-span bridge construction. The Parrotts Ferry Bridge in California has a main span of 195 m. The Pasco-Kennewick cable-stayed bridge in Washington is 299 m. The central span of the cable-stayed Vasco de Gama Bridge in Lisbon, Portugal, is 420 m. The Sunshine Sky Bridge, a typical cable-stayed bridge of 365 m main span, constructed at Tampa Bay, Florida, USA. The Chaco-Corrientes Bridge constructed in Argentina, South America, is the longest precast prestressed concrete cable-stayed box girder in the world at the time. California Guide Ways is the typical use of prestressed concrete simple-span box girders for the Bay area rapid transit system in San Francisco, California. The Lubha Bridge, once the longest single-span 172 m prestressed concrete box-girder-type continuous bridge in India, built across a 30 m deep gorge of the Lubha river in Assam. Zuari Bridge at Goa, is 807 m long, comprising prestressed concrete cantilever box girders with 4 main spans of 122 m, two end spans of 69.5 m, and a via duct with 5 spans of 36 m. Ganga Bridge at Patna, the once longest prestressed concrete bridge in the world, has a total length of 5575 m, consisting of continuous spans of 121.65 m long prestressed concrete girders of variable depth. Cable-stayed prestressed concrete bridge across the Brahmaputra at Jogighopa, Assam, with a span of 286 m between the two towers and two side spans of 114 m, comprises a single-cell prestressed concrete box girders [22].

Bridges play an important role in the normal operation of road traffic as the structures built to cross road obstacles. Bridge engineering has been unprecedentedly developed with the rapid development of social economy, showing a thriving scene. There are more than 912,000 highway bridges and 10,000 km of high-speed railway bridges in China in 2020. China began to develop prestressed concrete technology around the 1950s and was the first to apply prestressed reinforced concrete to the accessory of sleepers in railway tracks. With the acceleration of the construction of China's transportation industry, the prestressed concrete technology is gradually popularized and used nationwide. Especially in bridge engineering, it has grown the fastest. In the late 1970s, all kinds of bridges built in China basically used prestressed concrete structures. In the twenty-first century, the main materials of modern prestressed concrete are high-quality steel and high-strength concrete. The high-efficiency prestressed concrete is formed through very advanced production technology through modern design concepts and methods.

The Nanjing Yangtze River Bridge was completed in 1968. It is the first prestressed concrete bridge in China that integrates design and construction. The main bridge has ten holes and a total length of 1577 m. The successful completion of the Nanjing Yangtze River Bridge demonstrates that China's bridge construction has risen to a new level in both scale and technology. The Chongqing Yangtze River Bridge, built in 1980, is a prestressed concrete box girder structure with a main span of 174 m. The prestressed concrete T-beam bridge, built in Feiyunjiang, Zhejiang, in 1988, has a maximum span of 62 m. In the same year, the Luoxi Bridge, the main traffic road connecting Guangzhou urban area to Panyu, was built in Guangdong, with a total length of 1916 m. Its main span of 180 m also created a precedent for the construction of long-span PC continuous rigid frame bridges in China. Over the next ten years, more than 100 PC beam bridges with spans greater than 120 m were built nationwide. At the same time, cable-stayed bridges were gradually printed on the list of bridges in China. In 1975, the first cable-stayed bridge with a main span of 76 m was built in Yunyang County, Chongqing. The cable-stayed bridge on the Yellow River Highway in Jinan, opened to traffic in 1982, mainly adopts prestressed box girder in structure, with a main span of 220 m.

Under the condition of comprehensive strength, the development of modern prestressing technology on bridges is faster. For example, cable-stayed bridges such as Shanghai Nanpu Bridge and Yangpu Bridge, and suspension bridges such as Hong Kong Tsing Ma Bridge and Jiangyin Yangtze River Bridge from the perspective of design, construction, materials, equipment, corrosion protection, etc. continuously explore the characteristics and accumulate experience to provide foundation for the updated technology.

1.3 Corrosion of Strand in Prestressed Concrete

Prestressed concrete has been diffusely used in bridge construction because of its high strength, good compactness, small cracks, and superior spanning ability [4]. However, the durability degradation of these bridges has been gradually found during the serviceability period, caused by the bad construction quality, environmental erosion and material deterioration [27], as shown in Fig. 1.3. Strand corrosion can cause concrete cracking, degrade bond performance at the strand–concrete interface, lead to prestress loss, and deteriorate the capacity of bridges [3]. Therefore, it is important to study the durability and remaining service life of corroded prestressed concrete bridges for ensuring their standard operation and safety utilization.

Strand corrosion is one of the major reasons for the performance deterioration of PC bridges. In worldwide, accidents of prestressed concrete (PC) bridges caused by corrosion have been widely reported. A footbridge collapsed suddenly in Hampshire, England, in 1967. In 1980, a large number of corroded prestressing tendons were found on the Angell Road Bridge in north London. The Ynys-Y-Gwaa Bridge, UK, collapsed in 1985 due to the corrosion of post-tensioning tendons at the segment joints after only 32 years of service [12]. The Welsh Bridge in the USA suddenly failed due to strand corrosion at the joint positions in 1985. Additionally, Italy's Saint Stefano Bridge failed due to pitting corrosion of the prestressing steel near the box girder joints in 1999, after 40 years of service. The collapse of Lake View Drive Bridge in the USA in 2005 was caused by strand corrosion [11].

It is found that more than 200 durability problems of bridges caused by prestressing strand corrosion had been reported in worldwide during 1951–1979, which caused huge economic losses. A survey in 1982 indicated that ten safety accidents of bridges caused by strand corrosion had been reported in USA during 1978–1982 [23]. In China, numerous of PC bridges have been built with the economic development. Under the combined effects of traffic growth and environment worsening, the durability of PC bridges has been gradually emerged during the serviceability. Reports from the railway department in 1994 indicated that more than 6000 defective concrete bridges were under the operation in China, accounting for 18.8% of the total number. Structural deterioration caused by corrosion has cause huge economic losses, which needs to be paid high attention.

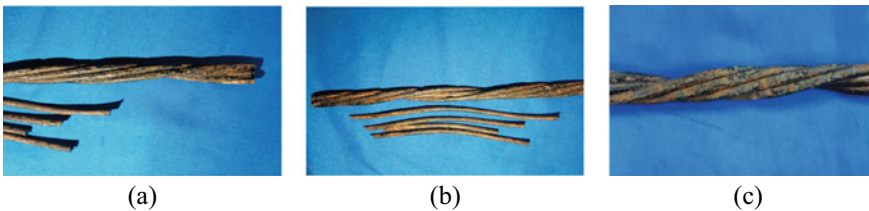


Fig. 1.3 Corrosion of prestressing strand in bridges

Strand corrosion has been found to be one of the primarily common problems in PC bridges [5, 13]. Corrosion can weaken the strand section area, the mechanical strength and bond properties of strand. The structure would be deteriorated due to these factors. The failure of prestressed concrete bridges would exhibit brittle characteristic without warning due to the high stress state of the strand, which leads to a huge economic loss. Existing investigations are mainly centered on the corrosion of reinforced concrete structures, and the related corrosion mechanism of ordinary steel has been studied extensively [8, 9, 28]. Few works on strand corrosion have been reported.

The corrosion morphology of strand is more complicated than that of ordinary steel owing to the combined effects of electrochemical corrosion, stress corrosion, and crevice corrosion [10]. First, the corrosion process of strand under the high stress state is faster than that of reinforcement steel. Second, the multiple steel wires are usually used as the prestressing strand in bridges, and the gap between the steel wires will provide a channel for the longitudinal migration of erosion medium, which promotes the corrosion propagation. How does strand corrosion evolve? What is the effect of high stress on corrosion-induced cracking? How does the bond between strand and concrete degrade? How to evaluate the effective prestress of strand after corrosion? How do these factors affect the bearing capacity of corroded PC beams? These problems need to be resolved.

The corrosion mechanism between the pretensioned and post-tensioned concrete bridges may be different because of their construction techniques [10]. The grouting defect will exist in the post-tensioned concrete bridges owing to bleeding and construction problems [20]. This defect not only weakens the ability of strand and concrete to work together but also weakens the strand protection, causing corrosion induced by erosion medium [21]. Without bellow protection, strands in pretensioned concrete bridges are easily to be corroded. Strand corrosion causes concrete cracking and bond degradation. Moreover, prestressing strand in pretensioned concrete beams transmits the prestressing force to concrete through interfacial bond stress, and the effective bond is peculiarly important compared with other concrete structures [6]. Corrosion-induced bond degradation not only reduces the ability of strand to work together with concrete but also affects the stress transfer, which can be easy to cause the anchorage failure of beams [1]. As mentioned above, the mechanical properties of corroded pretensioned and post-tensioned concrete structures are different, which needs to be discussed in several ways.

1.3.1 Mechanisms of Electrochemical Corrosion

The electrochemical corrosion generally occurs in strand. The passive film of strand in concrete is easily destroyed by the environmental media, such as carbon dioxide and chloride ions. When corrosive media including CO_2 and Cl^- , the reduction of the alkalinity in the concrete will partially or completely destroy the passivation state

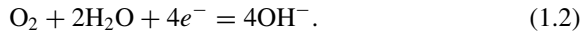
of the strand surface. A potential difference will occur at different parts of the strand surface, forming anodes and cathodes, which will lead to strand corrosion [18].

Liquid water in concrete usually exists in the form of $\text{Ca}(\text{OH})_2$ solution, which will make the concrete in a highly alkaline state. The strand in a highly alkaline state is easily oxidized by oxygen to form a dense passive film on the surface. The main component of the passive film is $n\text{Fe}_2\text{O}_3 \cdot m\text{H}_2\text{O}$, which can resist erosion by external harmful substances. With the continuous reaction of CO_2 in the air with $\text{Ca}(\text{OH})_2$ solution to form CaCO_3 , the concrete becomes less alkaline and the passive film is constantly damaged. When the passive film breaks down, the strand section, the passive film, and the pore water form a closed-circuit electrolytic cell. The closed-circuit will cause electrochemical corrosion of the strand. Electrochemical corrosion can be divided into three processes:

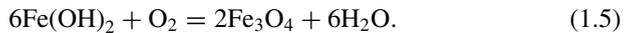
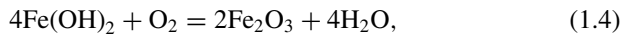
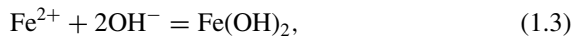
- (1) Oxidation reaction occurs at the anode region. The strand loses electrons becoming ferric ions where the passive film breaks down. The reaction can be schematically written as



- (2) Reduction reaction occurs at the cathode region. The strand gains electrons to OH^- where oxygen and pore water penetrate. The reaction can be schematically written as



- (3) Corrosion products are created as a result of corrosion. The OH^- generated by the reduction reaction moves to the place where the passive film of the strand is damaged. Then the OH^- forms $\text{Fe}(\text{OH})_2$ with the Fe^{2+} at the passive film break down. In an oxygen-rich environment, $\text{Fe}(\text{OH})_2$ will be oxidized to a red corrosion product (Fe_2O_3). In an oxygen-deficient environment, a part of $\text{Fe}(\text{OH})_2$ will be oxidized to black corrosion products (Fe_3O_4). The reaction can be schematically written as



When the PC structures are exposed to a chloride ion rich environment, the chloride ions will continuously spread to the surface of the strand. The strand passive film will be damaged as the critical chloride ion concentration is reached. The chloride ion will act as a catalyst with Fe^{2+} to produce the corrosion products (Fe_2O_3 , Fe_3O_4), as shown in Fig. 1.4. The reaction can be schematically written as

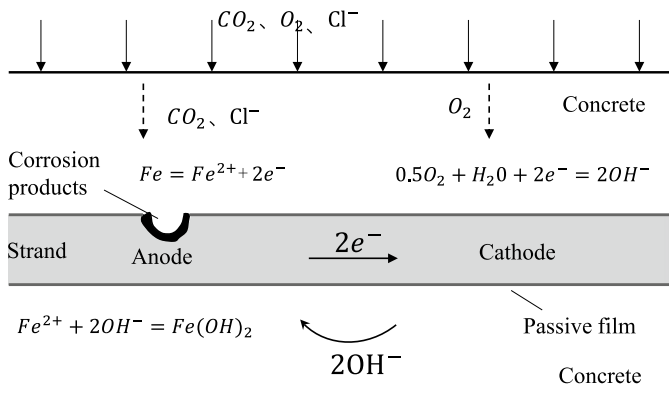
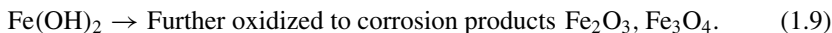
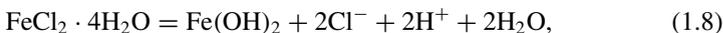
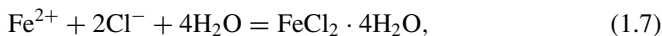


Fig. 1.4 Schematic diagram of electrochemical corrosion mechanism

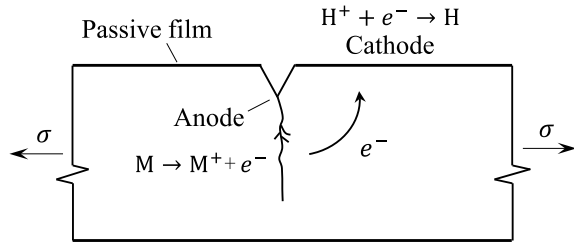


1.3.2 Mechanisms of Stress Corrosion

The existence of high stresses in the strand will change the corrosion mechanism of the strand. Under the coupled action of high stress and corrosive environment, strand will suffer from traditional electrochemical corrosion and stress corrosion [25], as shown in Fig. 1.5. In the coupling of high stress and corrosive environment, micro-cracks occur on the strand surface. The stress corrosion mechanism includes two types of anodic dissolution stress corrosion and hydrogen-induced cracking stress corrosion [26]. Micro-cracks lead to brittle fracture of the strand at well below the tensile strength in a form of corrosion, which is called as the stress corrosion.

High stresses in the strand will cause local cracking of the passive film to expose fresh fracture surfaces. The fractured surface acts as the anode. The rest of the unbroken passive film acts as the cathode. The pore water acts as the electrolyte solution to form a closed-circuit electrolytic cell. Cracks extend internally as the strand fracture surface at the anode dissolves. Due to the existence of high stress, the cracks at the fracture surface are constantly cracking which makes it hard to form a

Fig. 1.5 Schematic diagram of stress corrosion mechanism



new passive film. Under the continuous action of the electrochemical reaction, the strand at the anode fracture surface dissolves and the cracks continue to expand to the inner depth. The brittle fracture strength of stranded wire is much lower than the tensile strength. This corrosion behavior is known as anodic dissolution stress corrosion [24]. The hydrogen and chloride ions absorbed by the strand during the manufacturing process undergo an electrochemical reaction to produce hydrogen. Hydrogen accumulates at the fracture surface of the strand caused by high stresses. When the hydrogen concentration reaches the critical hydrogen concentration, it will cause the strand to become brittle and crack at the fracture face. Constant cracking of the strand leads to hydrogen brittle fracture of the strand. This corrosion behavior is known as hydrogen-induced cracking stress corrosion [19].

1.3.3 Influence Factors of Strand Corrosion

Corrosion of strand in concrete is influenced by many factors, e.g., the medium (gas, liquid, solid), temperature, humidity, freezing, etc. The surrounding environment is the external factor that affects the corrosion of strand. The position of the strand, the diameter of the strand, the type of concrete, permeability, cracking, alkalinity, the use of additives, the thickness of the protective layer, the strength level, and quality of the concrete are the internal factors affecting the corrosion of the strand. The factors affecting the corrosion of strand in general are as follows.

1. PH value of concrete

For strand in concrete, when PH is greater than 11.5, they are completely passivated and corrosion will not occur. When the PH gradually decreases from 11.5 to 9, the strand passive film is gradually damaged and the corrosion rate gradually increases. When the PH is between 9 and 10, the strand is completely depassivated and the corrosion rate is not affected by the PH. When the PH is less than 4, the corrosion rate of the strand increases sharply.

2. Cl^- concentration in concrete

The sources of Cl^- in concrete are both internal mixing and external penetration. The internal Cl^- is mainly derived from antifreeze such as CaCl_2 , which is added

during the concrete mixing process. Most of the Cl^- is adsorbed by the cement slurry and is present in the form of bound Cl^- , which have little effect on strand corrosion. Concrete in seawater environment and highway concrete with deicing salt on pavement are the sources of external penetration type Cl^- . The Cl^- in the external environment gradually accumulates at the concrete–strand interface through the concrete protective layer, so that the concentration of Cl^- in the strand surface solution gradually increases. When Cl^- reaches the critical concentration, the strand begins corrosion.

3. Environmental conditions

Environmental conditions such as temperature, humidity and drying alternation, seawater splash, and sea salt penetration are the external factors that cause the corrosion of strand, which have obvious effects on the corrosion of strand in concrete structures. When the self-protection ability of concrete does not meet the requirements or the concrete cover is cracking and other defects, the influence of external environmental factors will be more prominent. The actual investigation results show that the service life of concrete structure in dry and non-corrosive media is 2–3 times longer than that in wet and corrosive media.

4. Thickness of protective layer, integrity, and density of concrete

Concrete protective layer prevents infiltration of corrosive medium, oxygen, and water into the structure. The thicker the protective layer, the smaller the oxygen concentration gradient, and the slower the corrosion rate. However, the excessive thickness of concrete cover will not only reduce the ultimate bending resistance of concrete members but also change the angle of oblique section of punching failure and slightly reduce the ultimate punching resistance of concrete members. The intact degree of concrete cover has obvious influence on strand corrosion, especially on prestressed concrete structures in wet environment or corrosive medium. The density of concrete affects the permeability of concrete and the strand in the concrete with high permeability are more prone to corrosion.

5. Cement varieties and admixtures

Mineral admixtures, such as fly ash, can reduce the alkalinity of concrete, thereby affecting the corrosion of strand. Adding high-quality fly ash and other admixtures can reduce the alkalinity of concrete. At the same time, it can improve the density of concrete and change the internal pore structure of concrete. This can prevent the infiltration of external corrosive medium and oxygen and water, which is undoubtedly beneficial to prevent the corrosion of the strand. In recent years, research work has also shown that the addition of fly ash can enhance the corrosion resistance of concrete.

6. Carbonization degree of concrete

Carbon dioxide in the atmosphere diffuses into concrete and reacts with calcium hydroxide produced during hardening. Chemical reaction reduces the original strong alkaline of cement. When the PH drops to around 8.5, carbonation of the concrete occurs, which gives the strand the possibility of depassivation. The degree of concrete carbonation has a significant effect on the corrosion of the strand.

1.4 Contents of This Book

This book introduces the research results on the performance deterioration of existing prestressed concrete (PC) structures, clarifies the mechanical behavior of corroded prestressing strands, corrosion-induced cracking, bond degradation, prestress loss, and structural performance deterioration of PC structures and proposes the corresponding prediction models, which has an important guidance for the durability and maintenance design of PC structures.

This chapter provides the introduction, history and development of PC structures, practical application of PC structures, and corrosion of strand in prestressed concrete.

Chapter 2 is organized as follows. First, corroded prestressing strands are obtained by the artificial climate conditions. Then, the number and shape of corrosion pits are measured to investigate its probability distribution. Furthermore, static tensile tests are carried out to study the mechanical property of corroded prestressing strands.

Chapter 3 conducts an experimental study on corrosion-induced cracking in PC structures at first. Next, it proposes theoretical models for predicting the corrosion-induced cracking. Following this, it establishes the numerical model to simulate the concrete cracking induced by helical strand corrosion.

Chapter 4 studies the bond behavior between prestressing strands and concrete. First, the effect of corrosion on residual bond stress of the strand is clarified based on the pull-out test. Next, the bond behaviors of corroded strand in pretensioned concrete beams are investigated by the bending test.

Chapter 5 aims to develop an analytical model for predicting the bond strength of strand considering rotation effect at first. Then, the effect of corrosion-induced concrete cracking on the ultimate bond strength of the corroded strand is discussed. Following this, a simplified model is proposed to predict the bond stress–slip relationship between corroded strand and concrete.

Chapter 6 proposes an analytical model to evaluate the prestress loss in corroded pretensioned concrete structures, incorporating the coupling effects of concrete cracking and bond degradation. A model, combining the coupling effect of the Hoyer effect and the cracking caused by corrosion, is also proposed to predict the transfer length of pretensioned concrete beams.

Chapter 7 designs an experimental study with five specimens to explore the secondary anchorage, secondary transfer length, and residual prestress in locally corroded post-tensioned concrete beams after strand fracture. A numerical model is established to reproduce the process of strand fracture and the secondary anchorage of fractured strand.

Chapter 8 designs an experimental study with twenty post-tensioned concrete beams to study the influence of grouting defects, strand corrosion in insufficient grouting, and strand corrosion in full grouting on the flexural performance of post-tensioned concrete beams.

Chapter 9 proposes an analytical model to predict the flexural behavior of locally ungrouted PC beams at first. Then, a model is proposed to predict the bearing capacity of corroded PC beams considering bond degradation.

References

1. J.R. Casas, C. Crespo-Minguillon, Probabilistic response of prestressed concrete bridges to fatigue. *Eng. Struct.* **20**(11), 940–947 (1998)
2. H.-L. Chen, K. Wissawapaisal, Measurement of tensile forces in a seven-wire prestressing strand using stress waves. *J. Eng. Mech.* **127**(6), 599–606 (2001)
3. D. Coronelli, Corrosion cracking and bond strength modeling for corroded bars in reinforced concrete. *ACI Struct. J.* **99**(3), 267–276 (2002)
4. C.N. Dang, C.D. Murray, R.W. Floyd, W.M. Hale, J.R. Martí-Vargas, Analysis of bond stress distribution for prestressing strand by Standard Test for Strand Bond. *Eng. Struct.* **72**, 152–159 (2014)
5. M.S. Darmawan, M.G. Stewart, Spatial time-dependent reliability analysis of corroding pretensioned prestressed concrete bridge girders. *Struct. Saf.* **29**(1), 16–31 (2007)
6. Y. Deng, G. Morcou, Z.J. Ma, Strand bond stress–slip relationship for prestressed concrete members at prestress release. *Mater. Struct.* **49**(3), 889–903 (2016)
7. T. Dinges, *The History of Prestressed Concrete: 1888 to 1963* (2009)
8. M.P. Enright, M.F. Dan, Probabilistic analysis of resistance degradation of reinforced concrete bridge beams under corrosion. *Eng. Struct.* **20**(11), 960–971 (1998)
9. R. Francois, I. Khan, V.H. Dang, Impact of corrosion on mechanical properties of steel embedded in; 27-year-old corroded reinforced concrete beams. *Mater. Struct.* **46**(6), 899–910 (2013)
10. P. Gardoni, R.G. Pillai, M.B.D. Hueste, K. Reinschmidt, D. Trejo, Probabilistic capacity models for corroding posttensioning strands calibrated using laboratory results. *J. Eng. Mech.* **135**(9), 906–916 (2009)
11. K.A. Harries, Structural testing of prestressed concrete girders from the lake view drive bridge. *J. Bridg. Eng.* **14**(2), 78–92 (2009)
12. S. Iqbal, A. Ali, K. Holschemacher, T.A. Bier, A.A. Shah, Strengthening of RC beams using steel fiber reinforced high strength lightweight self-compacting concrete (SHLSCC) and their strength predictions. *Mater. Des.* **100**, 37–46 (2016)
13. T. Jiang, Q. Kong, P. Zhong, W. Lei, L. Dai, F. Qian, L. Huo, G. Song, Monitoring of corrosion-induced degradation in prestressed concrete structure using embedded piezoceramic-based transducers. *IEEE Sens. J.* **17**(18), 5823–5830 (2017)
14. C. Liu, X. Wang, J. Shi, L. Liu, Z. Wu, Experimental study on the flexural behavior of RC beams strengthened with prestressed BFRP laminates. *Eng. Struct.* **233**, 111801 (2021)
15. G.D. Mancarti, Strengthening California steel bridges by prestressing. *Transp. Res. Rec.* **950**, 183–187 (1984)
16. H. Mutsuyoshi, N. Duc Hai, A. Kasuga, Recent technology of prestressed concrete bridges in Japan, in *IABSE-JSCE Joint Conference on Advances in Bridge Engineering-II* (2010), pp. 46–55
17. E.G. Nawy, *Prestressed concrete, in A Fundamental Approach* (1996)
18. U. Nürnberger, Corrosion induced failure mechanisms of prestressing steel. *Mater. Corros.* **53**(8), 591–601 (2002)
19. R. Parkins, M. Elices, V. Sanchez-Galvez, L. Caballero, Environment sensitive cracking of pre-stressing steels. *Corros. Sci.* **22**(5), 379–405 (1982)
20. R.G. Pillai, P. Gardoni, D. Trejo, M.B.D. Hueste, K.F. Reinschmidt, Probabilistic models for the tensile strength of corroding strands in posttensioned segmental concrete bridges. *J. Mater. Civ. Eng.* **22**(10), 967–977 (2010)
21. R.G. Pillai, M.D. Hueste, P. Gardoni, D. Trejo, K.F. Reinschmidt, Time-variant service reliability of post-tensioned, segmental, concrete bridges exposed to corrosive environments. *Eng. Struct.* **32**(9), 2596–2605 (2010)
22. N.K. Raju, *Prestressed Concrete* (Tata McGraw-Hill Education, 2006)
23. M. Schupack, M.G. Suarez, *Some Recent Corrosion Embrittlement Failures of Prestressing Systems in the United States* (PCI, 1982)

24. J. Toribio, E. Ovejero, Microstructure-based modelling of localized anodic dissolution in pearlitic steels. *Mater. Sci. Eng.* **319**, 308–311 (2001)
25. L. Vehovar, V. Kuhar, A. Vehovar, Hydrogen-assisted stress-corrosion of prestressing wires in a motorway viaduct. *Eng. Fail. Anal.* **5**(1), 21–27 (1998)
26. N.A. Vu, A. Castel, R. François, Effect of stress corrosion cracking on stress–strain response of steel wires used in prestressed concrete beams. *Corros. Sci.* **51**(6), 1453–1459 (2009)
27. L. Wang, X. Zhang, J. Zhang, Y. Ma, Y. Xiang, Y. Liu, Effect of insufficient grouting and strand corrosion on flexural behavior of PC beams. *Constr. Build. Mater.* **53**, 213–224 (2014)
28. X.H. Wang, X.H. Gao, X.L. Liu, Shear behaviour of RC beams with corrosion damaged partial length. *Mater. Struct.* **45**(3), 351–379 (2012)
29. J. Yang, R. Haghani, M. Al-Emrani, Innovative prestressing method for externally bonded CFRP laminates without mechanical anchorage. *Eng. Struct.* **197**, 109416 (2019)

Open Access This chapter is licensed under the terms of the Creative Commons Attribution 4.0 International License (<http://creativecommons.org/licenses/by/4.0/>), which permits use, sharing, adaptation, distribution and reproduction in any medium or format, as long as you give appropriate credit to the original author(s) and the source, provide a link to the Creative Commons license and indicate if changes were made.

The images or other third party material in this chapter are included in the chapter's Creative Commons license, unless indicated otherwise in a credit line to the material. If material is not included in the chapter's Creative Commons license and your intended use is not permitted by statutory regulation or exceeds the permitted use, you will need to obtain permission directly from the copyright holder.



Chapter 2

Mechanical Behaviors of Corroded Prestressing Strands



2.1 Introduction

Corrosion will deteriorate the mechanical properties of the prestressing strands. The unique crystal structure, material composition, and surface micro–macro morphology of the prestressed strand give it typical pitting characteristics [2, 11]. Corrosion can reduce the cross-sectional area of the prestressed strand, contribute to stress concentration, and degrade its mechanical performance.

Under the coupling effects of corrosive environment and stress state, the micro-crack and void may appear on the strand surface, which can damage the material microstructure [2]. Corrosion can change the ultimate strength, elastic modulus, and elongation of strand. Vu et al. [12] investigated the stress corrosion cracking of steel wires, and indicate that the micro-cracks would cause a 25% decrease of elasticity modulus. Naito et al. [10] measured the mechanical properties of corroded prestressing tendons in Lake View Drive Bridge. Data point out that a 30% decrease of strand tensile strength caused by the pit corrosion (corrosion loss is greater than 20%). Gardoni et al. [4, 9] studied the effects of salt spray, grouting, and chloride ion on the mechanical properties of prestressing strands after corrosion, and a time-varying probability model of resistance of corroded prestressing strands was established. Yuan et al. [13] found that the corrosion characteristics and mechanical behavior of prestressed tendons would inevitably have certain differences under different corrosion environments. Accurate simulation of the actual corrosion status is an important prior condition for the study of the mechanical properties of prestressed strands. Compared to the electrochemical accelerated corrosion method, the artificial climate box is closer to the natural corrosion situation. The mechanical behaviors of corroded prestressing strands have not been investigated fully under artificial climate conditions.

Another important problem in studying the mechanical behavior of prestressing strand after corrosion is predicting the constitutive relation. The stress–strain constitutive relation of prestressed steel strand is simplified into elastic-hardening model by Zona et al. [14]. Lu et al. [8] offered a stress–strain constitutive model to predict

the mechanical behavior of strand, which can consider the area damage factor. Lee et al. [6] used the Monte Carlo method to establish a probabilistic forecasting of the ultimate strength of the strand after corrosion. Although there are some experimental and analytical study in the literatures, an overall satisfactory prediction of the constitutive relation of corroded strand has not been achieved, and there are huge differences among existing constitutive models. A general constitutive model of prestressing strand after corrosion needs to be further studied.

The chapter is organized as follows. First, the prestressing strands with different corrosion degrees by the artificial climate conditions is obtained. Then, the size and geometry of corrosion pits are measured and its probability distribution is investigated. Furthermore, static tensile tests are carried out to study the mechanical property of prestressing strands after corrosion. Following this, a constitutive model of corroded prestressing strand is proposed.

2.2 Corrosion Morphology and Microscopic Damage of Strands

2.2.1 Corrosion Morphology of Prestressing Strands

Nineteen specimens were designed, including one uncorroded specimen and 18 corroded specimens, and the test strand is made of 7 twisted wires with a diameter of 15.2 mm. The strand sample's length was 1.5 m. The strand's maximum tensile force was 267 kN, yield strength was 1830 MPa, ultimate strength was 1938 MPa, yield strain was 0.012, ultimate strain was 0.03, elastic modulus was 195 GPa, elongation rate was 5.5%, and weight per meter was 1104 g/m. To simulate the high-stress working status in the actual project, the strand is tensioned on a specially designed steel frame, as exhibited in Fig. 2.1a. The tensioning device was consisted of a steel frame and a special anchorage device. The steel frame was protected by epoxy resin to prevent corrosion. It could stretch two specimens at the same time. A dedicated anchoring device was designed to apply and release the prestressing of the strands, as shown in Fig. 2.1b. The middle cavity of the device was filled with fine sand. When releasing the prestressing force of the strand, it was only necessary to unscrew the stud in order to allow the sand to be released form the reserved hole.

The strand passes through the tensioning device, the pressure sensor, and the steel frame, with an extruded anchor at one end and a secondary tensioning anchor at the other end. Tension stress can be precisely controlled by pressure sensor and secondary tension anchor. The control tension stress of the strand is $0.75f_{py}$ (f_{py} is the yield strength of the strand). Under the action of preloading, the compaction of fine sand in the tensioning device will lead to a certain loss of prestress. Therefore, after the strand is tensor, it needs to be settled for a period of time. After the pressure sensor reads stable, the stress adjustment is performed through the second tensor anchor.

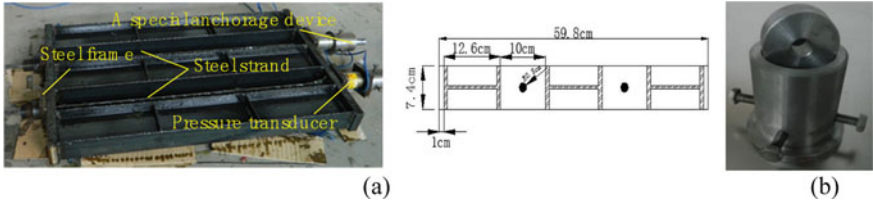


Fig. 2.1 Tensioning device: **a** strand tension steel frame, **b** tension releasing device

After stabilizing stress, the stretching strand sample is placed in an artificial climate environment to corrode the strand. As shown in Fig. 2.2a, the artificial climate test box composed of two parts: external components (condenser, solution storage tank, compressor, and cooling tower, etc.) and a computer central control room, which was used to corrode strand. Four spray nozzles in each upper corner of the climate box were used to generate salt fog, as shown in Fig. 2.2b.

The different corrosion degrees of specimens were obtained by controlling chloride ion concentration, stress level, and corrosion time. Table 2.1 shows the relevant parameters of the specimens. The initial tension stress of the strand was measured by a load cell. The R-series contained five groups, and the initial tension stress was 45% σ_s , where σ_s is the yield strength of the strand. The S-series contained four groups, and the initial tension stress was 75% σ_s . Each group contains two strand samples.

In the test process, it is necessary to check regularly whether the spray nozzle of salt spray is blocked. If it is blocked, it should be dredged in time and observed on the surface of corroded strand every day. The corrosion scenes of R₁₁ in different corrosion time are exhibited in Fig. 2.3. With the increase of corrosion time, the corrosion degree of strands gradually deepens, but each stage has its own corrosion characteristics. In the initial stage, the corrosion of the strand first occurred between the gaps of the steel wires. There was obvious crevice corrosion between the contact surfaces of the steel wires. There were only few local corrosion spots on the surface of the strand. With the increase of corrosion time, the corrosion on the surface of each steel wire of the strand becomes more intense, and the corrosion between the



Fig. 2.2 Artificial climate test box: **a** photo, **b** schematic

Table 2.1 Parameters of specimens

Series	Number		Chloride (%)	Stress level	Corrosion time (d)	Corrosion loss ρ (%)	Average corrosion loss (%)
Control specimen	R ₀	R ₀	–	–	–	0	0
R-series	R ₁	R ₁₁ , R ₁₂	5	$0.45\sigma_s$	30	4.34, 4.56	4.45
	R ₂	R ₂₁ , R ₂₂	5	$0.45\sigma_s$	45	8.89, 8.30	8.60
	R ₃	R ₃₁ , R ₃₂	10	$0.45\sigma_s$	45	9.96, 10.40	10.18
	R ₄	R ₄₁ , R ₄₂	10	$0.45\sigma_s$	60	14.82, 12.38	13.60
	R ₅	R ₅₁ , R ₅₂	15	$0.45\sigma_s$	60	21.30, 27.50	24.40
S-series	S ₁	S ₁₁ , S ₁₂	5	$0.75\sigma_s$	30	6.10, 6.45	6.28
	S ₂	S ₂₁ , S ₂₂	5	$0.75\sigma_s$	45	9.95, 9.57	9.76
	S ₃	S ₃₁ , S ₃₂	10	$0.75\sigma_s$	45	11.74, 10.80	11.27
	S ₄	S ₄₁ , S ₄₂	10	$0.75\sigma_s$	60	17.51, 19.50	18.51

steel wire gaps gradually weakens. The main reason may be that the accumulation of corrosion products in the gaps blocks the propagation of harmful ions, and harmful ions are more likely to spread on the surface of the steel strand. At this stage, the surface corrosion of the strand is relatively uniform, and the corrosion products are all attached to the surface of the steel strand. With the further increase of the corrosion time, the coating layer of the corrosion product on the surface of the strand is peeled off, which directly leads to the intensification of the corrosion loss on the surface of the strand and the appearance of obvious strip-shaped corrosion marks.

The section method was used to measure the corrosion loss of strands. The so-called section method was a method for determining the remaining area of the

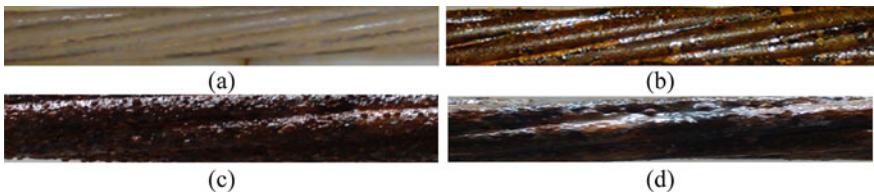


Fig. 2.3 Corroded strands: **a** 0 day; **b** 7th day; **c** 14th day; **d** 30th day

corroded strand by the section contour. First, the prestressing strand was taken out from the steel frame until the corrosion of the steel strand reaches the design corrosion time. Then, the corroded strand was cleaned with 12% hydrochloric acid solution, then neutralized by the alkali. Finally, the most corroded part of the strand was selected as the minimum cross-section of the strand. The strand was cut at the position of the measured section and applied paint on the section. The contour shape of the corroded strand was transferred to cardboard and then scanned into the computer. Through computer-aided software, such as CAD, the cross-sectional area of the rubbing profile was measured with the help of the grid size or reference coordinates, and then a more accurate cross-sectional loss rate was calculated. The corrosion loss of nineteen specimens is given in Table 2.1.

2.2.2 Microscopic Damage of Corroded Strands

After the accelerated corrosion, the LAW-600 electrohydraulic servo universal testing machine was used to stretch the corroded strands, as shown in Fig. 2.4. During the test, the loading speed was controlled by displacement, and the loading was carried out at a rate of 1 mm/min. The load data was automatically read by the tension tester, and the JZ-73 extensometer was used to measure its elongation. The gauge length of the extensometer was 500 mm. In order to prevent the damage to the extension gauge, when the first broken wire of the strand occurred [1], it was considered that the steel strand reached the ultimate tensile force, the extension gauge was removed, and the tensile load–deflection curve of the strand before this stage was obtained. After that, the test was continued at a rate of 2 mm/min until the fracture of each wire of the steel strand, and the effect of corrosion on the fracture shape of the steel strand was observed.

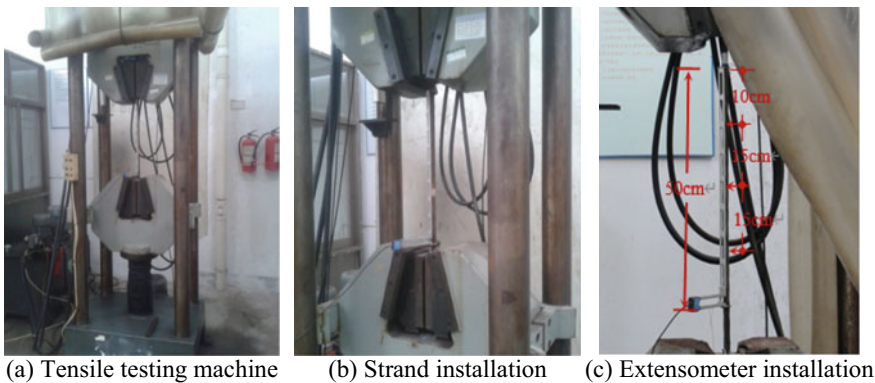


Fig. 2.4 Tensile test of corroded strand

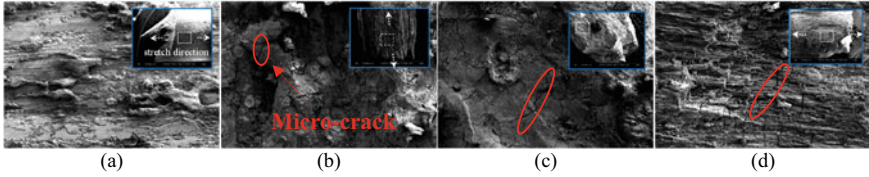


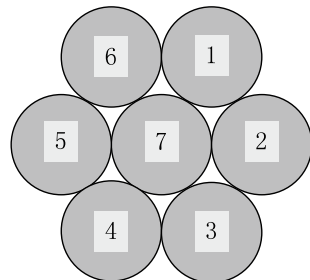
Fig. 2.5 Results of electron microscope scan: a R₀; b R₃₂; c S₃₂; d R₅₂

After the tensile test, a small section of the sample at the fracture of the edge wire of the steel strand was taken out, and the S-3000 N electron microscope was used to scan the electron microscope (SEM), as shown in Fig. 2.5. A total of four samples were taken out in this test, which were obtained from the uncorroded specimens R₀ and R₃₂, S₃₂, and R₅₁ with corrosion time of 45, 45, and 60 days, respectively. The samples were about 10 mm long and were placed in the scanning chamber of the electron microscope to observe the effect of corrosion on the surface morphology of the strand. The surface of the uncorroded sample R₀ was relatively smooth, while different forms of micro-cracks were found on the surface of the steel wire of other corroded specimens. Compared with R₃₂, the number of cracks in S₃₂ increased and the crack width became larger. For severely corroded specimen R₅₂, the crack width was more obvious, and more micro-cracks were found. This shows that the width and depth of micro-cracks on the wire surface increase significantly with the increase of corrosion loss. Comparing with R₃₂ and S₃₂, it can be found that higher stress levels lead to larger corrosion micro-cracks even if the corrosion losses are similar. This means that the high stress level can facilitate the spread of corrosion micro-cracks.

2.3 Corrosion Pits of Prestressing Strands

119 corrosion pits from seven wires of all corroded strands are counted, and the pit geometry is studied. For the convenience of description, the steel wires of each prestressed tendon are numbered, the side wires are numbered from 1 to 6, and the middle wires are numbered as 7, as shown in Fig. 2.6.

Fig. 2.6 Contour shape



The length of the corrosion pit has little effect on the maximum section loss of the steel wire, so the effect on the mechanical properties of the corroded steel wire can be ignored. Therefore, the key parameters of the pit only measure the maximum depth and width of the pit. The maximum width (L/mm) and maximum depth (H/mm) of each pit are measured and recorded using digital calipers and improved micrometers, respectively.

Under the same section loss, the maximum depth and maximum width of different pits are also quite different, as shown in Fig. 2.7. The stress concentration at the pit is mainly reflected in the sudden change of the loss section caused by the shape of the pit. If the sudden change of the loss section is sharp, the stress concentration will be obvious here; if the sudden change of the loss section is smooth, the stress concentration will be weak. The ratio of the maximum depth to the maximum width of the pit (referred to as the aspect ratio, denoted as B) can better reflect the degree of mutation of the loss section, so the key parameters of the pit should also select the depth–width ratio of the pit.

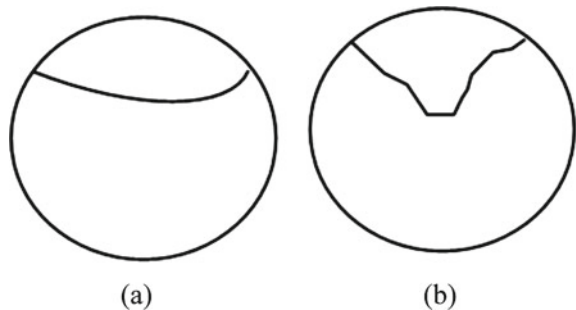
The geometric shape of corrosion pits is measured. There are three types of corrosion pits: spheroidicity, saddle, and pyramid, as shown in Fig. 2.8.

- (1) Spheroidicity pits: The maximum depth is between the pyramid-shaped pit and the saddle-shaped pit, the depth and width are larger than that of the saddle-shaped pit, and the mutation of the loss section is smoother.
- (2) Saddle pits: The maximum depth is small, the maximum width is large, the aspect ratio is small, and the sudden change of the loss section is not obvious.
- (3) Pyramid pits: The maximum depth is large, the aspect ratio is also large, and the loss section is sharply changed.

Statistics show that there were 52 spheroidicity pits, accounting for 44% of the total; 38 saddle pits, accounting for 32% of the total; and 29 pyramid pits, accounting for 24% of the total.

In relative terms, there are more pyramidal pits. This may be because the corrosion of prestressed strands is generally carried out in a point-to-surface sequence. When a certain point is corroded, when the environment and the surface material of the prestressed strand do not change abruptly, the corrosion will continue to expand around it, forming a circular shape on the surface of the prestressed strand. Since

Fig. 2.7 Mutation degree of different loss sections under the same corrosion loss



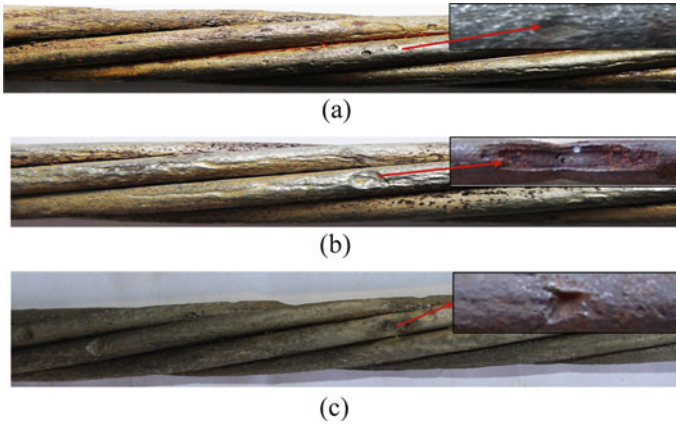


Fig. 2.8 Pit geometry: **a** spheroidicity pit; **b** saddle pit; **c** pyramidal pit

the generated corrosion products have a certain protective effect on the inside of the pit, the expansion of corrosion into the pit will be hindered to a certain extent. In the end, a pyramidal corrosion shape will be formed in the direction of the prestressed section.

2.4 Probability Distribution of Corrosion Pits

2.4.1 Frequency Distribution of Corrosion Pits

Analysis of the statistical data shows that when the corrosion loss of the corroded prestressed strands is 0.78–33.4%, the minimum value of the maximum depth of the pit is 0.12 mm and the maximum value is 2.79 mm; the maximum width has a minimum value of 0.33 mm and a maximum value of 4.45 mm; the depth–width ratio has a minimum value of 0.10 and a maximum value of 1.27. In order to further analyze the probability distribution law of the size parameters of corrosion pits, maximum width, the maximum depth, and depth–width ratio of the 119 pits were represented by frequency histograms, as shown in Fig. 2.9.

It can be seen from Fig. 2.9 that the probability distribution of the maximum depth of the pit obeys the Gumbel extreme value type I distribution, similar to the conclusions drawn in some existing study [2, 5], the maximum width distribution of corrosion pits has poor fit with the commonly used data analysis curves (such as normal distribution curve, lognormal distribution curve and Weibull distribution curve); the probability distribution of the depth–width ratio is very consistent with the lognormal distribution.

The development of corrosion has a certain randomness. In the early stage of corrosion, the surface of the prestressed strand is relatively smooth and easy to

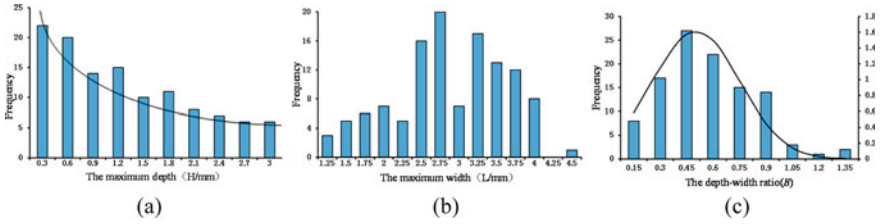


Fig. 2.9 Frequency distribution histogram: **a** depth; **b** width; **c** depth–width ratio

be corroded, thus forming a large number of corrosion pits. With the progresses of corrosion, the development of new pits is limited to a certain extent when the surface of the prestressed strand is occupied by the initial pits, and the corrosion mainly continues on the old pits. Due to the limitation, the expansion rate of the new corrosion pit is slower than that of the initial stage, and the probability that the corrosion area can exceed the old corrosion pit is small. However, after the rapid development of the old corrosion pits in the early stage, the corrosion products will hinder the later corrosion, the corrosion rate of the old corrosion pits slows down, and it is difficult for the rapid development of the old corrosion pits to penetrate the surface of the prestressed strand.

In order to study the relationship between the corrosion loss and the maximum depth, maximum width, and depth–width ratio of the corroded prestressed strand. The relationship between the maximum depth, maximum width, and depth–width ratio of the corrosion pits and the corrosion loss are shown in the Figs. 2.10, 2.11 and 2.12.

The maximum depth function $H(\rho)$, the maximum width function $D(\rho)$, and the depth–width ratio function $B(\rho)$ of corrosion pits are given as follows

$$H(\rho) = 0.5276\ln(\rho) + 0.0017, \tag{2.1}$$

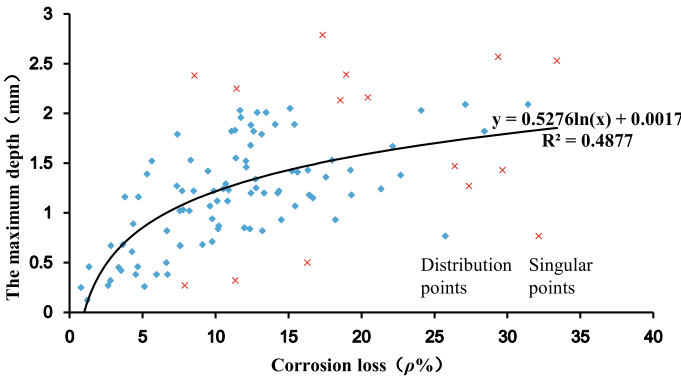


Fig. 2.10 Relationship between maximum depth and corrosion loss

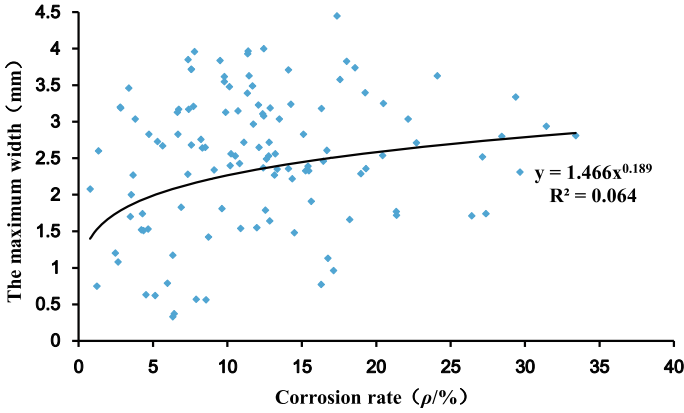


Fig. 2.11 Relationship between maximum width and corrosion loss

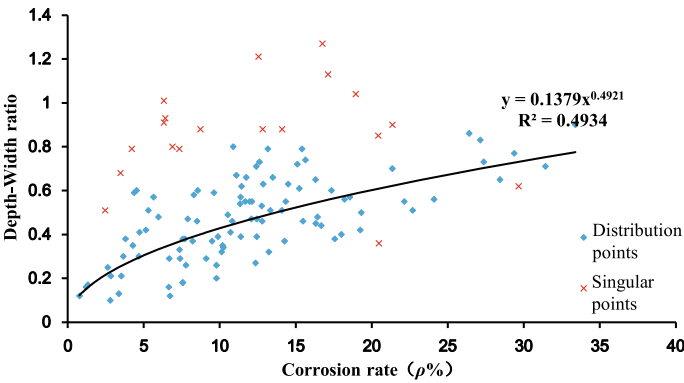


Fig. 2.12 Relationship between depth–width ratio and corrosion loss

$$D(\rho) = 1.466\rho^{0.189}, \tag{2.2}$$

$$B(\rho) = 0.1379\rho^{0.4921}, \tag{2.3}$$

where ρ is the corrosion loss of strand.

From Fig. 2.10, the maximum depth of corrosion pits also increases with the increase of corrosion loss. When the corrosion loss is small, the maximum depth of the pit increases rapidly. When the corrosion loss is large, the growth rate of the maximum pit depth gradually slows down. This is because the corrosion loss is small, the development time of pits is short, and it is still in the initial stage of development. After the formation of corrosion pits, the corrosion can be arbitrarily expanded around, the expansion speed is fast, so the maximum depth of corrosion pits

increases quickly. When the corrosion loss is large, the pit has gone through the initial stage of rapid development, and the pit has been corroded into a certain geometric shape. The corrosion products accumulated in the initial stage are deposited in the corrosion pit, which gradually hinder the corrosion expansion speed, but it cannot prevent the corrosion depth. Therefore, the growth speed of the maximum depth of the corrosion pit decreases, but the maximum depth still increases slowly with the increase of the corrosion loss.

Figure 2.11 represents the relationship between the maximum width and corrosion loss of the corrosion pit. The commonly used regression formula does not have a good applicability to the changes between them. The correlation coefficient R^2 is 0.064; this indicates that the dispersion of the regression curve is too large. As can be seen from Fig. 2.11, the maximum width of corrosion pits does not change much with the increase of corrosion loss, and its value is mainly in the range of 2–4 mm, indicating that corrosion loss has little influence on the maximum width of corrosion pits.

It can be seen from Fig. 2.12 that as the corrosion loss increases, the depth–width ratio of corrosion pits has gradually increased. The depth–width ratio is the ratio of the maximum depth to the maximum width of the pit. As the maximum depth increases with the increase of the corrosion loss, the maximum width shows a certain randomness in the middle width range and has no obvious correlation with the corrosion loss. The depth–width ratio increases with the increase of corrosion loss.

2.4.2 *K–S Test of Pit Size Parameters*

The frequency histogram of pit size parameters is not enough to explain the type of probability distribution, and it needs to be verified by hypothesis testing. Compared with the traditional test method (such as the χ^2 test method), the K–S test method has better adaptability to small samples. Therefore, this section uses the K–S test function to verify that the Gumbel extreme value type I curve has a good adaptability to the maximum depth of pits, and the normal distribution curve has a good adaptability to the distribution of the pit depth-to-width ratio.

In the K–S test, the selected significance level α is 0.05. If the result of the K–S test is less than 0.05, it is considered that “the probability distribution of the maximum depth of pits is Gumbel extreme type I” or “the probability distribution of the pit depth-to-width ratio is a normal distribution” is rejected. If the test result is greater than or equal to 0.05, the hypothesis is proved to be true. The K–S inspection results of the maximum depth and depth-to-width ratio of pits are given in Tables 2.2 and 2.3.

Table 2.2 Statistical analysis of K–S test parameters

	N	Mean	Standard deviation	Minimum	maximum	Percentile		
						25th	50th	75th
Maximum depth	10	11.9000	5.72422	6.00	22.00	6.7500	10.5000	16.2500
Depth–width ratio	9	12.1111	9.22557	1.00	27.00	2.5000	14.0000	19.5000

Table 2.3 K–S test results of the maximum depth and depth–width ratio of corrosion pit

N		Maximum depth	Depth–width ratio
Normal parameters (<i>a</i> , <i>b</i>)	Mean	11.900	12.111
	Std. deviation	5.7242	9.2256
Most extreme differences	Absolute	0.162	0.172
	Positive	0.162	0.172
	Negative	– 0.151	– 0.137
Kolmogorov–Smirnov Z		0.329	0.515
Significance (2-tailed)		0.637	0.824

It can be seen from Tables 2.2 and 2.3 that the significance levels of maximum depth and depth–width ratio of corrosion pits in K–S test are 0.637 and 0.824, respectively, both of which are greater than 0.05. It is proved that the hypothesis is established, the probability distribution of the maximum depth of corrosion pits obeys the Gumbel extreme value type I distribution curve, and the probability distribution of the depth–width ratio obeys the normal distribution curve.

The probability distribution function of the pit depth-to-width ratio of the corroded prestressing strand is

$$f(x) = \frac{1}{\sqrt{2\pi}\sigma} \exp\left[-\frac{(x - \mu)^2}{2\sigma^2}\right] = 0.7459 \exp\left[-\frac{(x - 12.11)^2}{170.2234}\right]. \quad (2.4)$$

The probability distribution of corrosion pit depth can be expressed as

$$f(x) = \exp\left[-\exp\left(\frac{x - 9.3226}{4.4654}\right)\right]. \quad (2.5)$$

2.5 Mechanical Behavior of Corroded Prestressing Strands

2.5.1 Relation Between Load and Displacement

The sample’s load–deformation curves are shown in Fig. 2.13. For corroded strand specimens, the load–deformation curve is greatly affected by corrosion. With the increase of corrosion time, the ultimate load and deformation of strands are reduced to a certain extent. The load–deformation curves of all the specimens are basically the same in the elastic stage, and the difference is mainly manifested after the yielding of the steel strand. The load–deformation curve of the uncorroded strand R₀ includes three stages: elastic stage, yielding stage, and hardening stage. An obvious plastic deformation at the hardening stage was found after R₀ fractures. For strand specimens with slight corrosion ($\rho \leq 10.4\%$), the load–deformation curve is divided into two distinct stages: the elastic deformation stage before yielding and the elastic–plastic deformation stage after yielding. The ultimate deformation of corroded strand specimens decreases with the increase of corrosion loss. However, the strand specimens with severe corrosion ($\rho > 10.4\%$), the load–deformation curve of the steel strand only has an elastic deformation stage. When the yield load is reached, the strand will break immediately and its ultimate deformation will be significantly reduced. This suggests that corrosion causes a reduction in the ductility of the strand.

2.5.2 Ultimate Strength, Strain, and Elastic Modulus

The ultimate strength of corroded strand can be written as follows

$$f_{pu,c} = \frac{F_{pu,c}}{A_{sc}} = \frac{F_{pu,c}}{F_{pu}} \cdot \frac{F_{pu}}{A_{s0}} \cdot \frac{A_{s0}}{A_{sc}} = \mu \cdot \frac{f_{pu}}{1 - \rho}, \tag{2.6}$$

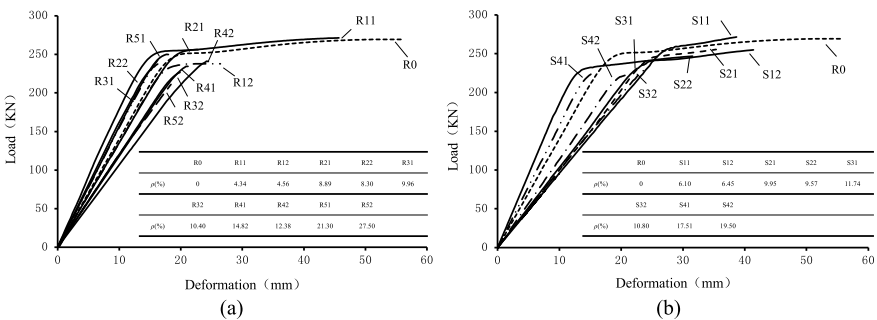


Fig. 2.13 Load–deformation curves of strands: a R-series, b S-series

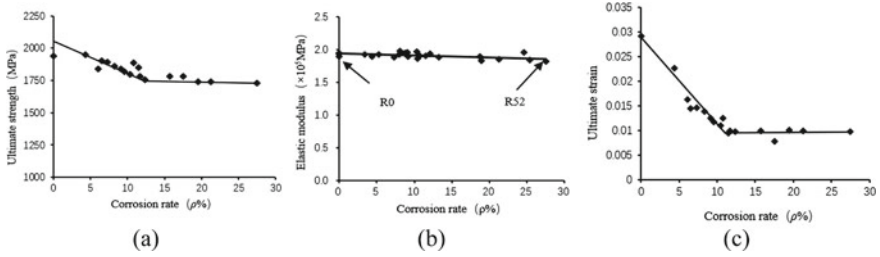


Fig. 2.14 Mechanical behavior of strand: **a** ultimate load; **b** elastic modulus; **c** ultimate strain

where $f_{pu,c}$ is the ultimate strengths of corroded strand, f_{pu} is the ultimate strengths of uncorroded strands; A_{s0} is the section area of uncorroded strand, $A_{s0} = 140 \text{ mm}^2$; A_{sc} is the minimum cross-sectional area of corroded strand; $F_{pu,c}$ is the maximum tensile loads of corroded strand, F_{pu} is the maximum tensile loads of uncorroded strands; and μ is the ultimate load ratio, $\mu = F_{pu,c}/F_{pu}$.

A double broken line is employed to describe the relation between ultimate strength and strand corrosion loss, as exhibited in Fig. 2.14a. The relation between ultimate load ratio (μ) and strand corrosion loss (ρ) is calculated as

$$\mu = \begin{cases} 0.95 - 0.25\rho & \rho \leq 10.4\% \\ 1 - 0.65\rho & \rho > 10.4\% \end{cases} \quad (2.7)$$

When the corrosion loss of strand is low ($\rho_c < 10.4\%$), its ultimate strength of corroded strands will drop rapidly. After that, the rate of decline in ultimate strength will differ, exhibiting a slower downward trend. At the same time, the propagation of corrosion micro-cracks will reduce the mechanical properties and ultimate strength of the strand significantly.

The relation between elastic modulus and corrosion loss is further presented to elucidate the elastic modulus of corroded strand, as exhibited in Fig. 2.14b. An effective method proposed by [7] was used to calculate the elastic modulus of corroded strand: disassemble the corroded strand into n parts, and then the elongation of corroded strand Δl is the sum of the elongation of n units; following this, the elastic modulus of corroded strand E_C , defined as the ratio of the stress σ and strain ε of corroded strand, is given as

$$E_c = \frac{\sigma}{\varepsilon} = \frac{F/A_{sc}}{\Delta l/l_0} = \frac{F \cdot l_0}{\Delta l \cdot A_{sc}}, \quad (2.8)$$

$$\Delta l = \sum_{i=1}^n \Delta l_i = \frac{Fl_0}{nE_p} \sum_{i=1}^n \frac{1}{A_{si}}, \quad (2.9)$$

where E_p is the elastic modulus of uncorroded strand; E_C is the elastic modulus of corroded strand; Δl is the elongation of corroded strand; l_0 is the gauge length of

the extensometer; F is the applied load; Δl_i is the elongation of the i th element of corroded strand, and A_{si} is the minimum section area of the i th element of corroded strand.

As Fig. 2.14b shows, comparing R_0 with R_{52} , the similar elastic modulus is found although they have different corrosion degrees, and the difference between them is only 6.67%. R_{52} is the most seriously corroded specimen in the all specimens, which had a large crack length and crack width on its surface. The similar conclusions have also been found in [3, 7]. The elastic modulus of corroded strand has been investigated, and it is found that there is only a slight change in the elastic modulus of corroded strand. Therefore, it is considered that corrosion has less impact on elastic modulus of strand.

The ultimate strain of corroded strand is given in Fig. 2.14c. The ultimate strain ratio (β) is used to reflect the effect of corrosion on ultimate strain, which is defined as the ratio of the ultimate strains of strand after corrosion to that of uncorroded strand. The relationship between ultimate strain ratio (β) and strand corrosion loss (ρ) is written as

$$\beta = 1 - 6.2\rho \quad \rho \leq 10.4\%. \quad (2.10)$$

When the degree of corrosion is low ($\rho_c < 10.4\%$), the increase in the ultimate strain of strand is almost linearly reduced; when the corrosion loss of strand is more than 10.4%, a little change has been found in the ultimate strain of corroded strands with the increase of corrosion loss.

2.6 Constitutive Model of Prestressing Corroded Strands

In this chapter, a simple and practical constitutive model is proposed. Zona et al. [14] found that the elastic-hardening model can describe a prestressing strand's stress-strain curve. Corrosion has little effect on the stress-strain curve in the elastic stage of the steel strand but has a greater effect on the stress-strain curve after yielding. The stress-strain curve of slightly corroded strands can be represented by a bilinear model, but the ultimate strength will decrease as the corrosion degree increases. The stress-strain curve will degrade into a single-linear model once the corrosion loss exceeds the critical value.

According to the above test results and assumptions, a simplified constitutive model of the corroded prestressing strands can be established, as exhibited in Fig. 2.15. The prestressing strand has no apparent yield point because it is high-strength steel wire. Under the code of GB/T 50010-2010 [1], for prestressing strand, the nominal yield strength is 85% of the tensile strength. The elastic modulus of the corroded strand can be evaluated by the uncorroded strand's elastic modulus. According to the observation results of experimental study, the critical corrosion loss is about 10.4%. The constitutive model of the prestressing corroded strand can be expressed as

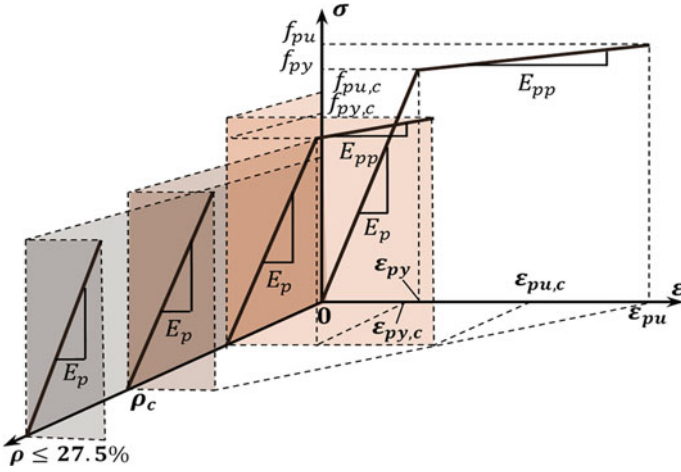


Fig. 2.15 Constitutive model of corroded prestressing strands

$$\sigma = \begin{cases} \rho \leq \rho_c & \begin{cases} E_p \varepsilon & \varepsilon \leq \varepsilon_{py,c} \\ f_{py,c} + E_{pp}(\varepsilon - \varepsilon_{py,c}) & \varepsilon_{py,c} < \varepsilon \leq \varepsilon_{pu,c} \end{cases} \\ \rho > \rho_c & E_p \varepsilon & \varepsilon \leq \varepsilon_{py,c} \end{cases}, \quad (2.11)$$

$$f_{py,c} = 0.85 f_{pu,c} = 0.85 \cdot \frac{\mu}{1 - \rho} \cdot f_{pu} (\rho \leq \rho_c), \quad (2.12)$$

$$E_{pp} = \frac{f_{pu,c} - f_{py,c}}{\varepsilon_{pu,c} - \varepsilon_{py,c}} = \frac{0.15\mu \cdot f_{pu} \cdot E_p}{(1 - \rho)E_p \cdot \beta \cdot \varepsilon_{pu} - 0.85\mu \cdot f_{pu}}, \quad (2.13)$$

where σ is the stress, ε is the strain, $\varepsilon_{pu,c}$ is the ultimate strains of corroded strand, ε_{pu} is the ultimate strains of uncorroded strand, and $\varepsilon_{pu,c} = \beta \varepsilon_{pu}$, $f_{py,c}$ is the yield strength of corroded strand, $\varepsilon_{py,c}$ is the yield strain of corroded strand, $\varepsilon_{py,c} = f_{py,c}/E_p$, E_{pp} is the hardening modulus of prestressing strand after yielding.

In order to prove the applicability of the simplified constitutive model of the corroded prestressing strands, the simplified constitutive model is used to predict the stress–strain curve of specimens R₁₂, R₃₂, R₅₂, S₁₁, S₂₁, and S₄₁, and compare it with the measured curve, as shown in Fig. 2.16. For all the specimens, the measured stress–strain curves are in good agreement with the predicted curves. It has been found that there are slight deviations between the two curves. These errors are mainly caused by two reasons, one is the uncertainty of experimental data, the other is the simplification of the model. Considering the complexity of corrosion process, the proposed model can be used to predict the stress–strain curve of prestressed strand after corrosion due to its good prediction accuracy.

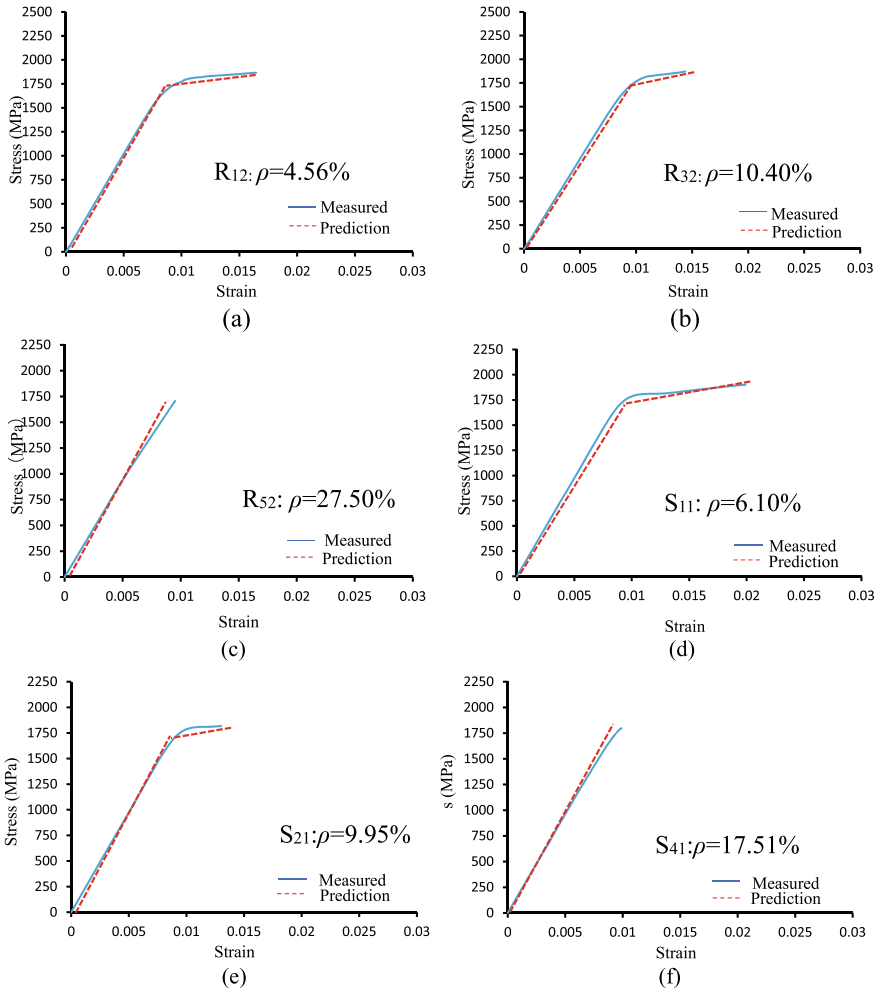


Fig. 2.16 Predicted and experimental curves: a R_{12} ; b R_{32} ; c R_{52} ; d S_{11} ; e S_{21} ; f S_{41}

2.7 Conclusions

1. The corrosion of the prestressed strand in the artificial climate environment first occurs between the gaps between the steel wires, and then the corrosion is transferred to the surface of the prestressed strand. The outer surface of the prestressed corroded strand erosion is obvious, the corrosion between the crevices of the inner prestressed strand is relatively slight.
2. A total of 119 corrosion pits are counted to investigate the geometric configuration of corrosion pits, and the geometric shapes of the corrosion pits are mainly divided into three categories: saddle pit, pyramid pit, and spheroidicity pit. Among these

three types of the corrosion pits, the number of spheroidicity pits is relatively large.

3. The probability distribution of the maximum depth of the pit obeys the Gumbel extreme value type I distribution, and the maximum width distribution of pits has poor fit with the commonly used data analysis curves. The depth–width ratio obeys the lognormal distribution, which is employed to reflect the corrosion morphology of steel wires.
4. There are some micro-cracks in the corroded strand under high stress. With the increase of corrosion loss, the width and depth of these micro-cracks gradually increase, but there is no obvious regularity in their length and propagation direction. The propagation of corrosion micro-cracks has a great effect on ultimate strength of strand but has a little effect on elastic modulus.
5. A simple and practical constitutive model is proposed to predict the stress–strain curve of corroded prestressing strand. With the increase of corrosion degrees, the stress–strain curve of the corroded strand gradually transforms from a bilinear model to a single-linear model.

References

1. Chinese Standard GB/T 50010-2010, *Code for Prestressed Concrete* (Ministry of Housing and Urban-Rural Development, Beijing, 2010) (in Chinese)
2. M. Darmawan, M. Stewart, Effect of pitting corrosion on capacity of prestressing wires. *Mag. Concr. Res.* **59**(2), 131–139 (2007)
3. R. François, I. Khan, V.H. Dang, Impact of corrosion on mechanical properties of steel embedded in 27-year-old corroded reinforced concrete beams. *Mater. Struct.* **46**(6), 899–910 (2013)
4. P. Gardoni, R.G. Pillai, M.B.D. Hueste, K. Reinschmidt, D. Trejo, Probabilistic capacity models for corroding posttensioning strands calibrated using laboratory results. *J. Eng. Mech.* **135**(9), 906–916 (2009)
5. C.-H. Jeon, J.-B. Lee, S. Lon, C.-S. Shim, Equivalent material model of corroded prestressing steel strand. *J. Market. Res.* **8**(2), 2450–2460 (2019)
6. J. Lee, Y.-J. Lee, C.-S. Shim, Probabilistic prediction of mechanical characteristics of corroded strands. *Eng. Struct.* **203**, 109882 (2020)
7. X. Liu, W. Zhang, X. Gu, Y. Zeng, Degradation of mechanical behavior of corroded prestressing wires subjected to high-cycle fatigue loading. *J. Bridg. Eng.* **22**(5), 04017004 (2017)
8. Z. Lu, F. Li, Y.G. Zhao, An Investigation of degradation of mechanical behaviour of prestressing strands subjected to chloride attacking, in *International Conference on the Durability of Concrete Structures*, Shenzhen, China, June 2016 (Shenzhen University, Shenzhen, China, 2016)
9. R.G. Pillai, P. Gardoni, D. Trejo, M.B.D. Hueste, K.F. Reinschmidt, Probabilistic models for the tensile strength of corroding strands in posttensioned segmental concrete bridges. *J. Mater. Civ. Eng.* **22**(10), 967–977 (2010)
10. C. Naito, R. Sause, I. Hodgson, S. Pessiki, T. Macioce, Forensic examination of a noncomposite adjacent precast prestressed concrete box beam bridge. *J. Bridg. Eng.* **15**(4), 408–418 (2010)
11. W. Vélez, F. Matta, P. Ziehl, Electrochemical characterization of early corrosion in prestressed concrete exposed to salt water. *Mater. Struct.* **49**(1), 507–520 (2016)
12. N.A. Vu, A. Castel, R. François, Effect of stress corrosion cracking on stress-strain response of steel wires used in prestressed concrete beams. *Corros. Sci.* **51**(6), 1453–1459 (2009)

13. Y. Yuan, Y. Ji, S.P. Shah, Comparison of two accelerated corrosion techniques for concrete structures. *ACI Struct. J.* **104**(3), 344–347 (2007)
14. A. Zona, L. Ragni, A. Dall’Asta, Finite element formulation for geometric and material nonlinear analysis of beams prestressed with external slipping tendons. *Finite Elem. Anal. Des.* **44**(15), 910–919 (2008)

Open Access This chapter is licensed under the terms of the Creative Commons Attribution 4.0 International License (<http://creativecommons.org/licenses/by/4.0/>), which permits use, sharing, adaptation, distribution and reproduction in any medium or format, as long as you give appropriate credit to the original author(s) and the source, provide a link to the Creative Commons license and indicate if changes were made.

The images or other third party material in this chapter are included in the chapter’s Creative Commons license, unless indicated otherwise in a credit line to the material. If material is not included in the chapter’s Creative Commons license and your intended use is not permitted by statutory regulation or exceeds the permitted use, you will need to obtain permission directly from the copyright holder.



Chapter 3

Corrosion-Induced Cracking of Prestressed Concrete



3.1 Introduction

Strand corrosion is considered as a significant deteriorating factor in existing reinforced concrete (RC) structures [4, 11]. The metallic iron can be changed to corrosion products after corrosion [2, 17]. The expansion pressure caused by corrosion around the concrete can induce the concrete cracking. Concrete cover cracking is regarded as an indicator of the durability for concrete structures [24].

A lot of research on the concrete cracking induced by steel corrosion has been carried out, which is made up of three aspects: experimental research, theoretical analysis, and numerical simulation. The electrochemical rapid corrosion method is mostly used in the corrosion expansion test; the effect of various parameters on corrosion products and crack propagation is studied systematically, such as the diameter of steel bars, concrete strength, corrosion current density, the thickness of concrete cover, and the type of steel bars. At present, a lot of achievements have been made in the experimental study on concrete cracking induced by steel corrosion. The rust expansion ratio increases with the increase of the strength of concrete and the thickness of concrete cover and decreases with the increase of steel diameter. Comparing the concrete cover cracking induced by steel corrosion under natural corrosive environment and rapid corrosion conditions, rust will not be filled in the corrosion-induced cracks before the surface of concrete cracks under rapid corrosion conditions, while the accumulation and filling of rust are simultaneously carried out in natural corrosive environment [3]. Stirrups can effectively restrict the propagation of cracks, and some scholars have also studied the different forms of corrosion-induced cracking between the stirrups with corrosion and the stirrups without corrosion [5]. Since the experimental research can only consider the influence of some factors on the concrete cracking induced by steel corrosion, how to adopt a unified test method for obtaining the effective test data is a significant issue for future research.

Many theoretical models of corrosion-induced concrete cracking are based on the uniform corrosion. According to the deformation characteristics of the corrosion

products and the situation that the corrosion products enter the cracks during the propagation of concrete cracks induced by strand corrosion [12], the residual strength of cracked concrete and corrosion products is considered or not considered. By introducing the elasticity theories, fracture mechanics, or damage mechanics, the formula for calculating the corrosion loss and the time of corrosion-induced cracking are established by employing the mechanical model of single-layer cylinder or double-layer cylinder [31]. The elastic mechanics model supposes that the concrete around the strands is a homogeneous linear elastic material, and the strand is uniformly corroded. The volume expansion of corrosion products increases uniformly. The concrete cover is completely cracked when the expansive pressure reaches the concrete tensile strength. The elastic mechanics model can better describe the corrosive cracking behavior of the ideal cylinder under the action of uniform expansion force. However, using the elastic mechanics theory model is inevitably unreasonable as the concrete is a quasi-brittle material mixed with multiple materials. For this reason, the fracture mechanics, damage mechanics, and other theories are developed further.

Fracture mechanics can consider the initial cracks and defects in the concrete, and crack initiation and propagation under the corrosion expansion of the strand. Damage mechanics can better consider the damage and the cracking process of the concrete cover. Some scholars have also simulated the stiffness degradation of the concrete cover by considering the stiffness degradation factor and have used the energy principle to calculate the degradation factor [16]. The supposition of uniform corrosion will underestimate the internal stress generated by corrosion products. With further theoretical research, some scholars have studied the propagation of longitudinal cracking under the influence of factors, such as non-uniform corrosion and applied loads [21]. Although the theoretical model can analyze the effects of various parameters on corrosion-induced cracking, how to accurately consider material properties, non-uniform corrosion, and loading effects is still difficulties in the current research.

The correct simulation of the expansive pressure at the steel–concrete interface is the key to realize the numerical simulation of concrete cracking induced by corrosion. The expansive pressure can be simulated by virtual internal pressure, temperature expansion ring, or radial displacement to obtain the mechanical response and the process of the concrete cover cracking induced by corrosion. The load/displacement distribution form and the process of concrete cover cracking induced by corrosion can be obtained by the finite element analysis method. Some scholars have considered the concrete anisotropy, and the cracking process is simulated by a two-dimensional lattice model and an embedded finite element model with bonded cracks [8]. Some scholars also used the Gaussian function to describe the state of non-uniform corrosion. The parameters of the finite element model include non-uniform coefficient, diffusion coefficient and uniform coefficient. This model describes the non-uniform corrosion well [22]. Three-dimensional (3D) model has recently been utilized to investigate concrete cracking induced by steel corrosion, which can simulate the longitudinal cracks in concrete. How to realistically simulate the concrete cover cracking process induced by steel corrosion is still a difficulty.

Existing research mainly focuses on the concrete cover cracking induced by steel corrosion in RC structures, and there are few reports on the corrosion-induced concrete cover cracking induced by strand corrosion in prestressed concrete (PC) structures. In PC structures, the prestressed strands are in a state of high stress for a long time, and the corrosion loss is higher than that of ordinary bars in the erosive environment. Furthermore, prestressing strands are usually larger in diameter, corrosion can easily cause concrete cracking.

The arrangement of this chapter is as follows. First, experimental study on concrete cover cracking induced by strand corrosion in PC structures are introduced. Next, theoretical models of the corrosion-induced cracking are proposed. Then, the numerical model is built to investigate the corrosion-induced concrete cover cracking considering helical strand.

3.2 Experimental Study on Corrosion-Induced Cracking

3.2.1 Filling of Strand Corrosion Products

3.2.1.1 Measurement of Crack Width and Strand Corrosion Loss

Twelve specimens were cast. All specimens had a cross-section of 150 mm × 150 mm, and the beam length was 1200 mm. Two groups, group S (no stirrups) and group RS, were designed to study the influence of stirrups. Each group is made up of six specimens. A seven-wire steel strand was arranged in the beam, and its diameter was 15.2 mm. Stirrups were arranged in the group RS, which had 8 mm diameter and 150 mm spacing. The HRB335 deformed bars arranged as constructional reinforcements in concrete had a 10 mm diameter. The details of specimens are shown in Fig. 3.1.

Crack widths in the specimens were obtained using artificial accelerated corrosion method [28]. To verify the independent influence of strand corrosion on concrete

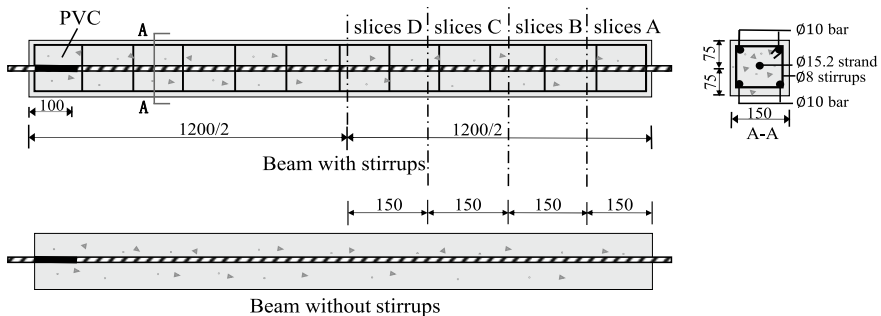


Fig. 3.1 Schematic diagram of the beams (Unit mm)

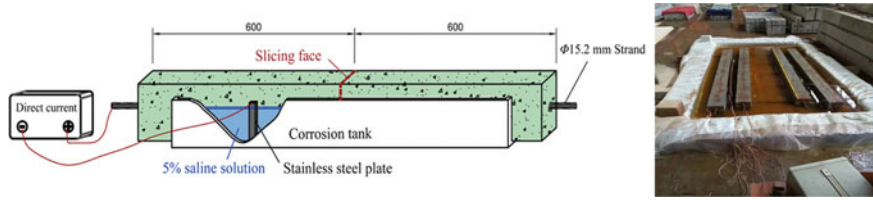


Fig. 3.2 Accelerated corrosion device

cracking, the surface of reinforcement was coated with epoxy resin to prevent it from corrosion. All specimen beams were immersed in the 5% NaCl solution in a designed tank. A direct current potentiostat and a stainless-steel plate were made up the corrosion system. The anode was the strand, and the cathode was the stainless-steel plate (Fig. 3.2).

The corrosion current was 0.3 A, and the current density used in the laboratories was about $270 \mu\text{A}/\text{cm}^2$. The specimens of group S were S6, S9, S10, S11, S12, and S13, and the corrosion time were 2, 9, 7, 3, 5, and 6 days, respectively. The specimens of group RS were RS3, RS7, RS9, RS10, RS11, and RS12, and the corrosion time was 7, 8, 14, 9, 3, and 3 days, respectively.

After accelerated corrosion of specimens, the longitudinal cracks could be found on the concrete surface. Due to the uncertainty of corrosion and material properties, there are different cracking widths in various regions. The crack widths were measured using a portable microscope, which has a 0.01 mm resolution.

Four cross-sectional slices with the thickness of 15 mm were cut out from each specimen, which were employed to investigate the radial crack pattern and the filling of corrosion products in the cracks. Figure 3.1 shows the locations of slices. The distribution of cracks in the radial direction can be described by the cracking angle. Due to the different filling positions of corrosion products in cracks, the filling of corrosion products in cracks can be reflected by the average rust-filling depth. The cracking angle was measured with a contour gauge. First, the contour shape of the crack in the radial direction on the graphic paper was drawn. After that, the concrete slices were crumbled. The filling shape of corrosion products in cracks was drawn on the graphic paper. Subsequently, two sketch maps were scanned into the computer. Finally, the aided drafting program was used to determine the cracking angle and the rust-filling depth.

The corrosion degree of strand was evaluated by measuring the average mass loss of the strand in 10 mm length. To measure the mass loss of corroded strand, the following procedure can be followed. First, the destructive method was used to remove the concrete cover. Next, the surface of the concrete was removed by slight knocking, and the strand was taken out. Following this, the strand was cleaned by 12% hydrochloric acid solution. Finally, the average mass loss of strand was measured in 10 mm length.

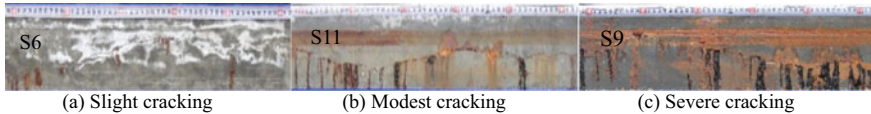


Fig. 3.3 Cracks and corrosion products on the surface of concrete

The first visible crack induced by strand corrosion was observed on the concrete by the portable microscope. Then the width of the crack became wider. A lot of corrosion products filled in cracks with the increase of corrosion products. The corrosion products filled the crack so much that these products flowed out from the longitudinal crack. Figure 3.3 exhibits the corrosion products on the surface of S6, S11, and S9, which range between 10 and 110 mm. The average crack widths of S6, S11, and S9 were 0.13, 0.48, and 0.83 mm, respectively. As the number of cracks increase, the more corrosion products adhere on the concrete surface.

The corrosion degree prediction of strands is an important part of evaluating the structural performance degradation. The crack width at every 10 mm position and the mass loss of strand were measured in the present study, as shown in Fig. 3.4.

As shown in Fig. 3.4, the width of cracks increases with the increase of the corrosion loss. The cracks at the mid-span position are wider than those of the end of the beam; the reason is that the mid-span of beam is immersed in the NaCl solution during the process of corrosion. Comparing with other position, corrosion is more severe on the strands at the mid-span position. Furthermore, the crack width is relatively large.

The relation between crack width and corrosion loss is described by the linear regression, which was used for analyzing the influence of stirrups on crack width. The relation is given in Fig. 3.5.

As Fig. 3.5 shows, corrosion of strand can accelerate the cracking of concrete cover. Stirrups can restrict the propagation of cracks induced by strand corrosion. In the case of similar corrosion loss, the crack widths of concrete in group S are wider than that in group RS. Stirrups used in structures can reduce the corrosion-induced crack width, which indicates that increasing the number of stirrups can restrict the propagation of cracks.

3.2.1.2 Cracking Propagation

The characteristics of internal cracks in concrete are a significant issue to study the cracking of concrete cover. The external cracks are easily to observe, but the feature of cracks in concrete is difficult to observe. Specimens were cut into slices for analyzing the feature of cracks in the radial direction. Figure 3.6a exhibits three cracks in a slice and labeled as: crack A, crack B, and crack C.

As shown in Fig. 3.6, a crack in the cross-section has three branches: crack A, crack B, and crack C. Since crack A was an internal crack, it did not extend to the concrete surface. By contrast, both crack B and crack C extended to the surface of

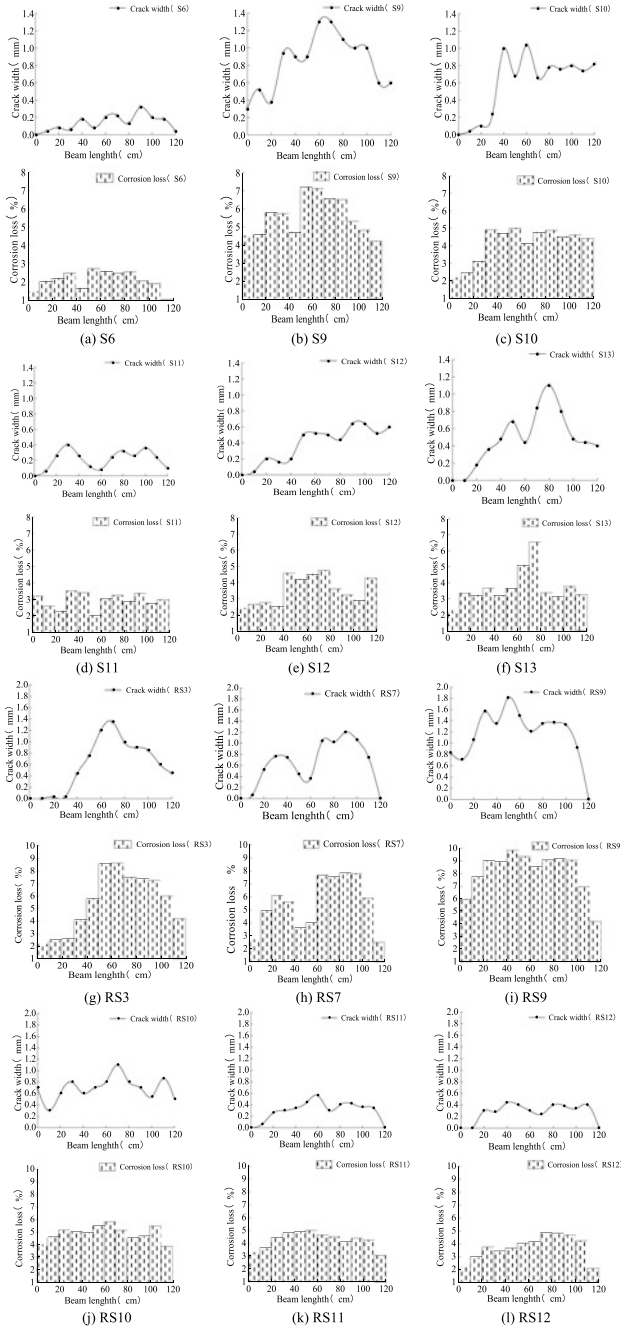


Fig. 3.4 Crack width and corrosion loss of group S and group RS

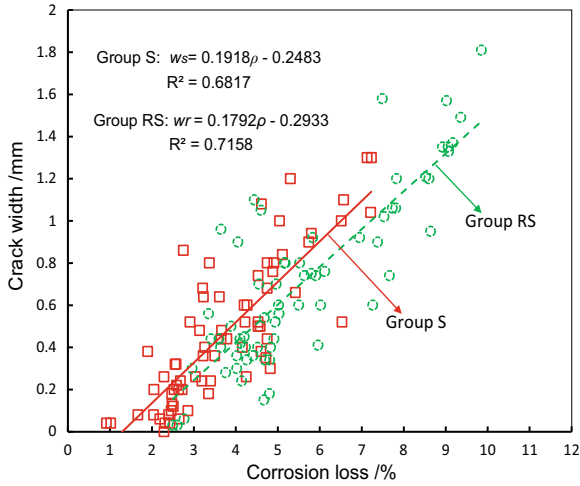


Fig. 3.5 Relation between crack widths and corrosion losses

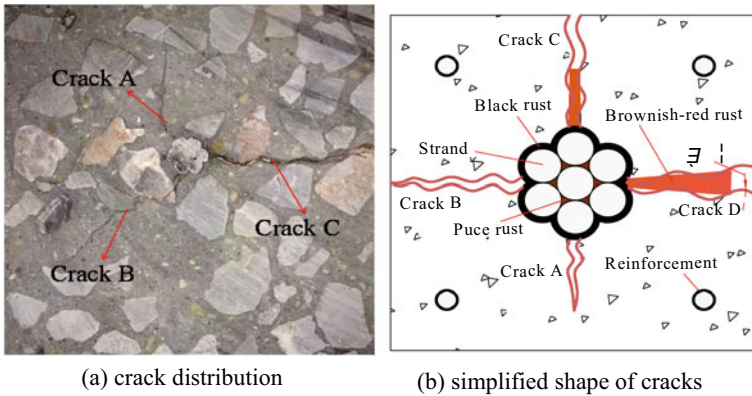
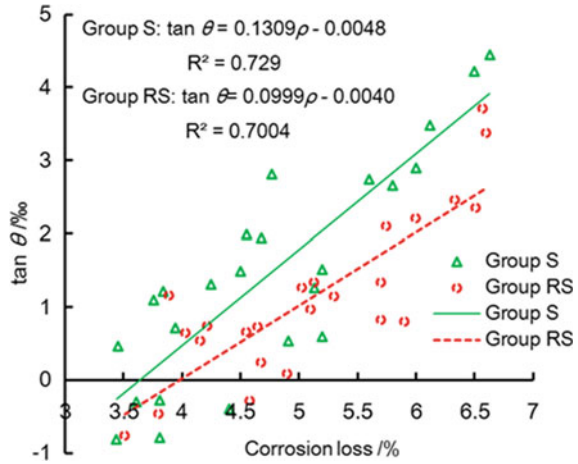


Fig. 3.6 Schematic diagrams of the crack propagation

concrete. It was found that the width of the crack C was the largest and became wider with increased radius. Due to the presence of aggregate near the bifurcation point, the cracks will be separated.

The crack width is different with different corrosion degrees. Figure 3.6b shows the feature of crack propagation. The cracks show different shapes at different stages and can be classified into three shapes, namely triangle, rectangle, and trapezoid. Before the appearance of the cover crack, the shape of internal cracks in concrete can be considered as a triangle (crack A). As the increase of corrosion degree, the crack extends to the surface of concrete (crack B), and the shape looks like a triangle. After the concrete crack is observed on the concrete surface, the crack width becomes

Fig. 3.7 Tangent of cracking angle and corrosion loss



larger, and the width is almost the same. At this time, the shape of crack is a rectangle (crack C). As the corrosion degree further increases, the crack widens. The shape of crack is simplified as a trapezoid (crack D). The corrosion products will accumulate at the interface between the strand and concrete and extend to the concrete surface. After this process, the crack shape will change from triangle to rectangle.

Figure 3.6b shows the schematic diagram of cracking angle θ . The change of the radial crack width is mainly represented by the cracking angle. When the crack in the radial direction narrows, the value of the cracking angle is below zero, and when the cracking angle is zero, the radial crack width is similar. After that, the crack width of the concrete surface exceeds the crack width of interface, and the value of the crack angle is larger than zero. The relation between $\tan \theta$ and corrosion loss is shown in Fig. 3.7.

As corrosion degree increases, the tangent of cracking angle will further increase. There are uncertainties in the measurement of both crack width and corrosion loss, which may be the reason for the discretization of the correlation between $\tan \theta$ and corrosion loss. In the present study, the relation between $\tan \theta$ and corrosion loss can be described by using the linear regression, and is given as follows

$$\tan \theta = a\rho - b. \tag{3.1}$$

3.2.1.3 Filling of Corrosion Products in Cracked Concrete

The concrete slices were disassembled for observing the filling of corrosion products in cracks. Figure 3.8 exhibits the concrete slices profiles of S6B, S9A, and S9C, respectively. Corrosion products mainly filled in the widest crack. Few corrosion products could be found in another small crack; the filling of corrosion products is

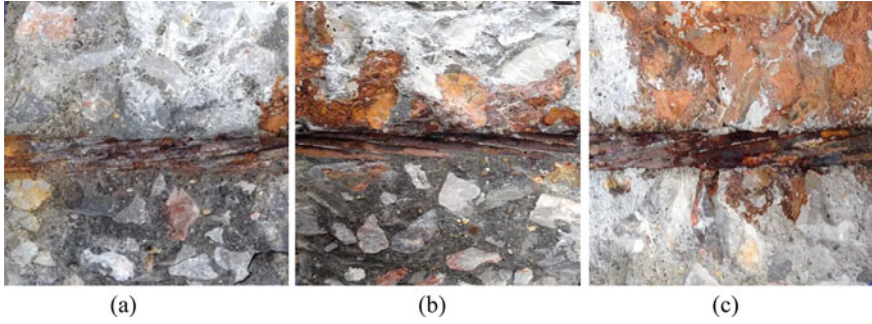


Fig. 3.8 Filling of corrosion products in cracks

shown in Fig. 3.8. The upper part of the profile is the location of the widest crack and the bottom part is the broken surface.

The filling of corrosion products depends on crack widths of concrete. By measuring the crack width of three concrete slices in Fig. 3.8, the crack widths were 0.08, 0.39, and 0.91 mm, respectively. Because corrosion products are more likely to accumulate in wide crack, corrosion products are the largest in the wide crack. The increase of crack widths can accelerate the propagation of corrosion products.

It is difficult to directly obtain the volume of corrosion products in the experimental testing. Correspondingly, the volume of corrosion products can be obtained through the rust-filling depth. After that, the rust-filling ratio f in the experimental testing can be represented by using the rust-filling depth R_i . The filling of corrosion products in the concrete slice can be represented by employing the average rust-filling depth. The filling of corrosion products can be reflected by the rust-filling ratio f , which is expressed as

$$f = \frac{R_i}{C}, \quad (3.2)$$

where C is the concrete cover.

By observing the experimental phenomena, it can be found that corrosion products cannot completely fill cracks even if the crack width is wide. As a result, the rust-filling ratio is below 1.0. The relation between rust-filling ratio and crack width is shown in Fig. 3.9.

As shown in Fig. 3.9, the fitting precision of linear regression is lower than that of polynomial regression. For both groups in the present study, two regression rust-filling ratio curves of group RS and group S are proposed as follows

$$f_s = \begin{cases} -0.773w_s^2 + 1.515w_s + 0.1353; & w_s \leq 0.79 \text{ mm} \\ 0.85; & w_s > 0.79 \text{ mm} \end{cases}, \quad (3.3a)$$

$$f_r = \begin{cases} -1.4938w_r^2 + 2.2011w_r + 0.085; & w_r \leq 0.63 \text{ mm} \\ 0.88; & w_r > 0.63 \text{ mm}, \end{cases} \quad (3.3b)$$

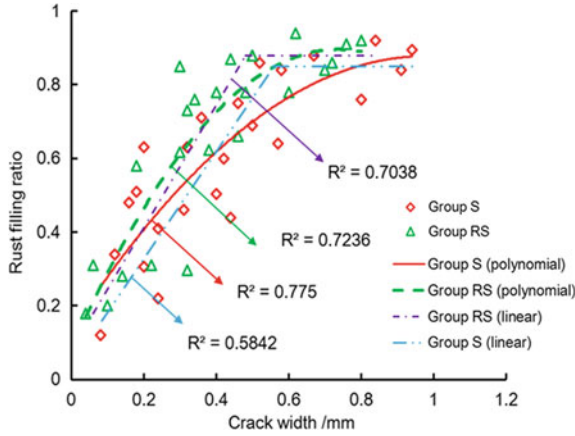


Fig. 3.9 Relation between rust-filling ratio and crack widths

where f_r is the rust-filling ratios of group RS; f_s is the rust-filling ratios of group S, and w_s is the crack widths of group S, w_r is the crack widths of group RS.

3.2.2 Concrete Cracking Under Combined Prestress and Strand Corrosion

3.2.2.1 Accelerated Corrosion and Corrosion Product Measurement

Twelve rectangular PC specimens were cast. All specimens had a cross-section of 130 mm × 150 mm, and the specimen length was 2000 mm. The specimen was arranged with a seven-wire steel strand, the diameter of the strand was 15.2 mm, the concrete cover was 42.4 mm, and the hanger bars were four deformed HRB400 bars, which had a concrete cover of 30 mm. The diameter of stirrups in the specimen was 6 mm, and the spacing was 100 mm. The details of the specimen are shown in Fig. 3.10.

The detailed parameters of beams are given in Table 3.1. In the present study, the prestress level was reflected by the initial tension stress of the strand. There were four prestress levels, which were 0, $0.25f_p$, $0.5f_p$ and $0.75f_p$, respectively, where f_p was the tensile strength of 15.2 mm strand, which was equals to 1860 MPa. The four prestress levels were used for investigating concrete cracking induced by strand corrosion under various stress states. Based on the corrosion time and construction technology, the beams consisted of three groups: group A, group B, and group C, which were pretensioned concrete, pretensioned concrete, and post-tensioned concrete, respectively.

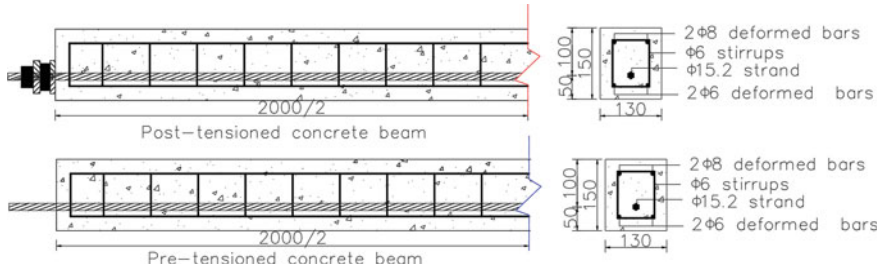


Fig. 3.10 Details of the beams (*Unit mm*)

Table 3.1 Test parameters of beams

Type	Beam no	Prestress (MPa)
Pretensioned concrete	Group A	PA0 0
		PA1 $0.25f_p$
		PA2 $0.5f_p$
		PA3 $0.75f_p$
Pretensioned concrete	Group B	PB0 0
		PB1 $0.25f_p$
		PB2 $0.5f_p$
		PB3 $0.75f_p$
Post-tensioned concrete	Group C	PC0 0
		PC1 $0.25f_p$
		PC2 $0.5f_p$
		PC3 $0.75f_p$

The concrete used the Type 32.5 Portland cement, which had a cement of 417 kg/m³, fine aggregates of 676 kg/m³, coarse aggregates of 1026 kg/m³, and a water-cement ratio of 0.44. To accelerate the corrosion degree of beams, the cement with 5% NaCl solution was employed in the concrete. The axial compressive strength test was conducted after the pretensioned and post-tensioned concrete beams poured and cured for 4 weeks.

In this experiment, components with different crack widths were obtained by electrochemical corrosion method. Epoxy resin was used to treat all ordinary reinforcement for studying the influence of corrosion on cracked concrete of prestressed concrete.

To study the expansion ratio of strand corrosion products, infrared (IR) spectroscopy and thermogravimetric (TG) analysis were used to measure the composition of the corrosion product samples. The steps were as follows: First, the corrosion products from cracks were collected; then, the corrosion product was dried with a drying box and ground into powder with a planetary grinder. Finally, the components of the corrosion products were measured based on IR and TG analysis. The Nicolet 6700 FTIR analyzer was used for infrared analysis. Dtg-60 h comprehensive

thermal analyzer was used for thermogravimetric analysis. The test environment was nitrogen environment, and the test temperature increased from 36 to 1000 °C at the rate of 10 °C/min.

3.2.2.2 Expansion Ratio of Strand Corrosion Products

The expansion of strand corrosion products will cause the cracking of concrete, and the composition of corrosion products will lead to different degrees of expansion. Infrared spectroscopy (IR) analysis was utilized to clarify the composition of corrosion products. Then, the content of iron oxide and iron hydroxide in the corrosion products were clarified using thermogravimetric (TG) analysis.

The principle of infrared spectroscopy analysis is that different substances have different absorption of infrared light waves and then perform qualitative or quantitative analysis. The composition of corrosion products can be obtained by infrared analysis. Figure 3.11 shows the infrared spectra of different samples.

Table 3.2 gives standard spectra for different types of rusts [23]. It can be seen from Fig. 3.11 that the corrosion product samples contain α -FeOOH, β -FeOOH, γ -FeOOH, α -Fe₂O₃ and Fe₃O₄, and the transmittance of each sample is not the same. It shows that the prestress has little influence on the composition of corrosion products, but it will change the proportion of each component.

The corrosion products of strands mainly consist of iron oxide and iron hydroxide. Heating can convert ferric hydroxide to ferric oxide, resulting in a change in the overall mass of the corrosion products. Based on this feature, the ratio of iron oxide

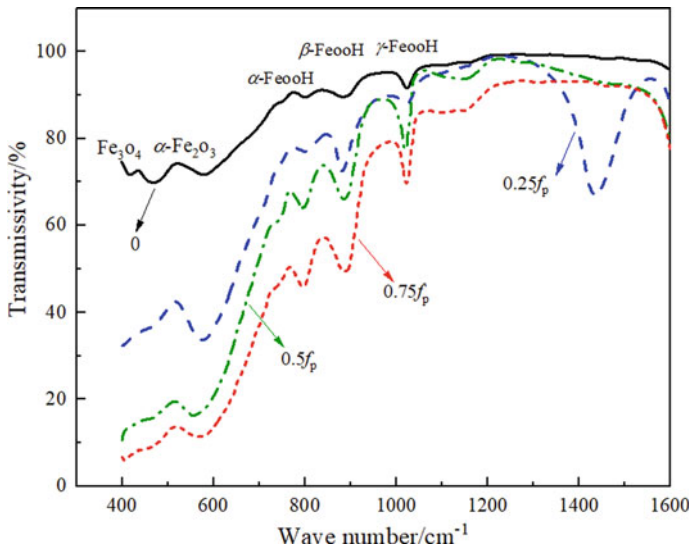


Fig. 3.11 Infrared spectrums of corrosion products

Table 3.2 Expansion ratio and standard spectra of rusts

Types	Rust expansion ratio	Peaks (cm ⁻¹), (relative intensity)
α -Fe ₂ O ₃	2.15	535(S), 464(M)
γ -Fe ₂ O ₃	2.32	690(S), 682(S), 550(VS), 475(W), 437(W), 418(VW)
FeO	1.71	492(VB, W)
Fe ₃ O ₄	2.10	556(500–700)(B, W), 404(300–500)(VB, W)
α -FeOOH	2.95	1399(M), 1260(VM), 881(S), 793(S), 608(W), 463(B, VW)
β -FeOOH	3.53	858(B, S), 670(B, S), (300–500) (B, S)
γ -FeOOH	3.07	1152(B, M), 1017(S), 737(VW), 487(VB, W)
δ -FeOOH	2.99	1110(B, S), 880(S), 786(VW), 617(B, VW), 493(B, W)

Note W is weak peak; M is medium peak; S is strong peak; VW is relative weak peak; VS is relative strong peak; B is broad band; VB is relative broad band

and iron hydroxide in the sample can be analyzed by thermogravimetric (TG) analysis. Based on the thermogravimetric (TG) analysis curve, the differential thermogravimetric (DTG) method can be used to further analyze the mass loss proportion of the corrosion products. Figure 3.12 shows the thermogravimetric and differential thermogravimetric curves of each sample.

Table 3.2 lists the standard expansion ratios of rusts [12]. It can be seen from Table 3.2 that the expansion ratios of α -Fe₂O₃, Fe₃O₄ are very close, and the expansion ratios of α -FeOOH, β -FeOOH, and γ -FeOOH are also similar. The expansion ratios of strand corrosion products are estimated by using the proportions of iron oxide and iron hydroxide, as shown in Table 3.3. It can be seen from Table 3.3 that the

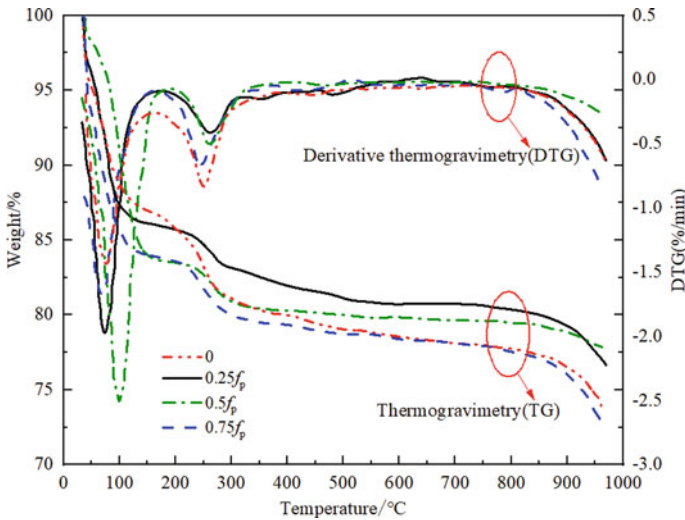


Fig. 3.12 TG and DTG curves of corrosion products

Table 3.3 Details of strand corrosion products

Prestress (MPa)	0	$0.25f_p$	$0.5f_p$	$0.75f_p$
Weight loss at 200–400 °C (%)	7	4	4	5
Mass percentage of iron hydroxide (%)	69	40	40	49
Mass percentage of iron oxide (%)	31	60	60	51
Rust expansion ratio	2.96	2.68	2.68	2.78
Average rust expansion ratio	2.78			

rust expansion ratio of each sample under different stress states is similar, and the influence of prestress on the rust expansion ratio of the strand is not significant. For this reason, the mean value (2.78) is suggested for the expansion ratio of the strand corrosion products obtained by the electrochemical accelerated corrosion test.

3.2.2.3 Crack Propagation Under Various Prestress

The expansion of corrosion products can cause tensile stress around concrete. When the tensile stress exceeds the tensile strength of concrete, micro-cracks can occur inside the concrete. Cracks will appear on the concrete surface as the micro-cracks gradually expand. In order to study the influence of prestress on the critical time of concrete cover cracking, Table 3.4 gives the critical time of cover cracking for each test beam. It can be seen from Table 3.4 that prestress can reduce the critical time of concrete cracking. To further verify the relation between crack propagation and prestress, the variation process of crack width with time is shown in Fig. 3.13.

Table 3.4 Critical time of cover cracking

Beam no./prestress	Time of cover cracking (h)	Cracking time decrement (%)
PA0/0	149	NA
PA1/ $0.25f_p$	147	1
PA2/ $0.5f_p$	125	16
PA3/ $0.75f_p$	121	19
PB0/0	154	NA
PB1/ $0.25f_p$	146	5
PB2/ $0.5f_p$	132	14
PB3/ $0.75f_p$	112	27
PC0/0	175	NA
PC1/ $0.25f_p$	162	7
PC2/ $0.5f_p$	150	14
PC3/ $0.75f_p$	138	21

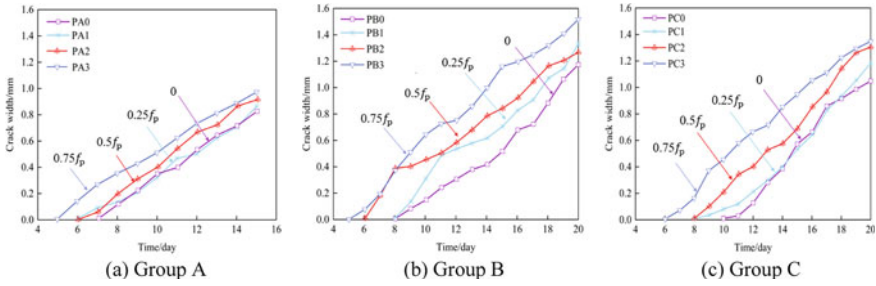


Fig. 3.13 Crack propagation of group A, group B, and group C

As Fig. 3.13 shows, the crack widths increase with the increase of the prestress. When the prestress was $0.75f_p$, the maximum crack widths of groups A, B, and C increased by 19, 30, and 30%, respectively.

It can be seen from Fig. 3.14 that slight corrosion of the strand will cause the concrete cover to crack. The crack width depends on the combined effect of the prestress and the degree of corrosion. The crack width increases with the increase of the corrosion loss and widens with the increase of the prestress. When the prestress is $0.75f_p$, the crack growth rate increases by 9%. When the corrosion loss of non-prestressed strand is 10%, the corresponding crack width is 0.76 mm. When the prestress is $0.25f_p$, $0.5f_p$, and $0.75f_p$, the crack width increases by 3, 7 and 11%, respectively. The prestress will accelerate the crack propagation rate and also increase the width of the crack.

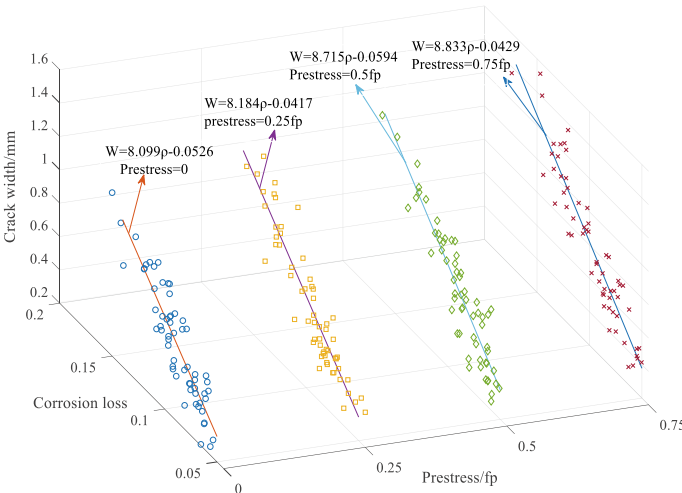


Fig. 3.14 Crack widths and corrosion losses

3.3 Prediction of Corrosion-Induced Cracking in PC Beams

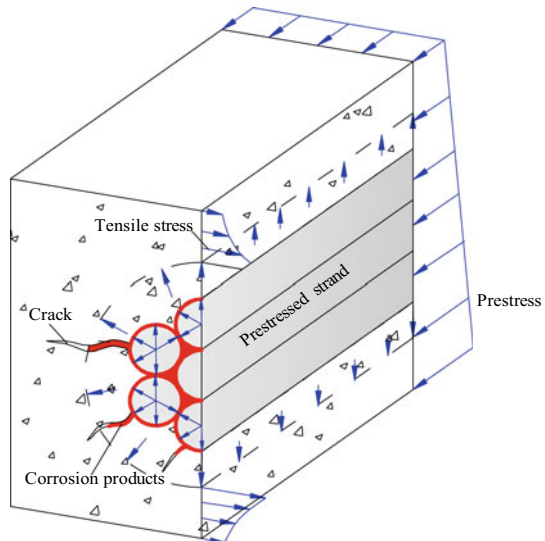
A model for predicting crack widths induced by strand corrosion in PC beams is proposed in this section. The residual stiffness of cracked concrete and the expansion ratio of rusts are considered in this model. Based on the deformation coordination relationship, the relation between the radius of crack propagation and corrosion loss can be estimated. By transforming the boundary conditions, the proposed model can predict the overall process of cracking from initiation to propagation.

3.3.1 Model for Corrosion-Induced Cracking

For prestressed concrete, the concrete will be subjected to the combined effect of prestress and expansion pressure during the corrosion process. How to reasonably consider the influence of the above factors on cracking of prestressed concrete is one of the key issues in this study. Figure 3.15 shows the stress distribution at the strand–concrete interface.

When the corrosion degree is slight, the corrosion products will generally surround the strand evenly, thereby generating a uniform expansion pressure. In this model, the concrete is simulated as a thick-walled cylindrical ring. When the tensile stress caused by expansion pressure reaches the tensile strength of the prestressed concrete, the concrete will produce micro-cracks. Before the concrete cover is completely cracked, the prestressed concrete cover is composed of two parts: the outer ring uncracked

Fig. 3.15 Schematic diagram of stress distribution in prestressed concrete



During the corrosion process, concrete is in a biaxial stress state: tensile stress caused by expansion pressure and compressive stress caused by prestress. The biaxial stress state of concrete can be written as [25].

$$\frac{\sigma_p}{f_{ck}} = \frac{1}{1 + KS}, \quad (3.7)$$

where $K = f_t/\sigma_p$, f_t is the tensile strength of concrete under the biaxial stress state; σ_p is the concrete compressive stress at the strand location; $S = f_{ck}/f_{tk}$, f_{ck} is the uniaxial tensile strengths of concrete, and f_{tk} is the uniaxial compressive strengths of concrete.

The compressive stress of concrete, $\sigma(y)$, can be written as

$$\sigma(y) = \frac{N_p}{A} + \frac{N_p e_p}{I} y, \quad (3.8)$$

where N_p is the prestressing force; A is the cross-sectional area of concrete; I is the inertia moment of cross-section of concrete; e_p is the eccentricity of strand; y is the distance from the position to section centroid. N_p is the prestressing force;

Combing Eqs. (3.7) and (3.8), the tensile strength f_t of concrete under biaxial stress state can be obtained. Assuming the smeared cracks are distributed uniformly on the cracked area. Based on this, the residual tangential stiffness of the cracked concrete can be represented by introducing a reduction factor, a , which is defined as [16]

$$a = \frac{f_t \exp(-\lambda(\bar{\varepsilon}_\theta - \bar{\varepsilon}_\theta^c))}{\bar{\varepsilon}_\theta E_c}, \quad (3.9)$$

where $\lambda = \pi \frac{f_t}{G_t} (R_0 + R_u)$, which is the material parameters; G_t is the fracture energy; $\bar{\varepsilon}_\theta$ is the average residual tangential strain of cracked concrete; $\bar{\varepsilon}_\theta^c$ is the average tangential strain of uncracked concrete; E_c is the elastic modulus of concrete.

Concrete becomes an anisotropic material after cracking. There is a difference between the radial elastic modulus and the tangential elastic modulus of concrete [16, 21]. Therefore, the radial and tangential stresses of cracked concrete, respectively, are written as

$$\sigma_r(r) = \frac{E_c}{1 - \nu_c^2} (\varepsilon_r(r) + \nu_c \sqrt{a} \varepsilon_\theta(r)), \quad (3.10a)$$

$$\sigma_\theta(r) = \frac{E_c}{1 - \nu_c^2} (a \varepsilon_\theta(r) + \nu_c \sqrt{a} \varepsilon_r(r)), \quad (3.10b)$$

where r is the radius at the cracked concrete region, $R_0 \leq r \leq R_u$; $\nu_c = \sqrt{\nu_1 \nu_2}$, ν_1 is the Poisson's ratios of concrete in the radial directions, ν_2 is the Poisson's ratios of concrete in the tangential directions.

For the cracked concrete, the concrete stress can be written as

$$\frac{\partial \sigma_r(r)}{\partial r} + \frac{\sigma_r(r) - \sigma_\theta(r)}{r} = 0. \quad (3.11)$$

The compatibility of the strain is $\varepsilon_r(r) = \frac{du(r)}{dr}$, and the compatibility of the displacement is $\varepsilon_\theta(r) = \frac{u(r)}{r}$. Then, the displacement of the cracked concrete is written as

$$\frac{d^2 u(r)}{dr^2} + \frac{1}{r} \frac{du(r)}{dr} - a \frac{u(r)}{r^2} = 0. \quad (3.12)$$

Combining the parameters $b_1(r)$ and $b_2(r)$ the displacement of the cracked concrete, $u(r)$, can be written as

$$u(r) = b_1(r)r^{\sqrt{a}} + b_2(r)r^{-\sqrt{a}}. \quad (3.13)$$

Substitution of Eq. (3.10a, b) into Eq. (3.13), Eq. (3.10a, b) can be rewritten as

$$\sigma_r(r) = \frac{\sqrt{a}E_c}{1 - \nu_c^2} \left[b_1(r)(1 + \nu_c)r^{\sqrt{a}-1} - b_2(r)(1 - \nu_c)r^{-\sqrt{a}-1} \right], \quad (3.14a)$$

$$\sigma_\theta(r) = \frac{aE_c}{1 - \nu_c^2} \left[b_1(r)(1 + \nu_c)r^{\sqrt{a}-1} + b_2(r)(1 - \nu_c)r^{-\sqrt{a}-1} \right]. \quad (3.14b)$$

For the uncracked concrete, the elasticity theory can model the stress state. The uncracked concrete is simulated as a thick-walled cylindrical ring. Based on the axial symmetry of the pressure inside the ring, there will be no displacement in the tangential direction of the uncracked concrete. The tangential stress, the radial displacement, and radial stress in the uncracked concrete, respectively, can be written as

$$\sigma_\theta(t) = \frac{R_u^2 P_u}{(R_c^2 - R_u^2)} \left(1 + \frac{R_c^2}{t^2} \right), \quad (3.15a)$$

$$u(t) = \frac{(1 + \nu_c)R_u^2 P_u}{E_c (R_c^2 - R_u^2)} \left[\frac{R_c^2}{t} + (1 - 2\nu_c)t \right], \quad (3.15b)$$

$$\sigma_r(t) = \frac{R_u^2 P_u}{(R_c^2 - R_u^2)} \left(1 - \frac{R_c^2}{t^2} \right), \quad (3.15c)$$

where t is the position at the uncracked concrete region; P_u is the expansive pressure; C is the thickness of concrete cover.

When the crack tip propagates to the position of R_u , $\sigma_\theta(t)$ in Eq. (3.15a) is equal to the concrete tensile strength f_t under the biaxial stress state. The expansive stress at the R_u position can be obtained as

$$P_u = f_t \frac{R_c^2 - R_u^2}{R_c^2 + R_u^2}. \quad (3.16)$$

The displacement and stress of the interface between cracked concrete and uncracked concrete satisfy the deformation coordination relationship. $\sigma_r(t) = \sigma_r(r)$ and $u(t) = u(r)$. Then, $b_1(r)$ and $b_2(r)$ can be obtained

$$b_1(r) = \frac{(1 - \nu_c)m + P_u(1 - \nu_c^2)/(\sqrt{a}E_c)}{2R_u^{\sqrt{a}-1}}, \quad (3.17a)$$

$$b_2(r) = \frac{(1 + \nu_c)m + P_u(1 - \nu_c^2)/(\sqrt{a}E_c)}{2R_u^{-\sqrt{a}-1}}, \quad (3.17b)$$

where $m = \frac{(1+\nu_c)f_t}{E_c(R_c^2+R_u^2)}[R_c^2 + (1 - 2\nu_c)R_u^2]$.

The average tangential strain of uncracked concrete, $\overline{\varepsilon_\theta^c}$, can be expressed as:

$$\overline{\varepsilon_\theta^c} = \frac{1}{R_u - R_0} \int_{R_0}^{R_u} \frac{u(t)}{t} dt. \quad (3.18a)$$

The $\overline{\varepsilon_\theta}$ in Eq. (3.9) over $[R_0, R_u]$ can be written as:

$$\overline{\varepsilon_\theta} = \frac{1}{R_u - R_0} \int_{R_0}^{R_u} \frac{u(r)}{r} dr, \quad (3.18b)$$

where $\overline{\varepsilon_\theta}$ is the average residual tangential strain of cracked concrete.

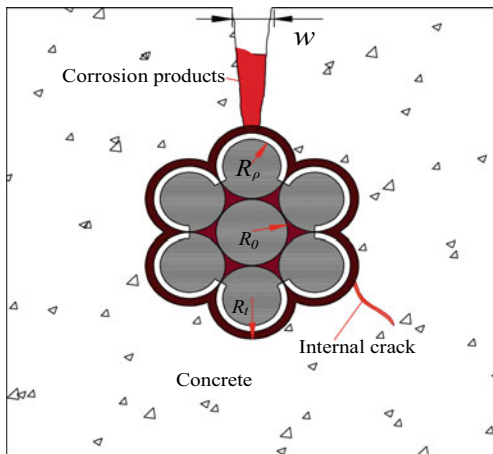
Substitution of Eq. (3.9) into Eq. (3.18a, b), the stiffness reduction factor, a , can be computed. Then, combining Eqs. (3.6) and (3.13), the corrosion loss of strand, ρ , can be determined as

$$\rho = \frac{4\pi(R_u + R_0)[b_1(R_t)R_t^{\sqrt{a}} + b_2(R_t)R_t^{-\sqrt{a}}]}{(n - 1)A_p}. \quad (3.19)$$

The concrete would fracture completely when the crack extends to the surface of concrete, i.e., when $R_u = R_c$, and the corrosion loss is equal to the critical corrosion loss of cover cracking.

After cover cracking, cracks appear on the surface of concrete. Corrosion-induced cracking is a continuous physical process that involves the crack initiation and propagation. Some study used two different approaches to simulate this continuous process, i.e., Dai et al. [7] used a mechanical model to predict the crack initiation and a geometrical relationship to describe the crack propagation. These two different approaches cannot explain the development of cracks, which may be the reason that

Fig. 3.17 Crack extends to the surface of concrete



the micro-crack effects of concrete are not able to compatible with the macroscopic continuity.

Visible cracks were observed on the concrete surface after the concrete cover was fully cracked. In this study, the whole process of concrete cracking from the initial stage to the propagation stage can be reasonably predicted by changing the corresponding boundary conditions. As shown in Fig. 3.17, the crack presents a trapezoidal shape in the cross-section after the concrete cover is cracked. The boundary conditions of the thick-walled cylinder in the theoretical model have changed; the solution of Eq. (3.13) should be rewritten as

$$u(r) = b_3 r^{\sqrt{a}} + b_4 r^{-\sqrt{a}}, \quad (3.20)$$

where b_3 and b_4 are parameters.

The changed boundary conditions can be rewritten as [6]

$$b_3(1 + \nu_c)R_c^{(\sqrt{a}-1)} - b_4(1 - \nu_c)R_c^{(-\sqrt{a}-1)} = 0, \quad (3.21a)$$

$$b_3 R_0^{\sqrt{a}} + b_4 R_0^{-\sqrt{a}} = R_t - R_0. \quad (3.21b)$$

The parameters of b_3 and b_4 can be estimated with Eq. (3.21a, b). Crack width on the surface of concrete, w_c , can be described as

$$w_c = 2\pi R_c \left[\varepsilon_\theta(R_c) - \frac{f_t}{E_c} \right], \quad (3.22)$$

where $\varepsilon_\theta(R_c)$ is the tangential strain on the concrete surface.

Substitution of Eq. (3.20) into Eq. (3.22), crack width on the surface of concrete can be rewritten as [6]

$$w_c = \frac{4\pi(R_t - R_0)}{(1 - \nu_c)(R_0/R_c)\sqrt{a} + (1 + \nu_c)(R_c/R_0)\sqrt{a}} - \frac{2\pi R_c f_t}{E_c}. \quad (3.23)$$

As mentioned above, Eqs. (3.6) and (3.23) can estimate the relationship of crack width and corrosion loss. The calculation of concrete cracking induced by corrosion expansion is sensitive to prestress parameters and the rust expansion ratios. The increased prestress and the rust expansion ratios will accelerate the rust expansion and cracking process.

3.3.2 Model Validation

Twelve corroded concrete beams were cast to validate the presented model. All specimens had a cross-section of 150 mm × 150 mm, and the beam length was 1200 mm. More details can be found in Sect. 3.2.2. Some details in the prediction model are taken as follows. The rust expansion ratio is selected as 2.78, and the fracture energy is taken as 0.088 N/mm. The elastic modulus of concrete is 32.5 GPa, and the Poisson's ratio of concrete is 0.18. Figure 3.18 depicts the predicted and experimental values.

It can be seen from Fig. 3.18 that the predicted crack widths are in good agreement with the experimental values. The mean error is 10.98%, and the standard deviations is 0.091. Simplified analytical model may produce predicted errors; uncertainty in

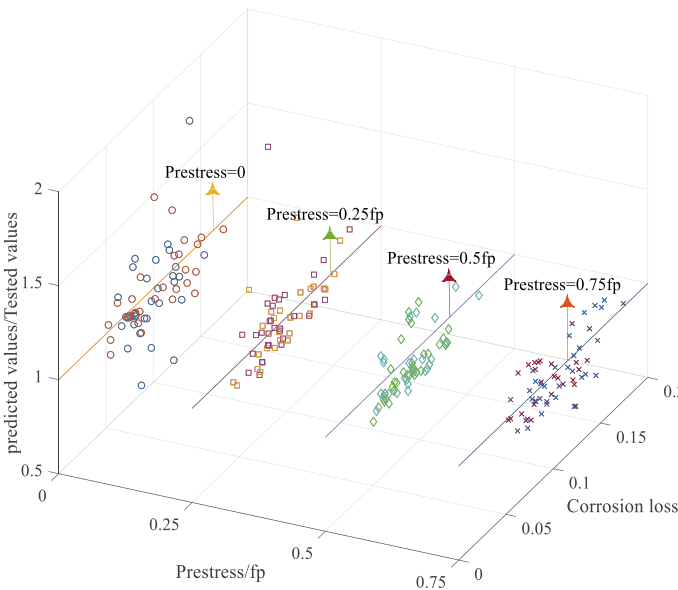


Fig. 3.18 Verification: crack width and corrosion loss

the measurement of experimental data may also cause predicted errors. The prediction error can be acceptable considering the complexity of corrosion propagation. The model comprehensively considers the combined effect of strand corrosion and prestress, which can accurately predict the corrosion-induced crack widths in PC beams.

3.4 Meso-scale Modeling of Strand Corrosion-Induced Concrete Cracking

3.4.1 3D Corrosion Expansion Model of Helical Strand

The seven-wire strand consists of one inner wire and six outer wires. After the strand corrosion occurs, spatial helicity of strands will affect the spatial distribution of corrosion products. Therefore, the 3D corrosion expansion model should take the spatial helicity of strands into consideration.

The core wire is wrapped around by the outer wire C . Figure 3.19a shows the lay length of strand L_D , which represents the outer wire length. The lay length of the strand L_D is related to the coefficient of lay length λ and the diameter of strand D . The lay length of the strand L_D can be expressed as

$$L_D = \lambda D. \tag{3.24}$$

At the position x_d , the center of the outer wire will change through rotating the outer wire C clockwise around O by an angle θ . Figure 3.19b shows the process of the change. The rotating angle θ at the position x_d is defined as

$$\theta = \frac{x_d}{L_D} \cdot 2\pi. \tag{3.25}$$

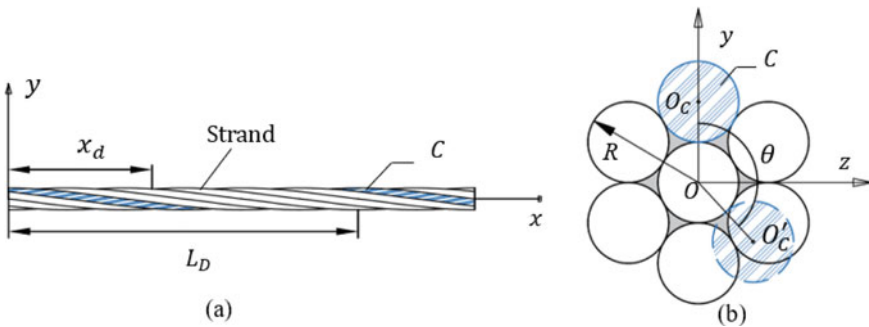


Fig. 3.19 Spatial helicity of the strand: a lay length, b cross-section

The outer wire of the strand is in shape of a spiral, and the calculation of its arc length depends on the rotation angle θ . In this study, the radius of the outer wire is equivalent to the radius of the core wire. At the position x_d , the arc length of the outer wire L can be written as [10]

$$L = \frac{\theta}{2\pi} \sqrt{4\pi^2 R^2 + L_D^2}, \tag{3.26}$$

where R is the strand radius.

To simulate the volume expansion of corrosion products, there are three commonly used loading methods in numerical simulation, which are radial strain loading, displacement loading, and thermal expansion loading [13, 26]. Radial strain loading applies radial initial strain and target strain at the interface between concrete and steel bar to achieve volume expansion. Displacement loading applies radial displacement at the interface to achieve volume expansion. The thermal expansion method is different from the first two. The main body of the load is the strand itself. By defining the thermal expansion coefficient of the strand and predefining the initial temperature, adding a heating load in the load step can realize the volume expansion process of the strand. The thermal expansion method heats up the whole solid model and does not need complex operations. It is more convenient than other loading methods for simulating the spatial expansion of the strand. Therefore, the spatial expansion model in this study is built by thermal expansion loading method.

In the present study, the strand corrosion expansion is regarded as uniform corrosion, as shown in Fig. 3.20. The shape of each steel wire with uniform expansion does not change, and the volume increases uniformly. The center of the core steel wire remains unchanged, while the center of the outer steel wire changes from O_1 to O'_1 .

Corrosion expansion causes an increase in the outer area of the steel wire, and S is the increased area of outer steel wire, which consists of two parts: S_1 and S_2 . S_1 is the area bounded by the small circle and the tangent OA , and S_2 is the area enclosed

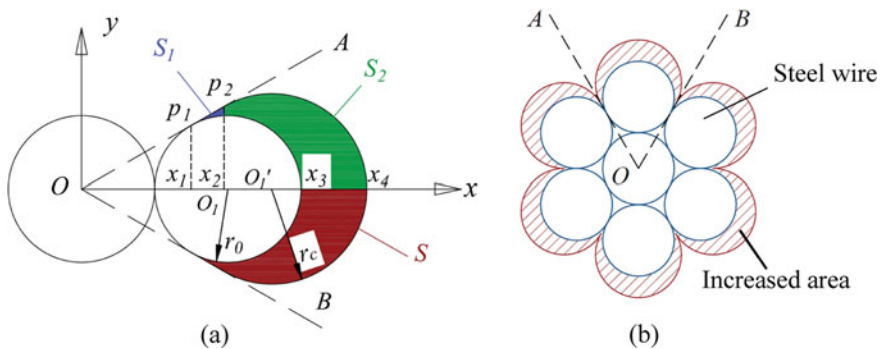


Fig. 3.20 Corrosion expansion pattern: **a** the single outer wire, **b** increased area of corrosion products

by the big circle and the small circle. r_0 is the initial radius of the steel wire, and r_c is the radius of the steel wire with corrosion products.

$$S = S_1 + S_2. \quad (3.27)$$

Based on the geometric relationship, S_1 and S_2 can be calculated as follows

$$S_1 = \int_{x_1}^{x_2} \left[\frac{1}{\sqrt{3}}x - \sqrt{r_0^2 - (x - 2r_0)^2} \right] dx, \quad (3.28)$$

$$S_2 = \int_{x_2}^{x_3} \left[\sqrt{r_c^2 - (x - 2r_c)^2} - \sqrt{r_0^2 - (x - 2r_0)^2} \right] dx \\ + \int_{x_3}^{x_4} \left[\sqrt{r_c^2 - (x - 2r_c)^2} \right] dx, \quad (3.29)$$

$$x_1 = \frac{3}{2}r_0, \quad (3.30)$$

$$x_2 = \frac{3}{2}r_c, \quad (3.31)$$

$$x_3 = 3r_0, \quad (3.32)$$

$$x_4 = 3r_c. \quad (3.33)$$

The thermal expansion loading method is used to simulate the corrosion expansion process of the strand. The relationship between the temperature increase of the corroded wire Δt and the change in the diameter of the corroded wire ΔD should be obtained first. Based on the law of thermal expansion, ΔD can be written as

$$\Delta D = 6(r_c - r_0) = 6r_0\alpha\Delta t, \quad (3.34)$$

where α is the thermal expansion coefficient.

The relationship between the raised temperature Δt and the increased area of the outer wires S can be obtained by combining Eqs. (3.27) and (3.34). Then, the radius of the corroded outer wires, r_c , can be calculated using Eq. (3.34).

When the arc length of the outer steel wire is L at the position x_d , the total increased volume of the corroded strand V_i is written as

$$V_i = 12SL. \quad (3.35)$$

The total volume of strand corrosion products V can be written as

$$V = V_i + V_r = nV_r. \quad (3.36)$$

When the arc length of the outer steel wire is L at position x_d , the initial volume of the strand V_s is written as

$$V_s = \pi r_0^2(x_d + 6L). \quad (3.37)$$

Combining Eqs. (3.35)–(3.37), the corrosion loss of strand ρ can be expressed as

$$\rho = \frac{12SL}{\pi r_0^2(x_d + 6L)(n - 1)}. \quad (3.38)$$

3.4.2 Meso-scale Model of Heterogeneous Concrete

A model of corrosion-induced cracking should consider the heterogeneity of concrete. Micromechanics treats concrete as a three-phase heterogeneous composite material consisting of coarse aggregate, hardened cement colloid, and interfacial bonding bands. Randomly distributed aggregates are inserted into concrete using the Monte Carlo method [29]. For aggregate-graded concrete to have the best density and strength, it must satisfy the Fuller curve [29], which can be used to determine the particle size distribution of aggregates in concrete. Then the cumulative percentage of aggregates $p(d)$ can be expressed as

$$p(d) = 100 \left(\frac{d}{d_{\max}} \right)^M, \quad (3.39)$$

where M is the exponent of the equation ($M = 0.45\text{--}0.70$), M is taken as 0.45 in this study; d_{\max} is the maximum size of aggregate particles.

Aggregate size distribution conforms to a common grading curve. The volume of aggregate V_a within the grading segment $[d_s, d_{s+1}]$ can be computed as:

$$V_a[d_s, d_{s+1}] = \frac{p(d_{s+1}) - p(d_s)}{p(d_{\max}) - p(d_{\min})} R_a V_c, \quad (3.40)$$

where V_c is the volume of concrete; R_a is the volume percentage of the aggregates. d_{\min} is minimum size of aggregates.

Figure 3.21 exhibits the meso-scale model. Using the spherical aggregate improves the computational efficiency and reduces the computational complexity of the meso-scale model. The 10-node quadratic tetrahedral element was used as the element type in the meso-scale model. The red part in Fig. 3.21 is a strand with

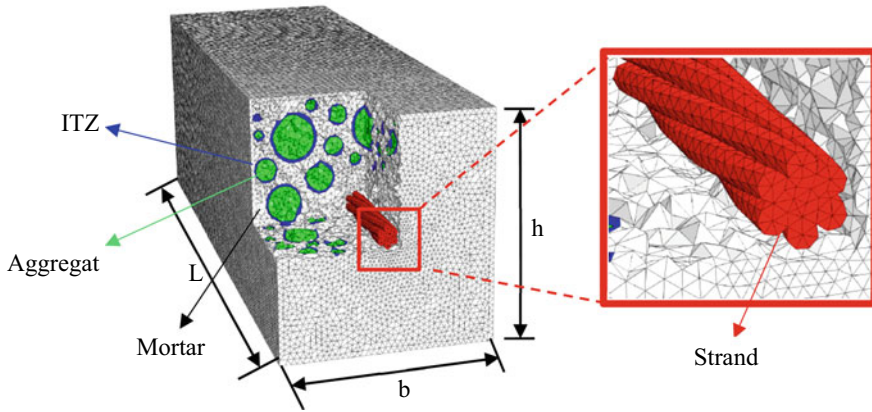


Fig. 3.21 Meso-scale numerical model

the diameter of 15.2 mm. According to the A416M standard [1], the lay length was selected to be 14 times of the strand diameter. The thickness of ITZs is between 20 and 50 μm in the practical concrete. If the thickness of the ITZs is set too small in the model, the mesh in ABAQUS cannot be divided, and the difference of mesh size is too large to be calculated. Maleki et al. [20] compared the numerical models of ITZ with different thicknesses and found that when the thickness of the ITZ layer is in the range of 20–30 μm , the impact on the strength and mechanical properties of the whole structure is small. When the thickness of the ITZ layer exceeds 500 μm , the overall mechanical properties of the model will be distorted. According to this, in order to improve the computational efficiency, the thickness of the ITZs was selected as 300 μm .

Lubliner et al. [18] proposed a nonlinear analytical model, which is called as the concrete damaged plasticity (CDP) model. The model is commonly used for analyzing corrosion-induced concrete cracking behavior in ABAQUS. When describing the inelastic behavior of concrete, the CDP model comprehensively considers the tensile, compressive plasticity theory, and elastic damage of isotropic materials, and the model can realize the mechanical behavior of concrete under low confining pressure, dynamic load, or cyclic load simulation. Considering the irreversible failure behavior of the material after it is damaged, the stiffness of the material gradually decreases, and the final fracture occurs. The CDP model combines the isotropic elastic damage theory and the multiple hardening plasticity theory. Not only that but also the CDP model defines the behavior related to the strain rate, which can control the stiffness recovery of the material during the reverse action of the cyclic load. With the help of the ABAQUS/Standard, the material can be strengthened by using viscoplastic regularization constitutive equations. Therefore, the plastic damage and failure behavior of concrete can be effectively simulated by means of the concrete plastic damage coupled constitutive relation model.

Figure 3.22 shows the uniaxial stress–strain curves of the components in the CDP model. The damage of CDP model in ABAQUS realizes the reduction of model stiffness by defining the equivalent strain after damage and defines the plastic yield surface in the effective stress space. In the CDP model, the evolution of its plastic loading (yield or failure) surface is controlled by two special hardening variables, namely the equivalent tensile plastic strain $\bar{\varepsilon}_t^{pl}$ and the equivalent compressive plastic strain $\bar{\varepsilon}_c^{pl}$. Lubliner et al. [18] proposed that the CDP model of ABAQUS adopted the yield function and, Lee and Fenves [15] proposed the modified non-associated potential plastic flow rule. The damage variable d_t varies from 0 to 1, ‘0’ is no damage and ‘1’ is complete damage, which can be determined by the constitutive relationship of the damaged concrete in ABAQUS. Kmiecik et al. [14] recommended to select the viscosity parameter as zero in concrete. Detailed description of parameters was given in [30]. Therefore, the stress–strain relation of the component in concrete can be written as

$$\sigma = (1 - d_t)E_0 : (\varepsilon - \varepsilon^p), \tag{3.41}$$

where E_0 is the initial Young’s modulus of the component in concrete. ε^p is the plastic strain tensor.

Different material properties of components in concrete lead to different concrete damage modes. The reason that damage rarely occurs in aggregates is that the strength of the aggregate was relatively higher than that of the mortar matrix and ITZs. The aggregate was considered as a linear elastic material in the present model. In this model, the Young’s modulus and strength of ITZ are both 83.3% of that of the mortar matrix. The details of the model can be used as a reference for related research [9, 19], and the details are listed in Table 3.5.

After defining the thermal expansion coefficient of the strands in the model, the uniform expansion of the strands can be realized by applying the loading conditions of increasing temperature. The initial temperature of the strand is set as 1 °C, and the

Fig. 3.22 Uniaxial stress–strain curves in CDP model

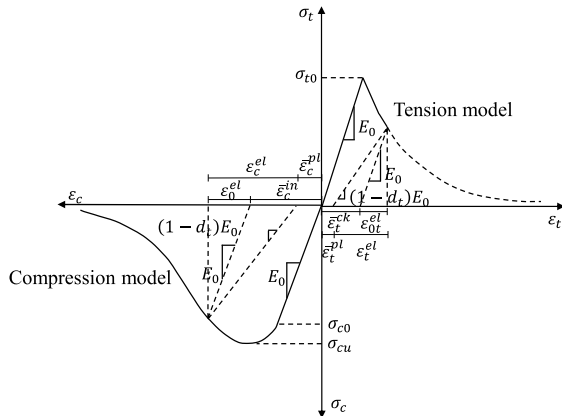


Table 3.5 Details of the CDP model

Constituents	Mortar matrix	ITZ	Aggregate	Strand
Yong's modulus E (GPa)	30	25	50	195
Poisson's ratio ν	0.20	0.20	0.16	0.30
Tensile strength f_t (MPa)	2.40	1.99	–	–
Compressive strength f_c (MPa)	22.70	18.84	–	–
Fracture energy G (N/m)	70	55	–	–
Dilation angle ψ°	30	30	–	–
Eccentricity η	0.1	0.1	–	–
Invariant stress ratio K_c	0.667	0.667	–	–
Biaxial/uniaxial compression plastic Strain ratio f_{b0}/f_{c0}	1.16	1.16	–	–

final temperature is calculated according to the formula in Sect. 3.4.1 and determined according to the required corrosion loss. The coefficient of thermal expansion α is set to $1.2 \times 10^{-5}/^\circ\text{C}$. It should be noted that the actual corrosion expansion generally occurs in the cross-section. For ordinary steel bars with circular cross-sections, it is more convenient to realize the corrosion expansion load in the YZ plane. For strands with twisted structures, the expansion of the YZ plane requires independent temperature field loading for each unit, which may cause local distortion problems. Therefore, this model adopts the method of overall heating. However, the uniform volume expansion will make the displacement in each part of the strand along the length. Due to the special surface of the strand and close occlusion with the concrete, this displacement will cause the internal concrete to be subjected to additional longitudinal tension and even cracks. This is not consistent with the actual corrosion process. The model needs to constrain the longitudinal displacement of the strand, so that it can only expand in the Y and Z directions. The bottom of the model is set as a fixed end to constrain its displacement.

3.4.3 Model Validation

In order to verify the rationality of the spatial corrosion expansion model of strands, three corroded concrete beams were cast, which had a cross-section of 150 mm \times 150 mm, and the beam length was 1200 mm. Each beam was embedded with a seven-wire steel strand, which was made of seven wires. The thickness of the concrete cover of all beams was set to be 67.4 mm. After the uniaxial compressive test of the same batch of poured concrete specimens at the same age, the average compressive strength of concrete was 32.5 MPa. Figure 3.1 presents the details of the specimens. The accelerated corrosion is used to corrode the specimens. The current density used in the present study was $270 \mu\text{A}/\text{cm}^2$. The corrosion time of S6, S9, and S12 was

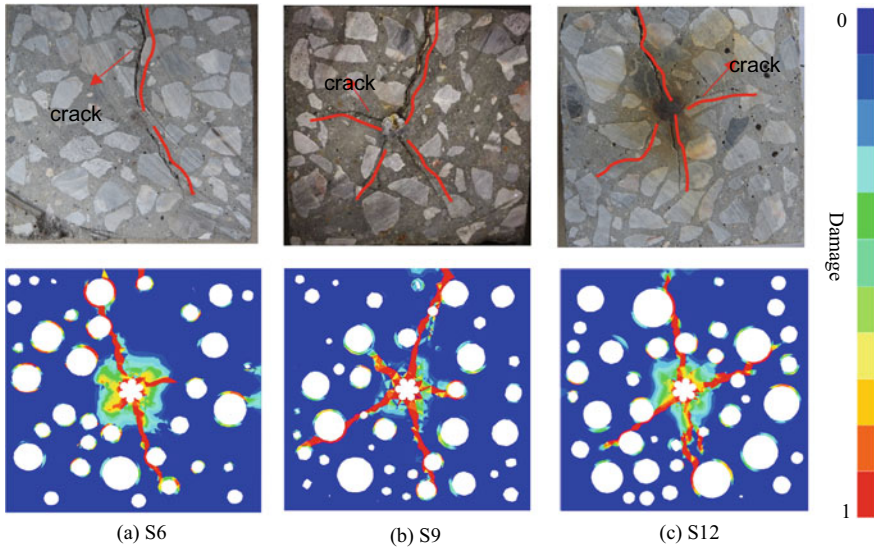


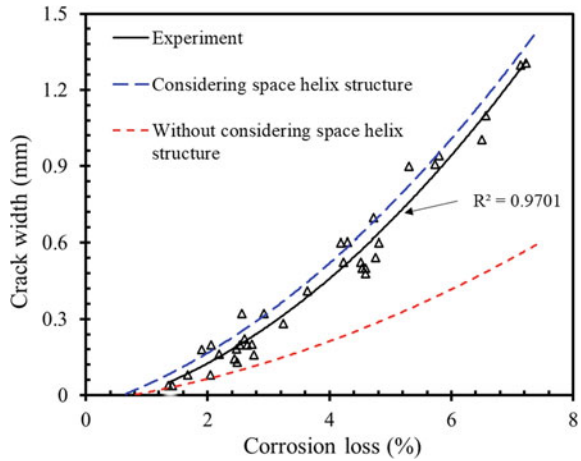
Fig. 3.23 Numerical simulation and experimental results

set to be 2, 9, and 5 days, respectively, which were controlled by the current density and corrosion time. Wang et al. [27] displayed the details of the beam specimens.

After the concrete beams were subjected to accelerated corrosion, longitudinal cracks first appeared. The crack widths can be measured by a crack measuring instrument, which has a precision of 0.01 mm. For measuring the mass loss of the strand, the rust needed to be removed from the surface of the strand. Figure 3.23 shows the position of cracks appeared on the cross-section of the specimens.

As shown in Fig. 3.23, three sections were selected from the experimental beams and the numerical simulations. It can be seen that the numerical simulation results are close to the experimental results. The spatial corrosion expansion model of strand based on thermal expansion method can effectively simulate the strand corrosion-induced concrete cracking. In the initial stage of corrosion, the corrosion products fill the gaps between the strands and the mortar matrix. When the gaps at the interface are filled, the corrosion products continue to accumulate, and the concrete adjacent to the strands will be subjected to additional stress. This stress reaches the tensile strength of concrete and initial damage occurs. The corrosion loss increases gradually, and the accumulation of corrosion products causes the initial cracks to expand outwards, and finally the cracks pass through the concrete cover and extend to the concrete surface. In the numerical simulation results, it was also found that some initial damage first appeared in the ITZ layer with lower strength. When the cracks extended to the ITZ layer, the cracks would connect with each other to form a fracture zone. When the aggregate strength was higher, the expansion pressure is not enough to make the cracking of aggregate, and the crack is difficult to penetrate into the aggregate. It

Fig. 3.24 Crack width and corrosion loss



can be seen that the extension path of the crack will be affected by the aggregate distribution due to the existence of the aggregate and the ITZ layer.

Comparing the numerical simulation results with the experimental results in the present study, the effectiveness of the proposed model is verified. After the element is completely failed, the crack width can be represented by using the relative displacement of the two nodes on the element. Figure 3.24 shows the relation between crack width and corrosion loss.

The numerical simulation that considers the spatial helicity of strand is named as the simulation A, and the numerical simulation that does not consider the spatial helicity of strand is named as the simulation B. Comparing the results of the simulation B, the simulation A has better accuracy with the experimental results. When the corrosion loss is 7%, the crack width of the model considering the spatial helicity was 5% larger than the experimental value, while the crack width of the model without considering the spatial helicity was 56% smaller than the experimental value. This shows that taking the spatial helicity of the strand into consideration can greatly improve the prediction precision of cracks induced by strand corrosion. Helical strands corrosion-induced cracking can be rationally modeled by using the proposed 3D numerical simulation.

3.4.4 Influencing Parameters for Corrosion-Induced Cracking

The spatial helicity of strands affects concrete cracking induced by strand corrosion. In this section, the effects of the spatial helicity and the lay length of the strand on corrosion-induced cracks are discussed.

3.4.4.1 Effect of Strand Space Helix Structure

For investigating the effect of the spatial helicity of the strand on the corrosion-induced concrete cracking, the simulation A (considering the spatial helicity of the strand in the model) and simulation B (without considering the spatial helicity of the strand in the model) were built. The strand in simulation B was cylindrical, which seems like the reinforcement bar. Figure 3.25 shows the concrete cracking model. The corrosion loss is 0.32%, which is the critical corrosion loss when the concrete cover cracks appear in simulation A. However, longitudinal cracks appeared on the concrete surface in simulation B. Simulation A has a larger number of cracks than simulation B.

Figure 3.26 shows the spatial distributions of the corrosion expansion pressure for the strand and reinforcement bar. It can be seen from the Fig. 3.26 that the maximum expansion pressure in simulation A is 10.68 MPa, while the simulation B is 13.55 MPa. The results indicate that the expansion pressure will be overestimated by neglecting the spatial helicity of the strand.

Under the influence of stress concentration, corrosive cracks are first generated at the top of the peripheral steel wire. The expansion pressure in simulation B is always concentrated at 0° , 90° , 180° , and -90° , which are the thinnest directions from the surface of concrete to the surface of steel bar. In addition, under the combined effect of the corrosion expansion pressure concentrated in the two directions with an included angle of 90° , the concrete within the included angle of 45° first reaches the tensile strength and cracks, which is consistent with the crack path of the circular section steel bar in Fig. 3.25.

Figure 3.27 shows a comparison of the maximum crack widths on the concrete surface in the two models. In order to explore the influence of the twisted structure of the strand and the thickness of the concrete cover on the crack width induced by rust expansion, the position with the largest relative displacement on the surface crack path was selected for analysis, and it was compared as the maximum crack width.

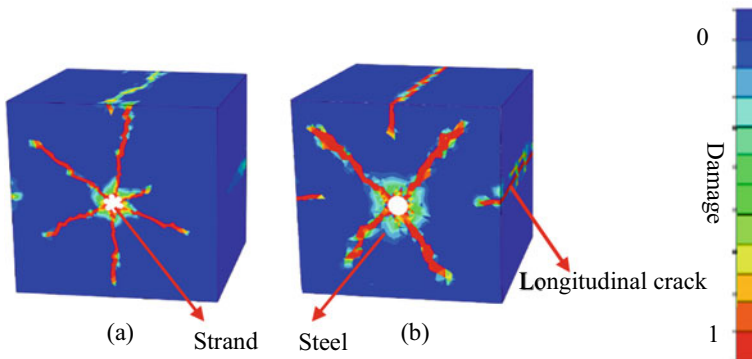


Fig. 3.25 Concrete cracks induced by corrosion: **a** simulation A, **b** simulation B

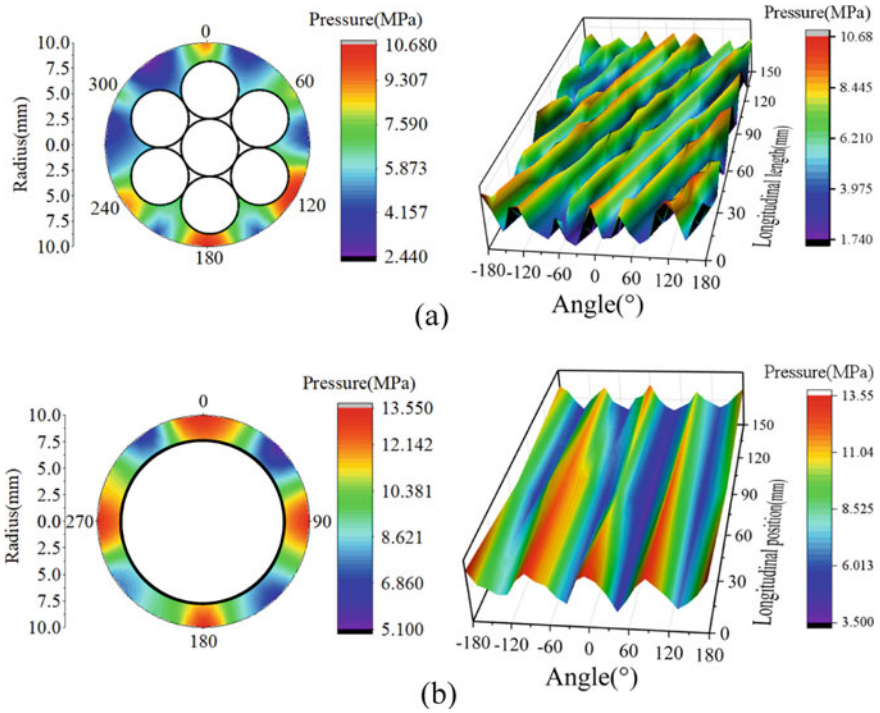
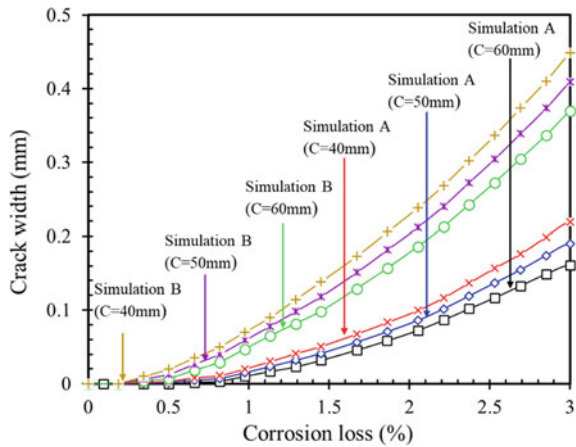


Fig. 3.26 Corrosion-induced expansion pressure: **a** simulation A, **b** simulation B

Fig. 3.27 Relation between crack widths and the different thickness of concrete cover



It can be seen from Fig. 3.27 that no matter whether the twisted structure is considered or not, the widths of crack induced by rust expansion always increase with the decrease of the thickness of the concrete cover. When the corrosion loss is 3%, compared with the model with a concrete cover thickness of 60 mm, the maximum crack width in the simulation A is reduced by 18%, while the simulation B is reduced by 26%. It indicates that the increased thickness of concrete cover can effectively reduce the crack width. At the same time, the width cracks of simulation A are larger than that of the simulation B, which shows that the concrete expansion caused by the strand corrosion is more serious than that of the ordinary steel bar due to its special twist structure. Therefore, the corrosion of strands should be given great attention in practical engineering.

3.4.4.2 Effect of Strand Lay Length

This section further discusses the effect of strand lay length on concrete cracking. The actual processing lay length is generally 14–18 times the diameter of the steel strand, and most steel strands use 14 times the diameter as the lay length. Taking the diameter as the median, the average corrosion expansion pressure of strands with different lay lengths is calculated, which is shown in Fig. 3.28.

It can be seen from Fig. 3.28 that the average expansion pressure at the junction of the concrete and the strand decreases with the increase of the lay length. Compared the model with 12D lay length with the model with 16D lay length, the maximum average pressure for the model with 12D lay length, the strand diameter was approximately 2.93 times that of the model with 16D lay length. The average expansion pressure of each simulation will go through two peak points. The corrosion loss of each group reaching the peak point A is similar. The peak point A represents the initial damage, so after reaching the peak point A, the concrete enters the plastic stage. The peak point B represents that all the concrete around the strand is damaged and enters the plastic stage. After the peak value of point B, the average expansion pressure

Fig. 3.28 Relation between average expansion pressure and lay lengths of strand

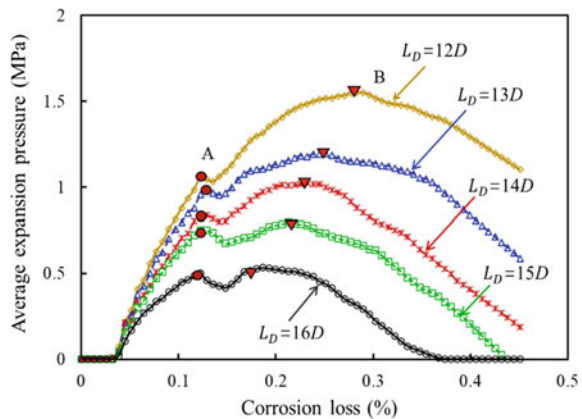
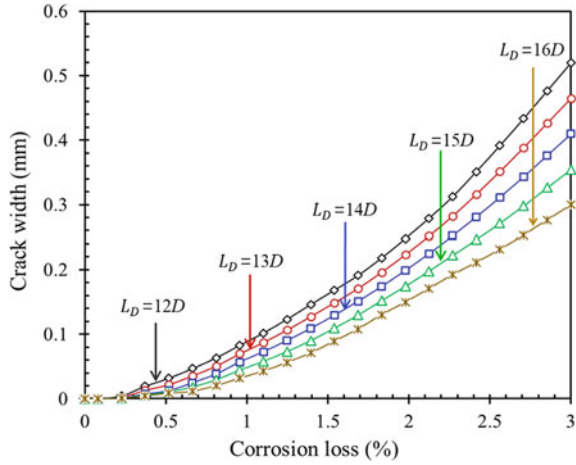


Fig. 3.29 Crack widths induced by corrosion under different lay lengths of the strand



begins to decrease, the reason may be that the concrete can no longer withstand the expansion pressure. When the lay length is $12D$, the critical corrosion loss required to reach the peak point B is 0.28%. For the model with $16D$ lay length, the corrosion loss reaching the peak point B is only 0.19%, which indicates that the lay length of the strand will increase with the reduction of the corrosion loss required for all the damage of the concrete around the strand.

Figure 3.29 shows a comparison of maximum crack widths on the concrete surface under different strand lay lengths. The crack width induced by strand corrosion decreases with the increase of the lay length. The critical corrosion loss of concrete cover increases with the increase of the strand lay length. When the strand lay length increases, correspondingly, the critical corrosion loss of the concrete cover also increases.

Combined with the comparison and analysis of the average corrosion expansion pressure of strands with different lay lengths in Fig. 3.28, for strands with small lay lengths, the angle of twisting of the inner and outer steel wires per unit length is larger, and the angle where the expansion pressure is concentrated is along the longitudinal direction. The change is large. After the initial damage occurs, the rust expansion pressure continues to increase in different directions, which promotes the formed cracks to be subjected to the stress of both sides, and the cracks expand to both sides and extend outwards faster. This eventually results in wider crack widths for strand models with smaller lay lengths.

3.5 Conclusions

1. The filling of the corrosion products varies with crack propagation. Before reaching the critical width, the rust-filling ratio increases with the increase of crack width. When the crack width exceeds the critical width, the rust-filling ratio will not change. Stirrups used in concrete can inhibit the propagation of cracks.
2. Prestressed strands have an adverse effect on corrosion-induced cracking, and the critical corrosion loss of concrete cover cracking decreases with the increase of prestress.
3. The critical corrosion loss of cover cracking increases with the increase of concrete tensile strength and concrete cover thickness and decreases with the increase of rust expansion ratio and strand diameter.
4. Considering the twisting structure of the strand can improve the prediction accuracy of the numerical model for corrosion-induced cracking, the spatial distribution of the expansion pressure induced by strand corrosion is different to that induced by reinforcement bar corrosion because of the space helix structure of the strand.
5. The corrosion of strand with a large lay length will generate a small expansion pressure, and the lay length has a little effect on the critical corrosion loss of strand in the initial damage of the concrete.

References

1. ASTM, *Standard Specification for Steel Strand, Uncoated Seven-Wire for Prestressed Concrete* (West Conshohocken, 2006)
2. I. Balafas, C.J. Burgoyne, Modeling the structural effects of rust in concrete cover. *J. Eng. Mech.* **137**(3), 175–185 (2011)
3. K. Bhargava, A. Ghosh, Y. Mori, S. Ramanujam, Analytical model for time to cover cracking in RC structures due to rebar corrosion. *Nucl. Eng. Des.* **236**(11), 1123–1139 (2006)
4. A. Bossio, T. Monetta, F. Bellucci, G.P. Lignola, A. Prota, Modeling of concrete cracking due to corrosion process of reinforcement bars. *Cem. Concr. Res.* **71**, 78–92 (2015)
5. C. Cao, M.M. Cheung, B.Y. Chan, Modelling of interaction between corrosion-induced concrete cover crack and steel corrosion rate. *Corros. Sci.* **69**, 97–109 (2013)
6. L. Chun-Qing, R.E. Melchers, Z. Jian-Jun, Analytical model for corrosion-induced crack width in reinforced concrete structures. *ACI Struct. J.* **103**(4), 479–487 (2006)
7. L. Dai, L. Wang, J. Zhang, X. Zhang, A global model for corrosion-induced cracking in prestressed concrete structures. *Eng. Fail. Anal.* **62**, 263–275 (2016)
8. X. Du, L. Jin, Meso-scale numerical investigation on cracking of cover concrete induced by corrosion of reinforcing steel. *Eng. Fail. Anal.* **39**, 21–33 (2014)
9. X. Du, L. Jin, G. Ma, Numerical simulation of dynamic tensile-failure of concrete at meso-scale. *Int. J. Impact Eng* **66**, 5–17 (2014)
10. S.R. Ghoreishi, P. Davies, P. Cartraud, T. Messenger, Analytical modeling of synthetic fiber ropes. Part II: A linear elastic model for 1+ 6 fibrous structures. *Int. J. Solids Struct.* **44**(9), 2943–2960 (2007)

11. H. Gurdián, E. García-Alcofel, F. Baeza-Brotons, P. Garcés, E. Zornoza, Corrosion behavior of steel reinforcement in concrete with recycled aggregates, fly ash and spent cracking catalyst. *Materials* **7**(4), 3176–3197 (2014)
12. S.J. Jaffer, C.M. Hansson, Chloride-induced corrosion products of steel in cracked-concrete subjected to different loading conditions. *Cem. Concr. Res.* **39**(2), 116–125 (2009)
13. L. Jin, M. Liu, R. Zhang, X. Du, Cracking of cover concrete due to non-uniform corrosion of corner rebar: a 3D meso-scale study. *Constr. Build. Mater.* **245**, 118449 (2020)
14. P. Kmiecik, M. Kamiński, Modelling of reinforced concrete structures and composite structures with concrete strength degradation taken into consideration. *Arch. Civil Mechan. Eng.* **11**(3), 623–636 (2011)
15. J. Lee, G.L. Fenves, Plastic-damage model for cyclic loading of concrete structures. *J. Eng. Mech.* **124**(8), 892–900 (1998)
16. C.-Q. Li, S. Yang, Prediction of concrete crack width under combined reinforcement corrosion and applied load. *J. Eng. Mech.* **137**(11), 722–731 (2011)
17. T. Liu, and Weyers, R.W., Modeling the time-to-corrosion cracking in chloride contaminated concrete structures. *Mater. J.* **95**(6), 7 (1998)
18. J. Lubliner, J. Oliver, S. Oller, E. Onate, A plastic-damage model for concrete. *Int. J. Solids Struct.* **25**(3), 299–326 (1989)
19. H. Ma, W. Xu, Y. Li, Random aggregate model for mesoscopic structures and mechanical analysis of fully-graded concrete. *Comput. Struct.* **177**, 103–113 (2016)
20. M. Maleki, I. Rasoolan, A. Khajehdezfuly, A.P. Jivkov, On the effect of ITZ thickness in meso-scale models of concrete. *Constr. Build. Mater.* **258**, 119639 (2020)
21. S.J. Pantazopoulou, K. Papoulia, Modeling cover-cracking due to reinforcement corrosion in RC structures. *J. Eng. Mech.* **127**(4), 342–351 (2001)
22. X. Pengwei, Y. Ning, S. Linwang, L. Guobao, W. Lebin, Finite element analysis of expansive behaviour due to reinforcement corrosion in RC structure. *Procedia Eng.* **12**, 117–126 (2011)
23. A. Raman, B. Kuban, A. Razvan, The application of infrared spectroscopy to the study of atmospheric rust systems—I. Standard spectra and illustrative applications to identify rust phases in natural atmospheric corrosion products. *Corros. Sci.* **32**(12), 1295–1306 (1991)
24. A.O.S. Solgaard, A. Michel, M. Geiker, H. Stang, Concrete cover cracking due to uniform reinforcement corrosion. *Mater. Struct.* **46**(11), 1781–1799 (2013)
25. M.E. Tasuji, A.H. Nilson, Stress-strain response and fracture of concrete in biaxial loading. *J. Proc.* 306–312 (1978)
26. K.K. Tran, H. Nakamura, K. Kawamura, M. Kunieda, Analysis of crack propagation due to rebar corrosion using RBSM. *Cement Concr. Compos.* **33**(9), 906–917 (2011)
27. L. Wang, L. Dai, X. Zhang, J. Zhang, Concrete cracking prediction including the filling proportion of strand corrosion products. *Materials* **10**(1), 6 (2017)
28. L. Wang, X. Zhang, J. Zhang, J. Yi, Y. Liu, Simplified model for corrosion-induced bond degradation between steel strand and concrete. *J. Mater. Civil Eng.* **29**(4) (2016)
29. P. Wriggers, S. Mofteh, Mesoscale models for concrete: Homogenisation and damage behaviour. *Finite Elem. Anal. Des.* **42**(7), 623–636 (2006)
30. Q. Xiong, X. Wang, A.P. Jivkov, A 3D multi-phase meso-scale model for modelling coupling of damage and transport properties in concrete. *Cement Concr. Compos.* **109**, 103545 (2020)
31. J. Zhang, X. Ling, Z. Guan, Finite element modeling of concrete cover crack propagation due to non-uniform corrosion of reinforcement. *Construct. Build. Mater.* **132**, 487–499 (2017)

Open Access This chapter is licensed under the terms of the Creative Commons Attribution 4.0 International License (<http://creativecommons.org/licenses/by/4.0/>), which permits use, sharing, adaptation, distribution and reproduction in any medium or format, as long as you give appropriate credit to the original author(s) and the source, provide a link to the Creative Commons license and indicate if changes were made.

The images or other third party material in this chapter are included in the chapter's Creative Commons license, unless indicated otherwise in a credit line to the material. If material is not included in the chapter's Creative Commons license and your intended use is not permitted by statutory regulation or exceeds the permitted use, you will need to obtain permission directly from the copyright holder.



Chapter 4

Bond Behavior Between Strand and Concrete with Corrosive Cracking



4.1 Introduction

Bond behavior between concrete and strands plays a decisive role in sustaining performance of prestressed concrete (PC) beams, particularly for pretensioned concrete members [1, 12]. For PC structures exposed to an erosion environment, the strand is unavoidably corroded because of the invasion of chloride ions [9]. The invasion of chloride ions reduces the protection of the strand by surrounding concrete, which would further reduce the bond strength at the interface between concrete and strands.

Numerous study on the bond behavior of steel strand have been carried out by using the pull-out test. The reliability of the experimental result from the pull-out test was verified in showing strand bond performance [15]. Some theoretical models were also established to predict the bond behavior of steel strand [3, 14]. However, existing study indicate that little attention has been paid to the bond behavior of steel strands subjected to corrosion. Li and Yuan [8] experimentally studied the bond strength of corroded strand based on the pull-out test. This study mainly focuses on the bond behavior of corroded strand within short beams rather than the transfer of bond stress along long beams. And few researches have been carried out with the beam testing method to consider bond stress of strand and flexural situations in practical engineering structures.

Some scholars have compared and analyzed the difference in bond behavior between uncorroded prestressed strands and deformed steel bars. Ying et al. [16] found that the bond performance between concrete and steel strand with a diameter of 15.2 mm is worse than that between 16 mm ribbed steel bars and concrete. Youlin et al. [17] pointed out that the bond performance of the steel strand is between that of the ribbed steel bar and the smooth steel bar. Mao-mao et al. [10] found that the bond strength at the strand–concrete interface is worse than that of ribbed steel bar, but the maximum slip value of the steel strands is much larger than that of the latter. The ribbed steel bar within the pull-out specimen is often split and damaged, while the steel strand test is screwed out due to rotation. Fang-yuan and Ren-da [7] pointed out that the bond–slip curve between strands and high-strength concrete has an obvious

rising segment, yield segment, and ductile slip segment compared with the deformed steel bars. Chao et al. [4] found that the steel strand can provide effective friction and mechanical interlock force due to its helical structure after concrete cracking, and its residual bond force is better than that of deformed steel bars.

Some scholars have studied the bond properties between uncorroded prestressed strands and concrete. Morcoust et al. [13] found that the bond stress between 18-mm diameter uncorroded strand and surrounding concrete is proportional to the concrete compressive strength. It is indicated that the bond strength of steel strand is affected by some factors, such as the type of prestressed strands, the location of prestressed strands during pouring, and the concrete compressive strength. Dang et al. [6] pointed out that the bond performance of prestressed strands is closely related to concrete strength, surface condition of prestressed strands and Hoyer effect, leading to a non-uniform bond stress along the effective bond length. A bond–slip relationship model is established between prestressed strands and concrete based on experimental results.

At present, few scholars have studied the bond performance of prestressed strands subjected to corrosion. Morcoust et al. [13] explored the effect of corrosion pits on the bond properties of steel strands. The study found that the pits can improve the adhesion between corroded strands and concrete when the slip is small. The existence of the pits can cause the degradation of the adhesion when the slip is large. However, the steel strands were corroded first in this test, and then the concrete was poured, which is different from the actual corroded components. Li and Yuan [8] conducted an experimental study on the local bond–slip model of corroded steel strands. Results indicate that the corrosion leads to the degradation of the maximum bond stress, and the local bond–slip curve degenerates from the original three stages to two stages. In this test, the short pull-out specimen inevitably has a certain influence on the twisting effect of the steel strand. In addition, there is no specific prediction model for strand bond degradation caused by corrosion has been given yet.

The arrangement of this chapter is as follows. First, the effect of corrosion on the residual bond strength of strand is studied based on the pull-out test. Next, the bond behavior of corroded strand in pretensioned concrete structures is investigated by the bending test.

4.2 Bond Behavior of Strand with Corrosive Cracking in Pull-Out Specimens

4.2.1 Corrosion-Induced Concrete Cracking

In pretensioned concrete structures, seven-wire strands are often used as the main tensile reinforcement. The 15.2 mm diameter steel strand has been the most frequently used in practical projects. The twist steel strand with a 15.2 mm diameter was applied in this study. The basic parameters of the 15.2 mm strand are given in Table 4.1.

The experimental study contained 20 pull-out specimens. Two groups, group S (no stirrups) and group R (with stirrups), were designed to investigate the effect of stirrups on the strand bond. Each group contained ten beams. The smooth bars were used as the stirrups in group R, and the diameter and spacing of the stirrups are 8 mm and 150 mm, respectively. Four deformed bars with a diameter of 10 mm were set at the four corners of the specimens. The deformed bars were combined by the stirrups to form a whole. Group S does not include stirrups and linked bars. Specimens with stirrups and without stirrups were marked as R-x and S-x, respectively. The uncorroded beams in the two groups were marked as R-0 and S-0. The remaining beams with corrosion were marked as R-1 to R-9 and S-1 to S-9, respectively.

Each group consisted of one uncorroded beam (the control beam) and nine corroded beams. A 15.2 mm steel strand is arranged at the center of each beam, and a concrete cover is 67.4 mm. All beams were designed with a rectangular cross-section of 150 × 150 mm and a length of 1200 mm. The specific dimensions of the beams and the arrangement of the reinforcement are shown in Fig. 4.1. In addition, to reduce the compressive stress concentration at the loaded end, a 100-mm-long PVC pipe was placed over the strand surface to create an unbonded area, and the bond stress is ignored in this area, as shown in Fig. 4.1. Therefore, the effective bond length is 1100 mm.

All beams were cast with salted concrete. The average compressive strength is 35.1 MPa by testing three 150 mm × 150 mm × 150 mm concrete cubes. Among them, taking cement as a reference, 5% NaCl was put into the concrete mix to simulate the actual corrosion environment. The mass ratio of cement, water, fine aggregate

Table 4.1 Parameters of 15.2 mm prestressing strand

f_{py}/f_{ps} (kN)	E %(≥500 mm)	u_w (kg/m)	A_p (mm ²)	E_s (MPa)
234/265	≥ 3.5	1102	139.5	1.95×10^5

Note f_{py} and f_{ps} are the ultimate strength and yield strength of steel strand, respectively; e is elongation; u_w is unit weight; A_p is the cross-sectional area; E_s is the modulus of elasticity

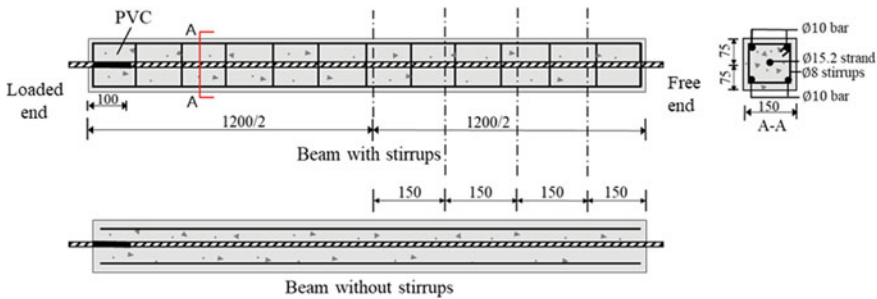


Fig. 4.1 Dimensions and reinforcement diagrams of beams (unit: mm)

and coarse aggregate was 1: 0.43: 1.27: 2.46. The stirrups and hanger bars of the beam were protected from corrosion by applying epoxy resin.

The electrochemical accelerated corrosion method is widely used in accelerated corrosion experiments because of its advantages, such as fast corrosion rate and simple installation. In this test, this method was also used to accelerate the corrosion of each beam. After concrete curing, the electrochemical accelerated corrosion was performed on the beams to obtain the different corrosion losses. The layout of the accelerated corrosion system is shown in Fig. 4.2. During the corrosion process, the pH test paper was often used to measure the acid–base content of the corrosion solution. The pH value of the corrosion solution was adjusted by the hydrochloric acid solution. The corrosion solution was always maintained at about 7. The electric current was set to 0.3A in the accelerated corrosion test. According to the area of the wire, the current density is about $270 \mu A/cm^2$. Corrosion time and corrosion loss of each beam are shown in Table 4.2. After accelerated corrosion testing, the corrosion-induced concrete cracks on each surface were recorded. First, the corrosion products on surface of the cracks were cleaned. Then, the cracks were marked and recorded on each concrete surface. Finally, the widths of crack were recorded at every 5-cm interval by using a crack width detector, and the accuracy of the crack width detector is 0.01 mm.

Additionally, the destructive method was used to measure the corrosion loss of steel strands after the loading test. First, the concrete cover was crushed and the steel strands were cut, and the concrete slag on the surface of the strand was cleaned up. Then, the corroded strands were soaked with a 10% hydrochloric acid solution for a period of time, and the acid was neutralized with alkali. Finally, the wires were dried and their remaining weight were measured with an electronic scale. The original

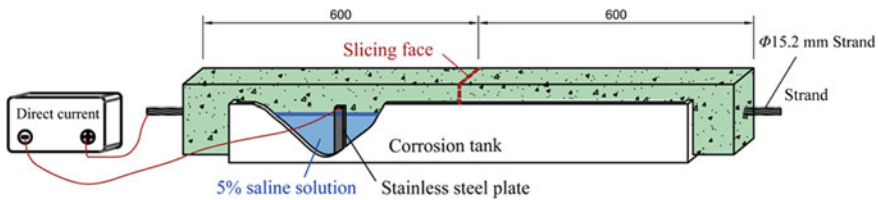


Fig. 4.2 Accelerated corrosion system

Table 4.2 Corrosion times of the beams

Test beams	R-0	R-1	R-2	R-3	R-4	R-5	R-6	R-7	R-8	R-9
Corrosion times	0	3	5	7	8	10	12	15	17	18
Corrosion loss	0	2.27%	2.32%	4.13%	5.78%	5.61%	8.07%	7.97%	8.19%	9.26%
Test beams	S-0	S-1	S-2	S-3	S-4	S-5	S-6	S-7	S-8	S-9
Corrosion times	0	3	5	7	8	10	12	15	17	18
Corrosion loss	0	1.07%	1.19%	2.02%	4.59%	3.12%	6.07%	5.82%	5.54%	6.49%

weight of a strand is 1101 g/m. Thus, the corrosion loss of the steel strand can be calculated according to the weight difference before and after corrosion. The average mass corrosion loss was used to characterize the corrosion degree of the beams in the present study.

After the corrosion test, the corrosive cracks on concrete surface of each corroded component were observed and recorded. The longitudinal concrete surfaces of each beam are designated surfaces 1, 2, 3, and 4, respectively. The location of the cracks is described in turn from the bottom surface counterclockwise. Significant cracks were detected on Surface 1 for all the corroded beams. In addition, other significant cracks were observed on Surfaces 1, 2, 3, and 4 of beams R-3, R-4, R-6, and R-7, respectively. The corrosion-induced crack width was recorded with a hand-held crack detector at uniform intervals of 5 cm. Figure 4.3 shows the distribution of the corrosion-induced cracks along the beam surfaces.

It can be seen from Fig. 4.3 that all the corrosive cracks develop along the direction of the steel strand. Due to the uncertainty or inhomogeneity of the corrosion, the crack width varies at different locations. To discuss the effects of crack on bond, the average crack width (W_{ave}) was applied to indicate the cracking degree of beams. For the beams with two or more cracks, W_{ave} is the sum of the average values of the multiple cracks. In addition, the corrosion loss of each beam was measured after the pull-out test. W_{ave} is shown in Fig. 4.3, and the corrosion loss of strand ρ is written in Table 4.2, respectively. It can be seen from Fig. 4.3 that the width value of corrosive crack is positively correlated with the corrosion loss.

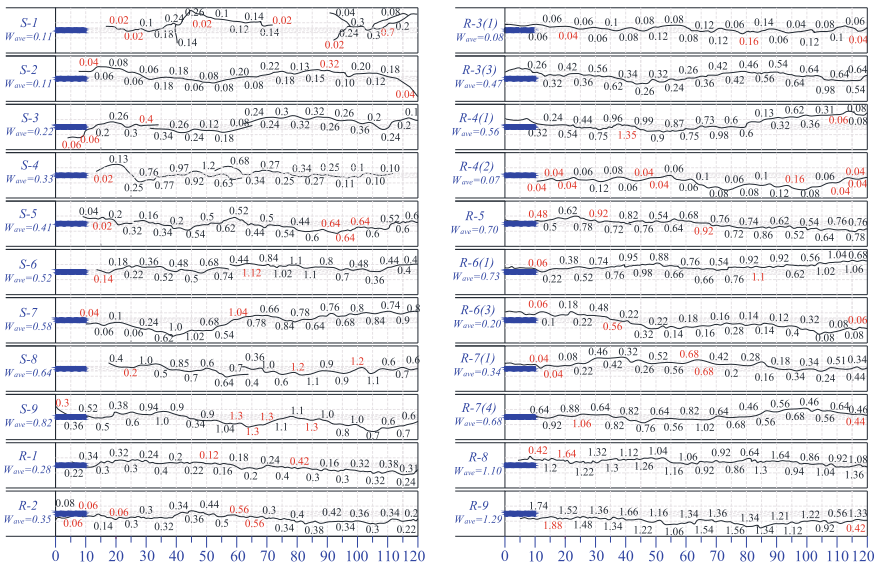


Fig. 4.3 Cracks caused by corrosion on concrete surfaces (unit: mm)

4.2.2 Concrete Strain

After the corrosion test, the pull-out test of corroded beams was carried out to investigate the characteristics of strand bond. The pull-out test was conducted by using a pull-out device. The applied load was measured by a load cell. The displacements at the loaded end and the free end were measured by the electronic digital dial gauges. A special plate with an angle dial was designed and fastened to the loaded end, which can twist with the steel strand. The twisting angle of strand can be directly measured as the swept angle of the fixed dial gauges. The details of the pull-out test setup are shown in Fig. 4.4.

In order to study the transfer of bond stress of strand within the embedded length, sixteen strain gauges of 2 cm in length were evenly set on the two opposite surfaces of each beam to analyze the stress transfer during the pull-out test. The spacing of the strain gauges was 150 mm. Therefore, the strains of the concrete cross-sections could be obtained by averaging the strains between the two opposing surfaces. The strains of steel strand are derived from the force equilibrium equation between strand and concrete. Figure 4.4 shows arrangement of the strain gauges.

The whole pull-out test was controlled by the applied load. First, a loading rate of 5 kN was used before the initial relative slip between strand and concrete, which can be detected at the free end of the beam. After the strand moving, a loading rate of 3 kN was applied until the maximum pull-out load was reached or the steel strand was broken. At each loading step, the applied load, slips at two ends, and the twisting angle of strand were measured, separately.

As previously described, the concrete strains were recorded on the two opposite surfaces. It should be noted that there are cracks on Surface 1 of all the beams. All strain gauges are placed on surfaces 2 and surfaces 4. The concrete strain on each cross-section was acquired by averaging the two opposing strains (see Fig. 4.4). The typical strain distribution for uncorroded and corroded beams in groups S and R is shown in Fig. 4.5.

As Fig. 4.5 shown, the distribution of concrete strain is not uniform during the loading process. Concrete strains increased from the free end to the loaded end. The decrement of concrete strain was influenced by concrete cracking. Under the same pull-out load, concrete strain on the uncorroded beam reduces to 0 within a short bond length. The concrete strain in cracked beam decreases slowly. The bond length of the cracked beam is much longer than that of the uncorroded beam. It is shown

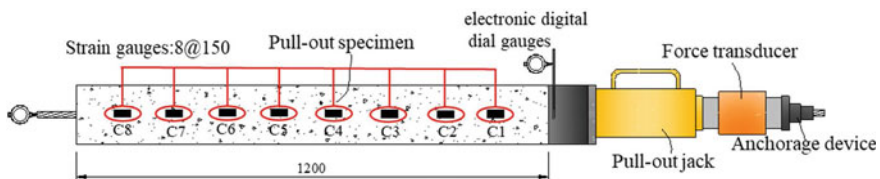


Fig. 4.4 Loading test device

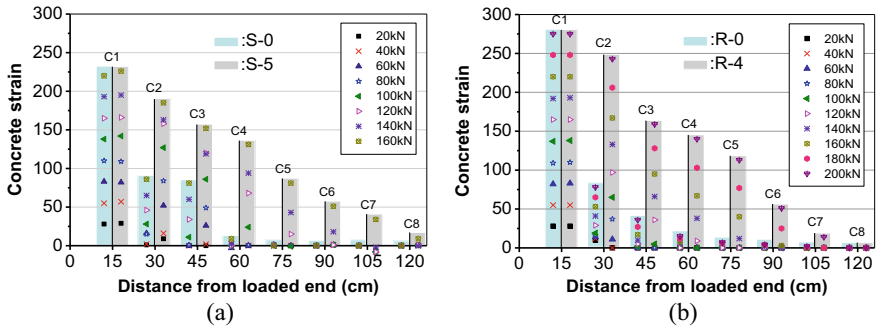


Fig. 4.5 Comparison of concrete strains between a S-0 and S-5; b R-0 and R-4

that concrete cracking reduces the bond performance. To resist the pull-out load, the cracked beam requires a longer bond length.

The bond property of the beams after concrete cracking was evaluated based on the effective bond length of steel strands. In this test, the bond length was obtained based on the concrete surface strain. The bond length is equal to the distance from the loaded end to the point where the strain value drops to zero. The bond length under the different pull-out loads is shown in Fig. 4.6.

The corrosion-induced cracks increased with the bond length for the all beams. Crack length and bond length of different beams under the loading of 80 KN are shown in Table 4.3. It is also shown that the bond strength of beams decreased after concrete cracking. In addition, the presence of stirrups delays the increase in bond length. The width of corrosive cracks in beams S-3 and R-1 is similar, while the bond length of R-1 with stirrups is 66% lower than that of S-3.

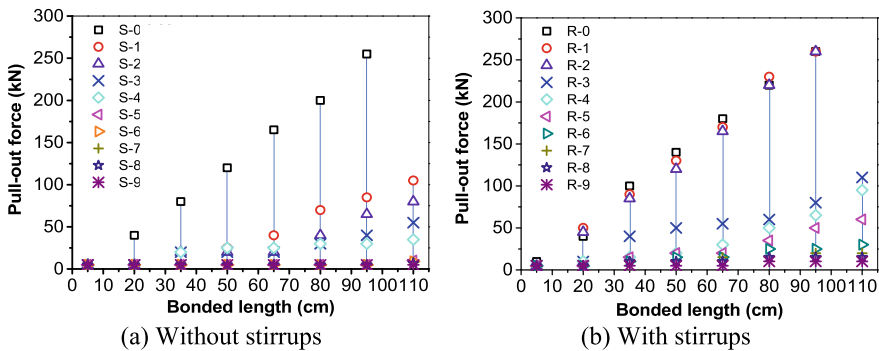


Fig. 4.6 Bond length at various loading levels: a group S; b group R

Table 4.3 Crack length and bond length under the loading of 80 KN

Test beams	S-1	S-3	S-5	S-7
Crack length (mm)	0.11	0.22	0.41	0.58
Bond length (cm)	45	90	110	110
Test beams	R-1	R-3	R-5	R-7
Crack length (mm)	0.28	0.55	0.70	1.02
Bond length (cm)	32	95	110	110

4.2.3 Twisting of Strands

In the pull-out test, it was found that the steel strand rotated along the twisting direction, which was different from the pull-out test of the deformed steel bars. The pull-out slip of corroded strand is composed of the twisting slip and the longitudinal slip. The longitudinal slip refers to the direct pull-out slip, which is similar to the deformed steel bars. The twisting slip refers to the slip caused by the rotation of steel strands. In this test, the effect of corrosion on bond properties was investigated by measuring the twisting angle of the strand. As described in Sect. 4.2.2, visual inspection was used to determine the twisting angle. The twisting angle at the ultimate state could be influenced by the tensile and yielding of strand. Therefore, the twisting angle at 75% of the maximum pull-out load was utilized to define the twisting behavior of beams.

Effects of corrosion on the twisting of strand are measured by using the normalized twisting angles. The normalized twisting angles are ratios of the typical twisting angles to the corresponding slippages. The strand would act like a screw twisting along the concrete nut, if the confinement stress of the concrete nut is enough. In this case, the normalized twisting angles could be equal to the ratio of circumference angle to the pitch length of strand, which is equal to 1.6. Through the collected experimental data, it was found that the normalized twisting angles for beams ranged from 0.5 to 1.35, which are less than 1.6. This verifies that the longitudinal slip of strand is accompanied by twisting slip. The normalized twisting angles decrease with the increasing corrosion loss. This suggests that the longitudinal slip becomes increasingly significant in severely corroded beams. This phenomenon is caused by: (1) cracks caused by corrosion deteriorating the confinement of concrete; (2) the concrete gear effect decreases with the increases of the section area loss of the outer wires. In other words, there is less contact area between the concrete gear and the strand.

4.2.4 Pull-Out Force and Slip

Figure 4.7 shows the pull-out force–slip curves of all beams. Figure 4.7a and c show the pull-out force–slip curves at the loaded end. It can be seen from the figure

that for all beams, the slip gradually propagates with the increase of the pull-out load. All the curves have a linear growth phase followed by a nonlinear increase phase. The formation of the linear stage is due to the elastic deformation of concrete cover. After that, as the slip increases, the bond behavior begins to locally damaged, leading to nonlinear increase. Eventually, the pull-out beam failed when it reaches maximum pull-out load or when the strand broken. Corrosive cracks of concrete and the confinement of stirrups affected the two stages and the bond failure of beams.

The bond stiffness of the beam is represented by the slope of the pull-out load–slip curves. The combined effects of corrosive cracks of concrete and stirrups play a role in the degradation of bond stiffness. The bonds stiffness of the beam without stirrups (Fig. 4.7a) diminishes rapidly after concrete cracking. This downward trend continued until the crack width reached 0.58 mm. When this crack width is exceeded, the bond stiffness begins to stabilize. For the beams with stirrups, the degradation of the bond stiffness is significantly different from that of the beams without stirrups. The bond stiffness does not begin to decrease until the corrosive crack width reaches 0.35 mm, as shown in Fig. 4.7c. As the crack continues to propagate, the bond stiffness decreases rapidly. The bond stiffness tends to be stable when the corrosive crack width exceeds 1.02 mm.

The above-mentioned effects of corrosive cracks on the bond stiffness can be attributed to the effects of concrete confinement and stirrups. For the beams without

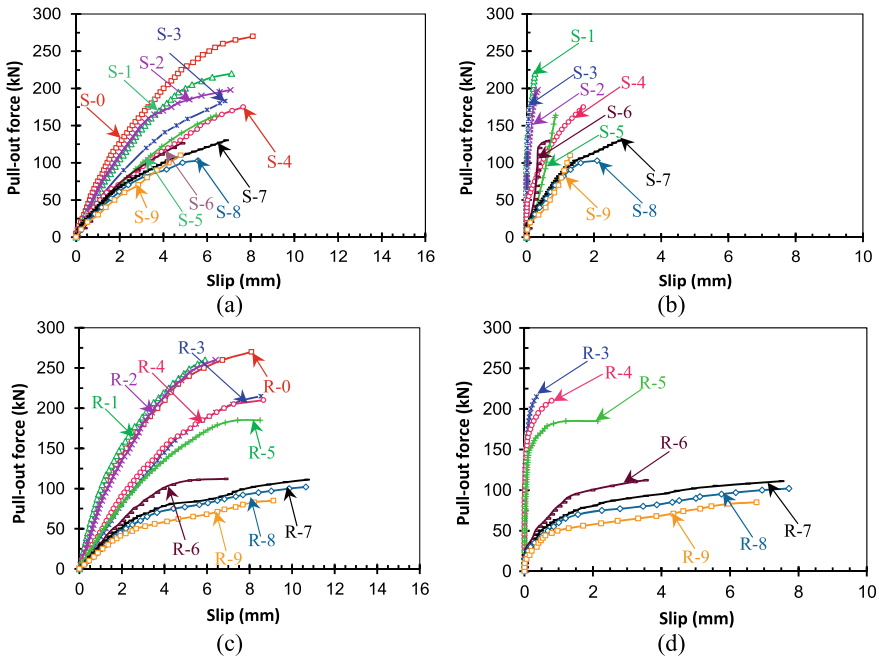


Fig. 4.7 Pull-out load and slip: **a** group S at loaded end; **b** group S at free end; **c** group R at loaded end; **d** group R at free end

stirrups, the confinement is mainly provided by the external concrete. The corrosive cracking led to a decrease in concrete confinement, reducing the bond stiffness of the beams. When the corrosive crack exceeds a certain critical width, only the residual friction force between strand and concrete can provide the bond force. Under this circumstance, the performance of strand bond degrades to a steady state.

For the stirrup-added beams, both concrete and stirrups play a restraining role on steel strand. During the concrete cracking, the presence of stirrups limits the expansion force caused by corrosion. Therefore, the bond stiffness does not start to decrease slowly until the crack width reaches 0.35 mm. Instead of the beam without stirrups, the bond stiffness decreases promptly after concrete cracks. Similarly, the corresponding critical crack width is significantly higher than that of the beam without stirrups when the beams with stirrups reach a stable bond stiffness. For the beams with stirrups, the bond stiffness does not stabilize until the crack width exceeds 1 mm. Therefore, the presence of stirrups weakens the decrease in bond stiffness induced by concrete corrosive cracking.

The pull-out force–slip relationship at the free end of beams is shown in Fig. 4.7b, d, respectively. For the beams without corrosion S-0, R-0 and the beams with lightly corrosion R-1, R-2, the slip at the free end could not be detected due to the fracture failure of strand before the relative slip occurs. For the remaining beams, all strands were pulled out, and the corresponding slip at the free ends was also detected. When relative slip is detected at the free end, it indicates that the chemical adhesive force is completely invalid, resulting in a nonlinear relationship for all subsequent pull-out force–slip relationships at the free end. Bond stiffness at the free end for both the beams without and with stirrups decreases with the increase of crack width, which is consistent with that at the loaded end.

4.2.5 *Distribution of Bond Stress*

In this part, the influences of corrosion-induced cracking and stirrups on the degradation of the peak bond stress and the distribution of bond stress are studied based on the measured concrete strains.

According to the force equilibrium relationship between steel strand and concrete during the pull-out test, the distribution of bond stress along the entire embedded length can be obtained by the following steps. Firstly, according to the 16 strain gauges attached to the concrete surface, the beam is divided into seven sections in the longitudinal direction. The length of each section is 150 mm. Then, it is assumed that the cross-sectional concrete strain at the arrangement position of the strain gauge is uniformly distributed; the strain value of the steel strand at the cross-section can be obtained from the concrete strain. Finally, the average bond stress τ_i for each section can be calculated by converting between the concrete surface strain and the strand strain. The average bond stress τ_i of section i (i is the number of each section) is expressed as:

$$\tau_i = \frac{\Delta\varepsilon E_c A_C}{150\pi d}, \tag{4.1}$$

where $\Delta\varepsilon$ is the difference of concrete strain between adjacent gauges; d is the nominal diameter of steel strand; E_c is the elasticity modulus; A_C is cross-sectional area of the beam.

Under different pull-out loads, the average bond stress τ_i of each small section along the longitudinal direction can be obtained based on this method. Figures 4.8 and 4.9 show the distribution of bond stress for all beams under the pull-out loads of 40 kN, 80 kN, 120 kN, and the ultimate load, respectively. The distribution of bond stress is obtained by marking and connecting the center points of each section.

As shown in Figs. 4.8 and 4.9, for the beams with and without stirrups, the increase of the corrosive crack width significantly weakens the maximum bond stress peak under the same pull-out load. For the beam group without stirrups, compared with the uncorroded control beam S-0 under the pull-out load of 80 kN, it can be seen that the peak bond stresses of the beams S-2, S-5 and S-9 were reduced by 18%, 56%, and 58%, respectively. Similarly, compared with the uncorroded control beam R-0, the beams with stirrups R-2, R-5, and R-9 under the pull-out load of 80kN showed the reduction of 4%, 14%, and 66% in the peak bond stress, respectively. Under a consistent pull-out load, the maximum bond stress of the beams with stirrups is usually larger than that of the beams without stirrups. Figure 4.10 is a comparison diagram of the maximum bond stress on the beams with and without stirrups under the different pull-out loads. It can be seen that under the external pull-out loads of

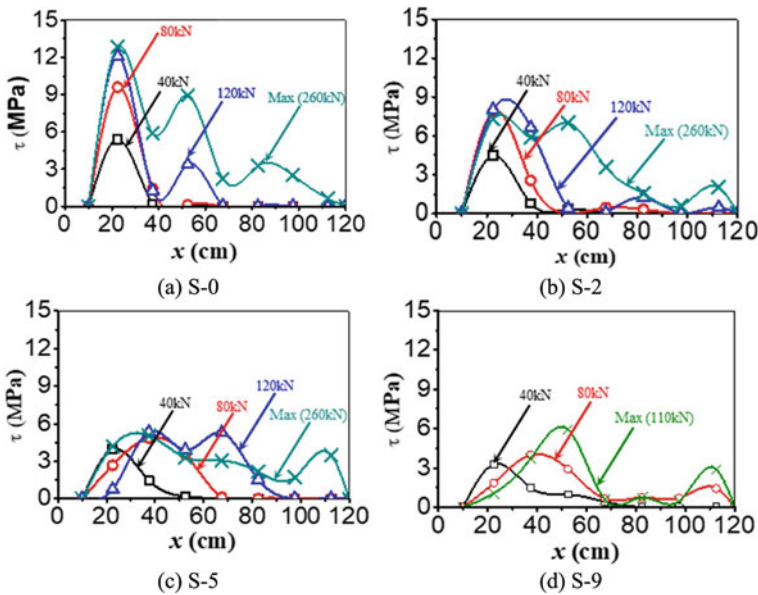


Fig. 4.8 Distribution of bond stress: beams without stirrups

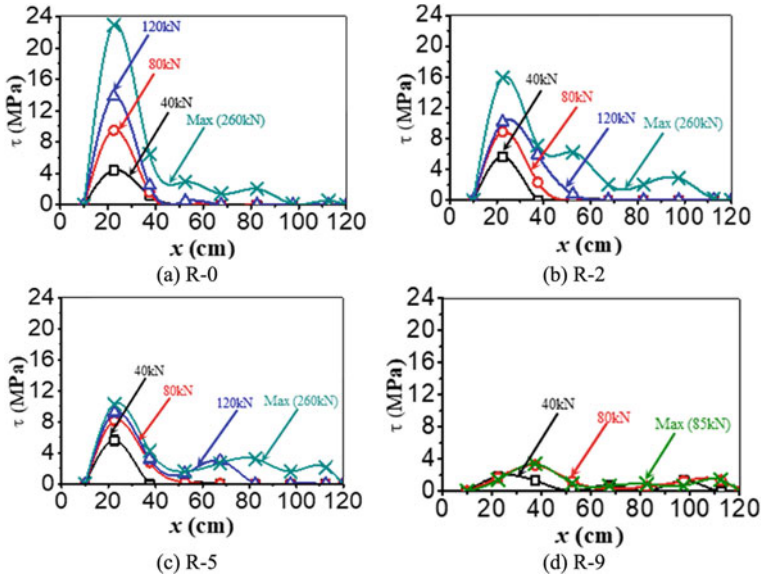


Fig. 4.9 Distribution of bond stress: beams with stirrups

40kN, the maximum bond stress of the beams with stirrups is 34.5% higher than that of the beam without stirrups. The maximum bond stress of the beams with stirrups is 42.5% higher than that of the beam without stirrups under the external pull-out loads of 80kN.

In addition, it can also be known from Figs. 4.8 and 4.9 that the width of the corrosive crack exceeds a certain critical value with the increase of the pull-out load. The maximum bond stress starts to move from the loaded end to the free end along the longitudinal direction of the strand. For the beams without stirrups, the movement of the peak bond stress first occurs in the beam S-5, and the corrosive crack is 0.41 mm through the analysis of the test results. Thereafter, the movement persisted as the cracks continued to increase. Therefore, it can be considered that the width of the critical crack of the beams without stirrups is 0.41 mm that causes the movement of the peak bond stress. For the beams with stirrups, however, the critical crack width is significantly higher than that of the beams without stirrups. In the current test, the movement of the peak stress was observed for beam R-9. Therefore, it can be considered that the critical crack width for the beams with stirrups causes the shift of the peak bond stress which is 1.29 mm. It can be seen that stirrups can effectually limit the movement of the peak bond stress between strand and concrete caused by corrosive cracks.

The current research presents a distribution parameter S_τ to quantitatively describe the uneven stress distribution of beams. S_τ is the sum of the squares of the differences between each segmental bond stresses τ_i and the overall uniform bond stress τ . S_τ is specifically expressed as follows:

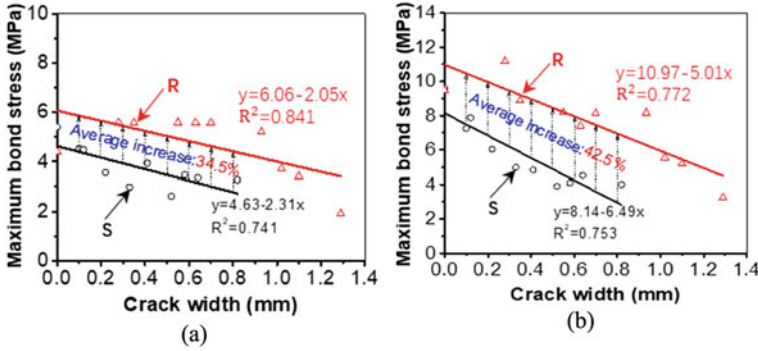


Fig. 4.10 Maximum bond stress: a at 40 kN; b at 80 kN

$$S_{\tau} = \frac{1}{n} \sum_{i=1}^n (\tau_i - \tau)^2, \tag{4.2}$$

where n is the number of subsections within the beam segment. The larger of τ_i illustrates the non-uniform distribution of the bond stress [19].

The effects of corrosive cracks on S_{τ} for all the beams under different pull-out loads are shown in Fig. 4.11. It can be seen that the complete cracking of concrete caused by corrosion obviously affects the development law of the parameter. At the same pull-out load, S_{τ} diminishes with the increase of crack width for all beams. In addition, the stirrups also have a significant effect on S_{τ} . For all the beams without stirrups, S_{τ} is made up of two stages. First, when the pull-out force increases, the parameter increases. Then, when the pull-out force surpasses a critical value, the parameter decreases. For beams with stirrups, when the crack width is greater than 0.70 mm, S_{τ} would cut down. When the crack width is the same, the increase of S_{τ} in beams with stirrups is significantly higher than the increase of S_{τ} in beams without stirrups.

The above phenomenon can be explained by the degradation of bond strength after concrete cracking. In initial phase of the loading in pull-out test, since the bond performance at this time is relatively good, it is ensured that S_{τ} has a certain increase. With the increase of the pull-out force and slip, bond stress is gradually decreased with the local bond failure, leading to the non-uniform distribution of bond stress. Concrete cracking in the initial stage cannot instantly reduce the bond stress of the beams with stirrups. Therefore, the distribution parameter S_{τ} can continue to increase until the cracks width reaches a certain critical value. The result suggests that stirrups can positively delay the degradation of the bond behavior caused by corrosion.

4.2.6 Bond Strength of Corroded Strand

The parameter τ is employed to indicate the bond stress in the current study. The bond stress τ is expressed as the pull-out load divided by the strand surface area within the embedded length. In this study, the influences of corrosion on the reduction of strand surface area are not taken into account. The bond stress τ of strand is denoted as [11]:

$$\tau = \frac{F}{\left(\frac{4}{3}\pi d\right)l_{\text{emb}}}, \quad (4.3)$$

where F , d , and l_{emb} are the pull-out load, the nominal diameter of strand, and the strand embedded length, respectively.

According to the existing research carried out by scholars [3], there are two types of bond strength between steel strand and concrete: τ_p and τ_m , which correspond to the pull-out loads at initial slip of the free end and the pull-out load, respectively. The two parameters had been employed to predict the bond stresses between steel strand and concrete. Also, τ_p and τ_m are used to reflect the bond strength, which are supplied by the chemical adhesion between strand and concrete and overall bond strength of beams, respectively. Therefore, the two parameters were calculated for all beams in this pull-out test.

For the beam with strand slip at the free end, the embedded length l_{emb} is regarded as the total bond length of 1100 mm. For the beams: S-0, R-0, R-1, and R-2, however, there are no slips happened at the free end until beam failure. τ_p cannot be determined directly. In this situation, l_{emb} is calculated using the concrete strain of beams described in Sect. 4.2.2. The embedded length is equal to the distance from the loaded end to the cross-section when the concrete strain is 0. For the uncorroded beams, the bond strength τ_p can be considered equal to τ_m based on the similar pull-out test by Cousins et al. [5]. The bond strengths τ_p and τ_m for all the beams are given in Table 4.4. Figure 4.12 shows the normalized bond strengths τ_p and τ_m .

The normalized bond strength τ_p is shown in Fig. 4.12a. It can be seen from Fig. 4.12a that the bond strength τ_p drops rapidly to a small value as the crack width increases for the beams without stirrups. When the crack width exceeds 0.4 mm, the residual bond strength basically disappears completely, which can be approximately considered to be equal to 0. This result indicates that concrete cracking reduces the bond stress provided by the chemical adhesive forces. For beams with stirrups, the bond strength τ_p does not begin to degrade until the crack width exceeds 0.35 mm. And the rate of descent is lower compared to the beams with stirrups. The residual bond strength of the beam with stirrups is also greater than that of the beam without stirrups. This finding suggests that the stirrups can effectively mitigate the reduction in the chemical adhesion caused by concrete cracking.

The normalized bond strength τ_m for all beams is shown in Fig. 4.12b. τ_m decreases with the increase of the crack width, and the stirrups have a positive influence on τ_m . In the case of the same crack widths, the degradation of τ_m in beams with stirrups is

Table 4.4 Experimental results of the pull-out tests

Number	W_{ave} (mm)	F_p (kN)	τ_p (MPa)	F_m (kN)	τ_m (MPa)	τ_p/τ_m	Number	W_{ave} (mm)	F_p (kN)	τ_p (MPa)	F_m (kN)	τ_m (MPa)	τ_p/τ_m
S-0	0	–	4.07	265	4.07	1.00	R-0	0	–	4.38	265	4.38	1.00
S-1	0.11	105	3.18	220	3.18	0.48	R-1	0.28	–	4.38	265	4.38	1.00
S-2	0.11	81	2.87	198	2.87	0.41	R-2	0.35	–	4.30	260	4.30	1.00
S-3	0.22	57	2.62	183	2.62	0.30	R-3	0.55	110	1.58	215	3.08	0.51
S-4	0.33	35	2.50	175	2.50	0.20	R-4	0.63	95	1.36	210	2.99	0.45
S-5	0.41	12	2.34	164	2.34	0.07	R-5	0.70	60	0.86	185	2.64	0.32
S-6	0.52	9	1.80	129	1.80	0.07	R-6	0.93	30	0.43	112	1.60	0.27
S-7	0.58	8	1.80	130	1.80	0.06	R-7	1.02	20	0.29	111	1.58	0.18
S-8	0.64	7	1.47	103	1.47	0.07	R-8	1.10	15	0.22	102	1.46	0.15
S-9	0.82	5	1.57	110	1.57	0.05	R-9	1.29	10	0.14	85	1.22	0.12

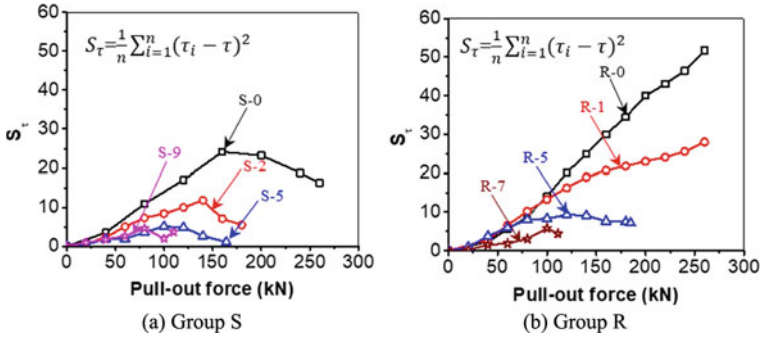


Fig. 4.11 Relationship between S_τ and pull-out force

less than the degradation of τ_m in the beams without stirrups. For instance, the beam without stirrups S-6 decreased by 53% contrast with S-0. The reduction ratio is 1.76 times compared to the beam with stirrups R-3. This result indicates that the stirrups have an active effect in the bond strength after concrete cracking. Generally speaking, the stirrups enhanced the residual bond stress by about 25% in this research.

4.3 Bond Behavior of Corroded Strand in PC Beams

4.3.1 Corrosion Loss and Corrosion-Induced Crack

In the present study, nine specimens (PS0-PS8) were designed. Among them, eight specimens (PS1-PS8) were accelerated by the technique of electrochemical corrosion. Specimen PS0 was used as an uncorroded control specimen for comparison with the other eight corroded specimens. The design rectangular cross-section of specimens is 200 mm × 350 mm, and the length of specimens is 4000 mm. A hollow section (500 mm × 60 mm × 70 mm) positioned in the center of beam separated each beam into two independent bonded parts (labeled A and B). By installing PVC pipes around the steel strand, an unbounded zone with a length of 200 mm was created at the end of both bonded zones. Each bonded part of specimens was detailed with a 1300 mm embedded length; the embedded length falls between the 1024 mm transfer length and 2048 mm development (anchorage) length acquired from Eq. (12.4) in ACI 318-11 (ACI 318-11).

All the specimens have a 15.24 mm prestressing strand. The concrete cover of the specimens is 67.4 mm. Two 16 mm and two 10 mm deformed bars are located in the tension and compression section of specimen, respectively. The stirrups with the diameter of 10 mm were also used to reinforce each specimen at 100 mm intervals. To ensure the independent corrosion of steel strand, the 15.2 mm strand was segregated

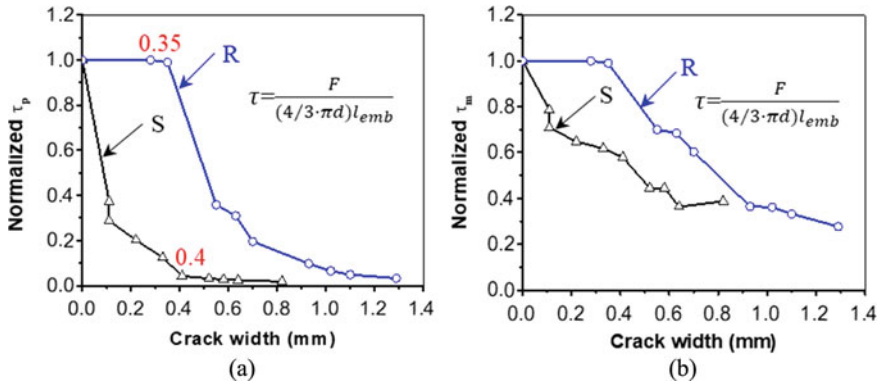


Fig. 4.12 Effect of crack induced by corrosion on the relative bond stress: a τ_p ; b τ_m

from the remainder reinforcements. The other steel bars in the specimens were coated with epoxy coating to prevent corrosion. The specimen details as shown in Fig. 4.13.

The nominal yield and ultimate strengths of the 15.2 mm strand are 1830 MPa and 1860 MPa, respectively. The elastic modulus of steel strand is 195 GPa. The deformed bars were used for the stirrups, the bottom and top bars. The deformed bars have the nominal yield strengths of 400 MPa and the ultimate strengths of 570 MPa. The elastic modulus of deformed bars is 200 GPa, and the diameters of strands are 10 mm and 16 mm, respectively.

Before concrete is poured, the steel strands were pretensioned to 75% of their nominal tensile strength (1860 MPa), i.e., 1395 MPa. The tensioning was completed after two days; the loss of prestress caused by the stress relaxation of the prestressed steel strands was eliminated by the pad steel sheets. That is, the stress of the steel strand was tensioned to 1395 MPa again, and the excess space was filled with steel sheets of appropriate thickness. Additionally, 5% NaCl was prepared to accelerate the corrosion process. During the construction of specimen, three concrete cubes (150 × 150 × 150 mm) were manufactured for obtaining the compressive strength of concrete. After curing at 28 days, the three cubes were tested, and the average compressive strength was 42.6 MPa.

The prestressing strands in specimens PS1-PS8 were accelerated by an electrochemical technique. First, two water tanks were hang below of the two separated bond sections. To keep the corrosive solution from leaking out, a structural glue was used to fill the space between concrete and water tank. Then, the tanks were filled with a 5% saline solution. The accelerated corrosion device is shown in Fig. 4.14.

During the accelerated corrosion test, a stainless-steel plate was immersed in the solution and connected to the DC power supply cathode. And anode was connected to the exposed strand at the end of specimen. To speed up the corrosion, a current density of 200 $\mu A/cm^2$ was used. PC beams were subjected to the different corrosion process to acquire the varied degrees of strand corrosion. The corrosion durations for specimens PS1-PS8 were given in Table 4.5. After the accelerated corrosion test, the

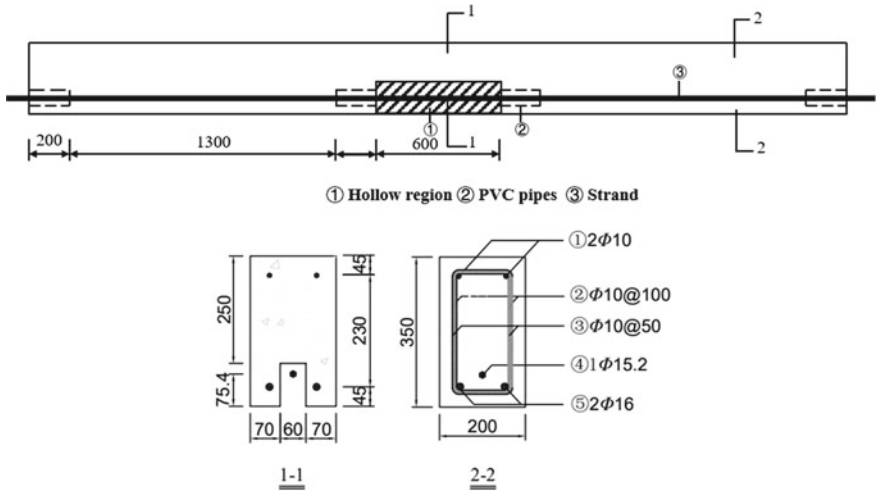


Fig. 4.13 Details of beams (Unit: mm)

Table 4.5 Durations of corrosion for beams

Specimens	PS1	PS2	PS3	PS4	PS5	PS6	PS7	PS8
Corrosion time	5	7	8	10	15	18	22	25

corrosive cracks on the surface were recorded by the following steps. Firstly, the rust around the cracks was cleared and the specimens allowed to dry for 1–2 days. After that, the shape and location of the corrosive cracks were recorded next to the surface cracks of the specimen. Finally, the crack width was measured by a crack width detector. The accuracy of the crack width detector is 0.01 mm, and the measured crack spacing is 10 cm.

The corrosion-induced crack propagates longitudinally along the steel strand at the bottom of specimen. Crack width and corrosion loss varied along the length of steel strand. The crack width and the corrosion loss increase as the corrosion time. The average crack width of specimens (W_{ave}) and the average corrosion loss of specimens (q), shown in Table 4.6, were used in the subsequent study.

4.3.2 Effect of Corrosion on Force–Slip Response of Strand

Following the accelerated corrosion operation, the specimens were subjected to the bond tests. All the specimens were simply supported over a span of 3600 mm. A MTS loading device with the capable of 300kN was used to apply the monotonic loaded. The external force was applied symmetrically on the specimen. The distance

Table 4.6 Corrosion parameters of specimens

No	PS1		PS2		PS3		PS4	
Part	A	B	A	B	A	B	A	B
w_{ave} , mm	0.11	0.13	0.14	0.11	0.20	0.31	0.29	0.24
q , %	2.98	2.97	3.57	3.17	4.76	5.25	4.97	5.23
No	PS5		PS6		PS7		PS8	
Part	A	B	A	B	A	B	A	B
w_{ave} , mm	0.26	0.36	0.32	0.37	0.47	0.36	0.39	0.32
q , %	6.47	7.34	7.98	8.10	8.32	8.08	9.21	9.24

between the two loading points is 1000 mm. The schematic diagram of the loading device of the specimen is shown in Fig. 4.13.

As can be seen in Fig. 4.13, the pull-out force is slowly applied to the middle strand of the test specimen as the external bending load increases. The slip of the steel strand during the loading was recorded by setting four electronic digital dial gauges at the respective loading ends and free ends. For measuring the slip of strand at the loading end, since the gap in the middle of the specimen is small, the clamps were fixed on the steel strand and extended from the bottom of the specimen, and then the electronic digital dial gauges were placed on the clamps. For the free end, the electronic digital dial gauges were placed directly on the steel strand and parallel to the longitudinal direction of steel strand. In addition, an electronic extensometer was set at the exposed position of the bottom steel strand to record the strain's change of the mid-span strand during the loading process of the specimen. The experimental setup is presented in Fig. 4.15.

The testing procedure was conducted by gradually increasing load levels. The testing process was artificially divided into two stages. Firstly, the load increments of 5 kN were employed before the initial flexural cracking appeared in the tensile area. After that, the load increments of 3 kN were applied until the maximum load was

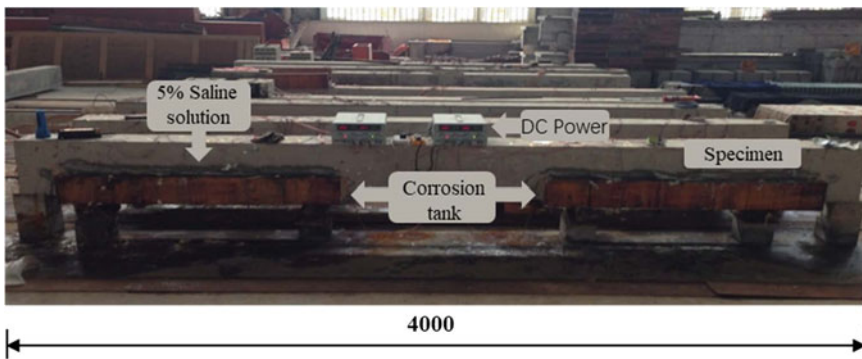


Fig. 4.14 Accelerated corrosion device

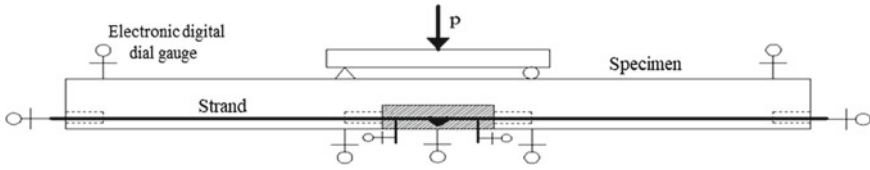


Fig. 4.15 Bond test for corroded PC beams

reached or the strand fractured. During each loading, the load was held for 5 min, and then the experimental data of each loading stage was recorded. The typical feature of beam failure is the concrete crushing at the compression area.

The bond characteristics of a prestressing strand can be efficiently reflected by the force–slip response. The key for determining the structural response is to measure the pull-out force at the loaded end. For the specimen bond test, the pull-out force (T_p) can be written as:

$$T_p = F_p - F_{\text{eff}}, \tag{4.4}$$

where F_p and F_{eff} are the tensile force of strand and the effective prestressing force for specimens, respectively.

In the bond test, the tensile force of strand cannot be directly measured. The pull-out force can be inferred using the strain increments measured during loading of the prestressing strand.

As shown in Fig. 4.16, there are two types of strain increment: yielding before failure and fracture without yielding. The steel strands yield during loading when the corrosion loss of the specimen is less than 6.91%. Once the level of corrosion is exceeded, the yielding phenomenon of the strand disappears. The steel strand has reached its ultimate strength before yielding and the steel strand fractured.

The curve of pull-out load versus strain increment relates to the constitutive relation of corroded strands. Some study on the constitutive relation of corroded strands show that the stress–strain relationship of corroded strands is closely related to the degree of corrosion of steel strands [18]. When the strand is slightly corroded, the stress–strain relationship of the strand can be expressed by a bilinear elastic relationship model. When critical value ρ_c below the corrosion losses, an elastic model can be used to represent the stress–strain relationship. The constitutive relation of the corroded strands is expressed as

$$\sigma = \left\{ \begin{array}{l} E_p \varepsilon, \quad \varepsilon \leq \varepsilon_{py} \\ E_p \varepsilon_{py} + (\varepsilon_p - \varepsilon_{py}) \frac{E_p \varepsilon - E_p \varepsilon_{py}}{(\varepsilon_{pu} - \varepsilon_{py})}, \quad \varepsilon_{py} < \varepsilon \leq \varepsilon_{pu} - \frac{\rho}{\rho_c} (\varepsilon_{pu} - \varepsilon_{py}) \end{array} \right\} \rho \leq \rho_c$$

$$\varepsilon \leq \varepsilon_{py} \quad \rho > \rho_c \tag{4.5}$$

where ε_p and σ are the strain and stress of corroded strand, respectively; E_p is the uncorroded strand elastic modulus; ε_{py} and ε_{pu} are yield strain and ultimate strain of strand, respectively; f_{pu} is ultimate strength of strand, which can be acquired based on the ultimate flexural load.

By replacing the strain ε in Eq. (4.5) with the strain increment $\Delta\varepsilon_p$ of the steel strand, the stress increment $\Delta\sigma_p$ during the loading process of the steel strand can be calculated. Then, T_p can be expressed as:

$$T_p = \Delta\sigma_p A_p \tag{4.6}$$

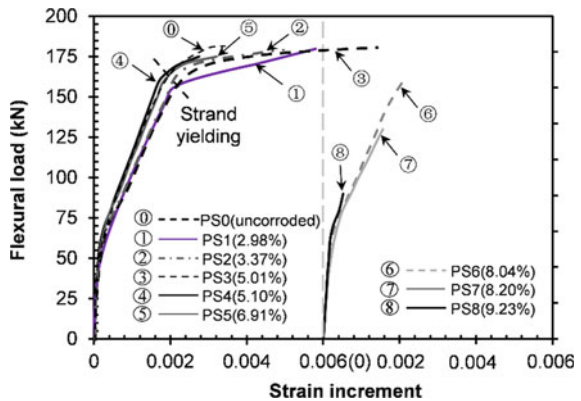
where A_p is the cross-sectional area of steel strand.

Figure 4.17 shows the relationship between the recorded bending load and the calculated pull-out load during the test. It can be seen from Fig. 4.17 that the relationship between the two loads varies with the increase of the corrosion loss. First, when the corrosion loss of strand is lower than 6.91%, the corrosion has little effect on the relationship. As the corrosion deepens, the ultimate pull-out load begins to decrease due to the occurrence of strand breakage. However, the pull-out load during the initial loading stage showed a similar trend regardless of the corrosion condition.

For all test specimens, the relationship between flexural load and slip under each load level can be obtained by recording the slip of steel strands. The force–slip relationships are established by combining these data with the relationships between the pull-out force and flexural load presented in Fig. 4.17. The force–slip responses at the loaded ends and free ends are shown in Figs. 4.18 and 4.19, respectively. The curve for the specimen without corrosion separated the force–slip curves at the loaded ends into two groups, which are depicted in Fig. 4.18a, b, respectively. Additionally, the corrosion loss of each bonded segment identified in the figure is the average corrosion rate obtained by combining all the small subsections.

As can be seen in Fig. 4.18, the force–slip response at the loaded ends of specimens was affected by the strand corrosion. When the corrosion loss is less than 7.98%, the force–slip curves have an initial linear growth stage followed by a nonlinear growth

Fig. 4.16 Relation between flexural load and strand strain increment



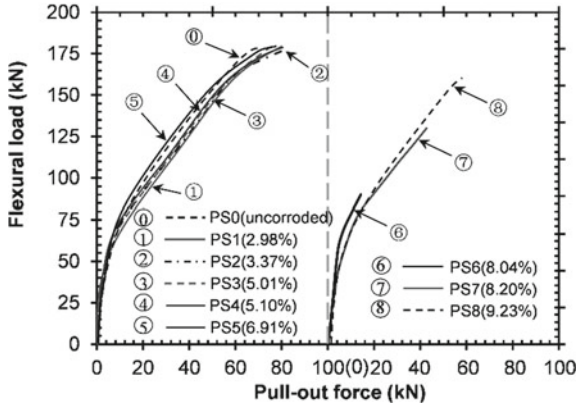


Fig. 4.17 Relation between flexural load and pull-out force

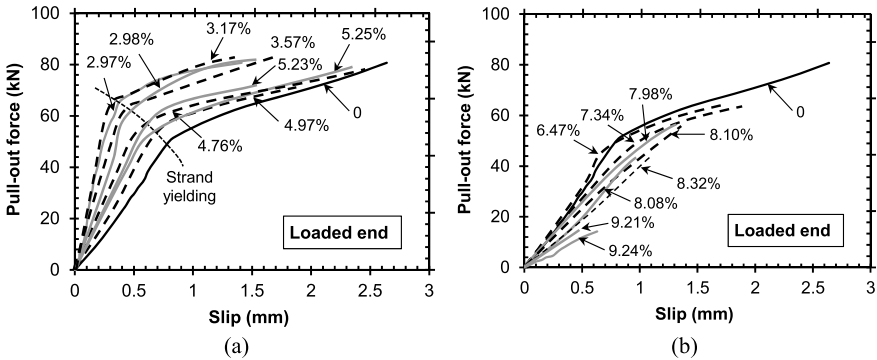


Fig. 4.18 Force-slip responses at the loaded end

stage. The generation of the linear stage is due to the sufficient bond strength and the elastic deformation of the strand. Secondly, the bond properties were locally impaired because of the yielding or excessive slip of strand, leading to an increase in slip nonlinearity. However, the nonlinear stage of slip vanishes as the corrosion of specimens deepens. This indicates that the specimens with the greater corrosion losses are destroyed before the maximum bonding strength is reached.

Additionally, the bond stiffness is expressed by the slope of the force-slip relationship curve, which can also be used to analyze the effect of corrosion of steel strand on the force-slip relationship. As we can see in Fig. 4.18, the effect of strand corrosion on the bond stiffness depends on the loss of corrosion. When the corrosion loss is lower than 5.25%, the strand corrosion has a significant effect on the bond stiffness. Minor corrosion raises the coefficient of friction between strand and concrete. The longitudinal confinement provides external pressure on the strand after concrete cracking. These two factors lead to the higher bond stiffness than the control

specimen. When the corrosion rate is greater than 6.47%, the bond stiffness begins to decrease compared to the control specimen, especially for the specimens with corrosion loss greater than 8.08%.

The effects of strand corrosion on the force–slip relationship at the free and loaded end were investigated. The force–slip curves at the free end are shown in Fig. 4.19. As shown in Fig. 4.19, there is a clear distinction between the force–slip relationship at the free and loaded end. There is no slip of the free end was detected at the beginning of the bond test. After initial slip, the slip grows linearly at the free end, which could be attributed to the yielding of strand and the damage to the chemical adhesion.

Force–slip curves at the free ends were affected by the strand corrosion. As we can see in Fig. 4.19, when the corrosion loss of the specimen is less than 5.25%, strand corrosion can improve the bond stiffness. This finding is in line with the results obtained at the loaded end of the specimen. For specimens with the higher corrosion losses, the strand fractured first before any slips were discovered at the free end of the specimen. There is no slip data of specimens found in Fig. 4.19. The above situation shows that the maximum tensile strength (fracture) of the steel strands was reached before the pull-out force transfers to the prestress transfer region. This demonstrates that the bond strength did not achieve the maximum value. It also implies that the reduction in tensile strength of corroded strands may be more important than the bond behavior in the determination of the structural bearing capacity.

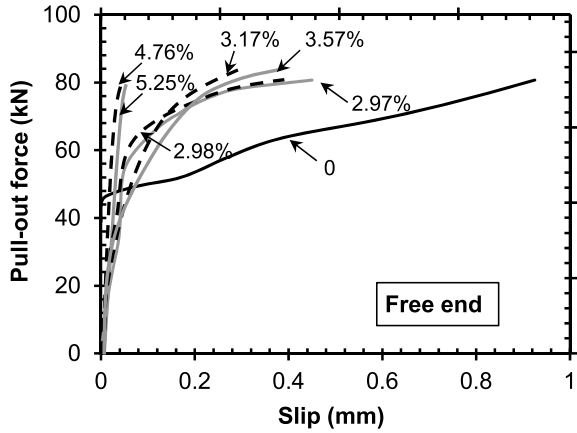
The corrosion-induced cracking also had an effect on the bond stiffness. When the corrosion crack was less than 0.31 mm, the bond stiffness was in a rising state. After that, with the increase of the degree of corrosion, the width of the corrosion crack was also further widened. The bond stiffness shows a downward trend due to the reduction of the confinement around the steel strand. This was notably true for the specimens with corrosion-induced cracks larger than 0.36 mm.

4.3.3 Failure Mode and Bond Strength

Strand corrosion significantly affects the failure modes of specimens. During bond testing, two failure types were observed: concrete crushing and strand fracture, as indicated in Fig. 4.20. For the uncorroded control specimen PS0, the pull-out failure of the steel strand occurs before the concrete in compression region was crushed, as shown in Fig. 4.20a. Ultimately, the concrete at the top of specimen was eventually crushed due to the continuous deformation of the test specimen mid-span. For specimens with a corrosion loss lower than 5.25% (PS1–PS4), when the corrosion crack width is lower than 0.31 mm, the force–slip relationship curve of the test specimens shows that the bond stiffness was increased compared to the control specimen. Under the circumstance, the corroded specimens failed due to concrete crushing before the strand was completely pulled out. This indicates that the strand bond had the capacity to grow further but did not attain its maximal bond strength.

When the corrosion loss exceeds 6.47% or the crack width exceeds 0.36 mm (PS5–PS8), the failure mode of the specimens was transferred from concrete crushing to the

Fig. 4.19 Force–slip curves at the free end



steel strand breaking failure (Fig. 4.20b). During the fracture process of steel strand, one of the external steel wires first broken and failed, which was accompanied by an instantaneous drop of the flexural load. After the first steel wire broken and before the second steel wire broken, the flexural load of the specimen can continue to increase, but the maximum bearing capacity after each loading is lower than the previous maximum bearing capacity.

For each specific loading level, the average bond stress τ of the specimens was calculated as the tensile force of strand divided by its effective bond surface area. So the average bond stress is calculated as [11]:

$$\tau = \frac{F_p}{\left(\frac{4}{3}\pi d\right)l_{emb}}, \tag{4.7}$$

where F_p , d , and l_{emb} are the tensile force of strand, the nominal diameter of strand, and the embedded length of strand, respectively.

Corroded strands in PC specimens have different bond strengths depending on the loading phases. Three bond strength types were introduced to analyze the effect of corrosion on the bond stress of steel strands under external loads. Three bond stresses types are τ_c , τ_y , and τ_u , which correspond to bond stress of strand at initial cracking, strand yielding, and specimen failure, respectively. Figure 4.21a, b show the influence of steel strand corrosion losses and corrosion crack on the bond stresses τ_c , τ_y and τ_u , respectively.

As shown in Fig. 4.21a, the bond stress at initial cracking remained at 2.15 MPa for each specimen. These findings illustrate that corrosion had little impact on the degradation of the bond stress during initial cracking. The effect of strand corrosion on the yield strength and the bond stress depends on the corrosion degree at failure of the specimen. When the corrosion loss does not exceed a certain critical value, the corrosion had no effect on the two bond stresses. On the basis of linear interpolation method, the critical corrosion losses of the two bond stresses corresponding to the

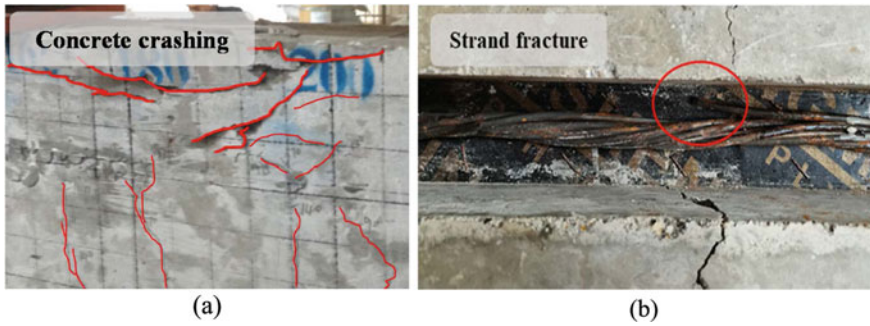


Fig. 4.20 The failure modes of PC beams

yield of strand and the failure of the specimens can be obtained as 5.25% and 4.4%, respectively. It is worth pointing out that the ultimate bond stress between strand and concrete did not reach the maximum bond strength because of the concrete crushing with the corrosion loss lower than 5.25%. τ_u is defined as the bond stress corresponding to the maximum pull-out load of strand.

In this situation, the measured ultimate bond stress of corroded strands was almost the same as that of uncorroded steel strands. When the corrosion loss was higher than the critical corrosion losses, both the bond stresses start to decrease with the increase of the corrosion degree. From the linear regression analysis of these data, it can be seen that the decrease of ultimate bond stress was significantly faster than that of the bond stress when the steel strand yields. When the corrosion loss of specimens reached 8.10% and the strand fractured without detecting yielding, the two bond stresses values were exactly equal and began to decrease together with increasing corrosion loss.

As compared with the ultimate bond stress of the uncorroded specimen PS0, the ultimate bond stresses of corroded specimens with corrosion losses of 5.25%, 7.34%, 8.10%, 8.32%, and 9.24% decreased by 7.5%, 11.4%, 14.6%, 20.4%, and 32.4%, respectively. Among these corroded specimens, for the corroded specimen PS6, the corresponding corrosion loss and corrosion-induced crack width were 8.1% and 0.37 mm, respectively. The ultimate bond stress (2.63 MPa) and ACI allowable anchorage bond stress (2.64 MPa) were almost identical. The above ACI allowable anchorage bond stress (2.64 MPa) was obtained by uniformly distributing the tensile strength of strand over the effective surface of the anchor length. This result indicates that the ACI code is relatively conservative in calculating the bond stress along the strand in the anchorage zone.

The effects of the corrosion-induced cracks on the bond stress were studied and depicted in Fig. 4.21b. As can be seen in Fig. 4.21b, the above three bond stresses change with the corrosion cracks, which is basically consistent with the effect of the corrosion loss. For the bond stress at the initial cracking stage, the change in bond stress of all the specimens is relatively small. Through linear regression analysis, it can be seen that the concrete cracks do not begin to degrade the yield bond stress and

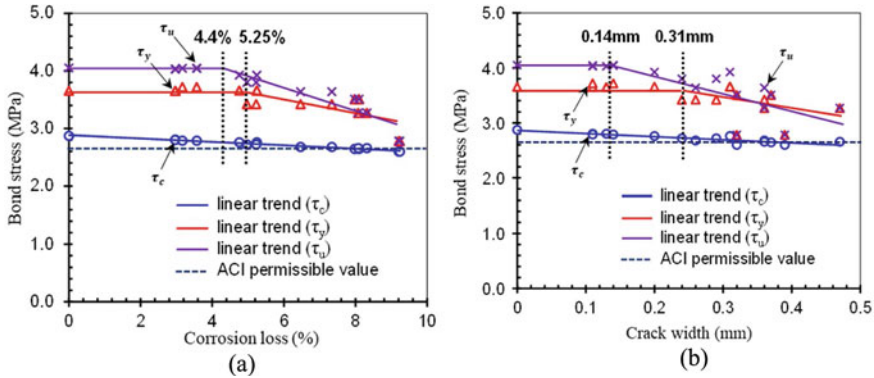


Fig. 4.21 Effect of corrosion on bond stress: **a** corrosion loss; **b** crack width

ultimate bond stress until the crack width reaches 0.23 mm and 0.14 mm, respectively. Thereafter, the two bond stresses between concrete and strand decrease with the further expansion of the crack width.

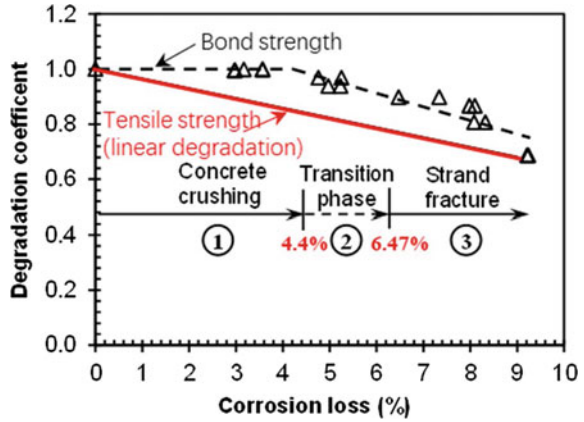
4.3.4 Degradation of Strand Bond and Tensile Strengths

The bond behavior and the tensile strength of steel strands are two key factors for determining the ultimate bearing capacity and failure modes of PC structures. When the strand corrodes, both of these controlling factors change as the strand corrosion. Premature failure of either the bond strength or the tensile strength may result in failure of the specimens. Therefore, it is necessary to determine the controlling factors for the structural performance of the specimen at different corrosion levels. The normalized bond and the tensile strength under various corrosion losses are shown in Fig. 4.22.

As shown in Fig. 4.22, the effect of corrosion on the bond strengths and the tensile strengths of strand depended on the corrosion degree. Firstly, the ultimate bond strength of strand does not begin to show a downward trend until the corrosion loss reaches 4.4%. The tensile strength of corroded steel strand, based on the existing experimental research, shows a linear downward trend with the increase of the corrosion loss [8]. Therefore, the combined effects of the bond strength caused by the strand corrosion and the degradation of the tensile strength are analyzed for the failure mode and the ultimate bearing capacity of the test beams.

First, concrete crushing in the compressive regions resulted in the failure of the uncorroded specimen and corroded specimens (PS1–PS4) with corrosion losses less than 5.25%. Region 1 in Fig. 4.22 displays these results. The ultimate capacity of corroded specimens was 180 kN, which is the same as the ultimate capacity of the uncorroded specimen. In these circumstances, there is no reduction in bond strength of corroded specimens compared to uncorroded specimens. Additionally, once the

Fig. 4.22 Degradation of strand with corrosion bond and tensile strength



prestressing strand is corroded, its ultimate tensile strength rapidly decreases [18]. Nonetheless, before the strand reached its ultimate tensile strength, the corroded specimens ruptured because of the insufficient concrete strength. At this corrosion stage, i.e., when the corrosion loss is less than 5.25%, the degradation of bond strengths and tensile strengths had no effect on the failure mode and the ultimate capacity for specimens.

When the corrosion loss of the strand increases to 5.25–6.47%, the bond strength of strand starts to decrease. At the same time, the tensile strength of strand continues to decline [18]. Within the corrosion range as shown in region 2 of Fig. 4.22, the failure mode of the specimen begins to transfer from concrete crush in compression zone to the fracture failure of strand. At this time, the degradation of the tensile strength caused by strand corrosion has a tendency to determine the failure mode and the ultimate bearing capacity of the specimens.

When the corrosion loss of the specimen exceeds 6.47%, the bond strength and the tensile strength of steel strand continue to decrease with the increase of corrosion. At this time, compared with the degradation of the tensile strength, the degradation of the bond strength is significantly lower than that of the tensile strength due to the degradation of the tensile strength. In this circumstance, the corroded specimens failed due to strand breakage, rather than a pull-out failure or concrete crush. At the same time, the ultimate capacity of the corroded specimens also rapidly degraded. This result indicates that the corrosion-induced degradation of the tensile strength of strand is more decisive for the bearing capacity and failure mode of the specimens than the degradation of the bond strength.

4.4 Conclusions

1. Corrosion-induced concrete cracking decreases bond properties. The bond stiffness and bond strength of the specimens without stirrups decreases immediately after concrete cracking. For the specimens with stirrups, the stirrups help to prevent the deterioration of bond properties caused by concrete cracking. In the pull-out test, the residual bond strength in the presence of stirrups is about 25% higher than the specimen without stirrups.
2. Corrosion-induced concrete cracking increases the bond length under a certain pull-out load. Also, stirrups have a good influence on the restriction of stress transfer and the increase of the bond length. In the pull-out test, for specimen S-3 and specimen R-1 with the similar cracks, the use of stirrups reduces bond length by approximately 66%.
3. Corrosion-induced concrete cracking decreases the maximum bond stress of specimens. When the corrosion crack width exceeds the critical value, the peak bond stress of beams begins to move from the loaded end to the free end with the increase of the pull-out load. The existence of stirrups can significantly increase the critical width value. For specimens with stirrups and without stirrups, the critical crack widths are 0.41 mm and 1.29 mm, respectively.
4. Strands corrosion has different effects on the bond stress of PC specimens at different loading stages. Before the initial concrete cracking, the influence of strand corrosion on the bond stress is basically negligible. Secondly, the influences of strand corrosion on the bond stress depend on the corrosion loss and the degree of concrete cracking. When the corrosion loss is relatively small, the degradation of yield and ultimate bond stress caused by corrosion can be neglected. However, further corrosion reduces the yield bond stress and the ultimate bond stress.

References

1. H.G. Abrishami, D. Mitchell, Bond characteristics of pretensioned strand. *Mater. J.* **90**(3), 228–235 (1993)
2. ACI Committee 318. Building code requirements for structural concrete (ACI 318-11) and commentary. American Concrete Institute, Farmington Hills, MI, 473 (2011).
3. L.M. Brearley Jr., D.W. Johnston, Pull-out bond tests of epoxy-coated prestressing strand. *J. Struct. Eng.* **116**(8), 2236–2252 (1990)
4. S.-H. Chao, A.E. Naaman, G.J. Parra-Montesinos, Bond behavior of strand embedded in fiber reinforced cementitious composites. *Strain* **50**(2), 56–71 (2006)
5. T.E. Cousins, M. Badeaux, S. Moustafa, Proposed test for determining bond characteristics of prestressing strand. *PCI J.* **37**(1), 66–73 (1992)
6. C.N. Dang, C.D. Murray, R.W. Floyd, W.M. Hale, J.R. Martí-Vargas, Analysis of bond stress distribution for prestressing strand by standard test for strand bond. *Eng. Struct.* **72**, 152–159 (2014)
7. L. Fang-yuan, Z. Ren-da, Test study on the bond-slip relationship between high strength concrete with steel cable. *Sichuan Build. Sci.* **29**(4), 4–6 (2003). (In Chinese)

8. F. Li, Y. Yuan, Effects of corrosion on bond behavior between steel strand and concrete. *Constr. Build. Mater.* **38**, 413–422 (2013)
9. J. Mangual, M.K. ElBatanouny, P. Ziehl, F. Matta, Acoustic-emission-based characterization of corrosion damage in cracked concrete with prestressing strand. *ACI Mater. J.* **110**(1), 89–98 (2013)
10. D. Mao-mao, S. Xiao-zu, Z. Yong, Experimental study on bond behavior of ribbed bar and strand. *J. Build. Mater.* **13**(2), 175–181 (2010) (In Chinese).
11. J.R. Martí-Vargas, E. García-Taengua, P. Serna, Influence of concrete composition on anchorage bond behavior of prestressing reinforcement. *Constr. Build. Mater.* **48**, 1156–1164 (2013)
12. J.R. Martí-Vargas, P. Serna, W.M. Hale, Strand bond performance in prestressed concrete accounting for bond slip. *Eng. Struct.* **51**, 236–244 (2013)
13. G. Morcous, A. Hatami, M. Maguire, K. Hanna, M. Tadros, Mechanical and bond properties of 18-mm-(0.7-in.-) diameter prestressing strands. *J. Mater. Civ. Eng.* **24**(6), 735–744 (2012)
14. A. Pozolo, B. Andrawes, Analytical prediction of transfer length in prestressed self-consolidating concrete girders using pull-out test results. *Constr. Build. Mater.* **25**(2), 1026–1036 (2011)
15. D.R. Rose, B.W. Russell, Investigation of standardized tests to measure the bond performance of prestressing strand. *PCI J.* **42**(4), 56–80 (1997)
16. W. Ying, Z. Wenzhong, W. Jide, J. Jun, A preliminary study of bond-anchorage of strand and strand bundle. *Ind. Constr.* **24**(3), 19–23 (1994). (In Chinese)
17. X. Youlin, Y. Bingxun, J. Hong, C. Youfan, Z. Long, An experimental study on Three-ply stranded wire for engineering application. *Ind. Constr.* **28**(9), 31–36 (1998). (In Chinese)
18. X. Zhang, L. Wang, J. Zhang, Y. Liu, Corrosion-induced flexural behavior degradation of locally ungrouted post-tensioned concrete beams. *Constr. Build. Mater.* **134**, 7–17 (2017)
19. Y. Zhao, H. Lin, K. Wu, W. Jin, Bond behaviour of normal/recycled concrete and corroded steel bars. *Constr. Build. Mater.* **48**, 348–359 (2013)

Open Access This chapter is licensed under the terms of the Creative Commons Attribution 4.0 International License (<http://creativecommons.org/licenses/by/4.0/>), which permits use, sharing, adaptation, distribution and reproduction in any medium or format, as long as you give appropriate credit to the original author(s) and the source, provide a link to the Creative Commons license and indicate if changes were made.

The images or other third party material in this chapter are included in the chapter's Creative Commons license, unless indicated otherwise in a credit line to the material. If material is not included in the chapter's Creative Commons license and your intended use is not permitted by statutory regulation or exceeds the permitted use, you will need to obtain permission directly from the copyright holder.



Chapter 5

Bond–Slip Model of Corroded Strand Considering Rotation Effect



5.1 Introduction

The bond performance between prestressed steel strands and concrete is very important for PC structures. For convenience of calculation, the bond between steel strands and concrete can be idealized as the shear stress along the bond interface [23]. The strands are subject to corrosion due to the penetration of chloride ions in an aggressive environment. Damage to the contact surface and corrosion-induced concrete cracking destroys the strand bond.

Many researches have been undertaken to investigate the bond behavior of corroded steels in RC structures, which can be concluded as: experimental research, theoretical analysis, and numerical simulation. Most of the existing research on the bond strength under the influence of corrosion is carried out based on experiments [6, 31, 33]. And most experiments are based on the central pull-out test. Existing tests show that the bond strength of steel strands increases at the beginning of corrosion, decreasing beyond a certain critical corrosion state, and finally reaches a steady state. Based on the existing test results [38, 40] have established empirical formulas to evaluate the degradation of the bond strength of corroded strands. However, these test prediction results are highly dependent on test conditions and have limited application in practical engineering.

Some scholars experimentally explored the bond–slip behavior between corroded rebars and concrete with stirrup constraints. Almusallam et al. [3] studied the bond strength and failure modes of corroded RC beams with the pull-out tests. The effects of concrete cover thickness, steel diameter, concrete strength, type of stirrups, and crack widths on bond performance of corroded steels have been discussed. Al-Hammoud et al. [2] compared the difference of bond properties of corroded RC beams under static and dynamic loads. Choi et al. [13] discussed the difference of the bond properties of concrete structures under natural corrosion and accelerated corrosion. The accelerated corrosion method may underestimate the effect of corrosion on the bond degradation. Additionally, some scholars had also discussed the

degradation of bond behavior of corroded RC beams with common and recycled aggregates.

Some analytical models have also been proposed to predict the bond performance of corroded RC beams. Wang et al. [38] pointed out that the bond strength between corroded steel strands and concrete was affected by many factors, such as the corrosion degree, bar type, the adjacent spacing, and the number of stirrups. Among these factors, the corrosion degree is most significant to affect the bond strength. Some scholars proposed some models to predict the bond strength of corroded steel strands based on the thick-walled theory, which considering the relationship between corrosion depth of steel and the radial displacement of concrete. Chen et al. [12] proposed a model to predict the bond strength of corroded RC beams incorporating the softening behavior of cracked concrete. Abrishami et al. [1] established a computational model for the peak bond stress in the transfer and anchorage regions of pretensioned members.

Some scholars have employed the finite element software to numerically simulate the bond behavior of corroded RC beams. Lee et al. [23] used the bond plane unit and bond interface unit to model the bond behavior of corroded RC beams. Some researchers simulated the bond properties of corroded RC beams with two numerical methods, i.e., the friction and damage type method. Bolmsvik and Lundgren [9] discussed the influences of corrosion on the bond properties of ribbed and plain bars, respectively. Some scholars used the Lattice approaches to simulate the bond properties of corroded RC beams, which can reasonably model the influence of filling extent of corrosion products in cracks. These study are all based on deformed steel bars, and there are very few study on prestressed steel strands.

Based on the above research background, this chapter theoretically deduces and analyzes the bond strength model of corroded strands by considering the rotation characteristics caused by the twisting structure of steel strands. First, an analytical model is developed to predict the bond strength of uncorroded strands by considering strand rotation. Then, the influence of corrosion-induced concrete cracking on the ultimate bond strength of corroded strand is analyzed theoretically. Finally, the theoretical model of bond strength of corroded strands was acquired.

5.2 Bond Strength of Strand Considering Rotation Effect

The seven-wire prestressed steel strand is often used in bridges. This seven-wire steel strand is made by twisting and rotating the six outer steel wires around the central steel wire. Due to the twisted structure, the steel strand is often accompanied by concrete splitting or strand rotation when it reaches the ultimate bond strength. For the pull-out beams with seven-wire steel strands, two typical bond failure modes can be identified: concrete splitting failure and pull-out failure. The confinement of concrete on the strand determines these two failure modes, leading to different bond strengths case. Concrete splitting failure can be explained as the bond failure when the surrounding concrete completely splits, as seen in Fig. 5.1a. Concrete splitting

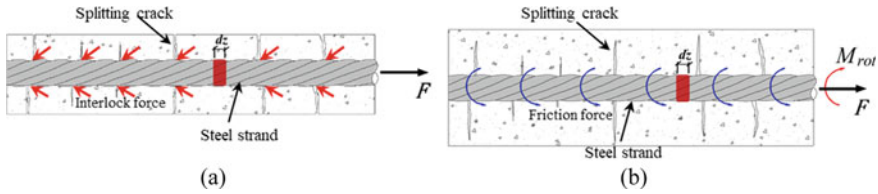


Fig. 5.1 Bond failure modes: **a** concrete splitting failure; **b** pull-out failure

failure occurs when steel strand is not sufficiently constrained by concrete cover. On the contrary, the type of pull-out failure occurs under a well-constrained condition. When the constraints are sufficient, due to the twisted structure of the steel strands, the steel strands have rotational slip before the maximum confinement stress of the concrete is reached, and the concrete is not completely split at this time, as shown in Fig. 5.1b. Various parameters determine the failure mode, including surface condition of strand, thickness of concrete cover, and tensile strength of concrete. Besides these parameters, the aggregate size may also play a role in determining the failure mode. The aggregate size has been shown to influence the interlock of ribbed bars.

In general, adequate concrete cover and additional reinforcements were designed around the steel strands to prevent splitting failure of the PC structures. This leads to the most common type of pull-out failure. However, the type of pull-out failure of steel strand differs from that of the deformed bars. When the pull-out failure occurs, the strands are not pulled out directly from concrete block. The steel strand tends to be pulled out by a helical movement around the tunnel formed by the concrete. The bond mechanism of strand determined the rotation behavior. This part theoretically analyzes the ultimate bond strength in the case of pull-out failure of the helical strand.

5.2.1 Theoretical Expressions for Bond Strength

In the part, a prediction model of bond strength is proposed according to the pull-out failure mode with strand rotation. In general, the bond stress between steel reinforcement and concrete can be regarded as a uniform shear stress along the bond interface. For a single seven-wire steel strand, the average bond stress τ_b is written as:

$$\tau_b = F_p / (i \cdot \pi \cdot d \cdot l_t), \tag{5.1}$$

where, F_p , l_t , and d are the tensile force, the bond length, and the nominal diameter of the strand, respectively; i is the perimeter factor, and its value can be taken as 4/3 for the seven-wire strand [23].

Steel strand consists of six outer helical wires wound on a straight wire in the center. Due to the helical shape of the outer wires, the projections of any cross-section of steel strand in its longitudinal direction do not entirely overlap within a

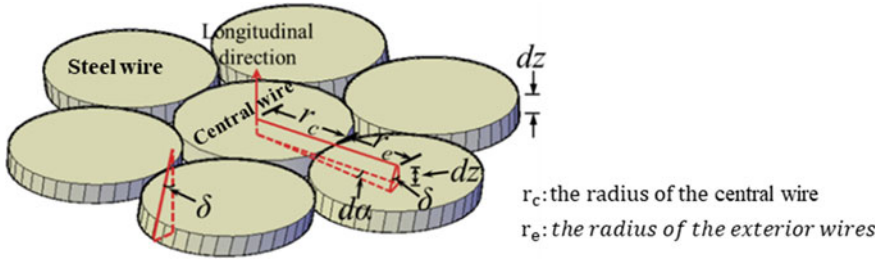


Fig. 5.2 Schematic diagram of a strand segment with the height of dz

lay length. Lay length is calculated as the distance for the outer wires turn around the center wire. It is supposed that the steel strand is longitudinally divided into several equal segments. The height of each segment is dz . A schematic diagram of a strand segment is shown in Fig. 5.2.

As can be seen in Fig. 5.2, the longitudinal extension of the length dz is related to a rotation of $d\alpha$ angle on the projection plane of strand. It is supposed that the six outer wires wrap uniformly around the straight wire in the center. The relationship between da and dz is written as:

$$\frac{d\alpha}{2\pi} = \frac{dz}{l_{\text{lay}}}, \quad (5.2)$$

where l_{lay} is the lay length of steel strand. According to the ASTM A416 standard, l_{lay} can be approximately considered as $14d$.

Additionally, the rotation of outer wires along the core wire produces an inclined angle δ (see Fig. 5.2), which can be written as:

$$\tan \delta = \frac{(r_c + r_e) \cdot d\alpha}{dz}. \quad (5.3)$$

For strands with exact diameter and lay length, δ can be computed by combining Eqs. (5.2) and (5.3). Therefore, the lay length is $14d$, δ can be determined to be 8.7° for different diameters of strands.

The mechanical interlock is produced on the helical ribs because of the inclined planes corresponding to the longitudinal direction. One segment projection along the longitudinal direction of the steel strand is shown in Fig. 5.3a.

The shaded part in Fig. 5.3a is the stress area where the rib of steel strand provides the interlocking force. The shaded part can be approximately regarded as six incomplete crescent shapes. It is assumed that the outer wire of steel strand has the same force. One of the outer wires with the crescent shape was taken for analysis, as shown in Fig. 5.3b. This simplified crescent-shaped rib is similar to the rib of the deformed bar. Due to the helical feature of the outer wires, the bearing faces are helical along the strand length, resulting in complex boundary conditions. It is assumed that the ribs providing mechanical interlocking are generated only by tangential movement

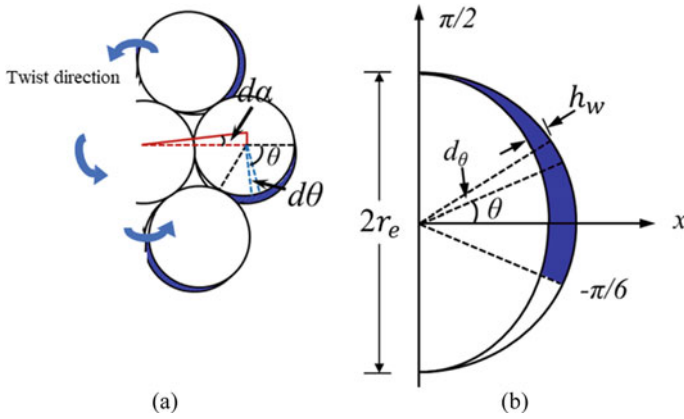


Fig. 5.3 **a** Projection of one segment along the longitudinal direction of the steel strand; **b** effective bearing face on the rib of an outer wire

of the outer wire and not by rotation of the central wire. Therefore, the helical surface can be simplified as a flat surface. The crescent-shaped rib is comparable to simulate the rib of deformed bars. The force analysis on the ribs of deformed bars is related to the force analysis of strand [11]. For a central embedded strand, it is assumed that the boundary conditions of the six outer wires are the same at a certain cross-section. Therefore, a steel wire is arbitrarily chosen for mechanical analysis. It is worth mentioned that the steel strand is considered as a whole, so the effect of the force between the steel wires is ignored.

Consider the forces acting on a rib section subtended by an angle $d\theta$ (see Fig. 5.3b). The corresponding area dA on the rib face is written as:

$$dA = h_w / \sin \delta \cdot r_e \cdot d\theta, \tag{5.4}$$

where h_w is the rib height; θ is the effective coverage angle of the incomplete crescent, the value range of θ is $[-\pi/6, \pi/2]$.

Figure 5.4a shows a force analysis of the mechanical interlock force on a single rib. It is assumed that pull-out failure happens when the shear stress on the bond interface exceeds the adhesion capacity and friction between the helical ribs and concrete. The mechanical interlocking forces acting on rib surface can be decomposed into dF_g inclined at an angle θ to the rib surface and dF_s parallel to the rib surface. dF_s and dF_g can be written as:

$$dF_s = \sigma_c \cdot dA, \tag{5.5}$$

$$dF_g = \sigma_n \cdot dA / \cos \phi, \tag{5.6}$$

where σ_c , is unit cohesion between bearing face of rib and concrete, which can be estimated as $0.11f_c$ [11], ϕ and σ_n are the friction angle between strand and concrete and the normal stress on the shear failure plane, respectively.

The forces dF_g and dF_s can be separated into forces dF_{pu} and dF_{bu} . dF_{pu} is parallel to the axial direction of steel strand and dF_{bu} is perpendicular to the axial direction of steel strand.

$$dF_{pu} = \left(\sigma_n \cdot \frac{dA}{\cos \phi} \right) \cdot \sin(\delta + \phi) + \sigma_c \cdot dA \cdot \cos \delta, \quad (5.7)$$

$$dF_{bu} = \left(\sigma_n \cdot \frac{dA}{\cos \phi} \right) \cdot \cos(\delta + \phi) - \sigma_c \cdot dA \cdot \sin \delta. \quad (5.8)$$

Integration of Eq. (5.7) along the rib bearing face results in the contribution to the total resisting force F_p

$$F_p = 6 \int_{-\pi/6}^{\pi/2} dF_{pu} d\theta = 6 \left[\frac{\sigma_n}{\cos \phi} \frac{\sin(\delta + \phi)}{\sin \delta} + \sigma_c \cdot \cot \delta \right] \cdot A_r, \quad (5.9)$$

where d_e is the diameter of outer wire; A_r is the area of one incomplete crescent shape, which can be written as:

$$A_r = \frac{2}{3} \left\{ \pi \frac{d_e^2}{4} - \pi \frac{d_e}{2} \left[\frac{d_e}{2} - \left(\frac{d_c + d_e}{2} \right) d\alpha \right] \right\}, \quad (5.10)$$

where d_c is the diameter of the central wire.

Ignoring the difference in diameter between the center wire and the outer wires, by combining Eqs. (5.9) and (5.10) result in F_p within the length of dz .

$$F_p = 2 \left[\frac{\sigma_n}{\cos \phi} \cdot \frac{\sin(\delta + \phi)}{\sin \delta} + \sigma_c \cot \delta \right] \pi d_e^2 d\alpha. \quad (5.11)$$

Substitution of F_p from Eq. (5.11) into Eq. (5.1) results in the bond stress:

$$\tau_b = \frac{3}{14} \pi \left(\frac{d_e}{d} \right)^2 \left[\frac{\sigma_n}{\cos \phi} \cdot \frac{\sin(\delta + \phi)}{\sin \delta} + \sigma_c \cdot \cot \delta \right]. \quad (5.12)$$

From Eq. (5.12), it can be seen that τ_b is relates to parameters, for instance, the ratio of outer wire diameter to nominal diameter of strand d_e/d , friction angle, ϕ , angle of inclination of strand ribs, δ , unit bond between concrete and steel strand, σ_c , and normal stress at the shear plane, σ_n . The following part explains to calculate normal confining stress, σ_n , by considering the strand rotation.

For pull-out failure of beams accompanied with the rotation of steel strand, by integrating of the radial component of the mechanical interlock, dF_{bu} produces a

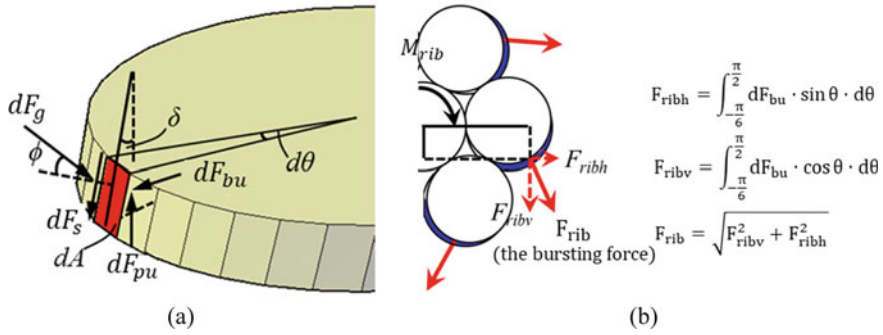


Fig. 5.4 **a** Force analysis on a single rib; **b** torque generated by bursting force

bursting force, F_{rib} , around the outer wires (see Fig. 5.4b). Therefore, the torque, M_{rib} , is applied on the steel strand because of the helical shape of outer wires. When M_{rib} applied to the strand overcomes the resistance provided by friction, strand begins to rotate in a helical way. Once the strand rotates, both bond strength and confining stress of steel strand reach the peak values, respectively. Therefore, the normal stress, σ_n , corresponding to pull-out failure of the beams accompanied by the strand rotation. σ_n is considered to be a critical confining stress, $\sigma_{n,crit}$, which can be acquired on the basis of the moment balance about the strand's center.

First, F_{rib} from the outer wire needs to be calculated. And F_{rib} is consisted of a vertical force, F_{ribv} , and a horizontal force, F_{ribh} , which are written as:

$$F_{ribv} = \int_{-\frac{\pi}{6}}^{\frac{\pi}{2}} dF_{bu} \cdot \cos \theta \cdot d\theta = \frac{3}{4} \left[\frac{\sigma_n \cos(\delta + \phi)}{\cos \phi \sin \delta} - \sigma_c \right] h_w d_e, \quad (5.13)$$

$$F_{ribh} = \int_{-\frac{\pi}{6}}^{\frac{\pi}{2}} dF_{bu} \cdot \sin \theta \cdot d\theta = \frac{\sqrt{3}}{4} \left[\frac{\sigma_n \cos(\delta + \phi)}{\cos \phi \sin \delta} - \sigma_c \right] h_w d_e. \quad (5.14)$$

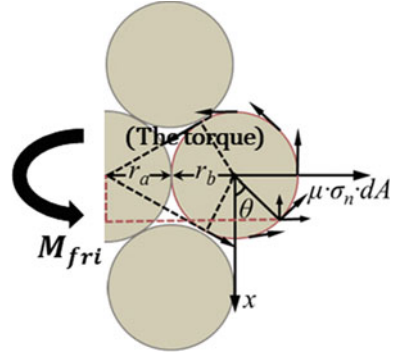
Therefore, F_{rib} , for a single outer wire is written as:

$$F_{rib} = \sqrt{F_{ribv}^2 + F_{ribh}^2} = \frac{\sqrt{3}}{2} \left[\frac{\sigma_n \cos(\delta + \phi)}{\cos \phi \sin \delta} - \sigma_c \right] h_w d_e. \quad (5.15)$$

The torque, M_{rib} , caused by the six outer ribs within the length of dz is written in terms of σ_n as:

$$M_{rib} = \frac{9}{2} \left[\frac{\sigma_n \cos(\delta + \phi)}{\cos \phi \sin \delta} - \sigma_c \right] d_e^3 dz. \quad (5.16)$$

Fig. 5.5 Torque generated by friction force



The torque, M_{fri} , was generated by the friction force around the steel strand. The friction force is considered to be evenly distributed throughout the rib face (see Fig. 5.5). In this instance, the torque, M_{fri} , supplied by the friction force can be written as

$$\frac{M_{fri}}{12} = \int_{-\pi/6}^{\pi/2} \mu \sigma_n dA \frac{d_e}{2} (\cos \theta)^2 + \int_{-\pi/6}^{\pi/2} \mu \sigma_n dA \sin \theta \left(\frac{d_e + d_c}{2} + \frac{d_e}{2} \sin \theta \right), \quad (5.17)$$

where $\mu = \tan \theta$, and μ is the friction coefficient.

The diameter of the central wire, d_c , is supposed to be same as the diameter of the outer wires, d_e . The torque M_{fri} supplied by the force of friction can be written as:

$$M_{fri} = \left(3\sqrt{3} + 2\pi \right) \frac{\mu \sigma_n}{\sin \delta} d_e^3 d\alpha. \quad (5.18)$$

The stress $\sigma_{n,crit}$ in Eq. (5.12) for pull-out failure of the beams accompanied with strand rotation can be acquired by equating Eqs. (5.16) and (5.18).

$$\sigma_{n,crit} = k \cdot \sigma_c, \quad (5.19)$$

where $k = 1 / \left[\frac{\cos(\delta + \phi)}{\cos \phi \cdot \sin \delta} - \left(\frac{2\sqrt{3}}{3} + \frac{4\pi}{9} \right) \frac{\tan \phi}{\sin \delta} \right]$.

Replacing $\sigma_{n,crit}$ from Eq. (5.19) into Eq. (5.12) results in the bond stress:

$$\tau_b = \frac{3}{14} \pi \left(\frac{d_e}{d} \right)^2 \left[\frac{k \cdot \sigma_c}{\cos \phi} \cdot \frac{\sin(\delta + \phi)}{\sin \delta} + \sigma_c \cdot \cot \delta \right]. \quad (5.20)$$

It is worth noting that $\sigma_{n,crit}$ in Eq. (5.19) is computed for the situation of pull-out failure accompanied with the rotation of steel strand, which only appears under a well-constrained condition. That is, if surrounding concrete supplied sufficient confinement on the strand, $\sigma_{n,crit}$ in Eq. (5.19) may be lower than the maximum

confining stress. In this instance, the maximum bond stress, $\sigma_{n,crit}$ should be used instead of the maximum confining stress to avoid overestimating the bond stress.

The compressive stress σ_n on the concrete is defined as the normal stress on the shear failure plane. σ_n is almost perpendicular to the longitudinal direction of strand. The generation of σ_n is closely relates to the helical characteristics of steel strand. Due to the shape of the helical ribs, the strand is forced to move perpendicular to the bond surface, resulting in radial confining stress around the steel strand. Consequently, the radial confining stress is assumed to be equivalent to the normal stress, σ_n .

5.2.2 Model Verification

In this part, some test results related to the pull-out test are collected. There is a total of 63 specimens, including 50 strands with a diameter of 12.7 mm and 13 strands with a diameter of 15.2 mm. The test data was compared with the results of the model analysis. Other details of beams such as the minimum thickness of concrete cover and bond length are shown in Table 5.1. Additionally, in the selected tests, all steel strands were tension-free before the pull-out test, which is consistent with the stress state in Eq. (5.12).

Before applying Eq. (5.20) in the calculation of ultimate bond stress for the pull-out failure with strand rotation, the maximum confining stress provided by concrete $\sigma_{n,max}$, for all the selected tests also needs to be confirmed to avoid overestimation of bond stress. For a center-embedded strand with a certain thickness of concrete cover

Table 5.1 Details of test beams from previous research and prediction results

	No. of beams	Concrete cover (mm)	Bond length (mm)	$\sigma_{n,max}/\sigma_{n,crit}$	Test/ prediction (Rotation is not considered)	Test/ prediction (Rotation is considered)
12.7 mm					Mean (S.D.)	
[24]	12	144	457	1.80	1.83(0.31)	1.04(0.17)
[31]	4	144	457	1.97	2.05(0.06)	0.96(0.25)
[6]	7	144	200	1.41	3.67(0.88)	1.03(0.17)
[22]	6	144	457	1.53	2.11(0.32)	1.02(0.15)
[29]	7	144	457	1.86	2.12(0.32)	0.95(0.23)
[33]	6	109	457	1.35	2.33(0.88)	0.92(0.36)
[10]	8	95	305	1.08	2.15(0.95)	1.02(0.31)
15.2 mm					Mean (S.D.)	
[6]	6	142	200	3.87	3.92(1.48)	1.01(0.34)
[10]	7	94	305	3.04	2.98(0.74)	0.99(0.17)

and concrete compressive strength, $\sigma_{n,\max}$ provided by the surrounding concrete to the steel strands can be considered as a constant value.

The concrete confining model proposed by Den [16] is introduced to determine the maximum confining stress $\sigma_{n,\max}$. The confining pressure model is closely related to the thickness of concrete cover and concrete strength. According to this study, the concrete surrounding steel strands can be regarded as a thick-walled cylinder. Among them, the inner radius of the cylinder is the nominal diameter of steel strand, the outer radius of the cylinder is minimum cover of concrete. The radial confining stress of concrete at different stages, such as uncracked, partially cracked stages and entirely cracked stages, was determined on the basis of the radial displacement at the interface of concrete. In partially cracked stage, when the splitting crack penetrates roughly 70% of the thickness of the cylinder wall, the maximum radial stress $\sigma_{n,\max}$ is reached (Den [16]). Further crack penetration results in rapid reduction of radial stress. The radial confining stress σ_n at partially cracked stage is written as:

$$\sigma_n = \frac{r_k}{r_s} f_{ct} \left(\frac{c^2 - r_k^2}{c^2 + r_k^2} \right) + f_{ct} \left[\frac{a \cdot 2\pi \varepsilon_c \cdot r_s}{2n \cdot w_0} \left(\frac{r_k}{r_s} - 1 \right)^2 + b \left(\frac{r_k}{r_s} - 1 \right) \right], \quad (5.21)$$

where $r_s = d/2$ is the nominal radius of steel strand; c is the minimum cover of concrete; r_k is the radius of crack front, its value is from r_s to c ; f_{ct} is the tensile strength of concrete; a and b are constants, and whose values related to the softening behavior of cracked concrete; $\varepsilon_c = f_{ct}/E_c$, where E_c is the elastic modulus of concrete; n and w_0 are the number of fictitious splitting cracks ($n = 3$) and the minimum crack width at concrete failure ($w_0 = 0.2$ mm), respectively [32].

The stress σ_n in Eq. (5.21) changes as the crack front r_k develops. However, $\sigma_{n,\max}$ is a constant value, which relates to a specific thickness of cover and concrete tensile strength. When r_k of beams penetrates into about 70% of the cylinder wall thickness, the radial confining stress reaches its peak value, that is, a constant value.

Before determining the maximum confining stresses and the critical confining stresses in Eqs. (5.19) and (5.21), it is necessary to determine the parameters, for example, tensile strength of concrete, f_{ct} , the unit adhesion between strand and concrete, σ_c , the inclination angle of rib, δ , and friction coefficient, μ . The tensile strength f_{ct} , can be correlate with the concrete compressive strength, f_c , as $f_{ct} = 0.56 \cdot f_c^{1/2}$ on the basis of ACI 318-14. σ_c , is considered as $0.11 f_c$ [11]. The strands in all data had not been coated; the angle of friction, θ , is estimated to be 20° on the basis of earlier study, which corresponds to the coefficient of friction, μ , of 0.36. The value of the inclination angle, δ , was taken as 8.7° in all the tests. It is assumed that there is no excess concrete is adhered to the bearing face to increase the angle of inclination in the case of pull-out failure.

Table 5.1 gives the ratio of the maximum confining stress $\sigma_{n,\max}$ and the critical confining stress corresponding to pull-out failure with strand rotation $\sigma_{n,\text{crit}}$ for the 12.7 mm and 15.2 mm steel strands, respectively.

The maximum confining stresses in Table 5.1 are larger than that of the confining stresses corresponding to pull-out failure accompanied with the strand rotation for

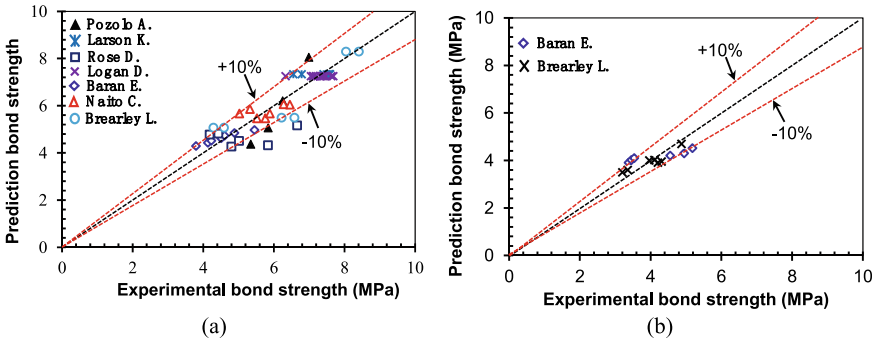


Fig. 5.6 Prediction and experimental bond strengths: a 12.7 mm strand; b 15.2 mm strand

all of the selected references. Therefore, the radial confining stress in Eq. (5.19) can be used in Eq. (5.20) to calculate the ultimate bond strength in the case of the pull-out failure of the strand. Table 5.1 and Fig. 5.6 illustrate the comparison between the experimental and predicted bond strengths.

The results in Fig. 5.6 and Table 5.1 show that the proposed model combines the pull-out failure and strand rotation to predict the ultimate bond strength between strand and concrete. The prediction accuracy can be improved by considering the strand rotation. By considering strand rotation, the average ratio of the test results to the predicted results for strands with a diameter of 12.7 mm is 0.92–1.04 with a minimum standard deviation of 0.15. For the strands with a diameter of 15.2 mm, this average ratio is 0.99–1.01 with a minimum standard deviation of 0.17.

5.3 Model for Bond Strength of Corroded Strand

5.3.1 Ultimate Bond Strength of Corroded Strand

In Sect. 5.2, a theoretical analysis of the bond strength of uncorroded seven-wire strands at concrete splitting failure is first carried out. Then, the mechanical interlocking forces on the loading bearing surfaces of steel strands are studied. The bond stress was expressed by the normal stress of the strand–concrete interface. In this section, by considering additional pressure induced by corrosion at the interface, the proposed bond model of an uncorroded strand is revised to predict the bond strength of corroded strand.

For Eq. (5.12) in Sect. 5.2, the bond stress of an uncorroded strand τ_b relates to parameters, for example, the ratio of the outer wire diameter to the nominal strand diameter d_e/d , angle of friction ϕ , inclined angle of the rib to the center line of the steel strand δ , unit adhesion strength σ_c , and normal stress along the shear face σ_n .

In order to supply a model for the corroded strand, some other parameters need to be added on the basis of the bond model for corroded deformed bars. The corrosion pressure at the interface is needed to be considered. The second thing is to modify the influence parameters in Eq. (5.12). Thus, the ultimate bond strength of steel strand with corrosion $\tau_b(\rho_p)$ can be written as:

$$\tau_b(\rho_p) = \tau_{CP}(\rho_p) + \tau_{AD}(\rho_p) + \tau_{COR}(\rho_p), \quad (5.22)$$

where ρ_p is the strand corrosion loss; $\tau_{CP}(\rho_p)$ is the contributions of maximum confining stress; $\tau_{AD}(\rho_p)$ is the adhesion stress; $\tau_{COR}(\rho_p)$ is the pressure induced by corrosion.

Assuming the same diameter reduction for all the seven corroded wires, and ignoring the original radius difference between the central and the outer wires, the radius of a random corroded wire is calculated as, $r_{es} = r_e - x$, where r_e is the radius of an uncorroded outer wire.

In the current investigation, it is considered that the corrosion effect was uniformly distributed. The corrosion loss ρ_p can be written as a function of corrosion penetration depth x as:

$$\rho_p = \left(1 - \frac{(r_e - x)^2}{r_e^2}\right) \times 100\%. \quad (5.23)$$

On the basis of the bond strength model of strand from Eq. (5.12) in Sect. 5.2, $\tau_{CP}(\rho_p)$, $\tau_{AD}(\rho_p)$, and $\tau_{COR}(\rho_p)$ can be written as

$$\tau_{CP}(\rho_p) = \frac{3}{14}\pi \left(\frac{d_e(\rho_p)}{d(\rho_p)}\right)^2 \frac{\sin(\delta + \phi)(\rho_p)}{\cos \phi(\rho_p) \cdot \sin \delta(\rho_p)} \sigma_{n,\max}(\rho_p), \quad (5.24a)$$

$$\tau_{AD}(\rho_p) = \frac{3}{14}\pi \left(\frac{d_e(\rho_p)}{d(\rho_p)}\right)^2 \cot \delta(\rho_p) \sigma_c(\rho_p), \quad (5.24b)$$

$$\tau_{COR}(\rho_p) = \mu(\rho_p) \cdot p_r(\rho_p), \quad (5.24c)$$

where $\sigma_{n,\max}(\rho_p)$ and $p_r(\rho_p)$ are the maximum radial confining stress on the interface supplied by surrounding concrete at bond failure and the corrosion-induced pressure, respectively.

For the quantitative evolution of other influence parameters of corrosion damage, it is assumed that the coefficient of friction μ exhibits a linear change with the corrosion penetration depth x . The coefficient of friction μ between corroded strand and cracked concrete is calculated as $\mu = 0.345 - 0.26(x - x_{cr})$ [7]. The chemical adhesion conditions at strand–concrete interface were altered because of the oxidation of steel strand and the accumulation of corrosion products. The adhesive stresses have been acted on the rib surfaces, which were quantitatively degraded. Some authors

have assumed that the adhesion of deformed bars varies linearly with the level of corrosion [12, 15, 39]. Based on the similarity of the bond mechanism between deformed bars and steel strand, it is assumed that the adhesion of corroded strand decreases linearly with the increasing corrosion loss x . And σ_c is calculated as $\sigma_c = 3 - 22.08(x - x_{cr})$, where x_{cr} is the critical penetration depth at concrete cover [7]. Apart from these, the corrosion pressure $p_r(\rho_p)$ and $\sigma_{n,\max}(\rho_p)$ need to be computed.

5.3.2 Corrosion-Induced Pressure at Bond Interface

Corrosive pressure at the interface is measured according to the processes below. Firstly, the radial displacement at the interface due to volumetric expansion of corrosion products is acquired by considering the section characteristics of the steel strand. Secondly, the confinement model proposed by Den [16] describes the functional relationship between radial pressure and radial displacement at the interface and is used to infer the variation of corrosion pressure, $p_r(\rho_p)$, with corrosion propagation.

On the basis of the thick-walled cylinder theory, the corrosive radial displacement at interface is inferred. The radius of the cylinder is the minimum concrete cover on the strand. In general, the propagation of corrosion products caused the development of multiple cracks from the strand-concrete interface to the outer surface of the concrete. Assuming that the direction of these cracks is to develop toward the outer surface of the concrete, radius of the crack front is written as r_i . The value of concrete strain at crack front r_i is consistent with the nominal tensile strain of concrete ε_{ct} , where $\varepsilon_{ct} = f_{ct}/E_0$. f_{ct} is the tensile strength of concrete; E_0 is the elastic modulus of concrete.

The volume loss of steel strand with corrosion per unit length ΔV_s is written as

$$\Delta V_s = 6(\pi r_e^2 - \pi r_{es}^2) = 6(2\pi r_e x - \pi x^2). \quad (5.25)$$

In order to simplify the calculation process, the corrosion products of the six outer wires are assumed to be evenly distributed along the nominal diameter of the strand. The outer radius of the corrosion products is r_r . Schematic diagram of the development of the corrosion products is depicted in Fig. 5.7.

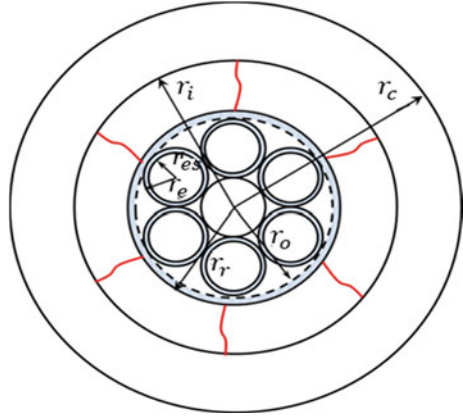
In the corrosion process, the products formed by corrosion of strand not only accumulate around the steel strand but also penetrate into the corrosion-induced cracks. The volume of the products formed by corrosion ΔV_r is expressed as:

$$\Delta V_r = m \cdot \Delta V_s = \pi(r_r^2 - r_0^2) + 6\pi(r_e^2 - r_{es}^2) + \sum w \cdot (r_i - r_r)/2, \quad (5.26)$$

where $\sum w$ is the sum widths of corrosion-induced cracks at the radius of r_r , which can be calculated as:

$$\sum w = 2\pi u_r |r = r_0 = 2\pi(r_r - r_0), r_r = r_0 + u_r. \quad (5.27)$$

Fig. 5.7 Thick-walled cylinder model



The corrosion-induced radial displacement $u_r|_{r=r_0}$ at interface is written as:

$$u_r|_{r=r_0} = r_r - r_0 = \frac{(m-1)(12r_c x - 6x^2)}{r_0 + r_i}, \quad (5.28)$$

where m is the volume expansion ratio of products formed by corrosion to its original steel strand. According to the type of products formed by corrosion, m ranges from 1.7–6.15 [30].

The concrete cover in the corrosion process can go through three stages according to the degree of cracking: namely uncracked stages, partially cracked stages, and complete cracked stages [12]. The radial displacement u_{r,r_0} gradually increases at radius r_0 . The analysis shows that the corrosion pressure was closely related to the radial displacement and the corrosion pressure in the uncracked stages and partially cracked stages. When concrete is completely cracked, the corrosion pressure gradually decreases. Since u_{r,r_0} has been represented by x in Eq. (5.28), the radial pressure model proposed by Den [16] is used to calculate p_r as the cracking stages develops. The radial pressure model associates u_{r,r_0} with the radial pressure.

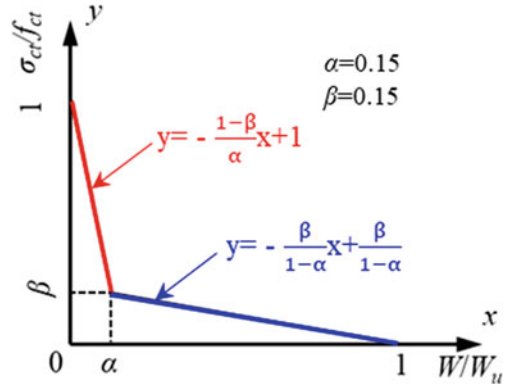
As for the uncracked stage of concrete, the functional relationship between u_{r,r_0} and p_r can be written as:

$$u_{r,r_0} = \frac{r_0 p_r}{E_0} \left(\frac{r_c^2 + r_0^2}{r_c^2 - r_0^2} + \nu_c \right), \quad (5.29)$$

where ν_c is the Poisson's ratio of concrete, and r_c is the radius of cylinder, which equals to the minimum concrete cover.

Equations (5.26) and (5.28) can be combined to acquire p_r at the uncracked stage, which can be expressed as:

Fig. 5.8 Bilinear model for softening concrete in tension [30]



$$p_r = \frac{(m-1)E_0(r_c^2 - r_0^2)(12r_b x - 6x^2)}{2r_0^2[r_c^2(1 + \nu_c) + r_0^2(1 - \nu_c)]}. \quad (5.30)$$

The maximum corrosion pressure $p_{r,1}$ at the uncracked stage of concrete appears when the value of circumferential tensile stress at the strand–concrete interface is equals to f_{ct} .

$$p_{r,1} = f_{ct} \frac{r_c^2 - r_0^2}{r_c^2 + r_0^2}. \quad (5.31)$$

The corrosion depth x_1 is obtained by substitution of Eq. (5.31) into Eq. (5.30). The corrosion depth x_1 corresponds to the initial cracking of concrete.

At partially cracked stage, both the uncracked cylinders and the cracked cylinders contribute to p_r and u_{r,r_0} , respectively. On the basis of the fictitious crack model, the contribution of the cracked cylinder to the radial displacement is calculated [32], which takes into account the bilinear softening properties of the cracked concrete. The bilinear softening model of cracked concrete is depicted in Fig. 5.8.

As shown in Fig. 5.8, the bilinear curve changes at this point (α , β). α and β are coefficients in the bilinear softening model, which are closely relevant to the performances of cracked concrete including fracture energy G_f , concrete tensile strength σ_{ct} , etc. On the basis of the CEB-FIB code, α and β are taken as 0.15, where W is the normalized crack width, and W is written as $W(r) = f_{ct} \cdot w(r) / G_f$, where $w(r)$ is the actual width of the crack at radius r . $G_f = 0.5 \cdot (\alpha + \beta) \cdot W_u \cdot f_{ct}$, where W_u is the localized deformation at failure.

The displacement u_{r,r_0} at partially cracked stage is written as:

$$u_{r,r_0} = r_i \varepsilon_{cr} (1 + \nu_c C_1) + \varepsilon_{cr} C_1 r_i \ln \frac{r_i}{r_0} + \varepsilon_{cr} b (r_i \ln(r_i / r_0) - (r_i - r_0)) + \frac{\varepsilon_{cr} a C_2}{4} (2r_i^2 \ln(r_i / r_0) + (r_i - r_0)(r_0 - 3r_i)), \quad (5.32)$$

where $C_1 = \frac{r_c^2 - r_i^2}{r_c^2 + r_i^2}$; $C_2 = \frac{2\pi \varepsilon_{ct}}{nW_u}$; n is the number of fictitious cracks. The influences of crack width on the tensile stress of concrete $\sigma_{ct,r}$ are represented by a and b . Table 5.2 show the values of coefficients a and b in different situations.

The stress p_r at partially cracked stage can be written as:

$$p_r = \frac{r_i}{r_0} f_{ct} C_1 + f_{ct} \left(\frac{a C_2 r_0}{2} \left(\frac{r_i}{r_0} - 1 \right)^2 + b \left(\frac{r_i}{r_0} - 1 \right) \right) \quad (5.33)$$

The functional relationship between the radius of crack front r_i and the penetration depth x can be acquired by equating Eqs. (5.28) and (5.32). The penetration depth, x_2 , corresponds to the completely cracked concrete cover, which can be acquired by substituting r_c into r_i . In addition, the stress p_r for different penetration depth, x , in the partially cracked stage can be obtained by substituting r_i into Eq. (5.33).

The contribution of the cracked cylinder to p_r in the complete cracked stage is comparable to that of the partially cracked stage. It is assumed that the total elongations Δ_{tot} of the cylinder at any radius r are the same, where $\Delta_{tot} = 2\pi r \cdot \varepsilon_{ct} + nW_u(\sigma_{ct,r}/f_{ct} - b)/a$. The displacement $u_{r,r0}$ at the complete cracked stage of concrete is written as:

$$u_{r,r0} = C_3 \frac{nW_0}{2\pi} + \varepsilon_{cr}(aC_3 + b) \left(r_c \ln \frac{r_c}{r_0} - r_c + r_0 \right) - \frac{aC_2 \varepsilon_{cr}}{4} \left(2r_c^2 \ln \frac{r_c}{r_0} - r_c^2 + r_0^2 \right) \quad (5.34)$$

where $C_3 = \Delta_{tot}/(nW_u)$.

The stress p_r can be written as

$$p_r = f_{ct}(aC_3 + b) \left(\frac{r_c}{r_0} - 1 \right) - \frac{f_{ct} a C_2 r_0}{2} \left(\left(\frac{r_c}{r_0} \right)^2 - 1 \right). \quad (5.35)$$

According to the Eqs. (5.30), (5.33) and (5.35), p_r can be calculated.

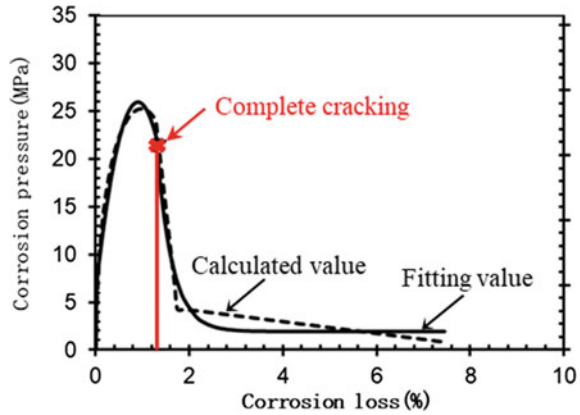
The corrosion pressure model mentioned before requires the iterative analysis during concrete cracking. Therefore, the expressions at different stages may be complicated in the actual structural evaluation. Therefore, a simplified equation is needed for effective evaluation on the basis of the existing equations. The original graph of the corrosion pressure during the corrosion process is shown in Fig. 5.9.

The general trend of the curve is almost parabolic until the concrete cracks completely. Then, the stress p_r drops sharply and slowly approaches an approximate stable value, which is consistent with the nature of an exponential function.

Table 5.2 a and b corresponding to softening behavior of cracked concrete

W (mm)	a	b
$0 < W/W_u \leq \alpha$	$-(1 - \beta)/\alpha$	1
$\alpha < W/W_u \leq 1$	$-\beta/(1 - \alpha)$	$\beta/(1 - \alpha)$

Fig. 5.9 Comparison of the corrosion pressure between computed value and fitting curve



Hence, a piecewise simplified function, which is divided by the critical corrosion loss ρ_{crit} , is acquired base on the data fitting of the computed values. Some parameters have been proven to influence the stress p_r , for example, thickness of concrete cover r_c , strength of concrete tensile f_{ct} , and diameter of steel strand r_0 , these parameters are also considered in the equation.

$$p_r = [-56.7\rho^2 + (94.2 + r_0)\rho + r_0^2 - 43.29] \cdot f_{ct}/r_0; \rho \leq \rho_{crit} \quad (5.36a)$$

$$p_r = (0.067 + 32.8 \cdot e^{-3\rho}) \cdot f_{ct} \cdot (r_c/r_0 - 1); \rho > \rho_{crit}. \quad (5.36b)$$

The existing model and the simplified equation predicted the comparison of corrosion pressure are shown in Fig. 5.9. There is a general satisfactory agreement.

5.3.3 Confining Stress at Bond Failure

In order to calculate the ultimate bond strength of corroded steel strand, it is necessary to determine the maximum confining stress $\sigma_{n,max}$, at bond failure in Eq. (5.24a). For beams without additional reinforcement, only the concrete acts as a constraint on the steel strands. For beams with additional reinforcement, $\sigma_{n,max}$ is supplied by the combined action of surrounding concrete and stirrups. Giuriani et al. [19] modified the constraint models of cracked concrete and stirrups for uncorroded bars to incorporate the influence of corrosion.

$$\sigma_{n,max}(\rho_p) = \sigma_{n,max c}(\rho_p) + \sigma_{n,max s}(\rho_p), \quad (5.37a)$$

$$\sigma_{n,max c}(\rho_p) = \left\{ \frac{b_p}{[d_0(\rho_p) + 2t_r(\rho_p)]} - 1 \right\} \left(a \frac{W_t}{W_0} + b \right) f_{ct}, \quad (5.37b)$$

$$\sigma_{n,\max s}(\rho_p) = \left\{ \frac{n_s A_s}{[d_0(\rho_p) + 2t_r(\rho_p)]S_v} \right\} \times E_{st} \sqrt{\frac{a_2 W_t^2}{\alpha_{st}^2 d_{st}^2} + \frac{a_1 W_t}{\alpha_{st} d_{st}} + a_0}, \quad (5.37c)$$

where $\sigma_{n,\max c}$ and $\sigma_{n,\max s}$ are the maximum confining stresses at bond failure supplied by the cracked concrete and stirrups, respectively; $t_r(\rho_p)$ is the thickness of corrosion layer; b_p is specimen width; n_s is the number of stirrups within the range of b_p ; A_s is the cross-sectional area of stirrups in the specimen; W_t is fictitious crack width; S_v is the spacing of stirrups; E_{st} is the elastic modulus of stirrups, d_{st} is the diameter of stirrups. a_0 , a_1 , a_2 are coefficients, which are obviously related to the local bond-slip law of stirrups. The values of these coefficients can be acquired from the study [19]. α_{st} is the shape factor for stirrups, and its value is 2.

It should be explained that for the case of pull-out failure, the confining stresses based on Eq. (5.37) does not consider the influence of strand rotation. As mentioned before, when the confining stresses provided by the concrete or transversal reinforcement is enough, the strand slip with rotation due to its twisting structure and then the pull-out failure occurs. Under the cases, beams fail as the strand rotates before the confinements of concrete and steel reinforcement are maximized, respectively. This means that the maximum confinement on Eq. (5.37) may be overestimated during the uncorroded stage and initial corrosion stage. In this case, the maximum confinement at pull-out failure accompanies with strand rotation, which needs to be considered.

For pull-out failure case, when the steel strand rotates, the integration of the radial component for the mechanical interlock, $dF_{bu}(\rho_p)$, leads to a bursting force, $F_{rib}(\rho_p)$, around the strand (see Fig. 5.10). Due to the helical structure of the outer wires, a torque, $M_{rib}(\rho_p)$, generates on the strand. Friction around the steel strand resisted this torque during the initial pull-out stage. As the pull-out force increases further, when the frictional force is no longer able to resist the torque, the steel strand begins to rotate in the concrete groove. When the steel strand rotates, the bond strength and the confining stress reach their maximums value, respectively. Therefore, the confining stress, $\sigma_n(\rho_p)$, corresponding to pull-out failure can be computed according to the balance of the central moment of the steel strand.

Firstly, the force $F_{rib}(\rho_p)$ from a single outer wire needs to be determined. $F_{rib}(\rho_p)$ is composed of a vertical component, $F_{ribv}(\rho_p)$, and a parallel component, $F_{ribh}(\rho_p)$, which can be expressed as:

$$\begin{aligned} F_{ribv}(\rho_p) &= \int_{-\frac{\pi}{6}}^{\frac{\pi}{2}} dF_{bu}(\rho_p) \cdot \cos \theta \cdot d\theta \\ &= \frac{3}{4} \left[\frac{\sigma_n(\rho_p) \cos(\delta + \phi(\rho_p))}{\cos \phi(\rho_p) \sin \delta} - \sigma_c(\rho_p) \right] h_r(\rho_p) d_c(\rho_p) \end{aligned} \quad (5.38a)$$

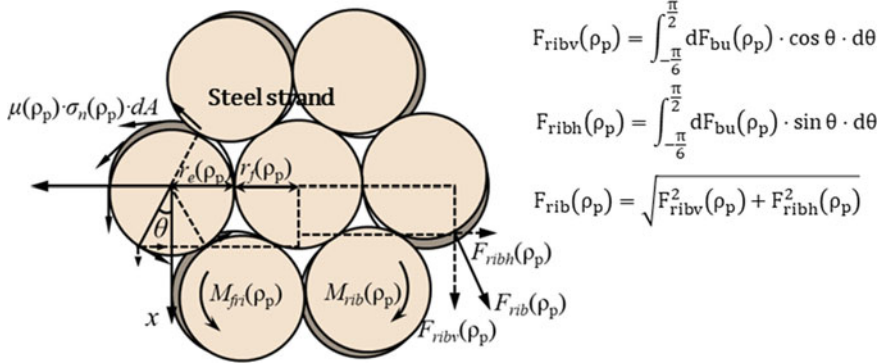


Fig. 5.10 Moment balance between bursting forces and friction forces

$$\begin{aligned}
 F_{ribh}(\rho_p) &= \int_{-\frac{\pi}{6}}^{\frac{\pi}{2}} dF_{bu}(\rho_p) \cdot \sin \theta \cdot d\theta \\
 &= \frac{\sqrt{3}}{4} \left[\frac{\sigma_n(\rho_p) \cos(\delta + \phi(\rho_p))}{\cos \phi(\rho_p) \sin \delta} - \sigma_c(\rho_p) \right] h_r(\rho_p) d_e(\rho_p) \quad (5.38b)
 \end{aligned}$$

Thus, the bursting force, $F_{rib}(\rho_p)$, for an outer wire can be acquired as:

$$\begin{aligned}
 F_{rib}(\rho_p) &= \sqrt{F_{ribv}^2(\rho_p) + F_{ribh}^2(\rho_p)} \\
 &= \frac{\sqrt{3}}{2} \left[\frac{\sigma_n(\rho_p) \cos(\delta + \phi(\rho_p))}{\cos \phi(\rho_p) \sin \delta} - \sigma_c(\rho_p) \right] h_r(\rho_p) d_e(\rho_p) \quad (5.39)
 \end{aligned}$$

The torque, $M_{rib}(\rho_p)$, induced by the ribs of the six outer wires within the length of dz can be written by $\sigma_n(\rho_p)$ as:

$$M_{rib}(\rho_p) = \frac{9}{2} \left[\frac{\sigma_n(\rho_p) \cos(\delta + \phi(\rho_p))}{\cos \phi(\rho_p) \sin \delta} - \sigma_c(\rho_p) \right] d_e^3(\rho_p) d\alpha. \quad (5.40)$$

For the torque, $M_{fri}(\rho_p)$, is supplied by the frictional force around the strand. The frictional force is supposed to be evenly distributed along the rib surface (see Fig. 5.10). The maximum torque, $M_{max}(\rho_p)$, supplied by the friction can be acquired as:

$$\frac{M_{max}(\rho_p)}{12} = \int_{-\frac{\pi}{6}}^{\frac{\pi}{2}} \mu(\rho_p) \sigma_n(\rho_p) dA \frac{d_e(\rho_p)}{2} (\cos \theta)^2$$

$$+ \int_{-\pi/6}^{\pi/2} \mu(\rho_p) \sigma_n(\rho_p) dA \sin \theta \left(\frac{d_f(\rho_p) + d_e(\rho_p)}{2} + \frac{d_e(\rho_p)}{2} \sin \theta \right). \quad (5.41)$$

Assuming $d_f(\rho_p) = d_e(\rho_p)$, the torque, $M_{\max}(\rho_p)$, can be simplified as:

$$M_{\max}(\rho_p) = (3\sqrt{3} + 2\pi) \frac{\mu(\rho_p) \sigma_n(\rho_p)}{\sin \delta} d_e^3(\rho_p) d\alpha. \quad (5.42)$$

The critical confining stress, $\sigma_{n,\text{crit}}(\rho_p)$, can be acquired by equating equations (5.38) and (5.40).

$$\sigma_{n,\text{crit}}(\rho_p) = \sigma_c(\rho_p) / \left[\frac{\cos(\delta + \phi(\rho_p))}{\cos \phi(\rho_p) \cdot \sin \delta} - \left(\frac{2\sqrt{3}}{3} + \frac{4\pi}{9} \right) \frac{\tan \phi(\rho_p)}{\sin \delta} \right]. \quad (5.43)$$

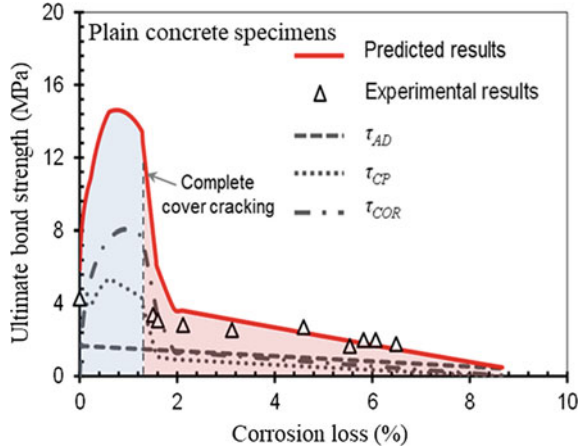
The critical confining stress in Eq. (5.43) is computed for the pull-out failure accompanied with the strand rotation. Under the cases, the beams fail at the critical confining stress. The confining stress in Eq. (5.37) and cannot reach the maximum. For the failure mode in this case, the critical confining stress should be substituted by the maximum confining stress to avoid overestimating the ultimate bond strength. When the critical confining stress of the corroded beams is greater than the maximum confining stress, the splitting failure of concrete occurs before pull-out failure. In this condition, $\sigma_{n,\text{max}}(\rho_p)$ for the ultimate bond strength can be obtained directly from Eq. (5.37).

5.3.4 Model Validation

The validity of the proposed model for predicting the ultimate bond strength between the corroded steel strand and cracked concrete is verified by comparing the experimental results with the predicted results. For comparison, the pull-out tests results of 15.2 mm corroded strand specimens are used [37]. In the experimental study, 20 pull-out beams without stirrups and with stirrups were designed. Corrosion of steel strand is accelerated to cause the cracking of concrete cover. All beams have the same dimension of 150 mm × 150 mm × 1200 mm. The effective bond length is 1100 mm and the thickness of concrete cover is 67.4 mm. For the beams with stirrups, there are nine smooth steel bars with the spacing of 150 mm for additional confinement. All tests were carried out by pulling the steel strand out directly from the concrete block to investigate the influences of corrosion-induced concrete crack on the strand bond. More details can be found in the Sect. 4.2 in Chap. 4.

Before calculating the ultimate bond strength, it is necessary to determine the parameters in the proposed model. In this test, the concrete's compressive strength

Fig. 5.11 Comparison between predicted and experimental results



f_c was 35 MPa; the tensile strength of concrete, $f_{ct} = 0.56(f_c)^{1/2} = 3.29$ MPa; the elastic modulus of concrete, $E_0 = 4735 \cdot (f_c)^{1/2} = 2.8 \times 10^4$ MPa; the concrete tensile strain during cracking, $\varepsilon_{ct} = 0.000117$; and Poisson’s ratio of concrete, $\nu_c = 0.2$. In addition, based on the known concrete properties, other parameters related to the softening behavior of cracked concrete are also estimated. The localized deformation at failure, $W_u = 0.2$ mm. The volume expansion ratio of products formed by corrosion m because of expansive products formed by corrosion is taken as $m = 4.25$. For the number of fictitious cracks n , based on the existing study, it was assumed that $n = 3$ or $n = 4$. On the basis of experimental evidence of concrete cracking caused by strand corrosion, this paper finally determined $n = 4$ [36].

The predicted results of the beams without and with stirrups are compared with the experimental results as shown in Figs. 5.11 and 5.14, respectively. The variation of three components $\tau_{CP}(\rho_p)$, $\tau_{AD}(\rho_p)$, and $\tau_{COR}(\rho_p)$, which are caused by the maximum confining stress, adhesion stress, and pressure, respectively, can also be expressed as functions of the corrosion loss.

From the comparison results in Fig. 5.11, the prediction of the ultimate bond strength of the beams without stirrups is in good agreement with the experimental results, especially when the corrosion loss is greater than 2%. It can be seen from the predicted results change with the development of the strand corrosion. The bond strength first increases in the early stage of concrete cracking. And then the bond strength drops when the cracks penetrate reach roughly 2/3 of concrete cover or the loss of corrosion exceeds 0.8%. In the initial stage of ascent, the corrosion pressure contributes most to the improvement of bond strength because both the interfacial bursting stress and the friction coefficient increase. This result is comparable to that of deformed bars with corrosion [7]. In the subsequent stage of descent, the concrete cover is completely cracked, the bond strength drops rapidly with a corrosion loss of 1.3%, and the contributions of both confining stress and corrosion pressure drop rapidly. When the corrosion loss is further increased to more than 2%, the bond strength is affected by a combination of the confining stress and the corrosion

pressure. At this stage, the proposed theoretical model can predict well the bond strength and the decrease tendency when corrosion loss increases further.

The predicted ultimate bond strengths for the beams with stirrups are shown in Fig. 5.12. The proposed model in this part can reasonably predict the evolution of the ultimate bond strength of the corroded strand, especially for the completely cracked concrete. In particular, the influence of the stirrups in delaying the deterioration of bond induced by corrosion can be well modeled by considering the additional contribution of the stirrups in the confinement model (see Fig. 5.13).

The effect of tensile strength of concrete on the evolution of bond strength is shown in Fig. 5.14. As predicted, the increased tensile strength can lead to the increase of the bond strength. This is because the contributions of corrosion pressure and confining stress are proportional to the tensile strength of concrete. Additionally, comparing the results of the two random curves shows that the discrepancy in bond strength gradually decreases as the corrosion progresses further. This phenomenon happens because of the softening behavior of concrete tensile strength. When the concrete

Fig. 5.12 Comparison between predicted and experimental results

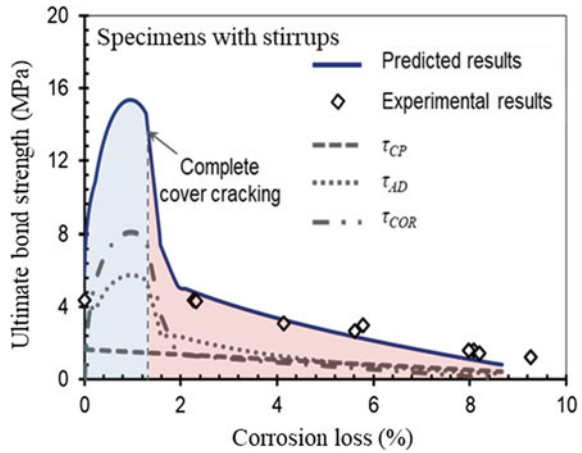


Fig. 5.13 Effect of stirrups in delaying bond deterioration

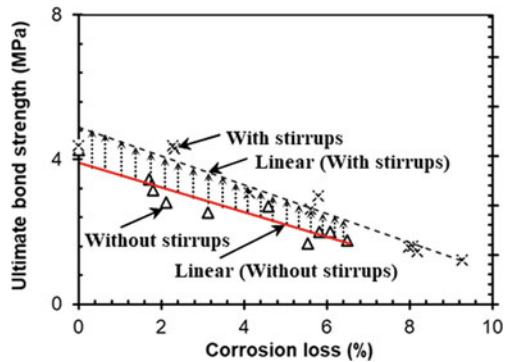
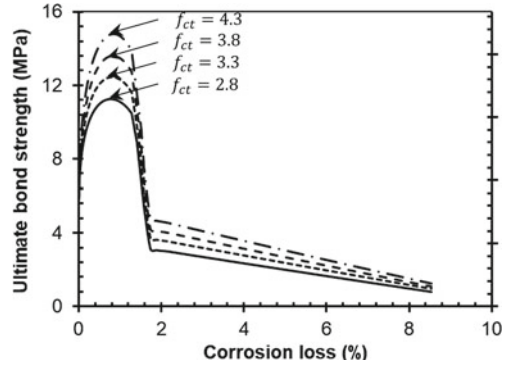


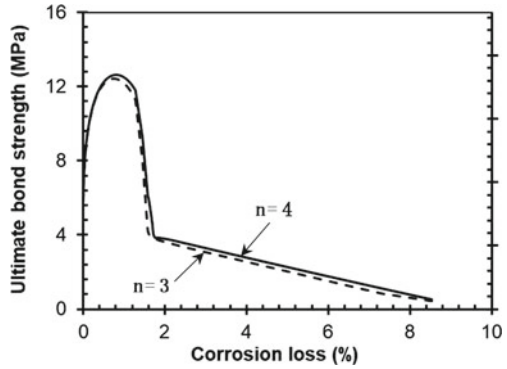
Fig. 5.14 Effect of concrete tensile strength on bond strength evolution



cover is completely cracked, the degradation of tensile strength reduces its influence on the bond strength.

Additionally, this section also studies the effect of the number of fictitious cracks n on the bond strength, as shown in Fig. 5.15. As mentioned earlier, n can be taken as 3 or 4, and the two values are compared in this section. According to the curve comparison results in Fig. 5.15, it can be known that the bond strength between strand and concrete of $n = 3$ is slightly lower than that of $n = 4$.

Fig. 5.15 Effect of number of fictitious cracks on bond strength



5.4 Model for Bond–Slip Between Corroded Strand and Concrete

5.4.1 Method for the Local Bond Characteristics

In this study, the numerical model proposed by Haskett et al. [20] is improved to acquire an appropriate local bond–slip relationship between the corroded strand and concrete. The experimental force–displacement curves are also used to calibrate the model parameters. Details are shown below.

With the assumed local bond–slip relationship, the expression of slip (s_p) at the loaded end under the applied force F_p is shown in Fig. 5.17. In order to simplify the calculation, the pull-out beam is divided into several sections. These sections were numbered from 1 to n , and any section i has length l_i . The values of force and slip on each section are taken from their average. The specific calculation steps are shown in Fig. 5.16.

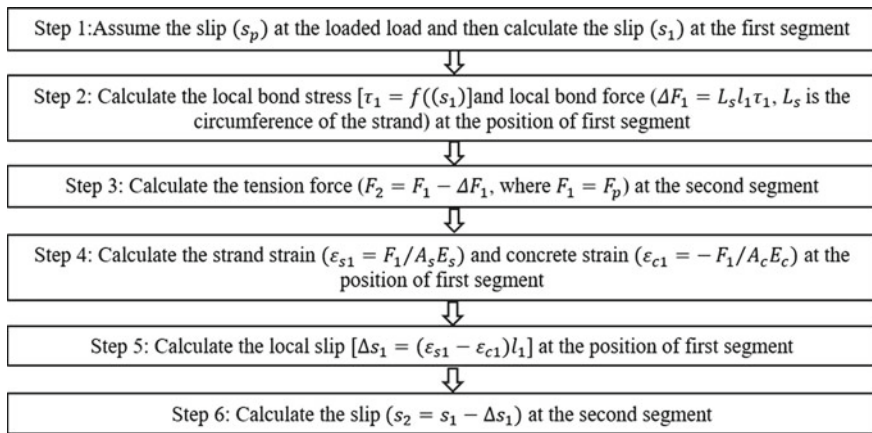


Fig. 5.16 Calculation flow chart

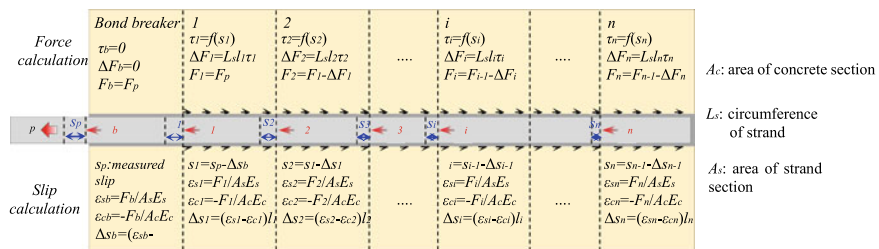


Fig. 5.17 Schematic diagram of the numerical analysis

F_2 and s_2 at the second section have been acquired. The numerical procedure continues to be repeated for calculating F_i and s_i of the remaining section (i) until the known boundary conditions are met the requirements. If the boundary conditions do not meet the requirements, the assumed loaded end slip (s_p) should be modified and the above process should be repeated.

According to the relative relationship between the bond length and the effective bond length, there are two boundary conditions. Firstly, for specimens with long bond lengths or when the pull-out load is small, the transmission of the pull-out force along the steel strand is limited to the inner section of the specimen and is not transmitted to the free end. The boundary condition currently is that the tension force (F_i) and slip (s_i) of the steel strand at one section (i) are both equal to 0. Secondly, for specimens with short bond length or when the pull-out load is large, the pull-out force is transmitted to the entire bond area, and the boundary condition at this time is that the tension force (F_n) of the steel strand at the free end is equal to 0.

The steel strand may yield during pull-out test. In that case, the influence of plastic deformation should be considered when the strain (ϵ_s) of strand is calculated. This study adopts the elastic–plastic constitutive model of steel strand proposed by Zhang et al. [40], which is written as:

$$\sigma = \begin{cases} \epsilon E_s & \epsilon \leq \epsilon_{sy} \\ f_{sy} + E_{sp}(\epsilon - \epsilon_{sy}) & \epsilon > \epsilon_{sy} \end{cases}, \tag{5.44}$$

where f_{sy} is the yield strength of strand; ϵ_{sy} is the yield strain of strand; and E_{sp} is the steel hardening modulus.

The strand strain considering the influence of plastic deformation, and the strand strain can be calculated as:

$$\epsilon_{si} = \begin{cases} \frac{F_i}{A_s E_s} & F_i \leq A_s f_{sy} \\ \epsilon_{sy} + \frac{F_i}{A_s E_{sp}} - \frac{f_{sy}}{E_{sp}} & F_i > A_s f_{sy} \end{cases}. \tag{5.45}$$

Some scholars pointed out that when the nonlinear deformation of concrete occurs, the concrete stress exceeds 33% of its compressive strength. Before that, the concrete is basically in the linear elastic deformation stage [21]. In this section, the maximum compressive stress of concrete is about 12 MPa. The measured compressive strength of each beam is between 34.1 and 35.6 MPa. Therefore, in order to simplify the calculation, the nonlinear deformation of concrete is not considered in the calculation.

5.4.2 Local Bond–Slip Between Corroded Strand and Concrete

In existing research, many models have been come up with to express the local bond stress–slip relationship. Figure 5.18a, b shows the piecewise uniform function

and the multi-variate linear function [4, 26, 35]. However, these two models are too simplistic for the current study. Figure 5.18c represents the logarithmic function [34]. The bond stress increases gradually with the increase of the load in this model. There is no descending section, which may lead to abnormally large bond stress. The CEB Model Code divides the function into four different zones. A plateau with the maximum bond stress is recommended to describe the bond behavior between the deformed bar and the concrete, as shown in Fig. 5.18d. But no plateau was observed experimentally by Eligehausen et al. [17].

In order to reflect the local bond behavior between deformed steel bars and concrete [20, 25], the CEB Model Code recommends an improved distribution of Fig. 5.18d, as shown in Fig. 5.19. The bond transfer is divided into three different zones: a nonlinear increase zone until the bond stress reaches a maximum, a linear decrease zone of the bond stress, and the zone of constant residual strength. The plateau with the maximum bond stress is removed from the improved model. As mentioned earlier, the bond mechanism is similar to that of deformed steel bars. Therefore, the improved local bond stress–slip model between deformed steel bars and concrete is also applicable to describe the bond behavior between steel strands and concrete.

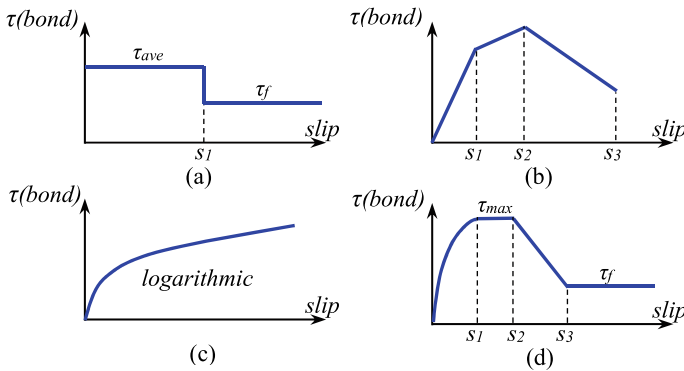
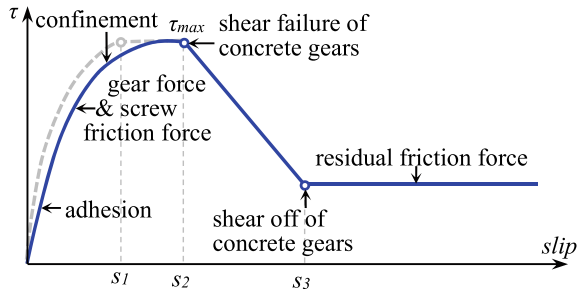


Fig. 5.18 Common local bond stress–slip models: **a** piecewise uniform distribution; **b** multi-linear distribution; **c** logarithmic distribution; **d** CEB Model Code suggested distribution

Fig. 5.19 Improved local bond stress–slip model



The bond mechanism and the bond failure mode can be described by this model. The bond force and the bond stiffness are provided by the adhesive force. With the increase of slip, the adhesive force gradually disappears. However, the slip and rotation of steel strands are resisted by the concrete, resulting in the frictional and mechanical interlock forces at the steel–concrete interface. The bond stress increases with the increase of slip and gradually increases to a maximum value. Subsequently, the local crushing and micro-cracks appear on the confining surface of the concrete. The bond stress gradually decreases until the slip is too large, and the concrete is sheared or crushed. At this time, the bond force is only provided by the longitudinal friction force, its value is small and basically constant.

On the basis of CEB Model Code, the improved bond stress–slip model can be written as:

$$\tau = \begin{cases} \tau_{\max}(s/s_2)^\alpha & 0 \leq s \leq s_2 \\ \tau_{\max} - (\tau_{\max} - \tau_f)\left(\frac{s-s_2}{s_3-s_2}\right) & s_2 \leq s \leq s_3 \\ \tau_f & s_3 \leq s \end{cases}, \quad (5.46)$$

where τ_{\max} and τ_f are the maximum bond stress and the residual friction stress, respectively; $\tau_f = 0.4\tau_{\max}$, α , s_2 and s_3 are the constants.

For the deformed steel bar, the maximum bond stress τ_{\max} is calculated as $1.25\sqrt{f_{ck}}$ and $2.5\sqrt{f_{ck}}$ corresponding to the good bond conditions and other bond conditions, respectively. f_{ck} is the characteristic compression stress of the concrete. τ_f is calculated as $0.4\tau_{\max}$. α and s_2 can be taken as 0.4 and 3 mm, respectively. s_3 represents the clear spacing between the two ribs of the deformed bar. As mentioned earlier, the bond mechanism of strands embedded in concrete is very similar to that of the deformed bars. Therefore, this section approximately adopts parameters, which are similar to that of the deformed steel bars to characterize the local bond characteristics of steel strands. Since there is no ribs in steel strand, it is assumed that s_3 is represented as the half of distance between the adjacent wires and concrete gear, $s_3 = 0.5s_l$, $s_l = s_t / \sin \alpha$, as shown in Fig. 5.20.

The parameters were applied to the local bond stress–slip model and calibrated using the beam PS0. The maximum bond stress τ_{\max} is taken as $1.25\sqrt{f_{ck}}$ and s_3 is taken as 12.0 mm. It can be seen from Fig. 5.21 that the computed load–displacement curve at the loading end is in good agreement with the experimentally obtained load–displacement curve at the loading end. The predicted failure mode of the beam PS0 is also consistent with the experimental result (i.e., the strand broken). It illustrates that the local bond stress–slip model and the assumed parameters are applicable for the uncorroded strand embedded in concrete.

For the corroded beams, these parameters need to be recalibrated. As mentioned earlier, strand corrosion not only influences the bond strength, but corrosion also influences the bond stiffness. Based on the Eq. (5.46), the bond stiffness is related to the maximum bond stress τ_{\max} , and the expression of the local bond stress–slip model is modified for corroded beams.

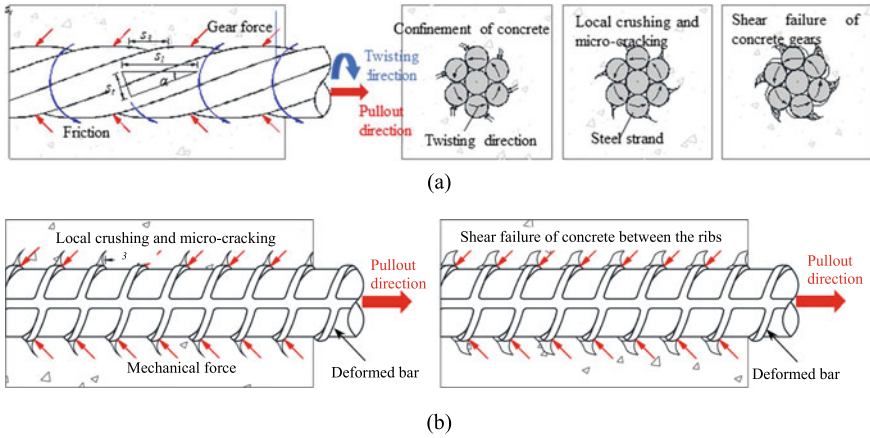
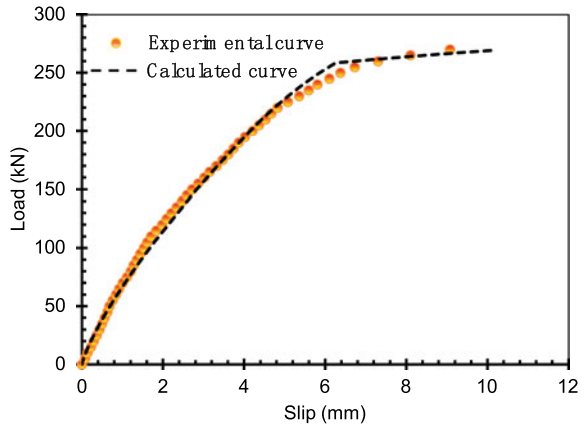


Fig. 5.20 Bond mechanism: a strand embedded in concrete; b deformed bar embedded in concrete

Fig. 5.21 Experimental and computed load–displacement curves for specimen without corrosion



The maximum bond stress τ_{\max} for the corroded beam is calibrated using the experimental data. Figure 5.22 shows a comparison between the tested and calibrated load–displacement curves for all the corroded beams. The computed curve and the experimental curve coincide well. This illustrates that the optimized local bond stress–slip model is also suitable for the corroded beams by modifying τ_{\max} .

Figure 5.22 shows the maximum bond stress τ_{\max} for the corroded beams. τ'_{\max} is the maximum bond stress for the uncorroded beams and its value is $1.25 \sqrt{f_{ck}}$. τ_{\max} for the beams PS1 and PS2 with the less corrosion rate are larger than τ'_{\max} for uncorroded beams. When the corrosion is severe, τ_{\max} for corroded beams is less than τ'_{\max} for uncorroded beams, and τ_{\max} decreases with the increasing of corrosion loss.

The influence of strand corrosion on bond behavior was investigated by using the normalized maximum bond stress R , which is defined as the ratio of the maximum

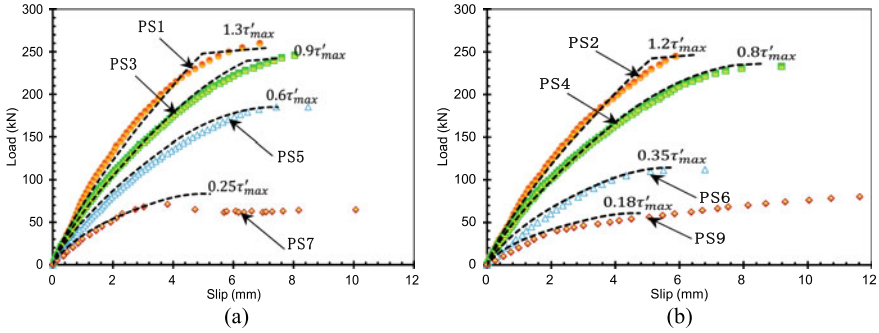


Fig. 5.22 Experimental and computed force–displacement curves for beams with corrosion: **a** Beams PS1, PS3, PS5, and PS7; **b** Beams PS2, PS4, PS6, and PS9

bond stress of corroded beam to the corresponding original beam, as shown in Fig. 5.23. Figure 5.23 also shows a fitting curve of R versus η . It can be observed from the figure that when the corrosion loss is less than 6%, R can be increased. However, the normalized maximum bond stress decreases significantly as corrosion propagates further. The bond behavior of the corroded PC and RC specimens subjected to the pull-out test have a similar variation law. [5, 8, 14, 18].

Based on the existing experimental data in Fig. 5.23, an empirical model is introduced to depict the gradual degradation of bond between corroded strands and concrete:

$$R = \begin{cases} 1.0 & \eta \leq 6\% \\ 2.03e^{-0.118\eta} & \eta > 6\% \end{cases} \quad (5.47)$$

In order to confirm the accuracy of the empirical model, the predicted load–displacement curves of the beam PS8 were compared with the experimental curves as shown in Fig. 5.24. The predicted curve is relatively close to the experimental curve before the excessive slip occurs in the steel strand. After the strand slip is too

Fig. 5.23 Maximum normalized bond strength as a function of corrosion

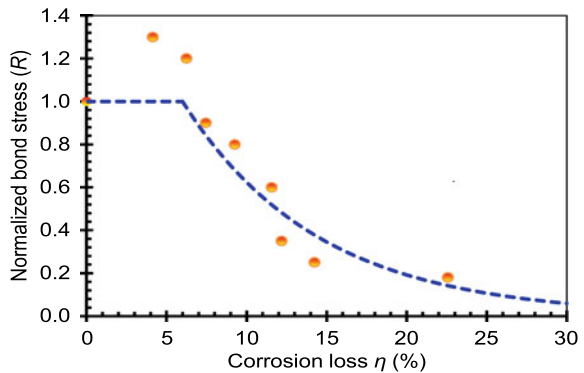
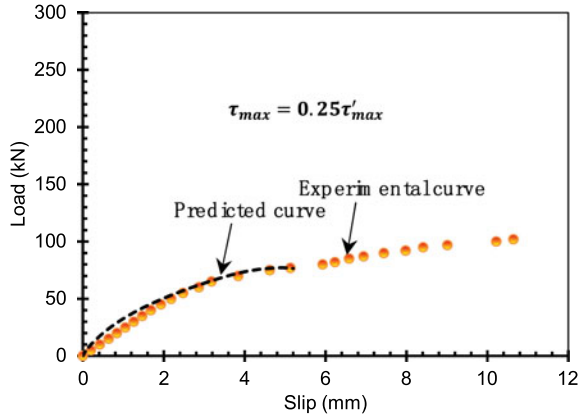


Fig. 5.24 Predicted and experimental load–displacement curves for beam SP8



large, the increase of the pull-out force is influenced by the uncorroded strand at the free end. This cannot be predicted by the empirical model and thus leads to some prediction errors. Generally, the empirical model has high prediction accuracy for the bond degradation between a corroded strand and concrete.

The study found an increase in bond strength for slightly corroded strands. The increase in bond strength is conducive for concrete members. The empirical model does not account for the increase in bond strength. When the corrosion loss is smaller than 6%, R for the steel strand is assumed to remain at the value of 1.0. When the corrosion loss exceeds 6%, R decreases exponentially. The empirical model can be used to predict the residual bond strength of the corroded strand embedded in concrete.

5.5 Conclusions

1. The proposed bond strength model in this paper is derived on the basis of the helical-shaped surfaces of the steel strand. Through theoretical analysis, the factors such as the interfacial confining stress, compressive strength of concrete, diameter of strand, and friction coefficient are considered and applied into the model.
2. A comparison between the predicted results and the experimental results from the literature shows that the empirical model can reasonably predict the ultimate bond strength. The prediction accuracy can be improved by considering the strand rotation.
3. On the basis of the helical-shaped characteristics of corroded strand, the bond strength model between corroded strand and cracked concrete is proposed. The contributions of corrosion pressure, adhesion, and confinement to the ultimate bond strength of corroded strand are considered.

4. The ultimate bond strength is in an increasing state at the initial stage of concrete cracking. The ultimate bond strength decreases when the crack penetrates into about 2/3 of the concrete cover or the corrosion loss of beams exceeds 0.8%. With the further expansion of the concrete cracking, the ultimate bond strength gradually decays to the residual value.
5. A simplified empirical model has been proposed to predict residual bond strength between corroded strand and concrete. When the corrosion loss is less than 6%, the normalized maximum bond stress is assumed to remain at the value of 1.0. When the corrosion loss exceeds 6%, the normalized maximum bond stress decreases exponentially.

References

1. H.G. Abrishami, D. Mitchell, Bond characteristics of pretensioned strand. *Mater. J.* **90**(3), 228–235 (1993)
2. R. Al-Hammoud, K. Soudki, T.H. Topper, Confinement effect on the bond behaviour of beams under static and repeated loading. *Constr. Build. Mater.* **40**, 934–943 (2013)
3. A.A. Almusallam, A.S. Al-Gahtani, A.R. Aziz, Effect of reinforcement corrosion on bond strength. *Constr. Build. Mater.* **10**(2), 123–129 (1996)
4. J.M. Alsiwat, M. Saatcioglu, Reinforcement anchorage slip under monotonic loading. *J. Struct. Eng.* **118**(9), 2421–2438 (1992)
5. Y. Auyeung, P. Balaguru, L. Chung, Bond behavior of corroded reinforcement bars. *Mater. J.* **97**(2), 214–220 (2000)
6. E. Baran, T. Akis, S. Yesilmen, Pull-out behavior of prestressing strands in steel fiber reinforced concrete. *Constr. Build. Mater.* **28**(1), 362–371 (2012)
7. K. Bhargava, A. Ghosh, Y. Mori, S. Ramanujam, Models for corrosion-induced bond strength degradation in reinforced concrete. *ACI Mater. J.* **104**(6), 594–603 (2007)
8. K. Bhargava, A. Ghosh, Y. Mori, S. Ramanujam, Suggested empirical models for corrosion-induced bond degradation in reinforced concrete. *J. Struct. Eng.* **134**(2), 221–230 (2008)
9. R. Bolmsvik, K. Lundgren, Modelling of bond between three-wire strands and concrete. *Mag. Concr. Res.* **58**(3), 123–133 (2006)
10. L.M. Brearley Jr., D.W. Johnston, Pull-out bond tests of epoxy-coated prestressing strand. *J. Struct. Eng.* **116**(8), 2236–2252 (1990)
11. J. Cairns, R.B. Abdullah, Bond strength of black and epoxy-coated reinforcement—a theoretical approach. *Mater. J.* **93**(4), 362–369 (1996)
12. H.-P. Chen, J. Nepal, Analytical model for residual bond strength of corroded reinforcement in concrete structures. *J. Eng. Mech.* **142**(2), 04015079 (2016)
13. Y.S. Choi, S.-T. Yi, M.Y. Kim, W.Y. Jung, E.I. Yang, Effect of corrosion method of the reinforcing bar on bond characteristics in reinforced concrete specimens. *Constr. Build. Mater.* **54**, 180–189 (2014)
14. L. Chung, S.-H. Cho, J.-H.J. Kim, S.-T. Yi, Correction factor suggestion for ACI development length provisions based on flexural testing of RC slabs with various levels of corroded reinforcing bars. *Eng. Struct.* **26**(8), 1013–1026 (2004)
15. D. Coronelli, Corrosion cracking and bond strength modeling for corroded bars in reinforced concrete. *Struct. J.* **99**(3), 267–276 (2002)
16. J.A. Den Uijl, A.J. Bigaj, A bond model for ribbed bars based on concrete confinement. *Heron-Engl. Edn.* **41**, 201–226 (1996)
17. R. Eligehausen, E.P. Popov, V.V. Bertero, Local bond stress-slip relationships of deformed bars under generalized excitations, *UCB/EERC83/23*, **4**, 69–80 (1982)

18. C. Fang, K. Lundgren, L. Chen, C. Zhu, Corrosion influence on bond in reinforced concrete. *Cem. Concr. Res.* **34**(11), 2159–2167 (2004)
19. E. Giuriani, G. Plizzari, C. Schumm, Role of stirrups and residual tensile strength of cracked concrete on bond. *J. Struct. Eng.* **117**(1), 1–18 (1991)
20. M. Haskett, D.J. Oehlers, M.S. Mohamed Ali, Local and global bond characteristics of steel reinforcing bars. *Eng. Struct.* **30**(2), 376–383 (2008)
21. H.B. Kaushik, D.C. Rai, S.K. Jain, Stress-strain characteristics of clay brick masonry under uniaxial compression. *J. Mater. Civ. Eng.* **19**(9), 728–739 (2007)
22. K.H. Larson, R.J. Peterman, A. Esmaily, Bond characteristics of self-consolidating concrete for prestressed bridge girders. *PCI J.* **52**(4), 44–57 (2007)
23. H.-S. Lee, T. Noguchi, F. Tomosawa, Evaluation of the bond properties between concrete and reinforcement as a function of the degree of reinforcement corrosion. *Cem. Concr. Res.* **32**(8), 1313–1318 (2002)
24. D.R. Logan, Acceptance criteria for bond quality of strand for pretensioned prestressed concrete applications. *PCI J.* **42**(2), 52–90 (1997)
25. X. Long, K.H. Tan, C.K. Lee, Bond stress-slip prediction under pullout and dowel action in reinforced concrete joints. *ACI Struct. J.* **111**(4), 977–987 (2014)
26. L.N. Lowes, A. Altoontash, Modeling reinforced-concrete beam-column joints subjected to cyclic loading. *J. Struct. Eng.* **129**(12), 1686–1697 (2003)
27. J.R. Martí-Vargas, E. García-Taengua, P. Serna, Influence of concrete composition on anchorage bond behavior of prestressing reinforcement. *Constr. Build. Mater.* **48**, 1156–1164 (2013)
28. J.R. Martí-Vargas, P. Serna, W. Hale, Strand bond performance in prestressed concrete accounting for bond slip. *Eng. Struct.* **51**, 236–244 (2013)
29. C. Naito, G. Brunn, G. Parent, T. Tate, Comparative performance of high early strength and self consolidating concrete for use in precast bridge beam construction', *ATLSS report*, 05–03 (2005)
30. S.J. Pantazopoulou, K. Papoulia, Modeling cover-cracking due to reinforcement corrosion in RC structures. *J. Eng. Mech.* **127**(4), 342–351 (2001)
31. A. Pozolo, B. Andrawes, Analytical prediction of transfer length in prestressed self-consolidating concrete girders using pull-out test results. *Constr. Build. Mater.* **25**(2), 1026–1036 (2011)
32. P. Roelfstra, Numerical method to link strain softening with failure of concrete. *Fracture Toughness Fracture Energy Concrete*, 163–175 (1986)
33. D.R. Rose, B.W. Russell, Investigation of standardized tests to measure the bond performance of prestressing strand. *PCI J.* **42**(4), 56–80 (1997)
34. H. Shima, L.-L. Chou, H. Okamura, Micro and macro models for bond in reinforced concrete. *J. Faculty Eng.* **39**(2), 133–194 (1987)
35. T. Ueda, I. Lin, N. Hawkins, Beam bar anchorage in exterior column-beam connections. In *J. Proc.* **83**(3), 412–422 (1986)
36. L. Wang, L. Dai, X. Zhang, J. Zhang, Concrete cracking prediction including the filling proportion of strand corrosion products. *Materials* **10**(1), 6 (2017)
37. L. Wang, J. Yi, J. Zhang, Y. Jiang, X. Zhang, Effect of corrosion-induced crack on the bond between strand and concrete. *Constr. Build. Mater.* **153**, 598–606 (2017)
38. L. Wang, X. Zhang, J. Zhang, J. Yi, Y. Liu, Simplified model for corrosion-induced bond degradation between steel strand and concrete. *J. Mater. Civ. Eng.* **29**(4), 04016257 (2017)
39. X. Wang, X. Liu, Bond strength modeling for corroded reinforcements. *Constr. Build. Mater.* **20**(3), 177–186 (2006)
40. X. Zhang, L. Wang, J. Zhang, Y. Liu, Corrosion-induced flexural behavior degradation of locally ungrouted post-tensioned concrete beams. *Constr. Build. Mater.* **134**, 7–17 (2017)

Open Access This chapter is licensed under the terms of the Creative Commons Attribution 4.0 International License (<http://creativecommons.org/licenses/by/4.0/>), which permits use, sharing, adaptation, distribution and reproduction in any medium or format, as long as you give appropriate credit to the original author(s) and the source, provide a link to the Creative Commons license and indicate if changes were made.

The images or other third party material in this chapter are included in the chapter's Creative Commons license, unless indicated otherwise in a credit line to the material. If material is not included in the chapter's Creative Commons license and your intended use is not permitted by statutory regulation or exceeds the permitted use, you will need to obtain permission directly from the copyright holder.



Chapter 6

Prestress Loss and Transfer Length Prediction in Pretensioned Concrete Structures with Corrosive Cracking



6.1 Introduction

Prestressed concrete is widely used in engineering structures because of its economical, durable and superior performance [8, 13]. Unfortunately, numerous accidents in recent years have raised concerns about the safety of existing prestressed concrete structures [17, 18]. There are many factors that contribute to the deterioration of PC structures, and strand corrosion is one of the major factors [28, 39]. The assessment of prestress loss and transfer length caused by corrosive cracking is necessary for the serviceability and safety of existing concrete structures.

The assessment of prestress losses due to corrosion is a complex issue. Reduction in cross-section of corroded strands, concrete cracking, and bond degradation can all lead to loss of prestress. Compared with post-tensioned concrete members, corrosion cracking and bond degradation have greater influence on effective prestress in pretensioned concrete structures. How to evaluate the prestress loss in pretensioned concrete structures caused by corrosive cracking still needs to be studied further. Numerous researches have been carried out to clarify the effects of the strand diameter, the effective prestress, the concrete strength as well as the concrete cover on the transfer length [9, 23, 24, 33]. However, the above study did not examine the effect that corrosion has on the transfer length of PC structures. The transfer length prediction of PC beams with corrosion cracking also should be researched further.

Youakim et al. [37] evaluated the long-term prestress losses in prestressed concrete structures according to the principles of strain coordination and force balance. Kottari et al. [16] further improved the calculation method of prestress loss proposed by AASHTO-LRFD code and investigated the sensitivity of parameters, such as concrete age, the relative humidity, the number of steel, and concrete strength. In order to ensure the effective transfer of steel strand prestress, the effective bonding between steel strand and concrete interface is very important. When the PC beams are in a corrosive environment, the steel strands in the concrete will gradually corrode [17, 18, 20, 29, 41].

Corrosive cracking reduces the bond properties of the strands, adversely affects the transfer of effective prestress in the structure, and ultimately degrades the structural properties [3, 14, 19, 30, 38, 40]. Compared with other concrete structures, prestress transfer is quite important for PC structures. Corrosion cracking reduces the bond stress of the strand, which adversely affects the transfer length. The researchers conducted an experimental study on the bonding behavior of corroded prestressed strands. The results show that the bond stress first increases to a certain degree and then decreases with the increase of corrosion degree [7, 21, 22, 34, 35].

In this chapter, an analytical model is presented to evaluate the prestress loss in the corroded structure, which takes into account the coupling effects of concrete cracking and bond degradation. Then, an analytical model is proposed to predict the transfer length of PC beams by combining the coupled effects of Hoyer effect and corrosion-induced cracks.

6.2 Calculation of Corrosion-Induced Expansive Pressure

Corrosion of steel strands can cause cracking of the concrete structure and reduce the bond strength between the concrete and the steel strands, resulting in a prestress loss of the steel strands. It is important to consider the effects of concrete cracking and bond degradation in the prestress loss assessment.

When the tensile stress in the circumferential direction caused by corrosion expansion is large than the tensile strength of concrete, concrete is assumed to crack. The concrete cracking situation caused by the corrosion is shown in Fig. 6.1. Seven-wire strands are commonly used as prestressed tendon in PC structures. When the strand is corroded in an adverse environment, the corrosion first starts from the outside of the strand, as illustrated in Fig. 6.1. After the steel strand is corroded, the corrosion loss ρ can be denoted as

$$\rho = 6\Delta A/A_p, \quad (6.1)$$

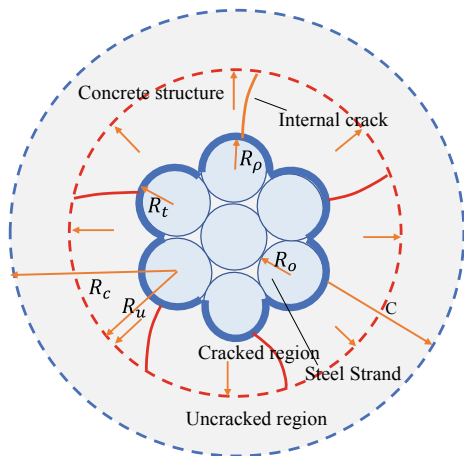
where ΔA is the area loss of single wire, $\Delta A = \frac{2}{3}\pi(R_0^2 - R_\rho^2)$, A_p is the cross-sectional area of the corroded strand, R_0 is the radiuses of wire before corrosion, R_ρ is after corrosion.

With the equivalent principle of volume, the volume reduction of strand ΔV_w per unit length can be written as

$$\Delta V_w = \frac{1}{\gamma - 1}(\Delta V_c + \Delta V_e), \quad (6.2)$$

where $\Delta V_w = 4\pi(R_0^2 - R_\rho^2)$; γ is the rust expansion ratio; ΔV_c is the volume of corrosion products in pores and cracks per unit length, and ΔV_e is the volume change of concrete unit length, $\Delta V_e = 4\pi(R_t^2 - R_0^2)$, R_t is the wire radius with corrosion products.

Fig. 6.1 Steel strand corrosion concrete cracking



Corrosion products filled in the pores and cracks, the volume per unit length can be expressed as [2]

$$\Delta V_c = 4\pi(R_t - R_o)(R_u - R_t), \quad (6.3)$$

where R_u is the radius of cracked area.

The concrete displacement u_c caused by expansive pressure can be calculated with Eqs. (6.1)–(6.3), which can be expressed as

$$u_c = R_t - R_o = \frac{(\gamma - 1)A_p\rho}{4\pi(R_u + R_o)} \quad (6.4)$$

The theory of elastic thick-walled cylinders is used to elaborate the concrete stress state. The hoop stress $\sigma_\theta(t)$ in uncracked concrete, radial displacement $u(t)$ in uncracked concrete are [32]

$$\sigma_\theta(t) = \frac{R_u^2 P_u}{(R_c^2 - R_u^2)} \left(1 + \frac{R_c^2}{t^2} \right) \quad (6.5a)$$

$$u(t) = \frac{R_u^2 P_u}{E_c (R_c^2 - R_u^2)} \left[(1 + \nu_c) \frac{R_c^2}{t} + (1 - \nu_c)t \right], \quad (6.5b)$$

where t is the radius of the uncracked concrete zone, $R_u \leq t \leq R_c$, $R_c = R_o + C$, C is the concrete cover; P_u is the expansion pressure, and the force is located at the interface between the cracked area and the non-cracked area; E_c is the elastic modulus of concrete, and ν_c is Poisson's ratio of the concrete.

According to the equivalence principle of stress distribution at the same location, the concrete tensile stress $\sigma_\theta(R_u)$ at the interface between uncracked region and cracked region should be equal to the concrete tensile strength f_t , i.e., $\sigma_\theta(R_u) = f_t$.

The expansive pressure at the interface between uncracked region and cracked region can be obtained with Eq. (6.5a), which can be expressed as

$$P_u = f_t \frac{R_c^2 - R_u^2}{R_c^2 + R_u^2}. \quad (6.6)$$

The radial displacement $u(r)$ can be calculated in the uncracked concrete by substituting Eq. (6.6) into Eq. (6.5b). Assuming that the radial displacement $u(r)$ in the cracked concrete still satisfies the linear distribution principle, the radial displacement can be given as

$$u(r) = \frac{f_t R_u^2}{E_c (R_c^2 + R_u^2)} \left[(1 + \nu_c) \frac{R_c^2}{r} + (1 - \nu_c) r \right], \quad (6.7)$$

where r is the radius of the concrete cracked region, $R_0 \leq r \leq R_u$.

The hoop stress $\sigma_\theta(r)$ in the cracked concrete can be calculated, which can be denoted as [27]

$$\sigma_\theta(r) = \begin{cases} E_c \varepsilon_\theta(r), & \varepsilon_\theta(r) \leq \varepsilon_{ct} \\ f_t \left[1 - 0.85 \frac{\varepsilon_\theta(r) - \varepsilon_{ct}}{\varepsilon_1 - \varepsilon_{ct}} \right], & \varepsilon_{ct} < \varepsilon_\theta(r) \leq \varepsilon_1, \\ 0.15 f_t \left[\frac{\varepsilon_u - \varepsilon_\theta(r)}{\varepsilon_u - \varepsilon_1} \right], & \varepsilon_1 < \varepsilon_\theta(r) \leq \varepsilon_u, \end{cases} \quad (6.8)$$

where $\sigma_\theta(r)$ is the hoop stress of concrete and $\varepsilon_\theta(r)$ is the hoop strain of concrete; ε_{ct} and ε_u are the strain corresponding to concrete tensile strength and the ultimate strain of concrete, respectively; ε_1 is the strain corresponding to 15% concrete tensile strength; ε_u is the limiting strain of concrete.

Before cover cracking, the expansive pressure would be resisted by the confining stress in the uncracked concrete and the residual tensile stress in the cracked concrete. The expansion pressure P_c at the interface between steel strand and concrete can be expressed as

$$P_c R_0 = P_u R_u + \int_{R_0}^{R_u} \sigma_\theta(r) dr. \quad (6.9)$$

After the concrete cover has cracked, the residual tensile strength in the concrete is mainly used to resist the expansion pressure generated by the corrosion products. The expansive pressure at the strand–concrete interface can be rewritten as [12, 32]

$$P_c R_0 = \int_{R_0}^{R_c} \sigma_\theta(r) dr \quad (6.10)$$

6.2.1 Prediction Model of Prestress Loss Under Corrosive Cracking

6.2.1.1 Stress Variation in Corroded Strand

The elements of half beam are numbered from 1 to n , as shown in Fig. 6.2. For any element i , the stress $f_{p,i}$ in the steel strand can be denoted as

$$f_{p,i} = f_{p,i+1} - \Delta f_{p,i}, \tag{6.11}$$

where $\Delta f_{p,i}$ is the local stress change in element i of the corroded strand, $1 \leq i \leq n$.

The contact area S between the outer wire and concrete is equal to two-thirds of the surface area, which can be written as $S = \frac{4}{3}\pi R_{\rho,i} l_i$, $R_{\rho,i}$ is the residual radius of corroded wire at the i element, l_i is the element length. The local stress variation in corroded strand can be written as

$$\Delta f_{p,i} = \frac{6S}{A_{p,i}(\eta)} \tau_{\eta}, \tag{6.12}$$

where $A_{p,i}(\eta)$ is the residual cross-sectional area of corroded strand at the i element.

6.2.2 Bond Degradation Due to Strand Corrosion

The geometrical shape of the strand can be reduced by corrosion. Corrosion cracking reduces the concrete restraint. All these factors affect the bonding performance of corroded strand. The bond strength can be evaluated in terms of restraint stress, expansive pressure, and bond stress. The stress in the bond of the strand τ_{η} that is corroded can be represented as

$$\tau_{\eta} = \tau_a + \tau_b + \tau_c, \tag{6.13}$$

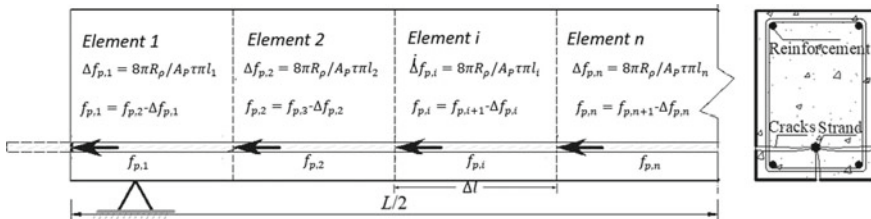


Fig. 6.2 Stress variation in corroded strand

where τ_a is the bonding stress at the bonding interface; τ_b is the confinement stress of the concrete, and τ_c is the bonding stress induced by the expansion pressure.

The adhesive stress of the corroded strand can be represented as [5]

$$\tau_a = \frac{k A_r [\cot \delta + \tan(\delta + \theta)]}{\pi D s_r} f_{\text{coh}}, \quad (6.14)$$

where k is rib count on ribs in the transverse direction; A_r is the area where the ribs are at right angles to the strand axis in the plane; δ is the rib orientation; θ is the friction angle between steel strands and concrete; D and s_r are the strand diameter and the rib spacing, respectively; f_{coh} is a factor of the bonding stress.

The confinement stress around the concrete is denoted as [11]

$$\tau_b = \frac{k C_r \tan(\delta + \theta)}{\pi} p_x, \quad (6.15)$$

where C_r is the shape factor constant; p_x is the maximum pressure at bond failure.

The bond stress induced by expansive pressure can be expressed as

$$\tau_c = k_c P_c, \quad (6.16)$$

where k_c is the coefficient of friction between the corroded strand and the cracked concrete.

Substituting Eqs. (6.14)–(6.16) into Eq. (6.13), the bond stress of corroded steel strand can be obtained. For pretensioned concrete structures, the prestress transfers from strand to concrete through the adhesive stress. Since corrosive cracking and bond degradation have been estimated, a model for corrosion-induced prestress loss can be proposed. The effective prestress of the uncorroded strand minus the effective prestress of the corroded steel strand can be defined as the prestress loss caused by corrosion. The effective prestress in corroded strand could be evaluated based on the strain compatibility and force equilibrium equations.

6.2.3 Calculation Flow Chart of Prestress Loss

For corroded pretensioned concrete structures, the prestress of strand at the beam end is zero, i.e., $f_{p,1} = 0$. The tension force of corroded strand $T_{p,i}$ can be calculated as

$$T_{p,i} = f_{p,i} A_{p,i}(\eta). \quad (6.17)$$

After corrosion, the strain change in strand at the i element $\Delta \varepsilon_{p,i}$ can be denoted as

$$\Delta\varepsilon_{p,i} = \frac{T_{pi}}{E_p A_p} - \frac{T_{p,i}}{E_p A_{p,i}(\eta)}, \tag{6.18}$$

where T_{pi} is the initial prestressing force of uncorroded strand at the i element; E_p is the elastic modulus of strand.

When the stress in the corroded strand equals the effective prestress, the strain change in concrete $\Delta\varepsilon_{c,i}$ should be equal to the change in strain of the corroded strand location $\Delta\varepsilon_{p,i}$ to maintain the strain compatibility, i.e., $\Delta\varepsilon_{c,i} = \Delta\varepsilon_{p,i}$. After corrosion, the concrete strain $\Delta\varepsilon_{p,i}$ for the i th element should be written as

$$\varepsilon_{cp,i} = \frac{T_{pi}}{E_c} \left(\frac{1}{A} + \frac{e_p^2}{I} \right) - \Delta\varepsilon_{c,i}, \tag{6.19}$$

where e_p is the rate of eccentricity of the steel strand; A is the cross-sectional area of concrete; and I is the moment of inertia of the gross section of concrete.

This study primarily investigates the prestress loss caused by strand corrosion, and corrosion of the steel reinforcements is not considered. The distribution of strain in the beam section is shown in Fig. 6.3. The steel strain in the tension region is $\varepsilon_{s,i}$, the steel strain in the compression region is $\varepsilon'_{s,i}$, which can be written as

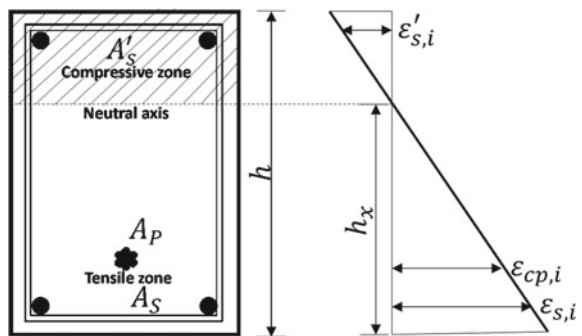
$$\varepsilon_{s,i} = \frac{h_x - a_s}{h_x - a_p} \varepsilon_{cp,i} \tag{6.20a}$$

$$\varepsilon'_{s,i} = \frac{h - h_x - a'_s}{h_x - a_p} \varepsilon_{cp,i}, \tag{6.20b}$$

where h is the height of beam; h_x is the length of the concrete beam from the center of gravity, a_p and a_s are the strand center and the tensile reinforcement center to the bottom of beam, respectively; a'_s is the height from the center of the stressed reinforcement to the top of the concrete beam.

The stress–strain behavior of steel bars can be described using an elastic–plastic constitutive model [11], which is given as

Fig. 6.3 Strain distribution in the cross-section



$$f_s = \begin{cases} E_s \varepsilon_s & \varepsilon_s \leq \varepsilon_{sy} \\ f_{sy} + E_{sp}(\varepsilon_s - \varepsilon_{sy}) & \varepsilon_s > \varepsilon_{sy} \end{cases}, \quad (6.21)$$

where f_s is the stress of reinforcement; ε_s is strain of reinforcement; E_s is the elastic modulus of reinforcement and E_{sp} is the hardening modulus of reinforcement; f_{sy} is the yield strength of reinforcement; ε_{sy} is yield strain of reinforcement.

$F_{s,i}$ is the reinforcement force in the tensile zones, $F'_{s,i}$ is the forces of reinforcements in the compression zones, which can be written as

$$F_{s,i} = A_s f_s(\varepsilon_{s,i}) \quad (6.22a)$$

$$F'_{s,i} = A'_s f'_s(\varepsilon'_{s,i}), \quad (6.22b)$$

where A_s is the section areas of reinforcement in tension zones, A'_s is the section areas of reinforcement in compression zones; $f_s(\varepsilon_{s,i})$ is the stresses of reinforcement in the tension, and $f'_s(\varepsilon'_{s,i})$ is the compression zones.

The mechanical behavior of concrete in tension can be simulated by a linear elastic constitutive law [25]. The nonlinear constitutive law of concrete proposed [6] by is utilized to describe the mechanical behavior of concrete in compression. The stress–strain curve of concrete is denoted as

$$f_c = \begin{cases} f'_c \left[2 \left(\frac{\varepsilon_c}{\varepsilon_0} \right) - \left(\frac{\varepsilon_c}{\varepsilon_0} \right)^2 \right] & \text{in compression} \\ E_c \varepsilon_c & \text{in tension} \end{cases}, \quad (6.23)$$

where f_c is the stress of concrete, ε_c is concrete strain, f'_c is the compressive strength of concrete, ε_0 is the strain corresponding to the concrete compressive strength and taken as 0.002.

The total force C_i of the concrete is denoted as

$$C_i = \int_{A_c} f_c dA_c, \quad (6.24)$$

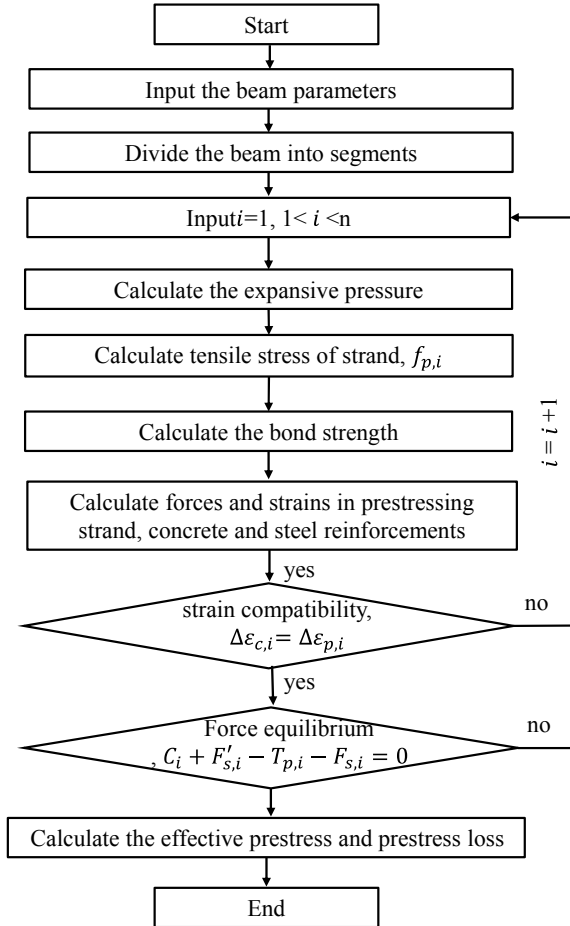
where A_c is the region of the damaged concrete section.

For corroded pretensioned concrete structures, the forces in prestressing strand, steel reinforcements, and concrete should satisfy the equilibrium equation, which can be written as

$$C_i + F'_{s,i} - T_{p,i} - F_{s,i} = 0. \quad (6.25)$$

As mentioned above, we propose a new model incorporating the coupling effects of concrete cracking and bond degradation to evaluate the corrosion-induced prestress loss. The flow chart of prestress loss calculation is shown in Fig. 6.4.

Fig. 6.4 Calculation flowchart of prestress loss



6.2.4 Evaluation of Effective Prestress

6.2.4.1 Accelerated Corrosion and Data Measurement

The concrete was poured with ordinary silicate cement. The concrete mix contained: 676 kg/m³ fine aggregates, 417 kg/m³ cement, and 1026 kg/m³ coarse aggregates. The concrete water–cement ratio was 0.44. To catalyze the corrosion process, sodium chloride was added to the concrete. The uniaxial compressive strength measured after 28 days of curing of the concrete elements was 44.1 MPa.

The testing parameters are given in Table 6.1. In order to study the prestress loss under different stresses and corrosion levels, four stress levels of strand were designed as 0, 0.25 f_p , 0.5 f_p , and 0.75 f_p , respectively, where f_p was 1860 MPa. The corrosion time of A and B groups was 15 days and 20 days, respectively.

Table 6.1 Concrete compressive strength

Beam No. (prestress)	PA0 0	PA1 $0.25f_p$	PA2 $0.5f_p$	PA3 $0.75f_p$	PB0 0	PB1 $0.25f_p$	PB2 $0.5f_p$	PB3 $0.75f_p$
Compressive strength (MPa)	42.8	43.5	44.8	43.9	41.6	45.9	43.4	46.8

The test was designed with eight concrete beams with a cross-section of 130×150 mm and the length of 2000 mm. The test beam was strengthened with 7-wire steel strands of 15.2 mm in diameter. The yield strength of the steel strand selected in the test was 1830 MPa, and the maximum strength was 1910 MPa. Stirrups with a diameter of 6 mm and a spacing of 100 mm were used in the beam, two 6 mm steel bars are set at the bottom of the beam as longitudinal reinforcement. The yield strength of deformed reinforcement was 400 MPa, and the ultimate strength of deformed reinforcement was 540 MPa. The details of the specimen are shown in Fig. 6.5. The concrete cover of reinforcement was 30 mm, and the concrete cover of strand was 42.4 mm.

The compressive strength of concrete is listed in Table 6.2. In this research test, electrochemical methods were used to accelerate the corrosion of strands. Only the effect of corrosion on the prestress loss of steel strands is considered, the epoxy resin is applied to the surface of steel bars to prevent corrosion. The accelerated corrosion device consists of a DC power supply and a stainless-steel plate. The steel strand is connected to the anode and the stainless-steel plate is connected to the cathode, and 10% sodium chloride solution is used as the corrosion solution. A constant potential meter is used to apply a DC current to the strand. The operating current during accelerated corrosion is 0.1 A.

After the accelerated corrosion, the crack width in 10 cm intervals on the concrete surface was measured using a portable microscope with a resolution of 0.01 mm. The average mass loss of the strand in the longitudinal direction was measured to reflect the corrosion level of strand in the global region. The average mass loss of strand

**Fig. 6.5** Details of specimen**Table 6.2** Testing parameters

Concrete Beam No	Group A				Group B			
	PA0	PA1	PA2	PA3	PB0	PB1	PB2	PB3
Corrosion time (Days)	15	15	15	15	20	20	20	20
Prestress (MPa)	0	$0.25f_p$	$0.5f_p$	$0.75f_p$	0	$0.25f_p$	$0.5f_p$	$0.75f_p$

Table 6.3 Experiment results summary

Beam No	PA0	PA1	PA2	PA3	PB0	PB1	PB2	PB3
ρ_c (%)	7.05	7.47	8.35	9.41	10.45	11.52	12.48	14.69
F_c (kN)	5.0	8.5	11.5	14.0	4.5	7.0	9.5	11.5
F_u (kN)	38.0	42.0	45.5	48.0	28.3	31.0	33.5	36.7
$F_{e,t}$ (kN)	0.0	52.6	89.7	120.7	0.0	37.5	56.4	74.0
$f_{e,t}$ (MPa)	0.0	409.0	704.1	958.5	0.0	304.9	463.6	624.0
Normalized prestress loss (%)	0.0	12.0	24.3	31.3	0.0	34.4	50.2	55.3

Note ρ_c is the mass loss, F_c is the cracking load, F_u is the ultimate load, $F_{e,t}$ is the prestressing force, $f_{e,t}$ is the effective prestress

in 10 cm intervals was measured to reflect the variation of the corrosion degree in different zones.

In the current study, the prestress loss was predicted using the uniform corrosion model, which is reasonable from the predicted results. In this experimental study, in order to reflect the longitudinal corrosion loss of steel strands and the change of crack width of concrete members, the crack widths of concrete members and the mass loss of steel strands are given at intervals of 10 cm. Corrosion-induced cracking will be accelerated under the action of prestress. Study have shown that the mass loss of corroded steel bars is closely related to the width of concrete cracks under corrosion [15]. In summary, it is feasible to use the concrete crack width to assess the mass loss of the corroded strand.

Comparison of the experimental data in Table 6.3. By changing the stress level of the strand from 0 to 75% f_p , the average increase in the mass loss is 37.0%. The results show that prestress can accelerate the mass loss of the strand. The mass losses of PA0 and PA3 were 7.05% and 9.41%, respectively. The mass losses of PB0 and PB3 were 10.45% and 14.69%, respectively.

6.2.5 Effective Prestress Evaluation

Four methods of estimating the effective prestress in prestressed concrete structures have been employed in the current research [4]: (1) Cut strands to representative lengths to measure the changes of strand strain; (2) cracking load determined by load test; (3) Measurement of the longitudinal strain in concrete at the prestressed strand's center of gravity as a function of time; (4) determine the lateral pressure used to close the cracks in the small cylindrical holes. All four methods require processing of the test results before calculating the effective prestress.

As illustrated in Fig. 6.6, a four-point flexural test was performed to obtain the load–deflection curves of corroded specimens. The test beams have a bending span of 600 mm and a net span of 1800 mm. The load is applied monotonically, and the

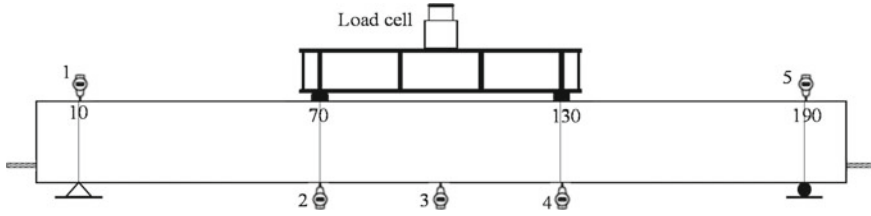


Fig. 6.6 Diagram of load testing

loading value is measured by a pressure transducer. Electronic digital micrometers are used to measure vertical deflection in loading points, support points, and spans. The load–deflection curves of the test beams were reflected by the mid-span displacements in Fig. 6.7. The cracking and ultimate loads for the beams are given in Table 6.3. As the applied load increases, the deflection of the beam increases accordingly. When the applied load reaches the failure load, the applied load suddenly decreases and the test beam fails.

During load testing, once the tensile stress exceeds the concrete tensile strength, cracks appear at the bottom of the test beam. The critical condition of concrete cracking can be expressed as

$$f_t = f_{p,\eta} A_p(\eta) \left(\frac{1}{A_c} + \frac{e_p}{I_c} y_b \right) - \frac{M_s}{I_c} y_b - \frac{M_c}{I_c} y_b, \quad (6.26)$$

where $f_{p,\eta}$ is the effective prestress in corroded PC beams; $A_p(\eta)$ is the remaining cross-sectional area of the corroded strand; y_b is the length from the center axis to the beam bottom; M_s is the bending moment due to the self-weight of the beam; M_c is the cracking moment; I_c is the moment of inertia of the total section the damaged concrete.

The effective prestressing force and prestressing loss of the corroded prestressed concrete structure can be estimated, as given in Table 6.3. Studies have found that the high stress of strand will accelerate the loss of prestress caused by corrosion. The prestress losses of PA1 and PA3 are 12.0% and 31.3%, respectively. The prestress losses of PB1 and PB3 are 34.4% and 55.3%, respectively. By changing the stress level of strand from 25% f_p to 75% f_p , the corrosion-induced prestress loss increases by 20.1% in the current experimental study.

6.2.6 Validation on Prestress Loss Model

For estimating the corrosion-induced prestress loss, the bond degradation is the vital factor and should be clarified at first. In order to study the effect of strand corrosion on the bond strength, bond strengths under different corrosion levels are given in

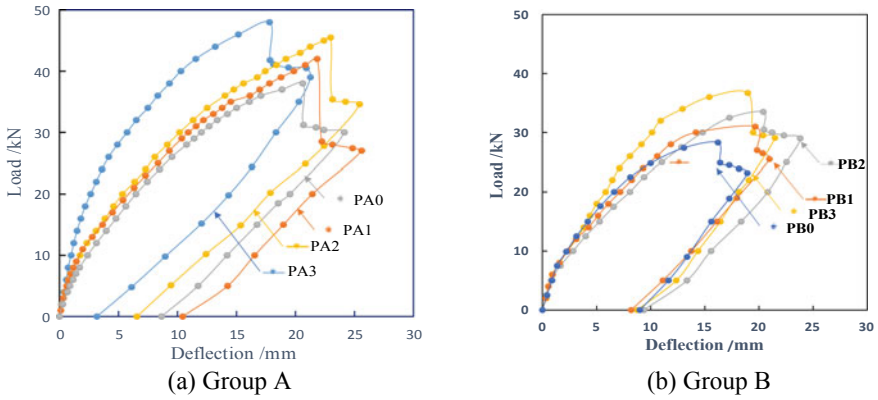


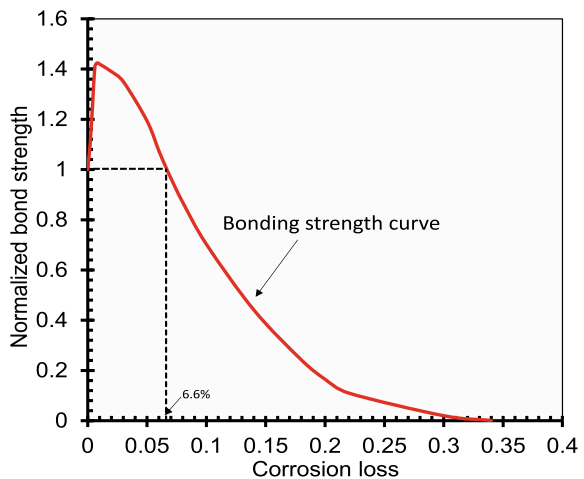
Fig. 6.7 Load–deflection curves

Fig. 6.8. The normalized bond strength in Fig. 6.8 is defined as the bond strength ratio of corroded strand to uncorroded strand.

As shown in Fig. 6.8, when the strand corrosion is less than 6.6%, the bond stress would increase with the increase of corrosion, and the further corrosion of the strand would gradually cause the bond stress to degrade. When the corrosion degree of the steel strand is less than 6.6%, the corrosion products increase the friction force and gear force of the interface between the steel strand and the concrete. Consequently, slightly corroded strand will result in an increase of the bond stress. Corrosion levels above 6.6% could lead to severe concrete cracking, reducing concrete confinement, and resulting in deterioration of bond stress.

The predicted effective prestress and experimental results are shown in Fig. 6.9. Strands with a corrosion loss of less than 6.6% are considered to have similar bond

Fig. 6.8 Adhesion strength at different corrosion losses



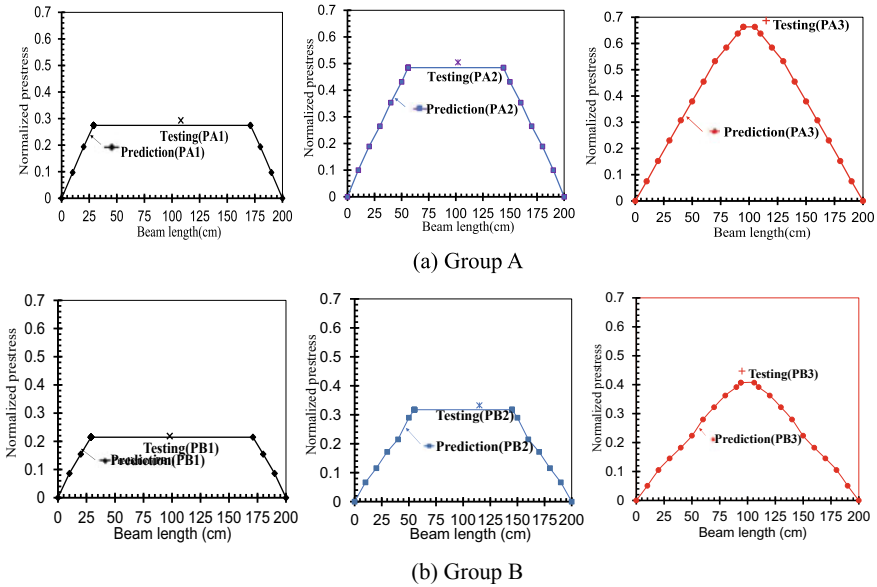


Fig. 6.9 Experimental and predicted prestress

stress to uncorroded strands. The prediction of the effective prestress was carried out by applying the bond strength model proposed in this study.

The average error of prediction is 4.8%, and standard deviation of prediction is 0.02. The prediction error is defined as $\frac{|P_t - P_p|}{P_t}$, where P_t is tested effective prestress, and P_p is predicted effective prestress. Errors in results may result due to model simplification. In addition, the uncertainty of the measured experimental data can also lead to errors. However, due to the complexity of the corrosion process, the accuracy of the model predictions is acceptable.

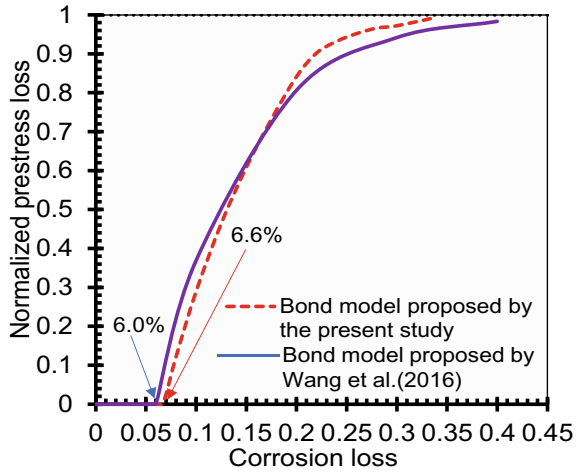
Wang et al. [32] designed ten beams to investigate the bond degradation at the strand–concrete interface under different levels of corrosion. An empirical model for predicting bond strength of corroded strand is proposed, which can be expressed as

$$R_\eta = \begin{cases} 1.0, & \eta \leq 6.0\% \\ 2.03e^{-11.8\eta} & \eta > 6.0\% \end{cases}, \tag{6.27}$$

where R_η is the bond stress ratio of corroded strand to uncorroded strand.

As shown in Fig. 6.10, the critical corrosion levels for this model [33] are 6.6% and 6.0%, respectively, and when the corrosion levels are below the critical values, the bond strength and effective prestressing are not reduced. Strand corrosion can cause severe cracking of PC beams when corrosion levels are exceeds the critical values, thereby reducing bond strength and effective prestress. When the corrosion level exceeds 34.0%, the effective prestress would drop to zero. The two models predict the prestress loss towards a similar direction, as shown in Fig. 6.10. The results show

Fig. 6.10 Prestress loss and corrosion loss



that the model proposed in this study can accurately predict the corrosion-induced prestress loss in prestressed concrete structures.

6.2.7 Prediction of Transfer Length Under Corrosive Cracking

6.2.7.1 Expansive Pressure Induced by Hoyer Effect and Corrosion

For predicting the transfer length of PC beams under corrosion cracking, the expansion pressure at the strand–concrete interface is an important parameter. During the corrosion of the test beam, the expansion pressure is influenced by the coupling effect of Hoyer effect and corrosion. As illustrated in Fig. 6.11, the expansion pressure caused by the strand corrosion products would influence the concrete cracking. In predicting the transfer length of corroded prestressed concrete structures, the Hoyer effect and the expansion pressure due to corrosion need to be considered. In this study, a prediction model of transfer length is proposed, which has the advantage of considering the coupling effect of Hoyer effect and steel strand corrosion. The theory of thick-walled cylinders was also applied to evaluate the expansion pressure [26], as shown in Fig. 6.12.

After tensioning the prestressed strand, the radius R_t is denoted as

$$R_t = \left(1 - \frac{f_{pt}}{E_p} \nu_p\right) R_0, \tag{6.28}$$

where R_0 is strand original radius, ν_p , f_{pt} , and E_p are Poisson’s ratio, the tensile stress, and the elastic modulus of strand, respectively.

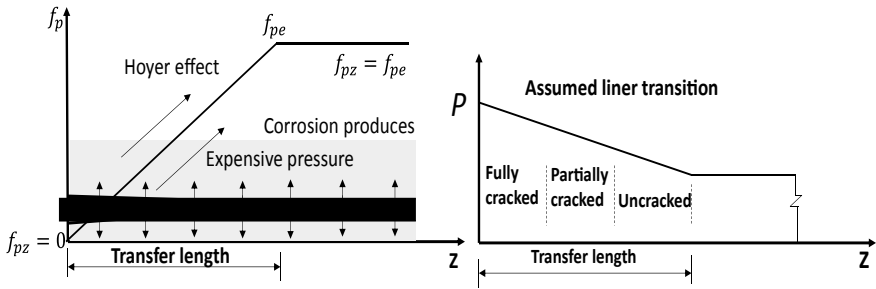
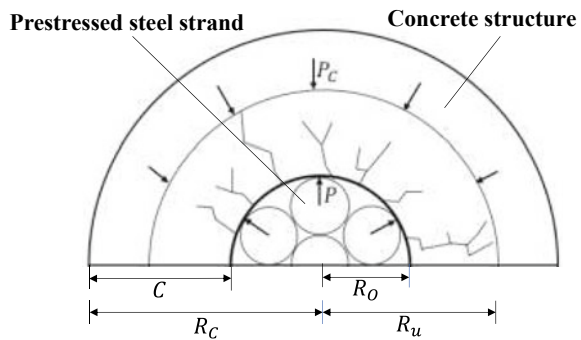


Fig. 6.11 Schematic diagram of the expansion pressure due to Hoyer effect and corrosion of steel strands

Fig. 6.12 Theory of thick-walled cylinders for concrete cracks



After prestress releasing, the radial displacement of the prestressed strand u is [26]

$$u = \frac{-P_h R_t}{E_c (1/R_c^2 - 1/R_t^2)} \left[\frac{(1 - \nu_c)}{R_c^2} + \frac{(1 + \nu_c)}{R_t^2} \right] - \frac{\nu_c f_{cz} R_t}{E_c}, \tag{6.29}$$

where R_c is the distance from the center of the strand to the edge of the concrete cover, E_c and ν_c are the elastic modulus and Poisson's ratio of concrete, respectively, f_{cz} and P_h are the concrete compressive stress at the strand location and the expansion pressure under the Hoyer effect, respectively.

At the location of the prestressed strand, the concrete longitudinal compressive stress f_{cz} can be denoted as

$$f_{cz} = f_{pz} A_p \left(\frac{1}{A} + \frac{e_p}{I_c} y_b \right), \tag{6.30}$$

where f_{pz} is the axial stress of strand at the corresponding position, A_p and A are the initial cross-sectional area of strand and the cross-sectional area of concrete, respectively, I_c is the moment of inertia of concrete cross-section, e_p is the eccentricity of

prestressing strand, y_b is the distance from the neutral axis of beam to the bottom of beam.

Considering the condition of Hoyer effect, the expansion pressure P_h is expressed as [26]

$$P_h = \frac{R_0(1 - \nu_p f_{pz}/E_p) - R_t(1 - \nu_c f_{cz}/E_c)}{(1 - \nu_p)R_0/E_p + [\nu_c - (R_t^2 + R_c^2)/(R_t^2 - R_c^2)]R_t/E_c} \quad (6.31)$$

The residual cross-sectional area of prestressing strand after corrosion A'_p can be obtained with the corrosion loss ρ as

$$A'_p = A_p(1 - \rho). \quad (6.32)$$

After the corrosion of steel strands in concrete, the concrete compressive stress can be rewritten as

$$f'_{cz} = (1 - \rho)f_{cz}. \quad (6.33)$$

Combining Eqs. (6.29)–(6.33), the radial displacement of prestressing strand u_c and the expansive pressure P induced by Hoyer effect and strand corrosion can be calculated as

$$u_c = \frac{-PR_t}{E_c(1/R_c^2 - 1/R_t^2)} \left[\frac{(1 - \nu_c)}{R_c^2} + \frac{(1 + \nu_c)}{R_t^2} \right] - \frac{\nu_c f'_{cz} R_t}{E_c} \quad (6.34)$$

$$P = \frac{R_0(1 - \nu_p f_{pz}/E_p) - R_t(1 - \nu_c f'_{cz}/E_c)}{(1 - \nu_p)R_0/E_p + [\nu_c - (R_t^2 + R_c^2)/(R_t^2 - R_c^2)]R_t/E_c} \quad (6.35)$$

6.2.8 Calculation of Transfer Length

The transfer of prestress in PC beams can be obtained by the bond strength between strand and concrete. Corrosive cracking of the concrete affects the expansion pressure and reduces the bond strength between the concrete and the strand, thus changing the transfer length of the PC beam. The bond stress τ can be written as

$$\tau = \mu \cdot P, \quad (6.36)$$

where μ is the coefficient of friction.

One-half of the beam is discretized into the several elements with a length of Δl to analyze the stress variation in prestressing strand, as shown in Fig. 6.13. The stress increment of strand $\Delta f_{p,i}$ at the i th element can be expressed as

$$\Delta f_{p,i} = \frac{\pi d'_p \tau_i}{A'_p} \Delta l, \tag{6.37}$$

where d'_p is the remaining diameter of strand after corrosion, τ_i is the bond stress of the corroded strand at the i th element.

Stress change of prestressing strand $f_{p,i}$ and strain change of prestressing strand $\Delta \varepsilon_{p,i}$, at the i th element can be written as

$$f_{p,i} = f_{p,i-1} + \Delta f_{p,i} \tag{6.38}$$

$$\Delta \varepsilon_{p,i} = \varepsilon_{p,0} - \frac{f_{p,i}}{E_p}, \tag{6.39}$$

where $\varepsilon_{p,0}$ is the initial prestrain of strand.

The concrete strain at the i th element $\varepsilon_{c,i}$ can be given as

$$\varepsilon_{c,i} = \frac{f_{p,i} A'_p}{E_c} \left(\frac{1}{A} + \frac{e_p}{I_c} y_b \right) \tag{6.40}$$

There is no stress in the strand at the end of beam. At the end of transfer length, the stress of strand is developed to the effective prestress. The transfer length can be determined when the strain change of prestressing strand at the i th element $\Delta \varepsilon_{p,i}$ is equal to the strain of concrete $\varepsilon_{c,i}$, i.e., $\Delta \varepsilon_{p,i} = \varepsilon_{c,i}$. The transfer length l_t in corroded PC beams can be written as

$$l_t = i \cdot \Delta l \tag{6.41}$$

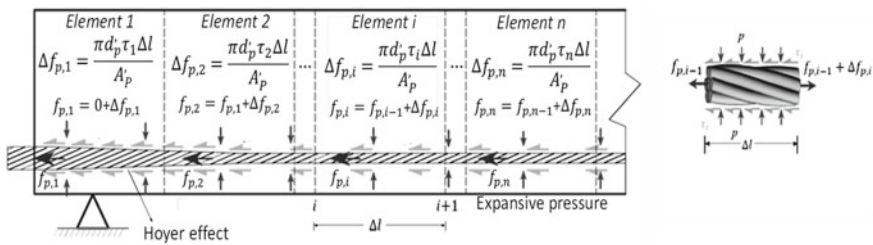


Fig. 6.13 Schematic of element discretization in corroded PC beams

6.3 Evaluation of the Transfer Length in Corroded PC Beams

6.3.1 Specimen Design and Data Analysis

Ten specimens were designed to study the transfer length in the corroded PC beams. The dimensions of the specimen beams were all the same, and a hollow slot was designed in the mid-span with a length of 500 mm, a width of 60 mm, and a height of 100 mm. The width of the test beam was 200 mm, the height was 350 mm, and the length of the beam was 3800 mm. The prestressing strand had a diameter of 15.2 mm and a concrete cover thickness of 67.4 mm.

Compressive reinforcement was two deformed reinforcement bars with the diameter of 10 mm embedded in the top of the beam. Two deformed bars with a diameter of 16 mm were set at the bottom of the beam as tensile bars. The spacing of the stirrups with the diameter of 8 mm was 70 mm at the end of the beam and 100 mm in the middle of the span.

The elastic modulus, yield strength, and ultimate strength of deformed bars were 200 GPa, 400 MPa and 570 MPa, respectively. The elastic modulus, yield strength, and ultimate strength of strand were 195 GPa, 1830 MPa, and 1910 MPa, respectively. The average compressive strength of the concrete after 28 days of curing was 41.7 MPa. Figure 6.14 illustrates the details of the test beam.

The electrochemical corrosion method was employed to achieve the corrosion of strand in this study. The reinforcement bars were coated with epoxy resin to avoid the corrosion. The uncorroded beam S0 was used as the control specimen. Nine specimens were classified into group A, group B, and group C based on the different corrosion positions, as shown in Fig. 6.15. Each group contained three specimens with different corrosion time, as given in Table 6.4.

As illustrated in Fig. 6.15, a 200 mm long trough made of PVC material was installed in the area of localized corrosion. The corrosion device is composed of three parts: DC power supply, prestressed steel strand, and stainless-steel plate immersed in

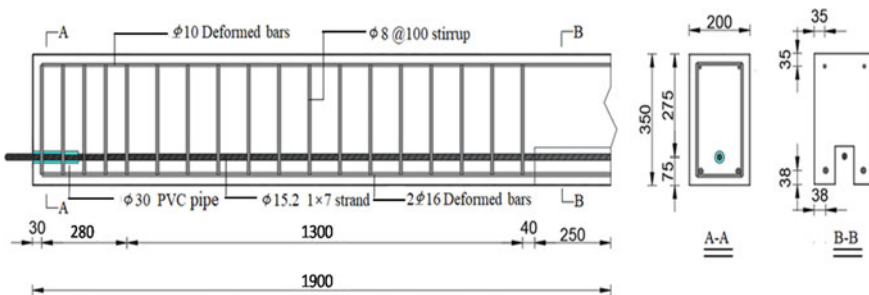


Fig. 6.14 Specimen details (Unit: mm)

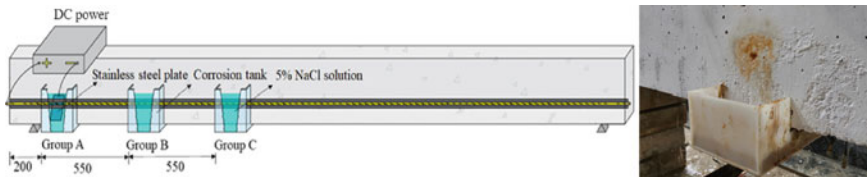


Fig. 6.15 Local corrosion location of specimens (Unit: mm)

Table 6.4 Corrosion location and corrosion schedule

No	Group A			Group B			Group C		
	A1	A2	A3	B1	B2	B3	C1	C2	C3
Corrosive time (day)	15	25	35	15	25	35	15	25	35
Corrosion loss (%)	14.8	25.1	35.0	14.7	25.1	34.3	15.1	24.4	35.4

chloride solution. The anode and cathode are connected by steel strands and stainless-steel plates, respectively. During the corrosion process, the working current intensity is 0.5 A.

There is a correlation between the width of the crack caused by corrosion and the effect of corrosion on the transfer length. The corrosion loss, average, and maximum crack widths of specimens were measured. Corrosion-induced crack widths increase as corrosion extends from the mid-span region to the ends of the beam. Comparing to B3 and C3, the average crack width of A3 increases by 4.8% and 22.2%, respectively. Comparing to B3 and C3, the maximum crack width of A3 increases by 6.9% and 25.6%, respectively (Fig. 6.16).

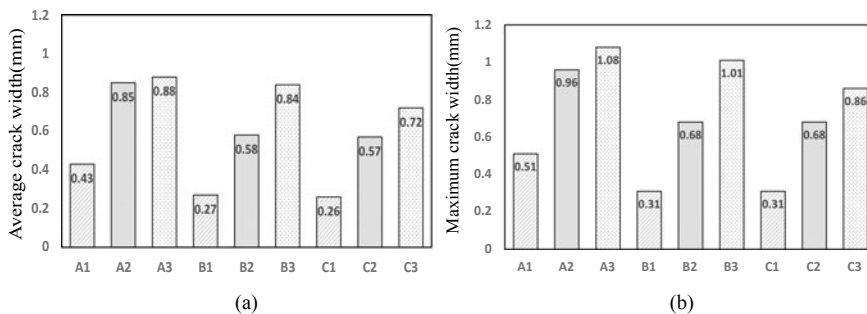


Fig. 6.16 Corrosion-induced crack width: a average value; b maximum value

6.3.2 Evaluation of Transfer Length Under Corrosive Cracking

There is a relationship between the effective prestress and the transfer length, and the transfer length can be evaluated by reverse calculation of the cracking load. The design standard for the transfer length in PC beams is defined in ACI 318 (ACI 318) as follows:

$$l_t = 0.048 f_{pe} d_p, \tag{6.42}$$

where f_{pe} is the effective prestress, d_p is the diameter of prestressing strand.

Under the applied load, the tensile stress of concrete at the bottom of the beam increases, and the effective prestress is expressed as

$$f_{pe} = \left(f_t + \frac{M_s}{I_c} y_b + \frac{M_c}{I_c} y_b \right) / \left[A'_p \left(\frac{1}{A_c} + \frac{e_p}{I_c} y_b \right) \right], \tag{6.43}$$

where M_s and M_c are the moment due to the beam’s weight and the cracking moment, respectively.

As mentioned above, the effective prestress can be obtained from the cracking load calculated by Eq. (6.43). The effective prestress in Eq. (6.42) can be used to estimate the transfer length of corroded PC beams. In this study, the cracking loads of the specimens are obtained from static tests, and the transfer lengths are estimated by the cracking loads.

The four-point bending test was used to measure the cracking load of beams. The supporting span of the test beam was set to 3500 mm. Loading is monotonic and progressive until the structure eventually fails. As shown in Fig. 6.17, the dial gauges were used to measure the vertical displacement at the point of load support and mid-span. The vertical displacement and crack width were recorded under each loading phase.

The vertical displacement of the mid-span is used to represent the deflection of the beam. The load–deflection curves of specimens are shown in Fig. 6.18. The whole loading process can be summarized in three stages: cracking point, yield point-, and damage point. When the applied load is less than the cracking load, the

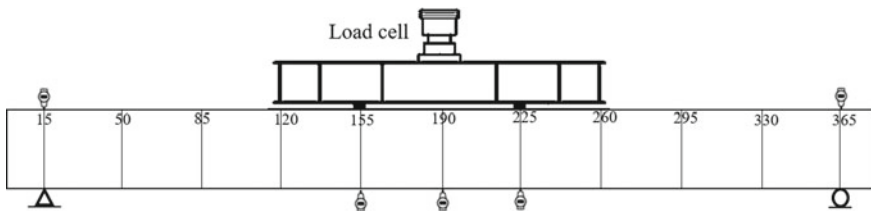
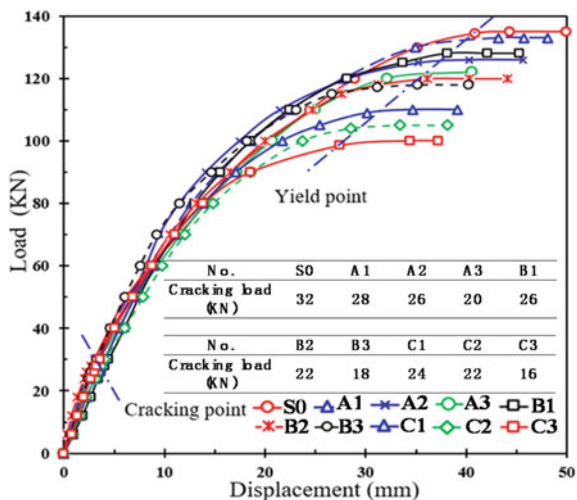


Fig. 6.17 Schematic diagram of the load device (Unit: cm)

Fig. 6.18 Load–deflection curves of the test beams



load–deflection curve of the test beam is approximately linear. Because the flexural stiffness mainly depends on the moment of inertia of the concrete section. Therefore, the strand corrosion has no significant effect on the bending stiffness of the test beams before concrete cracking.

The flexural stiffness of the test beams was significantly reduced when the corrosion of the strands increased. The flexural stiffness in group A, group B, and group C decreases gradually under the same corrosion loss. This indicates that under the action of corrosion, the flexural stiffness degradation of the mid-span area after concrete cracking will be more serious than that of the end area. Finally, when the strand in the compression zone breaks or the concrete is crushed, the beam will fail.

As illustrated in Fig. 6.18, the cracking and ultimate load of the test beam also decrease as the corrosion degree increases. Compared with S0, the cracking loads are reduced by 60.0%, 77.8%, and 100.0% for A3, B3, and C3, respectively. The ultimate loads of all groups decreased to different degrees, with A3 decreased by 10.7%, B3 decreased by 14.4%, and C3 decreased by 35.0%.

Using S0 as a control for the other groups, the transfer length in the test beam can be calculated by taking the concrete cracking load and the strand corrosion loss. The transfer length of PC beams increases with the increase of corrosion degree. The transfer lengths of A3, B3, and C3 increase by 24.3%, 17.7%, and 14.4%, respectively, as compared to S0. Besides, the transfer length caused by strand corrosion will also extend when the local corrosion position moves from the mid-span to the beam end. The transfer lengths of A3 and B3 increase by 8.6% and 2.9%, respectively, as compared to C3.

Table 6.5 Cracking load and transmission length of test beams

No	Crack load (KN)	Ultimate load (KN)	$l_{t,e}$ (mm)	$l_{t,p}$ (mm)
S0	32	135	700	732
A1	28	133	768	818
A2	26	126	845	897
A3	20	122	870	923
B1	26	128	745	795
B2	22	120	781	831
B3	18	118	824	876
C1	24	110	719	763
C2	22	105	774	724
C3	16	100	801	849

6.4 Model Validation and Parameter Sensitivity Analysis

6.4.1 Verification of Proposed Model

The experimental results were consistent with the prediction of the proposed model. During the corrosion process, the corrosion product will diffuse from the local corrosion area to the end of the sample. Assuming that the corrosion of the strand reduces from localized corrosion areas to the end of the beam in a linear fashion; in this research model, the corrosion loss of the beam end strand is reduced to zero. The elastic modulus of the concrete used in the model is 3.25×10^4 MPa. Poisson's ratio of the chain is 0.3. [36] demonstrates that the friction coefficient in prestressing strand varies from 0.23 to 0.7, and the friction coefficient μ is selected as 0.34 in the model. The theoretical transfer lengths in specimens are calculated and given in Table 6.5.

This study compares the theoretical transfer length of the test beam with the experimental transfer length, as shown in Fig. 6.19. The average error is 6.1%. The error in the data can be defined as $(l_{t,p} - l_{t,e})/l_{t,e}$ according to the experimental results, where $l_{t,p}$ is theoretical transfer length, and $l_{t,e}$ is experimental transfer length. The prediction error of the model is acceptable considering the uncertainty of the strand corrosion process, which means that the transfer length in PC beams under corrosive cracking can be accurately predicted by the proposed model.

6.4.2 Effect of Material Parameters on Expansive Pressure

The expansion pressure at the interface between the strand and the concrete is an important factor in assessing the transfer length of prestressed concrete beams under

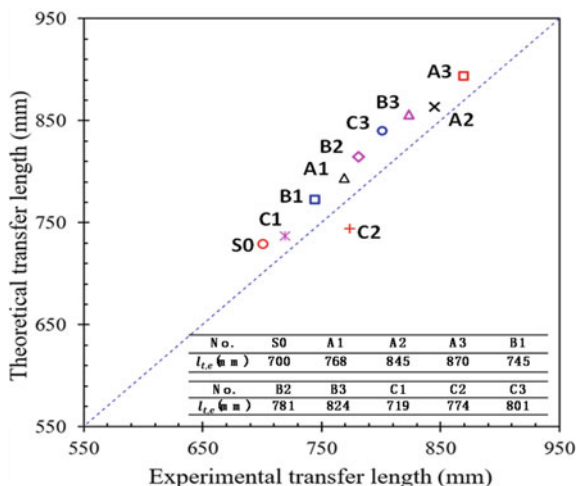


Fig. 6.19 Theoretical and experimental transfer length

corrosion. When the strand corrosion is 35%, the relationship between the expansion pressure and the normalized transfer length can be clarified, as shown in Fig. 6.20. The expansion pressure under the Hoyer effect coupled with corrosion is maximum at the end of the beam and decreases gradually along the longitudinal direction. At the end of the transfer length, the expansion pressure due to corrosion will be present, but the expansion pressure due to the Hoyer effect is zero. The expansion pressure at the end of the beam increases by 13.6% when the modulus of elasticity of the concrete increases from 3×10^4 MPa to 3.45×10^4 MPa. The expansion pressure at the interface between corroded steel strand and concrete has a more affected by Poisson's ratio than that by the elastic modulus of concrete.

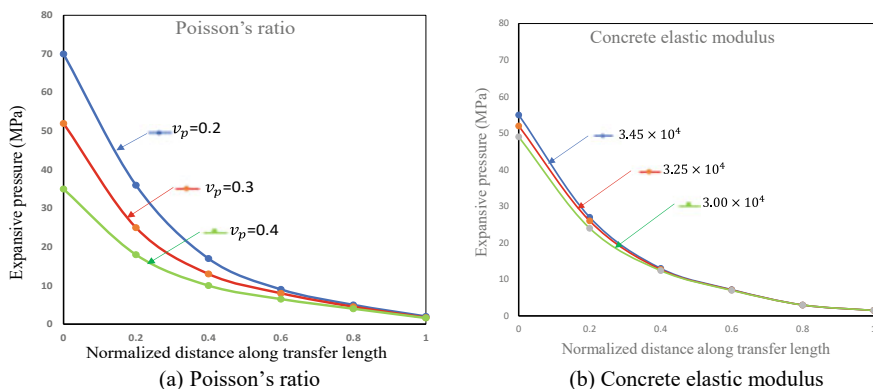


Fig. 6.20 Influence of material parameters on expansion pressure

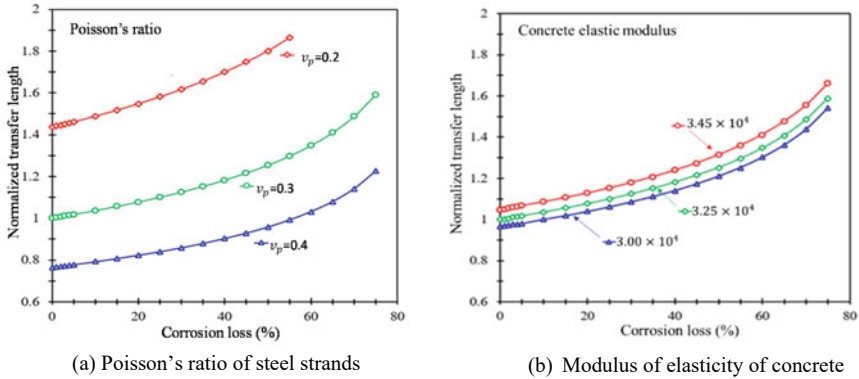


Fig. 6.21 Effect of material parameters on transfer length after strand corrosion

6.4.3 Effect of Material Parameters on Transfer Length

In this study, the transfer lengths at different levels of corrosion are discussed to evaluate the effect of corrosion on the transfer lengths, as shown in Fig. 6.21. The growth rate of the transfer length also increases accordingly as the corrosion degree of the strand increases. Under the corrosive cracking of PC beams, the transfer length decreases as Poisson’s ratio of the strand and the modulus of elasticity of the concrete increase. By changing Poisson’s ratio of strand from 0.2 to 0.4, the transfer length with the corrosion loss of 35% reduces by 88.2%. By changing the elastic modulus of concrete from 3×10^4 MPa to 3.45×10^4 MPa, the transfer length is reduced by 8.6% when the corrosion loss reaches 35%. Compared to the modulus of elasticity, Poisson’s ratio affects significantly the transfer length in beams with corrosive cracking.

6.5 Conclusions

1. A new model is proposed to predict the corrosion-induced prestress loss in prestressed concrete structures. The model takes into account the coupling effect of corrosion-induced concrete cracking and bond degradation.
2. Corrosion-induced cracking does not reduce the bond strength and effective prestress when the corrosion level does not exceed 6.6%. With the development of corrosion, the bond strength and effective prestress decrease, and the bond strength and effective prestress descend to zero when the corrosion level reaches 34.0%.

3. The high stress of strand will accelerate the corrosion-induced prestress loss. In the current experimental study, the prestress loss induced by corrosion increases by 20.1% by changing the strand stress level from 25 to 75% of the strand tensile strength.
4. An analytical model, incorporating the Hoyer effect and corrosion-induced cracking, is proposed to predict the transfer length in PC structures under corrosive cracking. The innovation of the proposed model is that it can consider the coupling effects of Hoyer effect and corrosion-induced cracking.
5. The transfer length depends on the corrosion positions and corrosion degrees. The transfer length with the corrosion loss of 35% will extend 8.6% when the corrosion position moves from the mid-span to the beam end. The transfer length increases by 24.3% once the corrosion loss of strand reaches 35%.
6. The transfer length of PC beams under corrosion cracking is influenced by Poisson's ratio of strand and modulus of elasticity of concrete. The transfer length under corrosion cracking increases accordingly with the increase of Poisson's ratio of strand and modulus of elasticity of concrete.

References

1. ACI318-14. *Building Code Requirements for Structural Concrete and Commentary*. (American Concrete Institute, Farmington Hill, 2011)
2. K. Bhargava, A.K. Ghosh, Y. Mori, S. Ramanujam, Model for cover cracking due to rebar corrosion in RC structures. *Eng. Struct.* **28**(8), 1093–1109 (2006)
3. F. Biondini, D.M. Frangopol, Life-cycle performance of deteriorating structural systems under uncertainty. *J. Struct. Eng.* **142**(9), F4016001 (2016)
4. L.A. Caro, J.R. Marti-Vargas, P. Serna, Prestress losses evaluation in prestressed concrete prismatic specimens. *Eng. Struct.* **48**(Mar), 704–715 (2013)
5. H.-P. Chen, J. Nepal, Analytical model for residual bond strength of corroded reinforcement in concrete structures. *J. Eng. Mech.* **142**(2), 04015079 (2016)
6. M. Collins, D. Mitchell, A. Felber, D. Kuchma. *RESPONSE V I.O. Provided with Prestressed Concrete Structures* (Englewood Cliffs, Prentice Hall NJ. 1991)
7. L. Dai, Y. Chen, L. Wang, Y. Ma, Secondary anchorage and residual prestressing force in locally corroded PT beams after strand fracture. *Constr. Build. Mater.* **275**, 122137 (2021)
8. C.N. Dang, R.W. Floyd, G.S. Prinz, W. Micah Hale, Determination of bond stress distribution coefficient by maximum likelihood method. *J. Struct. Eng.* **142**(5), 04016003 (2016)
9. C.N. Dang, C.D. Murray, R.W. Floyd, W.M. Hale, J.R. Marti-Vargas, A correlation of strand surface quality to transfer length. *ACI Struct. J.* **111**(5), 1245–1252 (2014)
10. Dario, Coronelli. Corrosion cracking and bond strength modeling for corroded bars in reinforced concrete. *ACI Struct. J.* (2002)
11. S. El-Tawil, Static and fatigue analyses of RC beams strengthened with CFRP laminates. *J. Compos. Const.* **5**(4), 258–267 (2001)
12. S.J. Han, D.H. Lee, S.H. Cho, S.B. Ka, K.S. Kim, Estimation of transfer lengths in precast pretensioned concrete members based on a modified thick-walled cylinder model. *Struct. Concr.* **17**(1), 52–62 (2016)
13. W. Han, J. Wu, C. Cai, S. Chen, Characteristics and dynamic impact of overloaded extra heavy trucks on typical highway bridges. *J. Bridg. Eng.* **20**(2), 05014011 (2015)

14. L. Jin, M. Liu, R. Zhang, X. Du, 3D meso-scale modelling of the interface behavior between ribbed steel bar and concrete. *Eng. Fract. Mech.* **239**, 107291 (2020)
15. I. Khan, R. François, A.J.C. Castel, Prediction of reinforcement corrosion using corrosion induced cracks width in corroded reinforced concrete beams **56**, 84–96
16. A.K. Kottari, P.B. Shing, Estimation of long-term prestress losses in post-tensioned girders. *ACI Struct. J.* (2013)
17. F. Li, Y. Yuan, C.-Q. Li, Corrosion propagation of prestressing steel strands in concrete subject to chloride attack. *Constr. Build. Mater.* **25**(10), 3878–3885 (2011)
18. S. Lim, M. Akiyama, D.M. Frangopol, Assessment of the structural performance of corrosion-affected RC members based on experimental study and probabilistic modeling. *Eng. Struct.* **127**, 189–205 (2016)
19. C. Lu, S. Yuan, P. Cheng, R. Liu, Mechanical properties of corroded steel bars in pre-cracked concrete suffering from chloride attack. *Constr. Build. Mater.* **123**, 649–660 (2016)
20. N. Lu, Y. Liu, M. Noori, X. Xiao, System reliability assessment of cable-supported bridges under stochastic traffic loads based on deep belief networks. *Appl. Sci.* **10**(22), 8049 (2020)
21. Y. Ma, Z. Guo, L. Wang, J. Zhang, Probabilistic life prediction for reinforced concrete structures subjected to seasonal corrosion-fatigue damage. *J. Struct. Eng.* **146**(7), 04020117 (2020)
22. Y. Ma, A. Peng, X. Su, L. Wang, J. Zhang, Modeling constitutive relationship of steel bar removed from corroded PC beams after fatigue considering spatial location effect. *J. Mater. Civ. Eng.* **33**(4), 04021019 (2021)
23. J. Marti-Vargas, P. Serna, J. Navarro-Gregori, J.L. Bonet, Effects of concrete composition on transmission length of prestressing strands. *Constr. Build. Mater.* **27**(1), 350–356 (2012)
24. P. Motwani, A. Laskar, Influence of excessive end slippage on transfer length of prestressing strands in PC members. *Structures* **20**, 676–688 (2019)
25. N.A. Vu, A. Castel, R. François. Response of post-tensioned concrete beams with unbonded tendons including serviceability and ultimate state. *Eng. Struct.* (2010)
26. H.B. Oh, S.E. Kim, C.Y. Choi, Theoretical analysis of transfer lengths in pretensioned prestressed concrete members. *J. Eng. Mech.* **132**(10), 1057–1066 (2006)
27. S.J. Pantazopoulou, K. Papoulia, Modeling cover-cracking due to reinforcement corrosion in RC structures. *J. Eng. Mech.* **127**(4), 342–351 (2001)
28. R.G. Pillai, D. Trejo, P. Gardoni, M.B.D. Hueste, K. Reinschmidt, Time-variant flexural reliability of posttensioned, segmental concrete bridges exposed to corrosive environments. *J. Struct. Eng.* **140**(8), A4014018 (2014)
29. X.-H. Shen, Q.-F. Liu, Z. Hu, W.-Q. Jiang, X. Lin, D. Hou, P. Hao, Combine ingress of chloride and carbonation in marine-exposed concrete under unsaturated environment: a numerical study. *Ocean Eng.* **189**, 106350 (2019)
30. D.V. Val, L. Chernin, M.G. Stewart, Experimental and numerical investigation of corrosion-induced cover cracking in reinforced concrete structures. *J. Struct. Eng.* **135**(4), 376–385 (2009)
31. L. Wang, X. Zhang, J. Zhang, J. Yi, Y. Liu, Simplified model for corrosion-induced bond degradation between steel strand and concrete. *J. Mater. Civ. Eng.* **29**(4), 04016257 (2017)
32. X. Wang, X. Liu, Bond strength modeling for corroded reinforcement. *Constr. Build. Mater.* (2006)
33. K. Warenycia, M. Diaz-Arancibia, P. Okumus, Effects of confinement and concrete nonlinearity on transfer length of prestress in concrete. *Structures*, **11**, 11–21 (2017)
34. L. Xiao, J. Peng, J. Zhang, Y. Ma, C. Cai, Comparative assessment of mechanical properties of HPS between electrochemical corrosion and spray corrosion. *Constr. Build. Mater.* **237**, 117735 (2020)
35. Y. Yang, J. Peng, X. Liu, S.C. Cai, J. Zhang, Probability analysis of web cracking of corroded prestressed concrete box-girder bridges considering aleatory and epistemic uncertainties. *Eng. Struct.* **228**, 111486 (2021)
36. S. Yi, R. Burgueho, Stress transfer characteristics of sheathed strand in prestressed concrete beams: computational study. *PCI J.* **59**(3), 95–109 (2014)
37. S. Youakim, A.G.S. Hida, V. Karbhari, Prediction of Long-Term Prestress Losses. *PCI J.* **52**(2), 15 (2007)

38. W. Zhang, X. Liu, X. Gu, Fatigue behavior of corroded prestressed concrete beams. *Constr. Build. Mater.* **106**, 198–208 (2016)
39. W. Zhang, Z. Ye, X. Gu, X. Liu, S. Li, Assessment of fatigue life for corroded reinforced concrete beams under uniaxial bending. *J. Struct. Eng.* **143**(7), 04017048 (2017)
40. W. Zhang, H. Yuan, Corrosion fatigue effects on life estimation of deteriorated bridges under vehicle impacts. *Eng. Struct.* **71**, 128–136 (2014)
41. W. Zhang, B. Zhou, X. Gu, H. Dai, Probability distribution model for cross-sectional area of corroded reinforcing steel bars. *J. Mater. Civ. Eng.* **26**(5), 822–832 (2014)

Open Access This chapter is licensed under the terms of the Creative Commons Attribution 4.0 International License (<http://creativecommons.org/licenses/by/4.0/>), which permits use, sharing, adaptation, distribution and reproduction in any medium or format, as long as you give appropriate credit to the original author(s) and the source, provide a link to the Creative Commons license and indicate if changes were made.

The images or other third party material in this chapter are included in the chapter's Creative Commons license, unless indicated otherwise in a credit line to the material. If material is not included in the chapter's Creative Commons license and your intended use is not permitted by statutory regulation or exceeds the permitted use, you will need to obtain permission directly from the copyright holder.



Chapter 7

Secondary Anchorage and Prestress Loss of Fractured Strand in PT Beams



7.1 Introduction

Prestressed concrete (PC) is widely used in large bridges, high-rise buildings, and other large structures because of its lightweight, low cost, and great durability [20, 22]. In recent years, however, there have been a lot of reports about the deterioration of existing PC structures [11, 29]. Corrosion can easily induce the phenomenon of pit corrosion in prestressing strand. This may cause the strand fracture without warning [16, 28, 36]. The effect of corrosion-induced strand fracture on residual prestress of post-tensioned concrete (PT) beams should be investigated fully to ensure the structural safety.

The prestress can be rebuilt through re-anchoring the corrosion-induced fractured strand with the grouting material. Due to the re-anchoring of fractured strand, the assessment of prestress generated by secondary anchorage becomes more challenging. At present, there is no study or specification that is available for determining the residual prestress in corroded PT beams after strand fracture, which may cause the erroneous assessment of structural behavior. The residual prestress in PT beams generated by secondary anchorage of fractured strand needs to be studied further.

The arrangement of this chapter is as follows. Firstly, the secondary anchorage mechanism of fractured strand in PT beams is explored. Then, the secondary anchorage generates residual prestress in PT beams, which is validated. Following this, a numerical model for secondary anchorage of fractured strand is built. Finally, the damage control section and flexural properties of PT beams with locally corrosion after strand fracture are evaluated.

7.2 Literature Review

7.2.1 Bonding Properties of Fractured Strand

The bonding properties between strand and concrete are crucial to the flexural properties of PC structures. Some scholars have carried out theoretical and experimental research on the bonding properties between uncorroded strand and concrete, forming a relatively complete research system [9, 20–23]. The erosion of external harmful substances will inevitably cause strand corrosion. Corrosion will not only reduce the size of its own cross-section, change the contact medium and contact conditions with the surrounding concrete, but also cause cracking of the concrete cover, resulting in the degradation of the bonding properties between strand and concrete [16].

Wang et al. [31] carried out accelerated corrosion test, pull-out test, and beam static loading test to explore the effect of the corrosion degree of strand on the bonding properties. This study shows that the bonding properties degradation has a relation with the strand corrosion degree. The critical corrosion loss of strand is 1.5%. When the corrosion degree is lower than 6.24%, corrosion can enhance the strand bonding properties. If the corrosion degree is greater than 9.26% or the crack width induced by corrosion is exceeded than 0.67 mm, the bonding properties are degraded significantly. The calculation model of bond strength, transfer length, and the constitutive model of bond stress–slip under different strand corrosion losses are established.

Liu et al. [17] researched the effect of strand corrosion loss, bond length, stirrup on the bonding properties. A calculation method of normalized bonding strength stress between strand and concrete under the effects of corrosion loss, stirrup spacing, and bond length is proposed. The bonding properties of strand first increase and then decreases as the corrosion degree increases. At the same time, this study points out that 1.5% is the critical corrosion loss.

Mao [18] studied the influence of the corrosion-induced crack width on the bonding properties. The research shows that the bond stiffness decreases linearly with the increase of the longitudinal corrosion-induced crack width. Morcouc et al. [24] studied the effect on strand bond strength caused by pitting corrosion. The study shows that corrosion pits can enhance the bond strength with a small slip occurring in slightly corroded strand, and conversely, corrosion pits will undermine the bond strength between strand and concrete with a large slip under severe corrosion.

At present, few scholars have explored the bonding properties between strand and grout. The fractured strand caused by corrosion will be re-anchored with the surrounding grout to form the new prestress [4]. El Zghayar et al. [10] conducted pull-out tests for investigating the bonding properties between strand and grout. The research shows that the bond stress between strand and grout can make the strand re-anchoring in the grouting material like the pretensioned member. The bond stress between strand and grout is determined by the grouting density of the bellow. Zhao et al. [35] explored the effect of bellow diameter and concrete protection layer thickness on the bonding properties between strand and grout by pull-out tests. It

indicates that the bonding properties of strand increase with the increase of thickness of protection layer and bellow diameter.

However, the aforementioned study all used the pull-out tests, which cannot simulate the bonding behavior between the strand and grout under the Hoyer effect and high stresses in the strand. Considering the Hoyer effect and the high stress, the bond anchorage mechanism, the formation of prestress, and the transfer length after strand fracture need to be further explored.

7.2.2 Prestress Loss of Fractured Strand

Corrosion of the strand will reduce the cross-section, cause the degradation of the mechanical parameters, reduce the bond strength, and decrease the restraint of the surrounding concrete, which cause the prestress loss in the strand. Some scholars have carried out experiments and theoretical research on the prestress loss of PC structures under the influence of strand corrosion.

Zhang et al. [34] studied the prestress loss in PT beams with different strand corrosion losses. The effect of changes in elastic deformation of corroded strand and concrete on prestress loss can be neglected. The study shows that the residual prestress in the PT beam decreased approximately linearly with increasing corrosion loss. A model is established to evaluate the residual prestress in the PT beam affected by strand corrosion.

Dai et al. [6] evaluated the loss of prestress in pretensioned concrete beams under different strand corrosion losses. A model is established for evaluating the prestress loss considering the coupling effect of corrosion-induced concrete cracking, bond strength degradation and other factors. The research shows that the prestress loss is influenced by the corrosion loss. The critical corrosion loss is 6.6%. When the corrosion degree is lower than 6.6%, the prestress is basically not lost. As the corrosion loss continues to increase, the prestress loss gradually increases. If the corrosion loss exceeds 34%, the prestress is basically lost.

Osborn et al. [26] conducted a prestress loss assessment on seven naturally corroded prestressed T-beams removed from a bridge in service for 42 years. An evaluation model for determining the residual prestress in prestressed T-beams under the influence of natural corrosion of strand is established. The study shows that the evaluation model was sufficiently accurate to assess prestress loss in the corroded prestressed T-beams.

At present, few work has been carried out to assess and analyze the residual prestress in PT structures after strand fracture. The fractured strand caused by corrosion will be re-anchored with the grouting material. Therefore, the prestress of the structure will not be completely lost. Coronelli et al. [5] qualitatively described the process of forming prestress between fractured strand and grout, but did not quantitatively analysis of the specific residual prestress in the structure. The evaluation and prediction of the residual prestress in PT structures after strand fracture requires further research.

7.3 Secondary Anchorage of Fractured Strand

7.3.1 Strand Fracture Test

Five specimens with the identical dimensions of 200 mm × 350 mm × 4000 mm were designed and manufactured. The five beams were divided into two parts: one contrast beam without the fracture of strand (PT0) and four beams with strand fractures at different positions (PT1, PT2, PT3, PT4). A seven-wire strand with a diameter of 15.2 mm was set at the beam bottom. The metal bellows had a diameter of 50 mm. Figure 7.1 shows the specimen details. Table 7.1 shows the mechanical property parameters of strand and reinforcement bars.

The concrete mixture has a weight ratio of cement, coarse aggregate, fine aggregate, and water as 1: 2.89: 2.06: 0.45, which was designed in accordance with the Chinese Technical Specification JGJ 55-2011. All beams were cast in the same manufactured batch. Three cube specimens measuring 150 mm × 150 mm × 150 mm were cast. The uniaxial compression test was used for determining the concrete compressive strength. The average 28-day compressive strength of concrete was 46.6 MPa.

Stress corrosion will lead to the brittle fracture of strand in corroded PT structures during the service life. To simulate the brittle fracture of strand, this study suddenly sawn the strand in concrete. A cavity of 30 mm × 125 mm × 70 mm was fabricated in the beams before casting, as shown in Fig. 7.1. After concrete and grout curing, the strand in cavity was sawn. The strands in the four beams fracture at four different positions. The fracture position of PT1 strand is in anchorage region. This paper used L to represent the specimen length. The fracture position of PT2 strand was in L/4 region. The fracture position of PT3 strand was in loading point region. The fracture

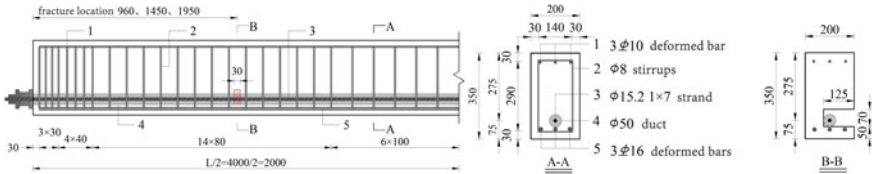


Fig. 7.1 Diagram of specimen details (Unit: mm)

Table 7.1 Mechanical property parameters of strand and reinforcement bars

Type	Diameter (mm)	Yield strength (MPa)	Ultimate strength (MPa)	Elastic modulus (GPa)
Strand	15.2	1860	1910	195
Tensile bar/ Compressive bar	16/10	400	540	200
Stirrup	8	300	420	210

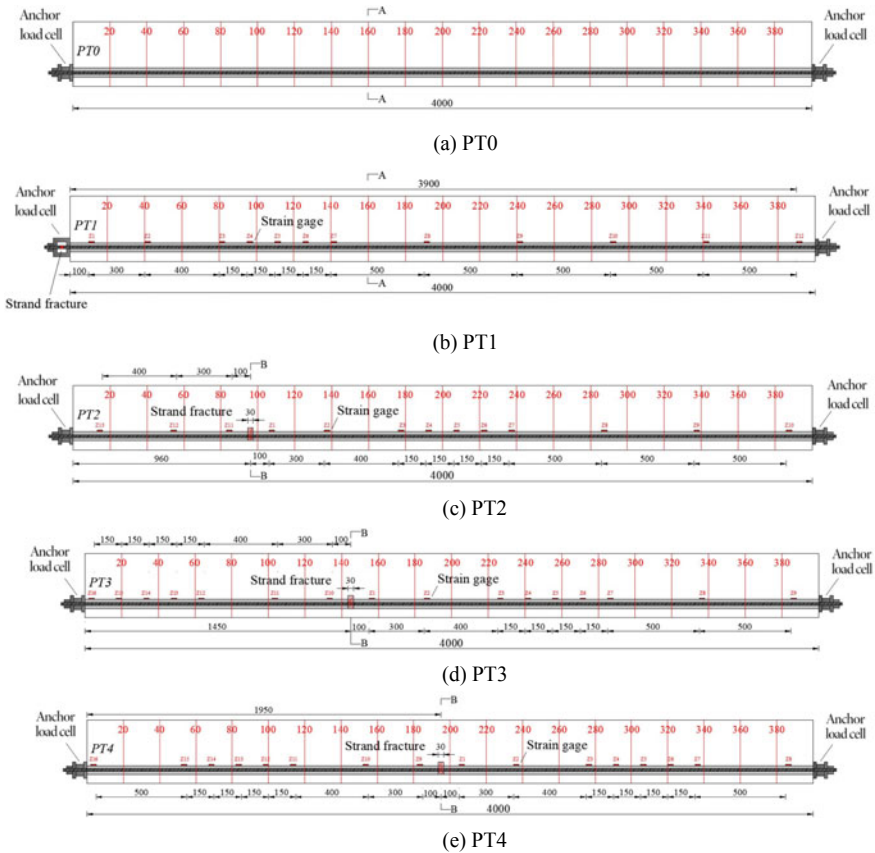


Fig. 7.2 Strand fracture positions and the location of strain gauges (Unit: mm)

position of PT4 strand was in mid-span region. The specific details of strand fracture in each specimen are shown in Fig. 7.2.

7.3.2 Mechanism of Secondary Anchorage

The severe corrosion can cause the strand to fracture in PT specimens. The retraction force induced by the retracement of fractured strand is firstly acted on the strand–grouting material interface. The interfacial force will be generated between grouting material and strand to prevent the retraction of the fractured strand, which makes the retraction force transfer along the length of beam. The interfacial force at the strand–grouting material, which has a relation with the retraction stage of fractured strand, is made up of chemical bond force, friction force, and mechanical interaction force. In the initial stage without slippage, the chemical bond force generated by the

bonding effect of grouting material on the surface of strand provides the interfacial force. When grouting material slips with strand, the chemical bond force disappears immediately, the friction force and mechanical interaction force are formed to prevent the fractured strand from retracing. The frictional force at the interface is the force of the grouting material to resist the relative slippage of fractured strand under the action radial stress. The retraction of the fractured strand will cause the helical ridge to extrude the grouting material forming an oblique squeeze force. Similarly, the mechanical interaction force is the horizontal part of the reverse oblique squeeze force generated by the grouting material obliquely squeezing toward the helical ridge of the strand.

The diameter of strand will decrease in comparison with its original diameter because of the Poisson effect when it is tensioned. After the strand fracture, the original tensile stress of the strand at the position of strand fracture will become zero, and the diameter will return to the initial diameter. With the gradual stress transfer of the fractured strand, the stress of the fractured strand increases gradually along the direction of the beam length, and its diameter will gradually decrease. The fractured strand will form an anchor wedge effect with the grouting material. Poisson's ratio and the tightness of the helical wires have an impact on the change degree of strand diameter. The change in the diameter of strand will produce an expansive pressure on the surrounding grouting material. Correspondingly, a radial stress will be generated in the strand by the surrounding grouting material, as shown in Fig. 7.3. The radial stress caused by the helical compaction and Poisson effect will lead to a larger friction force, and change the longitudinal interfacial force of the strand. The interfacial force is maximum at the fracture position of strand and gradually decreases along the longitudinal direction of strand.

In the current experiment, a duct is formed by withdrawing the embedded metal bellows and injecting grouting material into the duct. The grouting material, due to its slight dilatability and low viscosity, will fully fill the irregular surface of concrete resulting in a large mechanical interaction force and chemical bond force at the interface between grouting material and concrete. The secondary anchorage of fractured strand exists two interacting interfaces, which include the interface between strand

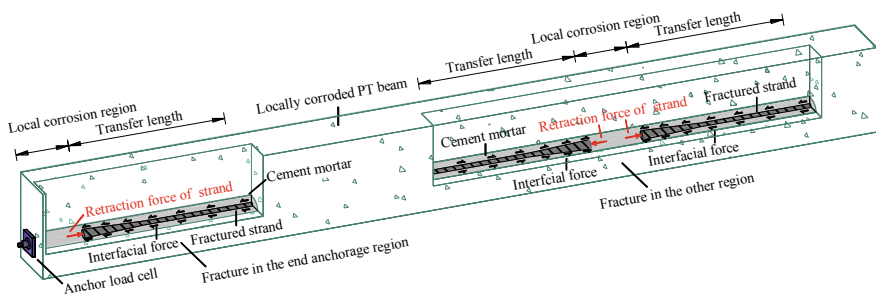


Fig. 7.3 Secondary anchorage of fractured strand (Left: Fracture in the end anchorage region; Right: Fracture in the other region)

and grouting material and the interface between grouting material and concrete. The retraction force of fractured strand first acts on the grouting material by the interfacial force at the interface between strand and grouting material. After that, the retraction force is further transferred to the concrete by the interfacial force at the interface between grouting material and concrete. By the effect of the above-mentioned action, the fractured strand will be re-anchored to generate the new prestress in PT structures, which is terms as the secondary anchorage, as shown in Fig. 7.3.

The fracture of strand forms a new type of anchorage, which differs from the anchoring form of the PC structures, with grouting material bond anchoring at the one end and anchorage anchoring at the other end. The fractured strand is anchored in the grouting material by the expansion effect of the fractured strand retraction, which is like to but not the Hoyer effect. Different transfer mechanisms will be caused by different strand fracture positions in PT beams. When strand fractures in the end anchorage region, the anchorage of fractured strand is only generated in one direction, as shown in Fig. 7.3. When strand fractures in the other region ($L/4$ region, $3L/8$ region and mid-span region), the fractured strand retracts toward two directions, as shown in Fig. 7.3. The prestress generated by fractured strand also forms the transfer length of secondary anchorage. The secondary transfer length is defined as the shortest length required for the beam produce an interface force to balance the retraction force of the fracture strand. When strand fractures in the end anchorage region, one transfer length is formed in the beams. When strand fractures in the other region, two transfer lengths are formed.

7.3.3 Secondary Transfer Length After Strand Fracture

In this study, the anchor load cells at the end of specimens were employed to monitor the residual prestress of fractured strand in specimens, as shown in Fig. 7.2. Some study evaluate the transfer length by longitudinal strain of strand [7, 8, 10, 25]. Therefore, the change of strand strain can be used to reflect the secondary transfer length after strand fracture. Coronelli et al. [5] found that the strain gauges were easy to break near the fracture position of strand. By attaching strain gauges on the metal bellows surface, the strand strain is indirectly obtained. This method can also effectively avoid the failure of strain gauges [10]. According to JTG 3362–2018 (JTG 3362-2018) and ACI 318-14 (ACI 318-14), the transfer length of seven-wire strand with 15.2 mm diameter was 972 mm and 1024 mm, respectively. Therefore, the strain gauges were densely arranged in the 900 mm–1300 mm region and sparsely arranged in the other region, as shown in Fig. 7.2.

The transfer length of secondary anchorage for each fractured strand is obtained from the combination of the grout strain profiles and the 95% Average Maximum Strain method, as shown in Fig. 7.4. Russell and Burns [27] given a detailed introduction to the 95% Average Maximum Strain method. Many scholars used this method

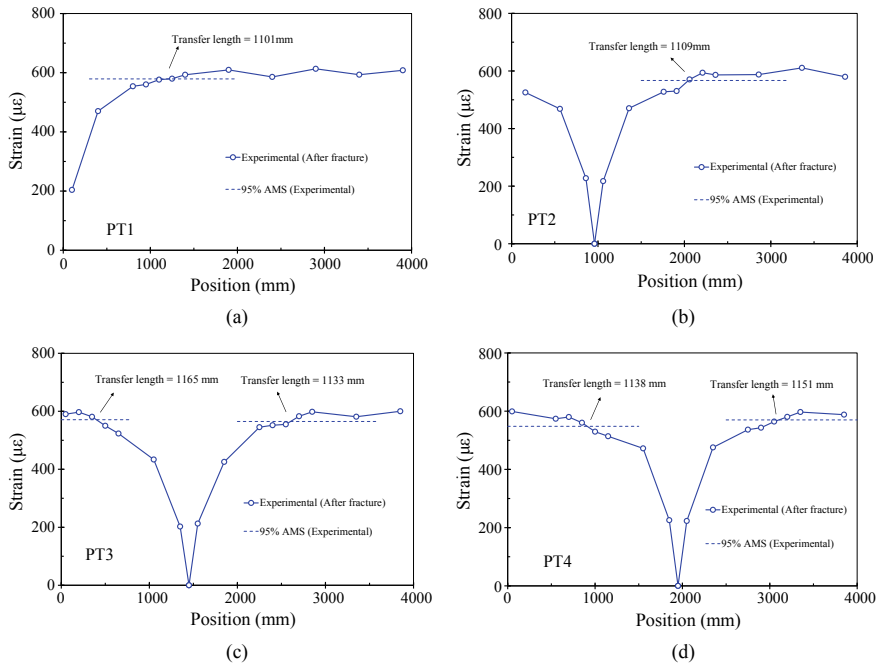


Fig. 7.4 Experimental strains and secondary transfer length

to evaluate the transfer length [1, 13, 25]. As shown in Fig. 7.4, the secondary transfer lengths after strand fracture range from 1101 to 1165 mm. Therefore, the transfer length of secondary anchorage in this research is represented by the average value of 1133 mm.

Figure 7.4 shows that the different strand fracture positions determine the different transfer mechanisms. Only one transfer zone is formed in specimens when the strand fractures in the end anchorage region (PT1). Two transfer zones are formed in specimens once the strand fractures in the other region (PT2, PT3, PT4). The strain at the fracture position of strand decreases to zero, indicating a complete loss of prestress at the location of the strand fracture. The strain data of the left fractured strand of PT2 is always in a state of increase, which differs from that of PT3 and PT4. This shows that when the length of beam on one side of fractured strand is smaller than the transfer length of secondary anchorage, the strain of strand does not tend to be stable.

7.3.4 Residual Prestress in Secondary Anchorage of Fractured Strand

The change of effective prestress includes three phases during the whole experiment. The first phase is prestressing, where the strand is tensioned. The second phase is casting of grouts. The third phase is the fracture of strand. The change of effective prestress in strand under different phases can be seen in Table 7.2. The effective prestress before strand fracture is lower than the initial prestress to a certain degree. The average prestress loss ρ_1 is 1.04%. The loss of prestress in this phase may be caused by the time-dependent loss, elastic compression of the grout, frictional loss, and anchorage loss. When the strand is fractured, the residual prestress will be rebuilt by secondary anchorage. As Table 7.2 gives, the residual prestress after strand fracture is lower than the effective prestress before strand fracture to a certain degree. The strand fracture position determines the prestress loss ρ_2 in secondary anchorage. When the length of fractured strand is beyond the length of secondary transfer, the average loss of prestress ρ_2 is 2.28%. It's worth noting that PT2 (left) has a prestress loss ρ_2 of 6.55%, and this loss of prestress is almost triple than the loss of other fractured strands. This is due to the length of fractured strand is only 945 mm, which cannot be completely anchored in the beam. In the current experiment, the residual prestress of fractured strand is represented by the average value of 1049 MPa.

Table 7.2 Effective prestress change of strand in different phases

Type	Initial prestress (MPa)	Effective prestress before strand fracture (MPa)	Prestress loss ρ_1 (%)	Residual prestress after strand fracture (MPa)	Prestress loss ρ_2 (%)
PT0	1124	1115	0.80	/	/
PT1	1119	1109	0.96	1087	1.94
PT2 (Left)	1090	1079	0.98	1009	6.55
PT2 (Right)	1090	1079	0.98	1039	3.77
PT3 (Left)	1084	1069	1.32	1046	2.17
PT3 (Right)	1084	1069	1.32	1049	1.87
PT4 (Left)	1089	1077	1.12	1061	1.53
PT4 (Right)	1089	1077	1.12	1051	2.39

7.4 Residual Prestress in PT Beams After Strand Fracture

7.4.1 Calculation of Residual Prestress

Several methods for determining the residual prestress in PC members have been proposed, including the decompression load method, the strand-cutting method, and the cracking moment method [3]. The decompression load method and strand-cutting method assess the residual prestress by testing the repeated load and the strand strain, respectively. Corrosion will cause the failure of strain gauge, which are attached to the surface of strand. The repeated load monitoring operation is complicated, which requires to be determined jointly by the strain gauge and crack opening sensor. The above methods are not suitable for determining the prestress generated by secondary anchorage.

The first cracking load is easily monitored, which is advantageous for evaluating the prestress generated by secondary anchorage. Additionally, the cracking moment test method is also used by some study to calculate the residual prestress in existing PC structures [12, 34]. The cracking moment method is used in this study to evaluate the prestress generated by secondary anchorage.

The corrosion-induced strand fracture can rebuild the new prestress by the secondary anchorage. Study have shown that the prestress in PC beams is related to its cracking load, and PC beams are easier to crack under a small prestress [3]. During the loading process, the bottom concrete of the specimen with fractured strand mainly bears the tensile stress caused by self-weight, the tensile stress caused by the applied load, and the precompression stress caused by secondary anchorage. The compression stress in the concrete at the bottom of the specimen beam is gradually decreased with the continuous application of the applied load. When the applied load causes the first crack in the bottom concrete of the specimen beam, the tensile stress on the bottom concrete at the crack equals the tensile strength of the concrete. The applied load currently is the cracking load. Based on the above principle, the residual prestress in locally corroded PT beams, P , generated by the secondary anchorage of fractured strand can be expressed as

$$P = \frac{M_s y_z / I_z + M_c y_z / I_z - f_t}{1/A + e y_z / I_z}, \quad (7.1)$$

where M_s is the bending moment formed by self-weight of beam; y_z is the distance between the bottom edge of the beam and the center of gravity of the converted section at the cracking position; M_c is the bending moment formed by cracking load; f_t is the concrete tensile strength; e is the distance from the center of strand at the cracking position to the center of the converted section; I_z is the inertia moment of test beam at cracking position; A is the composite sectional area.

The prestress redistribution in fractured strand will affect the cracking and the ultimate loads of the beam. The cracking behavior and the ultimate load of post-tensioned concrete with different fracture position of strand were studied through

static loading test. The beams were tested by four-point flexural test. The shear-flexural span and the pure-flexural span of beams were 1300 mm and 1000 mm, respectively. The applied load was imposed on the beams monotonously until the beams were failed. The load cell was used for measuring the load. The vertical displacement of supports, loading points, and mid-span sections were measured by five dial gauges. The 5 cm × 5 cm grids on each side of the beams were used to describe the crack distribution. The load device diagram is shown in Fig. 7.5.

The deflection of the beam in the following analysis presents the vertical displacement of mid-span. The load–deflection curves of beams are split into three regions by the cracking point and yield point, as shown in Fig. 7.6. In the first region before the cracking point, the load–deflection curves of beams have the similar deformation behavior. This shows that the effect of strand fracture on bending stiffness of PT beam before cracking can be ignored. The inertia moment of the concrete section determines the flexural stiffness of uncracked beam. The slopes of the curves for beams with fractured strand are less than the slope of PT0 in the second region after cracking point. This shows that the fracture of strand leads to a decrease in stiffness of beams after cracking of concrete. The degradation of stiffness increases with the fracture position of strand moving to the mid-span region. The deflection of beams

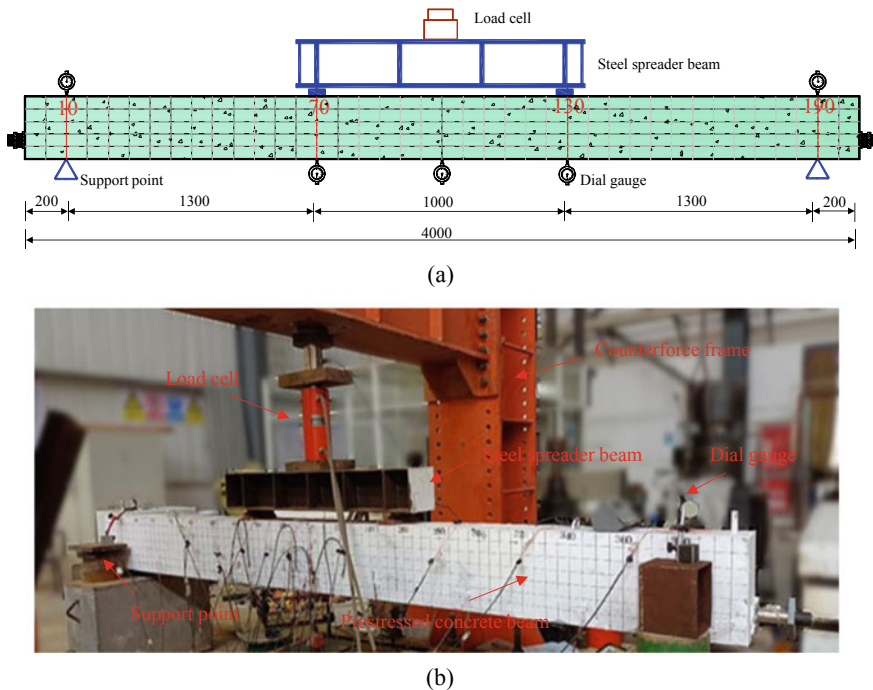
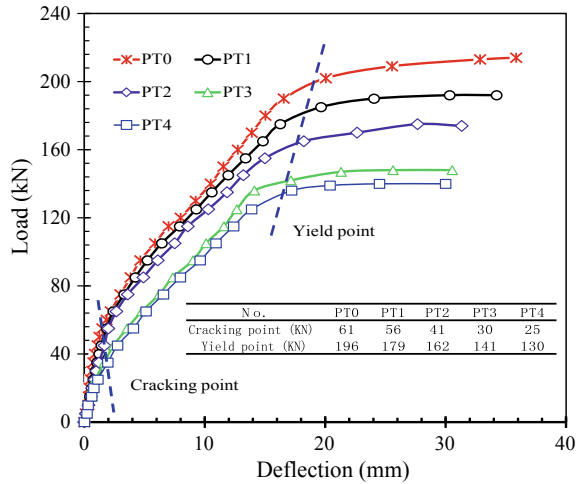


Fig. 7.5 Test loading layout (Unit: mm): a schematic diagram; b photograph

Fig. 7.6 Load–deflection curves of specimens



after yield point rapidly increases with a slight increase in the applied load. Eventually, the beam fails when the primary crack is beyond the critical width or when the concrete at the top of beam crushes.

Table 7.3 gives the cracking loads of beams. The cracking load of four PT specimens has a relation with the fracture position of strand. The cracking load of beams gradually decreases gradually as the strand fracture position moves from the anchorage region to the mid-span region. The residual prestress in PT specimens generated by secondary anchorage is computed by cracking load with Eq. (7.1), which is given in Table 7.3.

The residual prestress in PT beams is determined by the fracture position of strand. When the strand fractures in the anchorage region, the retraction force of fractured strand will be used to generate a new prestress to resist the applied load, and the prestress formed by secondary anchorage is only 13.68% lower than the initial prestress. As the fracture position of strand moves from the anchorage region to the mid-span region, the retraction force of fractured strand gradually decreases, and the corresponding prestress decreases. When the position of strand fracture is in the mid-span region, the prestress reduces by 95.38%. At this time, the prestress of

Table 7.3 Cracking load and residual prestress of the beams

Beam No	Fracture position	Cracking load (kN)	Residual prestress (kN)	Prestress loss (%)
PT0	Contrast beam	61	153.42	/
PT1	Anchor region	56	132.44	13.68
PT2	L/4 region	41	63.44	58.65
PT3	3L/8 region	30	44.94	70.71
PT4	Mid-span region	25	7.09	95.38

the beam is almost fully loss, and its crack resistance is degraded to the same as that of the comparison beam PT0.

7.4.2 Relation Between Residual Prestress and Strand Fracture Position

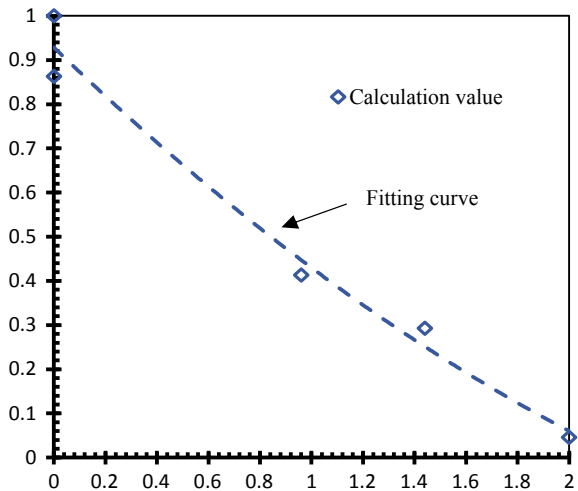
The prestress loss of PT structures caused by the fracture of strand is reflected by the ratio of residual prestress to initial prestress. Figure 7.7 shows the curve of the relation between residual prestress and fracture positions of strand. The residual prestress in PT beams, P_c , is written as

$$P_c = (0.0688L^2 - 0.5688L + 0.927)P_0, \tag{7.2}$$

where L is the distance between the fracture position of strand and the end of beam, P_0 is initial prestress in PT beams. The compatibility coefficient roughly follows the distributional pattern of the quadratic parabola, and its correlation coefficient R^2 with the parabola fitting is 0.9793.

The prestress in the cross-section varies along the anchorage length. It remains constant outside the length of secondary transfer [20, 22]. The anchorage length is defined as the minimum length required for the beam to produce an interface force to balance the retraction force of fractured strand. The first crack position of four PT specimens is beyond the transfer length. When the load at the cracking load in the current experiment is calculated, the prestress in the section is simplifies to a constant. It should be noted that the prestress in the cross-section along the length

Fig. 7.7 Relation between residual prestress and fracture position of strand



of secondary transfer becomes complicated after strand fracture, which needs to be studied further.

7.5 Numerical Model for Secondary Anchorage of Fractured Strand

7.5.1 Numerical Model Generation

A numerical model of 4000 mm × 200 mm × 350 mm with the same size of the specimens is established for predicting the transfer length and the residual prestress of secondary anchorage after strand fracture, as shown in Fig. 7.8a. The model with 25 mm meshing is used in the present research. Grout, concrete, reinforcement bars, and prestressing strand are simulated by different types of elements. The rectangular metal gaskets are placed to avoid the distortion of elements at the support, and then components are assembled. Grout and concrete are modeled with the eight-node hexahedral elements, and strand and reinforcement bar are modeled with the two nodes linear three-dimensional truss elements. The modeling of helical-shaped of strand will increase the complexity of the model and reduce the computational efficiency. Therefore, the strand shape is simplified as circular shape based on the principle of equal cross-sectional area.

The concrete damaged plasticity model proposed by Xiong et al. [33] is adopted to model the constitutive models of concrete and the grout (Fig. 7.8b, c). The stress–strain relationship ($\sigma - \varepsilon$) of tension and compression components is expressed by Eqs. (7.3) and (7.4).

$$\sigma_t = (1 - d_t)E_0(\varepsilon_t - \bar{\varepsilon}_t^{\text{ck}}) \quad (7.3)$$

$$\sigma_c = (1 - d_c)E_0(\varepsilon_c - \bar{\varepsilon}_c^{\text{pl}}), \quad (7.4)$$

where σ_t is components stresses in tension; σ_c is components stresses in compression; d_t and d_c are the damage variables of components for tension and compression; ε_t and ε_c are the strains of components in tension and compression; $\bar{\varepsilon}_t^{\text{ck}}$ is the components cracking strain; $\bar{\varepsilon}_c^{\text{pl}}$ is the equivalent plastic strain of the compression components; E_0 is the modulus of elastic of components.

The stress–strain relationship of reinforcement bars (Fig. 7.8d) adopts the bilinear constitutive model proposed by Li et al. [15], which is given in Eq. (7.5).

$$\sigma = \begin{cases} E_s \varepsilon & \varepsilon < \varepsilon_y \\ \sigma_y + 0.01 E_s (\varepsilon - \varepsilon_y) & \varepsilon \geq \varepsilon_y \end{cases}, \quad (7.5)$$

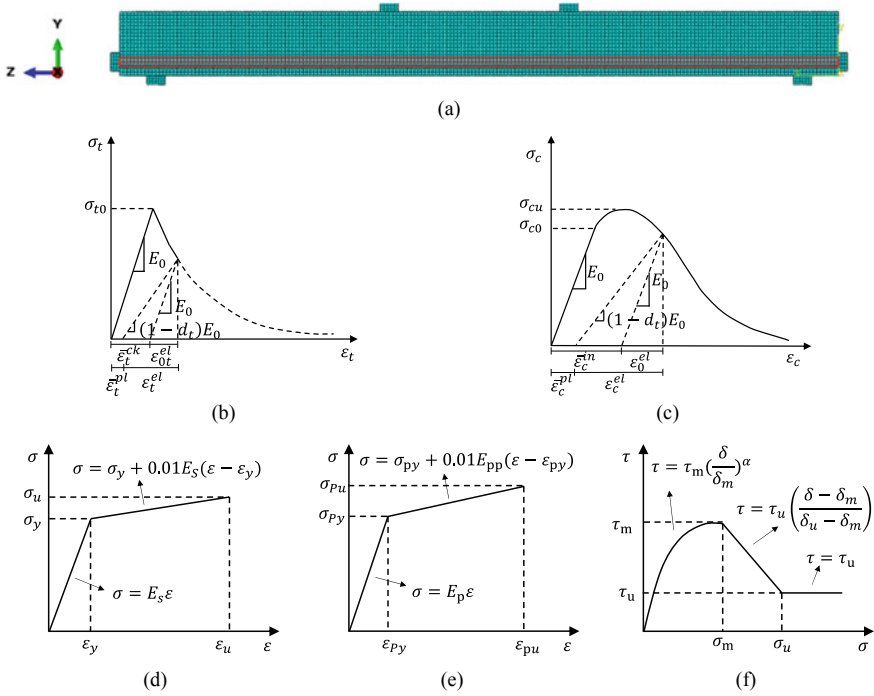


Fig. 7.8 Numerical simulation: **a** model, **b, c** uniaxial stress–strain curves of components in CDP model, **d** stress–strain of reinforcement bar, **e** stress–strain of strand, **f** bond stress–slip

where E_s is the modulus of elastic of reinforcement bars; σ_y is the yield strength of reinforcement bars; ε_y is the yield strain of reinforcement bars.

The stress–strain relationship of prestressing strand (Fig. 7.8e) adopts the bilinear constitutive model proposed by Wang et al. [30], which is given in Eq. (7.6).

$$\sigma = \begin{cases} E_p \varepsilon & \varepsilon < \varepsilon_{py} \\ \sigma_{py} + 0.01 E_{pp} (\varepsilon - \varepsilon_{py}) & \varepsilon \geq \varepsilon_{py} \end{cases}, \quad (7.6)$$

where E_p is strand modulus of elasticity; σ_{py} is the yield strength of strand; E_{pp} is the strand hardening modulus; ε_{py} is the yield strain of strand.

7.5.2 Interfacial Bond-Slip Simulation

In this model, different interfacial bond properties are assigned to the different situations. The reinforcement bar is embedded in the concrete to simplify the modeling. The strand–grout interface elements are modeled, and the interfacial bond-slip is simulated by two-node nonlinear springs, as shown in Fig. 7.9. The nonlinear spring

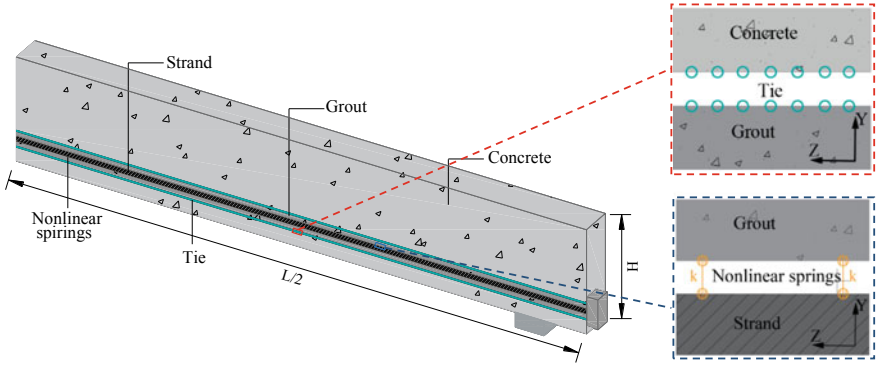


Fig. 7.9 Interaction of concrete–grout interface and grout–strand interface

consists of two nodes and each of them has one degree of freedom. The strand and the grout are attached to these two nodes. The nonlinear spring are set up at three directions x , y , and z , respectively, and the stiffness of nonlinear spring in two directions of x and y are set to infinity. This indicates that only relative movement in z directions is allowed for the two nodes of the nonlinear spring, i.e., only slippage along the strand’s longitudinal direction appears at the strand–grout interface. Assuming the interfacial bond slip only appears at the strand–grout interface, the numerical modeling is simplified by embedding reinforcement bars in concrete.

The numerical model (Fig. 7.8f) adopts the strand bond stress–slip model proposed by Wang et al. [32]. The bond stress–slip model can be split into three distinct stages: (1) nonlinear increasing stage; (2) linear decreasing stage; (3) constant residual bond stress stage, which is given in Eq. (7.7)

$$\tau = \begin{cases} \tau_m \left(\frac{\delta}{\delta_m} \right)^\alpha & 0 \leq \delta \leq \delta_m \\ \tau_m - (\tau_m - \tau_u) \left(\frac{\delta - \delta_m}{\delta_u - \delta_m} \right) & \delta_m \leq \delta \leq \delta_u \\ \tau_u & \delta_u \leq \delta \end{cases} \quad (7.7)$$

where τ_m is the maximum bond stress and its value is $1.25\sqrt{f_{ck}}$; f_{ck} is the concrete characteristic compressive stress; τ_u is the residual bond stress and its value is $0.4\tau_m$; the maximum bond stress δ_m corresponds to a slip of 3 mm, and the residual bond stress δ_u corresponds to a slip of 12 mm; α is the constant parameter and its value 0.4.

The bond stress–slip curve is split into several micro-segments. It is assumed that each micro-segment is sufficiently small, and the bond stress in each micro-segment is constant, i.e., the stiffness of spring is a constant in each micro-segment. According to the consistency between interfacial force and spring force in each micro-segment, the stiffness of spring $K(\delta_i)$ with the slip of δ_i can be obtained as shown in Eq. (7.8)

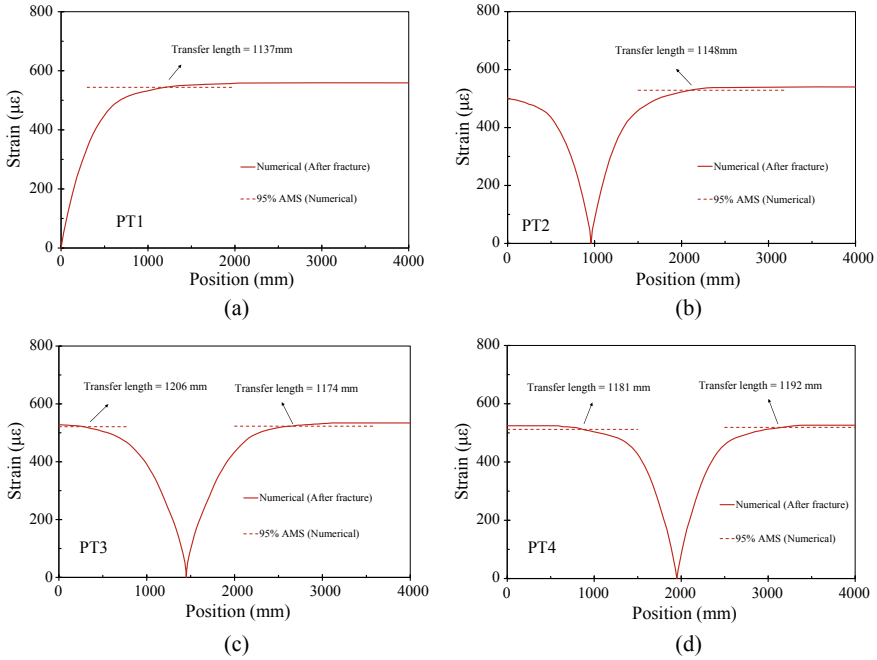


Fig. 7.10 Numerical strains and secondary transfer length

$$K(\delta_i) = \frac{\tau(\delta_i)C_p l_p}{d\delta_i}, \tag{7.8}$$

where $\tau(\delta_i)$ is the strand bond strength where the slip is δ_i ; C_p is the strand circumference; l_p is the strand length incorporated in every spring.

7.5.3 Strand Fracture Simulation

The strand under high stress is susceptible to stress corrosion. The stress corrosion may induce the brittle fracture of strand, which would alter the anchorage form of fractured strand. The new form of anchorage after strand fracture, which differs from the anchoring form of the PC structures, with one end grout bonded anchoring and the other end anchorage anchoring. The interaction of a model change in ABAQUS allows deactivation and reactivation elements to simulate partial model removal and reproduction, whether temporarily or for the remaining parts of analysis. Therefore, this model simulates the fracture of strand through the change of model interaction. The grout element is deactivated before the prestress simulation in order to avoid slippage of strand caused by prestress before the strand fracture. This model adopts

cooling method to simulate the prestress of strand. The reduction in temperature (ΔT) is written as

$$\Delta T = \frac{N_p}{\alpha E_p A_p}, \quad (7.9)$$

where N_p is the strand initial prestress; α is the thermal expansion coefficient and its value is $1.2 \times 10^{-5}/^\circ\text{C}$; E_p is the strand modulus of elasticity; A_p is the cross-sectional area of strand.

The fractured strand retracts toward the end of the specimen, which leads to slippage at the strand–grout interface. According to the bond stress–slip model of the nonlinear springs and strand, the model simulates the interfacial bond slip at the strand–grout interface. By using the above methods, the numerical model can well simulate the entire process of the secondary anchorage of fractured strand. The steps of numerical simulation for the entire process of the secondary anchorage after strand fracture are as follows:

- Step 1: Activate the numerical model elements, except grout;
- Step 2: Simulate the prestress of strand through the cooling method;
- Step 3: Reactivate the grout element to simulate the grouting process of post-tensioned concrete beam;
- Step 4: Reactivate the spring element between the prestress strand and grout to simulate the bond slip;
- Step 5: Deactivate the strand at the fracture position to realize the fracture simulation of the strand.

7.5.4 Model Validation

A comparison between the results of numerical model and the results of experiment verifies the rationality of the proposed model. Due to the strand is simulated by the two nodes linear three-dimensional truss element in this model, the strand is only subjected to interfacial force and prestress in the longitudinal direction. This causes the strand will only generate strain along the strand. Through the change of longitudinal strain of the grout in the numerical model, the length of secondary transfer after strand fracture can be indirectly obtained. Figure 7.10 shows the numerical strain curves after strand fracture.

After fracture of the strand, the strain in the fractured strand tends to be stable at a certain distance from the fracture location, apart from the strain of the left fractured strand of PT2, as shown in Fig. 7.10. This indicates that the fractured strand will be anchored in the beam by secondary anchoring. The comparison of the secondary transfer length between the experimental and the numerical calculated is given in Table 7.4. The average relative error of experiment and numerical calculation for the secondary transfer length of fractured strand is 3.5%, indicating that the numerical simulation can well predict the secondary transfer length of fractured strand.

Table 7.4 Experimental and numerical secondary transfer lengths of fractured strand

Type	PT1	PT2 (Left)	PT2 (Right)	PT3 (Left)	PT3 (Right)	PT4 (Left)	PT4 (Right)
Experimental results (mm)	1101	960	1109	1165	1133	1138	1151
Numerical results (mm)	1137	960	1148	1206	1174	1181	1192
Relative error (%)	3.3	/	3.5	3.5	3.6	3.8	3.6

The strand is only affected by the interface force and prestress, which are always along the strand. The change of stress in the direction of strand is regarded as the change of prestress in strand, which can be seen in Fig. 7.11. The longitudinal stress along the strand direction gradually increases from the fracture position of strand and finally tends to be constant outside the transfer region. The residual prestress of secondary anchorage after strand fracture can be expressed by the above constant stress. The residual prestress of fractured strand obtained by experimental measurement and numerical calculation is shown in Fig. 7.12. The results of numerical model correspond well to the results of experiment. The average relative error is 2.5%, which is acceptable when considering the variability of materials. This shows that the numerical model proposed in the current experiment can accurately predict the residual prestress of fractured strand.

The influence of different fracture positions on the residual prestress and secondary transfer length in the fractured strand was studied by using the strand at the left side of the fracture position as an example, as shown in Fig. 7.13. Once the length of fractured strand is beyond the length of secondary transfer, the secondary transfer length tends to become a constant. The fracture position of strand determines the residual prestress of fractured strand. When the length of fractured strand is smaller than the transfer length of secondary anchorage, the fractured strand cannot be entirely anchored in grout. This leads to the residual prestress in fractured strand much less than initial effective prestress. When the length of fractured strand is beyond the length of secondary transfer, the fractured strand will be completely re-anchored in concrete, and the prestress loss of fractured strand is small.

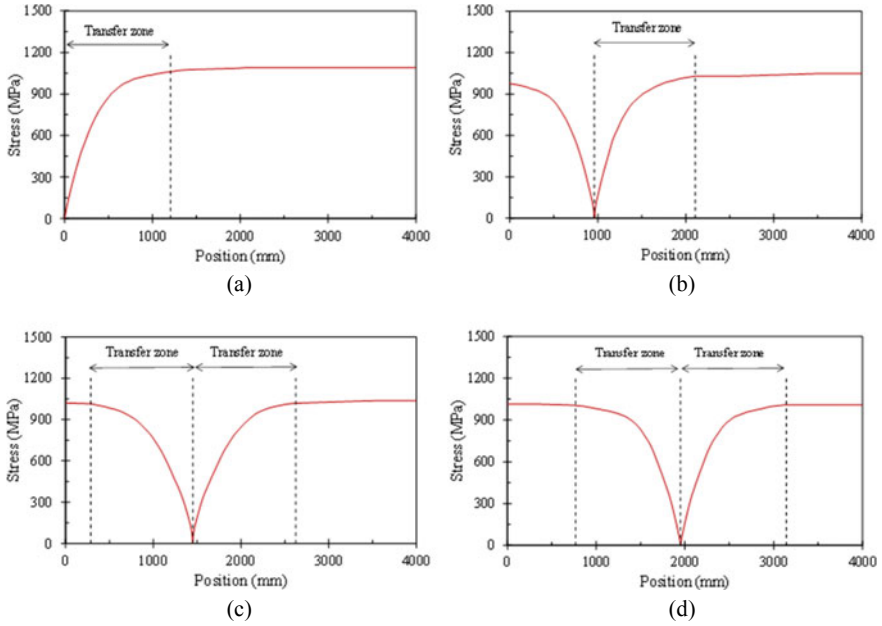


Fig. 7.11 Change of stress in the direction of strand in numerical model

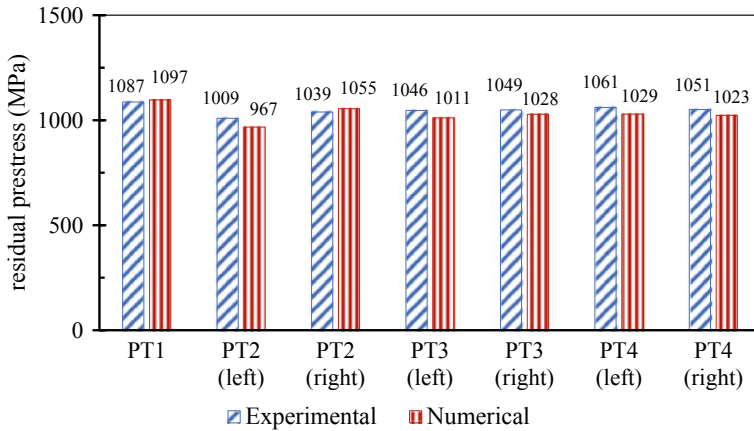


Fig. 7.12 Experimental and numerical residual prestress in fractured strand

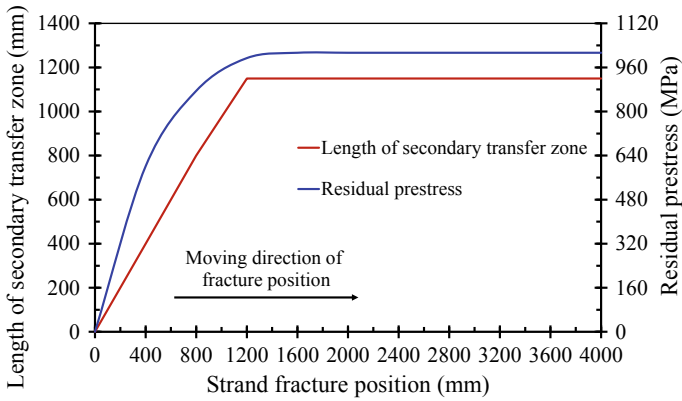


Fig. 7.13 Secondary transfer Length and residual prestress of fractured strand

7.6 Evaluation of Damage Control Section and Flexural Capacity After Strand Fracture

A calculation method is proposed to calculate the flexural capacity of PT beam after strand fracture according to the principle of the transfer of the damage control section. This method selects different damage control sections to calculate the flexural capacity in accordance with the fracture positions of strand. Some assumptions are made to simplify the calculation. (1) The prestress at fracture position of strand is completely loss. (2) The stress of the tensile and compressive bars is taken as the yield strength when the damage control section occurs in mid-span pure bending region. (3) When the damage control section occurs in fracture position of strand, the stress of tensile and compressive bars is taken as the ultimate strength and yield strength, respectively.

The calculation steps are as follows:

First, it is assumed that the damage control section occurs in the mid-span pure bending region. The flexural capacity of PT beams can be calculated as:

$$F_u = \frac{2}{L_2} \left[f_{iq} A_l h_1 + f_{sq} A_s h_2 - f_{yq} A_y h_3 - \frac{(f_{iq} A_l + f_{sq} A_s - f_{yq} A_y)^2}{2 f_{cd} b} - \frac{q L_1}{8} (4 L_2 - L_1) \right], \quad (7.10)$$

where F_u is the flexural capacity of PT beam after strand fracture; F_{iq} , F_{sq} , and F_{yq} are the yield strength of tensile bars, strand, and compressive bars, respectively; f_{cd} is the concrete compressive strength, A_s , A_s , and A_y are the cross-sectional area of tensile bars, strand, and compressive bars, respectively. h_1 , h_2 , and h_3 are the length from the top of beam section to the centers of tensile bars, strand, and compressive bars, respectively; L_1 is the length of beam; L_2 is the length between the loading

point and the support; b is the width of the beam section; q is the load concentration caused by beam weight.

Second, it is assumed that the damage control section occurs in the fracture positions of strand. The flexural capacity of PT beams can be calculated as:

$$F_u = \frac{2}{L_4} \left[f_{lu} A_l h_1 - f_{yq} A_y h_3 - \frac{(f_{lu} A_l - f_{yq} A_y)^2}{2 f_{cd} b} - \frac{q}{2} (L_1 L - L_1 L_3 - L^2) \right], \tag{7.11}$$

where f_{lu} is the ultimate strength of tensile bars. L position to the end of the beam; $L_4 = \begin{cases} L - L_3, & L < L_2 + L_3 \\ L_2, & L \geq L_2 + L_3 \end{cases}$, L_3 is the length between the support and the beam end.

Then, the F_u calculated by Eq. (7.10) is substituted into Eq. (7.11) to calculate the critical control section. When the strand fractures on the left of the critical control section, the PT beam takes the mid-span pure bending region as the damage control section to calculate the flexural capacity and the formula is Eq. (7.10). When the strand fractures on the right of the critical control section, the PT beam takes the fracture position of strand as the damage control section to calculate the flexural capacity, and the calculation formula is Eq. (7.11). Through the above steps, the flexural capacity of PT beam with different strand fracture positions can be calculated. The calculation flow chart is shown in Fig. 7.14.

The experimental results verify the accuracy of proposed calculation method. The calculated and tested flexural capacities are given in Table 7.5. The maximum

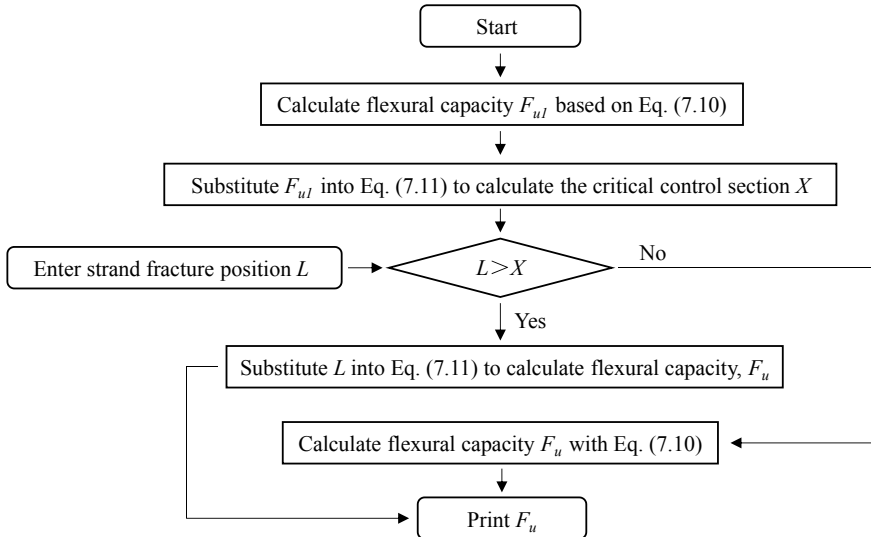


Fig. 7.14 Calculation flow chart of flexural capacity of PT beam after strand fracture

Table 7.5 Calculation data of flexural capacity of test beam

Type	PT0	PT1	PT2	PT3	PT4
Test value (kN)	214	192	175	148	140
Calculation value (kN)	202.21	202.21	202.21	148.30	142.17
Relative error (%)	5.83	5.05	13.46	0.20	1.53

relative error between the calculated flexural capacity and the tested flexural capacity is 13.46%, and the average relative error is 5.21%. This indicates that the calculation method can be used for evaluating the residual flexure capacity of PT beam after strand fracture.

7.7 Conclusions

1. The fractured strand will be anchored in the concrete by the interfacial force to form a new prestress. The transfer length of secondary anchorage in the locally corroded PT beam is 1133 mm. When the length of the fractured strand is beyond the length of secondary transfer, the prestress formed by the secondary anchorage decreases slightly compared with the initial prestress.
2. The fracture position of strand determines the residual prestress distribution of fractured strand. When the strand fractures in the anchorage region, the prestress loss is 13.68%. When the position of strand fracture moves from the anchorage region to the mid-span region, the loss of prestress increases. When the strand fractures in the mid-span region, the prestress loss can be up to 95.38%.
3. The feature of the numerical model is to use the model change interaction to simulate the fracture process of strand and the secondary anchorage of fractured strand. The prediction results indicate that the numerical model in the current study can predict accurately the residual prestress and length of secondary transfer of fractured strand.
4. A calculation method is proposed to calculate the flexural capacity of PT beam with fractured strand based on the transfer principle of damage control section. When the fracture position of strand is on the left of the critical control section, the PT beam takes the pure bending section as the failure section to calculate the flexural capacity; otherwise, the calculation of flexural capacity of PT beam should take the fractured position of strand as the damage control section.

References

1. A.O. Abdelatif, J.S. Owen, M.F. Hussein, Modelling the prestress transfer in pre-tensioned concrete elements. *Finite Elem. Anal. Des.* **94**, 47–63 (2015)
2. ACI318-14, *Building Code Requirements for Structural Concrete and Commentary* (American Concrete Institute, Farmington Hill, 2011)
3. N. Bagge, J. Nilimaa, L. Elfgren, In-situ methods to determine residual prestress forces in concrete bridges. *Eng. Struct.* **135**, 41–52 (2017)
4. S. Buchner, P. Lindsell, *Testing of Prestressed Concrete Structures During Demolition*, *Structural Assessment: The Use of Full and Large Scale Testing* (Butterworths, London, 1987), pp.46–54
5. D. Coronelli, A. Castel, N.A. Vu, R. François, Corroded post-tensioned beams with bonded tendons and wire failure. *Eng. Struct.* **31**(8), 1687–1697 (2009)
6. L. Dai, H. Bian, L. Wang, M. Potier-Ferry, J. Zhang, Prestress loss diagnostics in pretensioned concrete structures with corrosive cracking. *J. Struct. Eng.* **146**(3), 04020013 (2020)
7. L. Dai, H. Chen, L. Wang, Y. Ma, J. Zhang, Transfer length prediction in pre-tensioned concrete beams under corrosive cracking. *Struct. J.* **30**, 938–948 (2021)
8. C.N. Dang, R.W. Floyd, C.D. Murray, W.M. Hale, J.R. Martí-Vargas, Bond stress-slip model for 0.6 in. (15.2 mm) diameter strand. *ACI Struct. J.* **112**(5), 625 (2015)
9. C.N. Dang, C.D. Murray, R.W. Floyd, W.M. Hale, J.R. Martí-Vargas, Analysis of bond stress distribution for prestressing strand by Standard Test for Strand Bond. *Eng. Struct.* **72**, 152–159 (2014)
10. E. El Zghayar, K.R. Mackie, Z.B. Haber, W. Potter, Secondary anchorage in post-tensioned bridge systems. *ACI Struct. J.* **110**(4), 629–638 (2013)
11. R.W. Floyd, J.-S. Pei, J.P. Wright, Simple model for time-dependent bond transfer in pretensioned concrete using draw-in data. *Eng. Struct.* **160**, 546–553 (2018)
12. D.B. Garber, J.M. Gallardo, D.J. Deschenes, O. Bayrak, Experimental investigation of prestress losses in full-scale bridge girders. *ACI Struct. J.* **112**(5), 553–564 (2015)
13. B. Hwan Oh, E. Sung Kim, Y. Cheol Choi, Theoretical analysis of transfer lengths in pretensioned prestressed concrete members. *J. Eng. Mech.* **132**(10), 1057–1066 (2006)
14. JTG 3362-2018, *Codes for Design of Highway Reinforced Concrete and Prestressed Concrete Bridge and Culverts* (Ministry of Transport of the People's Republic of China (MOT) (2018).
15. C.Q. Li, S. Yang, M. Saafi, Numerical simulation of behavior of reinforced concrete structures considering corrosion effects on bonding. *J. Struct. Eng.* **140**(12), 04014092 (2014)
16. F. Li, Y. Yuan, C.-Q. Li, Corrosion propagation of prestressing steel strands in concrete subject to chloride attack. *Constr. Build. Mater.* **25**(10), 3878–3885 (2011)
17. Y. Liu, Y. Fan, Q. LI, Experimental study on bonding properties between corroded strands and concrete. *J. Build. Mater.* 1–13 (2020) (in Chinese)
18. Y. Mao, The low and model of corrosion of steel strands and concrete bonding performance degradation. *Chin. Overseas Architect.* **10**, 110–113 (2014). ((In Chinese))
19. J. Martí-Vargas, P. Serna-Ros, M. Fernández-Prada, P. Miguel-Sosa, C. Arbeláez, Test method for determination of the transmission and anchorage lengths in prestressed reinforcement. *Mag. Concr. Res.* **58**(1), 21–29 (2006)
20. J.R. Martí-Vargas, E. García-Taengua, P. Serna, Influence of concrete composition on anchorage bond behavior of prestressing reinforcement. *Constr. Build. Mater.* **48**, 1156–1164 (2013)
21. J.R. Martí-Vargas, W. Hale, E. García-Taengua, P. Serna, Slip distribution model along the anchorage length of prestressing strands. *Eng. Struct.* **59**, 674–685 (2014)
22. J.R. Martí-Vargas, P. Serna, W. Hale, Strand bond performance in prestressed concrete accounting for bond slip. *Eng. Struct.* **51**, 236–244 (2013)
23. J.R. Martí-Vargas, P. Serna, J. Navarro-Gregori, L. Pallarés, Bond of 13 mm prestressing steel strands in pretensioned concrete members. *Eng. Struct.* **41**, 403–412 (2012)
24. G. Morcou, A. Hatami, M. Maguire, K. Hanna, M. Tadros, Mechanical and bond properties of 18-mm-(0.7-in.-) diameter prestressing strands. *J. Mater. Civ. Eng.* **24**(6), 735–744 (2012)

25. B.H. Oh, E.S. Kim, Realistic evaluation of transfer lengths in pretensioned, prestressed concrete members. *Struct. J.* **97**(6), 821–830 (2000)
26. G.P. Osborn, P.J. Barr, D.A. Petty, M.W. Halling, T.R. Brackus, Residual prestress forces and shear capacity of salvaged prestressed concrete bridge girders. *J. Bridg. Eng.* **17**(2), 302–309 (2012)
27. B.W. Russell, N.H. Burns, Measurement of transfer lengths on pretensioned concrete elements. *J. Struct. Eng.* **123**(5), 541–549 (1997)
28. B. Šavija, M. Luković, J. Pacheco, E. Schlangen, Cracking of the concrete cover due to reinforcement corrosion: a two-dimensional lattice model study. *Constr. Build. Mater.* **44**, 626–638 (2013)
29. M. Soliman, D.M. Frangopol, Life-cycle cost evaluation of conventional and corrosion-resistant steel for bridges. *J. Bridg. Eng.* **20**(1), 06014005 (2015)
30. L. Wang, T. Li, L. Dai, W. Chen, K. Huang, Corrosion morphology and mechanical behavior of corroded prestressing strands. *J. Adv. Concr. Technol.* **18**(10), 545–557 (2020)
31. L. Wang, J. Yi, J. Zhang, R.W. Floyd, Y. Ma, Bond behavior of corroded strand in pretensioned prestressed concrete beams. *ACI Struct. J.* **115**(6) (2018)
32. L. Wang, X. Zhang, J. Zhang, J. Yi, Y. Liu, Simplified model for corrosion-induced bond degradation between steel strand and concrete. *J. Mater. Civ. Eng.* **29**(4), 04016257 (2017)
33. Q. Xiong, X. Wang, A.P. Jivkov, A 3D multi-phase meso-scale model for modelling coupling of damage and transport properties in concrete. *Cement Concr. Compos.* **109**, 103545 (2020)
34. X. Zhang, L. Wang, J. Zhang, Y. Ma, Y. Liu, Flexural behavior of bonded post-tensioned concrete beams under strand corrosion. *Nucl. Eng. Des.* **313**, 414–424 (2017)
35. S. Zhao, Z. Zhen, C. Li, R. Guo, Experimental study on bonding properties of prestressing strand in corrugated pipes. *Build. Sci.* **35**(11), 65–71 (2019). ((In Chinese))
36. Y. Zhao, X. Xu, Y. Wang, J. Dong, Characteristics of pitting corrosion in an existing reinforced concrete beam exposed to marine environment. *Constr. Build. Mater.* **234**, 117392 (2020)

Open Access This chapter is licensed under the terms of the Creative Commons Attribution 4.0 International License (<http://creativecommons.org/licenses/by/4.0/>), which permits use, sharing, adaptation, distribution and reproduction in any medium or format, as long as you give appropriate credit to the original author(s) and the source, provide a link to the Creative Commons license and indicate if changes were made.

The images or other third party material in this chapter are included in the chapter's Creative Commons license, unless indicated otherwise in a credit line to the material. If material is not included in the chapter's Creative Commons license and your intended use is not permitted by statutory regulation or exceeds the permitted use, you will need to obtain permission directly from the copyright holder.



Chapter 8

Flexural Behaviors of Corroded Post-tensioned Concrete Beams



8.1 Introduction

Post-tensioned concrete (PT) structures have high durability and are widely used in civil engineering, such as buildings and bridges. However, the deterioration affecting the service performance is identified in some existing concrete bridges [4]. The insufficient grouting or voids in the duct has been considered as one of the main causes, which was observed in the anchorage, deviator block, and mid-span region caused by improper construction [5, 12]. This defect can accelerate the corrosion loss of prestressing strand, resulting in the structural failure.

The existing research focuses on the evaluation of grouting quality and the improvement of grouting technology. In recent years, many non-destructive testing technologies for prestressed grouting have been developed, including shock echo, ground penetrating radar, ultrasonic method, visual technology, elastic wave. Wang et al. [14] used the shock echo method to conduct non-destructive testing of the grouting position of a box girder in Xiamen, China. On this basis, Zhou et al. [17] further combined wavelet transforms and neural network to detect grouting quality and accurately identified key parameters such as the location and size of grouting defects. Abraham and Cote [1] analyzed the influence of concrete slab thickness on the detection by shock echo method. In terms of grouting technology, the vacuum grouting process and some additives to change the fluidity of the slurry have been developed to improve the grouting quality [2, 11]. However, there is still a lack of systematic research on the effect of incompact grouting on the flexural performance of structures.

Some scholars have studied the flexural performance of corroded members under defect grouting. Zeng et al. [16] found that corrosion can easily cause bond failure slip between strand and concrete under defective grouting, resulting in the degradation of cracking load, flexural stiffness and bearing capacity. Minh et al. [8, 9] pointed out that the degradation of the residual prestressing force of the corroded strand in the defect grouting area is significantly faster than that in the dense grouting area. The effect of defective grouting on the flexural performance of components is ignored

in the study of Minh, and the degradation of bearing capacity is simply attributed to the effect of corrosion. The effect of defective grouting and strand corrosion on the degradation of bending capacity of components needs to be further clarified.

Some scholars have investigated the flexural behaviors of corroded prestressed concrete (PC) beams. Yu et al. [15] studied the flexural performance of post-tensioned bonded partially PC beams after corrosion of strand in the mid-span by electrochemical method. The study pointed out that the corrosion leads to the degradation of the ductility of the components, decreases the number of cracks, and increases the crack spacing. Rinaldi et al. [10] found that the corrosion failure mode of pretensioned prestressed concrete beams changed from concrete crushing failure to strand fracture failure, and the bearing capacity degraded significantly. Li and Yuan [7] pointed out that when the corrosion degree is small (less than 2.87%), the effect of strand corrosion on the cracking moment, ultimate moment of the component is not significant, but it leads to the broken of wires and significantly reduces the ultimate deflection of the beam.

In addition, some scholars have studied the flexural properties of corroded bridges. Zhu et al. [18] conducted a static load test on the beam of a railway bridge after severe corrosion of prestressed steel wire bundles and found that the corrosion reduces the stiffness of the beam, resulting in an increase of about 15% in the mid-span deflection of specimens. Harries et al. [6] dismantled the bridge of the Lake View highway in the USA, pointed out that the fracture of the steel strand is the main damage, and found that minor corrosion had little effect on the flexural capacity of members, but increased the risk of brittle failure. In the existing research, the corrosion loss of components is relatively low and relatively concentrated. However, the strand under high stress usually has a fast corrosion loss, and once they are corroded, it is very likely to be very serious, and even fracture. The bending resistance of components under different corrosion loss, especially at higher corrosion loss, needs to be further clarified.

The chapter is organized as follows. First, the experimental design including material property, grouting condition, accelerated corrosion, and loading test is introduced. Next, insufficient grouting-induced flexural behavior degradation of post-tensioned concrete beams is discussed. Following this, the influence of strand corrosion in insufficient grouting on beam's flexural behavior is analyzed. The effect of strand corrosion in full grouting on flexural behaviors is presented.

8.2 Design of Specimens with Different Defects

In this experiment, 20 PT beams were designed to analyze the effect of grouting defects, strand corrosion in insufficient grouting, and strand corrosion in full grouting on the flexural performance of PT specimens. Among them, specimens under insufficient grouting referred to as D series, numbered as D1-D5; specimens under insufficient grouting with strand corrosion referred to as PD series, numbered as PD1-PD8;

specimens under full grouting with strand corrosion referred to as PE series, numbers as PE1-PE7.

All PT beams adopt the same section size and reinforcement form: $b \times h = 150 \text{ mm} \times 220 \text{ mm}$, 2000 mm in total length. Two HPB235 plain bars with a diameter of 8 mm are arranged at the bottom, two HRB335 deformed bars with a diameter of 12 mm are arranged on the top, the diameter of the stirrups is 8 mm, and the spacing is 90 mm. A 7-wire steel strand was arranged in the beam, and its diameter was 15.2 mm. During the casting process, a duct with the diameter of 32 mm was reserved inside each beam to arrange strand. The details of the specimen are shown in Fig. 8.1.

The mechanical behaviors of prestressing strands and steel bars are given in Table 8.1. The initial tensile strength of strand is 75% of the ultimate strength, i.e., 1395 MPa. The concrete mixture has a weight ratio of cement, coarse aggregate, fine aggregate, and water as 1: 4.65: 2.11: 0.45. The compressive strengths of concrete after 28-day are given in Table 8.2.

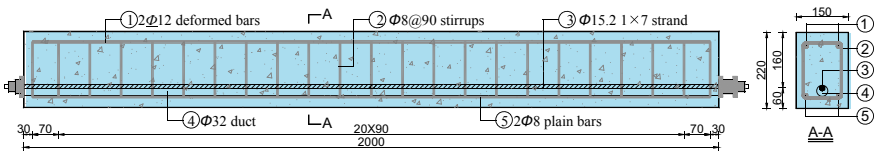


Fig. 8.1 Beam details (Unit: mm)

Table 8.1 Mechanical properties of steel bar and strand

Type	Diameter (mm)	Yield strength (MPa)	Elastic modulus (GPa)
Strand	15.2	1830	195
Ribbed steel bars (HPB335)	12	335	210
Round steel bars (HRB235)	8	235	210

Table 8.2 Compressive strength of concrete after 28-day

No.	Specimen1 (MPa)	Specimen2 (MPa)	Specimen3 (MPa)	Concrete strength f_c (MPa)
D1, D2, D3, D4	32.67	33.60	36.09	34.12
D5, PE7, PD7, PD8	34.60	31.54	36.70	34.28
PD1, PD2, PD3, PD4	32.44	33.07	29.95	31.82
PD5, PD6, PE5, PE6	33.04	32.60	31.40	32.35
PE1, PE2, PE3, PE4	32.60	33.41	35.11	33.71

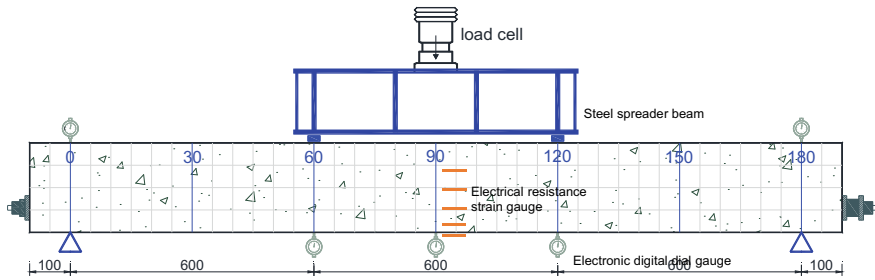


Fig. 8.2 Diagram of loading test (Unit: mm)

All the beams were simply supported over a span of 1800 mm and subjected to four-point loads applied symmetrically with a spacing of 600 mm for a bending test. The shear length was equal to the one-third of total span length. A view of the loading test setup is shown in Fig. 8.2.

The specimens were loaded through the control load. Loads 5 kN per step for uncorroded and lightly corroded specimens, and 2kN per step for severely corroded specimens. After reaching the ultimate load, the loading test is controlled by deflection, 2 mm per step, until the failure crack width or failure deflection of beams.

Five electronic digital dial gauges were used to test the vertical deflections at the mid-span, support settlements, and loading points. The concrete strains were measured through the electrical resistance strain gauges attached on the midspan section. Figure 8.2 shows the specific arrangement of strain gauges and dial gauges. Before the loading test, the surface of the specimens is painted white and divided by a 5.5×5 cm grids to facilitate the observation of the crack distribution and development.

8.3 Effect of Insufficient Grouting on Flexural Behaviors

8.3.1 Design of Insufficient Grouting

Group D consists of five beams with different grouting conditions: full grouting (FG) for D1 as the control beam, no grouting (UG) for D2, grouting in the half cross-section of duct (GHC) for D3, no grouting in the half span (UGHC) for D4, no grouting in central region (NGC) for D5. Figure 8.3 shows the specific grouting conditions and dimensions.

In the current experiment, two plugs placed in the duct are used to control the lengths and locations of the insufficient grouting. The grout was designed with high fluidity and mixed by cement, water and additive to ensure it could flow along duct by gravity. The channels were reserved at the end of specimens for ensuring that the

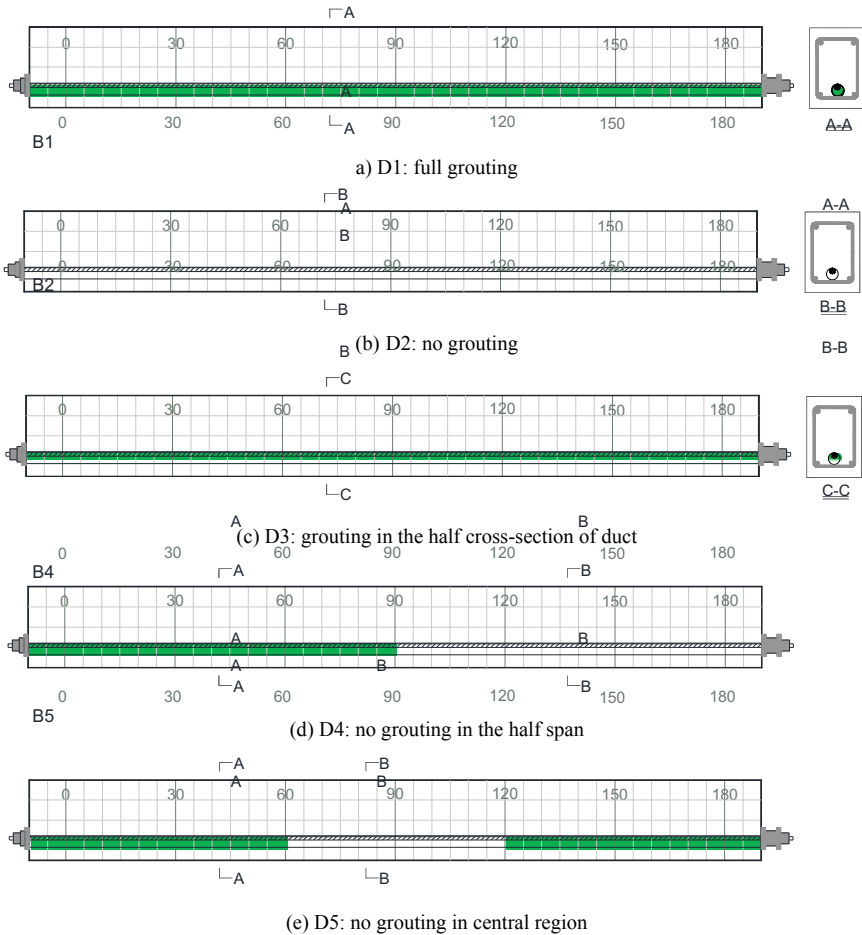


Fig. 8.3 Grouting conditions of group D (Unit: cm)

grout can be injected into duct after the prestress tensioning of strand. The void in D3 was grouted in the half cross-section of duct, which was generated by controlling the grout volume used in duct. After the beam failure, the construction quality of insufficient grouting was verified by manual observation. As shown in Fig. 8.4, the grouting situations containing no grouting, full grouting, and grouting in the half cross-section of duct for specimens agree with the original design.

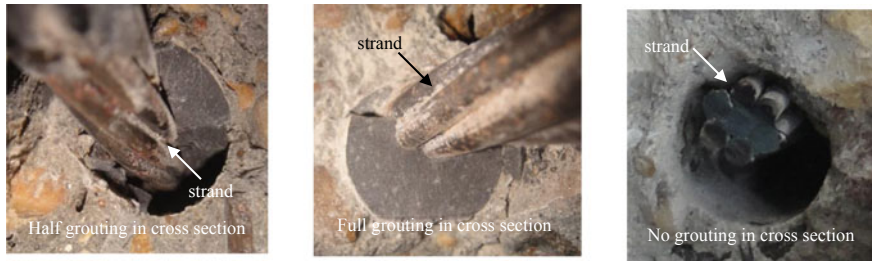


Fig. 8.4 Grouting conditions of beams

8.3.2 Cracking Behavior

Statistical analysis of the cracking loads, number of cracks, average crack spacing, and maximum crack width for all tested beams of group D are performed and given in Table 8.3. First, the influence of defect grouting conditions on cracking load is discussed. Compared with the control beam D1, the cracking loads of D3 and D5 are basically unchanged, and the cracking loads of D2 and D4 are reduced to a certain extent. Experimental data indicates that the case of no grouting within the pure-flexural spans and grouting in the half cross-section of duct does not lead to a reduction in the cracking load. However, no grouting or no grouting in the half span have a great influence on the cracking load, which will lead to the early cracking of the test beam.

As given in Table 8.3, except that the number of cracks and the spacing in the D3 beam are close to the baseline D1, the distribution and propagation of cracks in other defective grouting beams have changed to varying degrees. Compared with D1, the average crack spacing of D2, D4, and D5 increased by 34%, 8%, and 43%, respectively, and the crack number decreased by 29%, 14%, and 14%, respectively. Defect grouting resulted in a decrease in the number of cracks and an increase in the average crack spacing. The ultimate crack caps of the D series are shown in Fig. 8.5.

Table 8.3 Statistic cracks in group D

Beam No.	Grouting type	Crack load (kN)	Number of cracks	Number of crack reduction (%)	Average crack spacing (cm)	Spacing increase (%)	Maximum crack width (mm)	Width increase (%)
D1	FG	60	7	NA	12.2	NA	0.73	NA
D2	UG	50	5	29	16.3	34	1.98	171
D3	GHC	60	7	0	12.8	5	0.91	25
D4	UGHC	58	6	14	13.2	8	1.51	106
D5	NGC	60	6	14	17.4	43	1.56	114

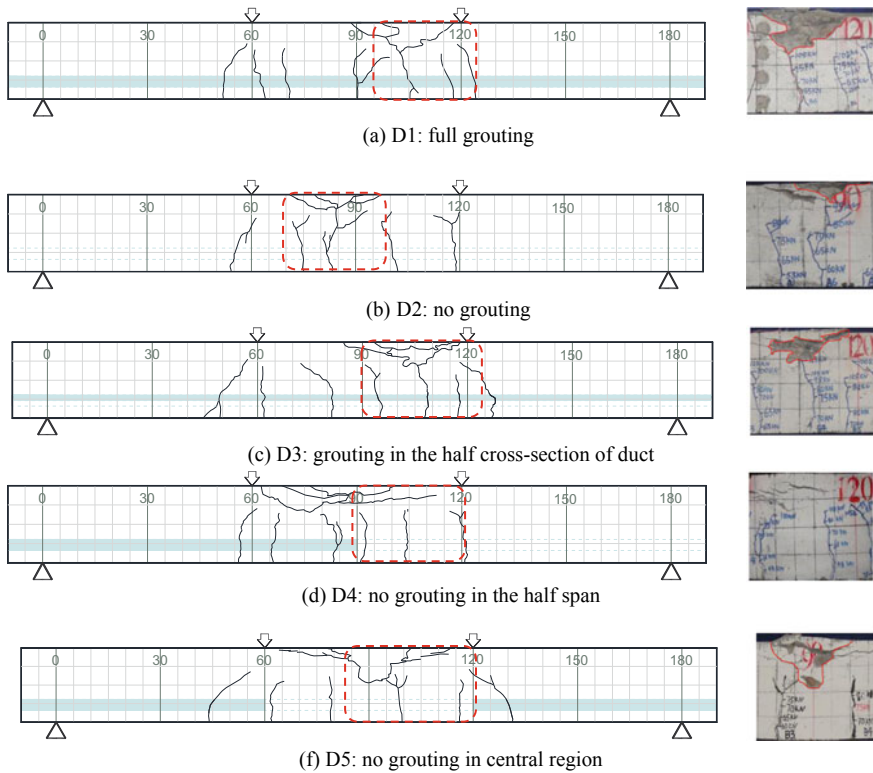


Fig. 8.5 Crack caps in group D

The difference of crack distribution can be attributed to the failure of the bond between the strand and the concrete due to no grouting. After beam cracking, concrete cracking causes tensile strain energy loss, and further reduces the energy loss of the effective bond. In other words, the tensile strain still exists in the cracking region with the effect bond, and a small load increment will likely generate new cracks. For the beam D3, grouting in the half cross-section of duct can still provide effective bond between strand and concrete, so D3 and baseline D1 have the similar cracks distribution. On the contrary, in the beams D2, D4, and D5, the defective grouting causes the degradation or failure of the bond. The residual tensile strain is small, and new cracks are not easy to appear around the cracks, resulting in fewer cracks and larger spacing in the specimen.

The influence of local no grouting on cracks distribution also depends on its length and location. D2 has the longest ungrouted section, it has the smallest number of cracks and the largest crack spacing. It can be seen that the distribution of crack becomes more pronounced as the ungrouted section gets longer. The ungrouted duct in D4 is within shear-flexural spans and its length is 100 cm, and it is within pure-flexural spans and 60 cm long for D5. D4 and D5 have the same crack number, but

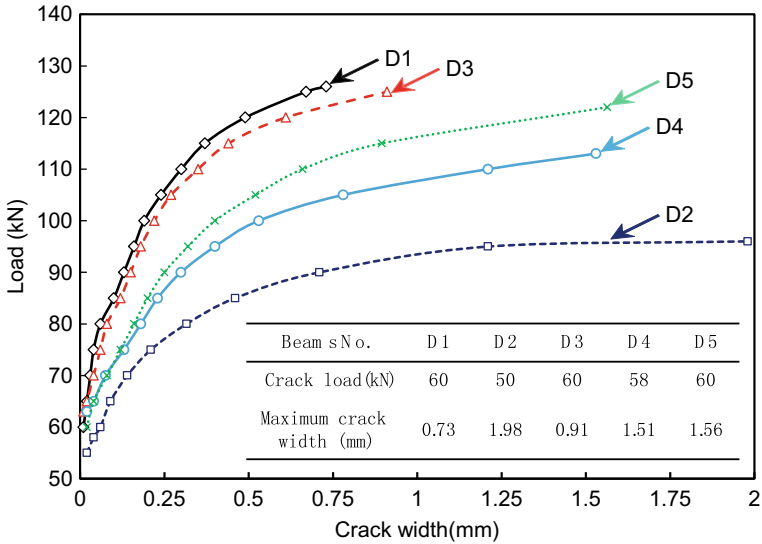


Fig. 8.6 Load-crack width curves in group D

the average spacing of cracks in D5 is significantly larger than that in D4. The effect of pure-flexural spans defect grouting on crack distribution is greater than that of shear-flexural spans defect grouting.

Following the cracking load, crack propagation was observed as the load increased. The main crack is the longest and widest crack. The load-main crack width curve for group D is shown in Fig. 8.6.

As can be seen in Fig. 8.6, the crack width expansion is fastest in D2 followed by that in D4 and D5. Compared with the baseline D1, the maximum crack widths of D2, D4, and D5 are increased by 171%, 106%, and 114%, respectively. For D3, its load-crack width curve is like D1. This is also because the beam B3 can still provide effective bond between the strand and the concrete, so its crack distribution and main crack expansion are like B1.

D4 and D5 have different localized non-grouting locations. The main crack width growth rate of the B4 is significantly faster than that of the B5. Under the same load, the main crack width of B4 is also larger than that of B5. This indicates that the influence of no grouting within shear-flexural span on the main crack propagation is greater than that in the pure-flexural span without grouting.

8.3.3 Load–Deflection Response

The following analysis uses the maximum mid-span displacement to reflect the deflection of the specimen. Figure 8.7 indicates the typical load–deflection curves

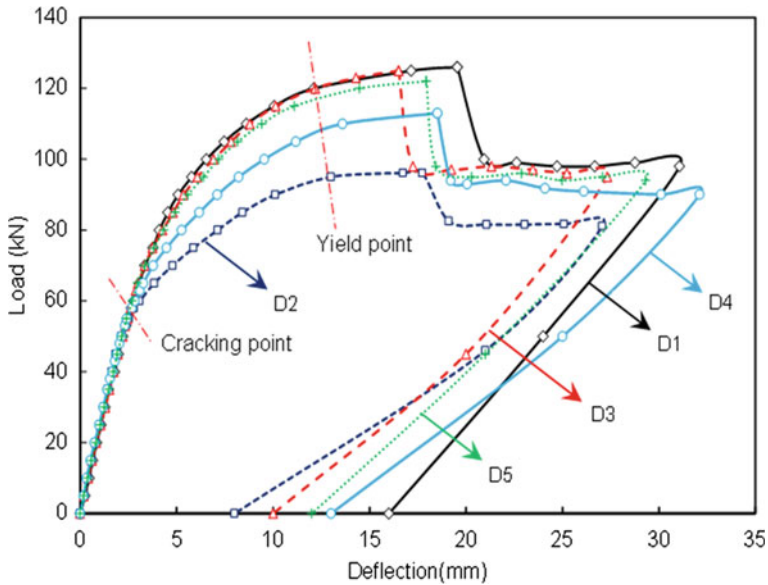


Fig. 8.7 Load–deflection curves for group D

of group D. There are two distinct points in the load-span deflection curve for each beam: cracking point and yield point. The load–deflection curve is divided into three distinct phases by these two points. The effect of defective grouting on each phase is discussed separately below.

Before the cracking load, each specimen is under the elastic deformation stage and the load–deflection curves is similar. This indicates that the influence of defective grouting on the stiffness of specimen at this stage is negligible. This is because the stiffness of the specimen before cracking is basically controlled by the concrete section, and the section loss caused by defect grouting has a little influence on beam stiffness.

Between cracking and yield loads, the bending stiffness of each beam was reduced to some extent. The stiffness of D3 and D5 is basically the same as that of D1, while the decrease of stiffness of D2 and D4 is significantly larger than that of D1. This shows that the ungrouted duct in pure bending regions and the grouting in the half cross-section of duct have little effect on the stiffness after concrete cracking. No grouting and no grouting in the half span have a greater impact on the stiffness after cracking.

After the yield load, all load–deflection curves were essentially close to horizontal, which means that a little increase of load will cause a significant deflection of beams. Then, the concrete crushing with an abrupt drop in the load–deflection curves induces a reduction in bearing capacity, as shown in Fig. 8.7.

8.3.4 Ultimate Strength and Failure Mode

The ductility of a concrete beam is generally defined as its ability to withstand deformation after yielding and before failure. The ductility can be reflected by deflection ductility factor (u) for concrete beams. The deflection ductility factor is defined as the ratio of the ultimate deflection (Δ_u) to the yield deflection (Δ_y) of beams at the mid-span. The ultimate deflection, yield deflection, and their deflection ductility factor of each beam at the mid-span are listed in Table 8.4.

The deflection ductility factor of the baseline D1 with full grouting is largest. Compared with D1, the other defect grouted test beams D2, D3, D4, and D5 decreased by 20.0%, 15.5%, 15.5%, and 17.4%, respectively. This indicates that defective grouting can degrade the ductility of concrete beams.

The failure mode of group D is the same. The strand failed first as the load increased, followed by the crushing of the concrete in the compression zone and the test beam was failed. Figure 8.5 shows the pattern of concrete crushing in group D. Defective grouting has little effect on the failure model of the beam, but results in a reduction in the height of the concrete crushing zone. Additionally, when the beam was unloaded after reaching its ultimate state, it was found that the beam immediately recovered some deflection and some cracks closed.

Table 8.4 shows the ultimate flexural capacity of beams in group D. The ultimate strengths between the baseline D1, D3, and D5 differed insignificantly. This shows that grouting in the half cross-section of duct and no grouting with pure-flexural span have little influence on the flexural capacity. Compared with D1, the ultimate strengths of beams D2 and D4 decreased by 23.8% and 10.3%, respectively. Therefore, it is easy to see that no grouting and no grouting in the half span has a large effect on the degradation of ultimate strength. Summary, the effect of defect grouting on the flexural behavior of specimen depends on its location and length, also determined by its ability to provide the effective bond strength and the good strain compatibility between concrete and strand.

Table 8.4 Summary of experimental results

No.	D1	D2	D3	D4	D5
Yield load (kN)	120	95	120	110	120
Ultimate load (kN)	126	96	125	113	122
Δ_y (mm)	12.12	12.99	12.18	13.60	13.48
Δ_u (mm)	19.55	16.73	16.51	18.51	17.95
u	1.61	1.29	1.36	1.36	1.33

Note Δ_y is the mid-span deflection in yield stage; Δ_u is the mid-span deflection in ultimate stage; u is the ratio of Δ_u and Δ_y

8.4 Effect of Strand Corrosion in Insufficient Grouting on Flexural Behaviors

Defective grouting causes harmful substances, such as chloride ions, water, and oxygen, to easily reach the strand surface after passing through the concrete cover, thereby causing corrosion of the strand. In this section, the deterioration of flexural behavior in ungrouted ducts due to the strand corrosion is investigated by PD group. The detailed grouting conditions of beams for the PD group are shown in Fig. 8.8.

8.4.1 Corrosion Characteristic of Strand

The area loss of strand in PD group was obtained by the artificial accelerated corrosion. A specially designed corrosion tank was installed in the defect grouting area of the beam, and a 5% brine solution was injected into the corrosion tank to connect the components into a current loop. During the corrosion process, the current starts from the positive pole of the power supply, flows through the corroded strand, the brine solution, the stainless-steel plate, and then returns to the negative pole of the power supply. Figure 8.9 is a physical view of the accelerated corrosion system.

During the corrosion process, the external current is stable at around 0.1 A. The current density is to be 0.0009 mA/mm². During the corrosion process, it was found that the corrosion current that could be applied to the test beam was very small, and it was far less than the ordinary reinforced concrete structure. This may be due to the smooth surface form manufacturing of strand. The passive film is easy to form around strand, and chloride is difficult to initiate extensive corrosion [3]. The corrosion of strand is mainly concentrated on the spare cells and shows the distinct

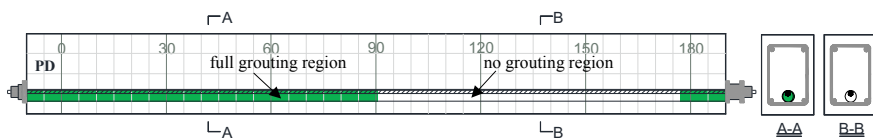


Fig. 8.8 Grouting conditions of group PD (Unit: cm)

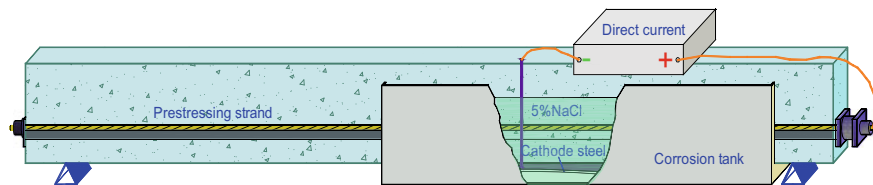


Fig. 8.9 Accelerated corrosion process

pitting characteristic. It is easy to reach the surface of prestressed strand without grouting after the saline solution penetrating into duct. In the experiment testing, it was found that the maximum cross-sectional loss of strand was approximately 3–10 times the corrosion loss calculated by Faraday’s law. Therefore, an empirical coefficient about 1/10–1/3 in the present experiment was multiplied to the theoretical time to evaluate corrosion time. The corrosion time and the maximum corrosion loss can be seen in Table 8.5.

The concrete surface of the beam was observed after the corrosion, and corrosion-induced cracks were found on the bottom surface of beams PD1-PD4, as shown in Fig. 8.10. The movement of corrosive liquid along interstitial gaps can lead to the extension strand corrosion in the longitudinal direction. Figure 8.10 shows the corrosion-induced cracking on the full grouting region in PD1-PD4, where l is the length of the corrosive crack and $w_{c,max}$ is the maximum width of the corrosive crack. Therefore, the insufficient grouting not only easily leads to the corrosion of strand in the defect region, but also reduces the ability on strand inside the sufficient grouting region to resist corrosion.

Some corrosion-induced cracks occurred on the fully grouted side of PD1-PD4 after corrosion, as shown in Fig. 8.10. PD1-PD4 corrosive cracks were 109 cm, 115 cm, 44 cm, and 51 cm in length and 0.4 mm, 0.64 mm, 0.06 mm, and 0.08 mm

Table 8.5 Corrosion time and the maximum corrosion loss in group PD

Beams	PD8	PD3	PD4	PD7	PD6	PD5	PD1	PD2
Corrosion time (d)	1	6	10	13	18	23	34	45
Maximum corrosion level η (%)	1.28	6.35	9.82	35.89	48.04	55.10	77.90	100.00

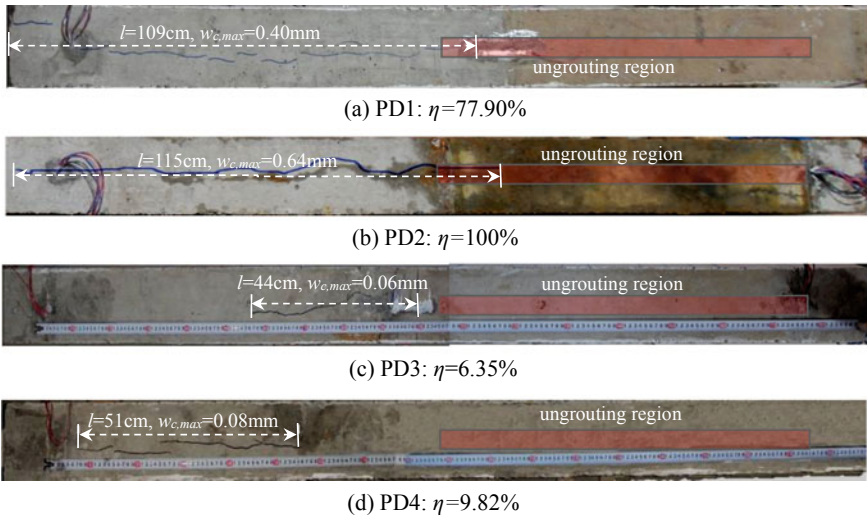


Fig. 8.10 Corrosion-induced cracking

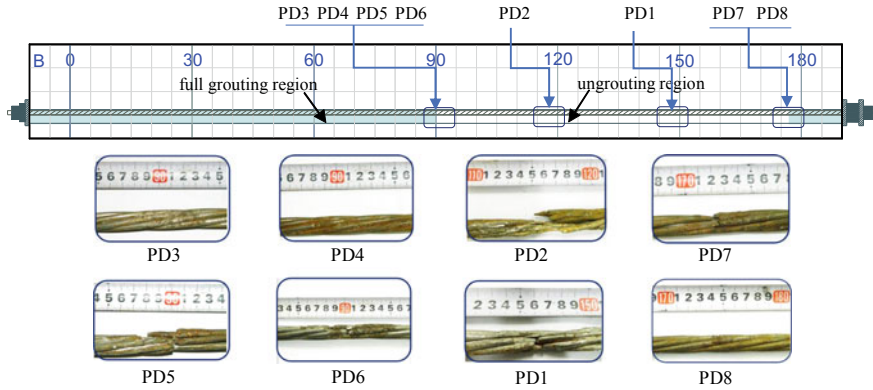


Fig. 8.11 Location and characteristic of the maximum corrosion loss in group PD

in maximum width, respectively. The corrosion-induced cracking in insufficient grouting region is more significant than that in fully grouted region. After the specimens were loaded, the concrete cover was knocked out to observe the corrosion of strands. The corrosion of strands in concrete beams under defective grouting has obvious pitting corrosion characteristics. The corrosion pits are mainly concentrated in the ungrouted area. The corrosion loss of strand in the PD group is shown in Fig. 8.11.

The strand is taken out and its corrosion loss is measured. The corrosion loss of the beam is given in Table 8.5. In this test, the corrosion loss of the control beam PD8 was 1.28%, and the maximum corrosion loss of other beams was 100%. In the following, the influence of corrosion of strand under defective grouting on the flexural performance of concrete beams will be discussed from the aspects of crack behavior, flexural deformation, failure modes, and ultimate load of group PD.

8.4.2 Cracking Behavior

The difference between the corrosion loss and cracking load can be reflected with the cracking load ratio of the other corrosion beam to the control beam PD8. The cracking load of a prestressed concrete structure is closely related to the effective prestress of the strand, and corrosion of the strand inevitably causes a loss of prestress and thus affects the cracking load. The cracking loads of the PD group are given in Table 8.6, and the relationship between the cracking load ratio and the corrosion loss is shown in Fig. 8.12.

As Fig. 8.12 shows, the cracking load ratio decreases with increasing corrosion level. The cracking load ratio $\eta_c(\rho)$ under different corrosion degree can be expressed as follows:

Table 8.6 Statistics of cracks in group PD

Beam No.	Corrosion loss (%)	Cracking load	Number of crack	Number of crack reduction (%)	Average spacing (cm)	Spacing increase (%)	Maximum crack width (mm)	Width increase (%)
D4	0	58	6	NA	13.2	NA	1.51	NA
PD8	1.28	60	9	-50	9.3	-30	0.75	-50
PD3	6.35	45	8	-33	9.6	-20	0.91	-40
PD4	9.82	40	9	-50	10.0	-24	1.32	-13
PD7	35.89	35	5	17	16.0	21	1.49	-1
PD6	48.04	35	5	17	13.3	1	1.76	17
PD5	55.10	25	3	50	18.0	36	2.50	66
PD1	77.90	15	3	50	18.5	40	3.48	130
PD2	100	10	3	50	10.0	24	3.70	145

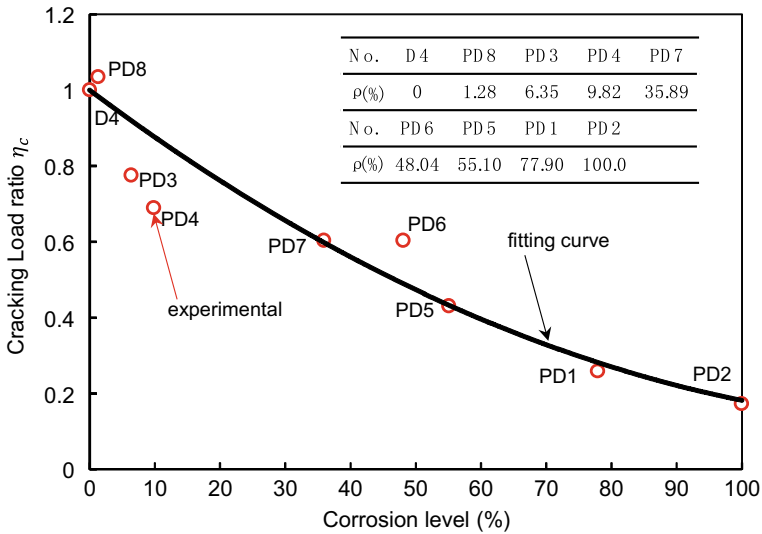


Fig. 8.12 Cracking loads of group PD

$$\eta_c(\rho) = 0.4672\rho^2 - 1.2855\rho + 1, \tag{8.1}$$

where ρ is the corrosion loss of strand. The cracking load ratio roughly follow the distributional pattern of the quadratic parabola, and its correlation coefficient R^2 with the parabola fitting is 0.8983.

The prestress loss caused by corrosion also alter the distribution of cracks. Figure 8.13 shows the crack distribution for the group PD. Combining the statistical data in Table 8.6, it can be found that different corrosion degrees have different effects on the distribution of cracks in concrete beams.

For the beam PD8, PD3, and PD4 with corrosion loss below 10%, the number of cracks is larger, the crack spacing is less, and its distribution is more uniform. This suggests that slight strand corrosion is beneficial to the development of cracks in concrete beams, resulting in an increase in the number of cracks and a reduction in spacing, which in turn slows the formation of main cracks.

With the increase of the corrosion degree, the crack distribution of beams become extremely uneven. The number of cracks decreases and the spacing increases, as shown in Fig. 8.13e–i. Additionally, the cracks are mainly concentrated in the ungrouted region of the corroded beam, which is due to the flexural stiffness in fully grouted region is greater than that in ungrouted region.

The widest crack was selected as the main crack, and its change under the different corrosion degrees was analyzed. Figure 8.14 shows the load–crack width curves of the group PD. In the present experiment, it can be observed that the strand corrosion of 10% seems to be a critical value. For the beams PD8, PD3, and PD4 with a corrosion loss of less than 10%, the propagation rates of their main cracks are basically the same, and the width of the main cracks grows very slowly after the appearance of the main cracks. However, for the beams PD7, PD6, PD5, PD1, and PD2 with high corrosion loss, its width increases rapidly once the main crack appears, and the beams have a very wide main cracks under the ultimate state. It can be seen from Table 8.6 that compared with the control beam PD8, the ultimate main crack widths of the beams PD7, PD6, PD5, PD1, and PD2 increase by 99%, 135%, 233%, 364%, and 393%, respectively. This is due to the reduction in the number of cracks, and fewer cracks must expand rapidly to meet the needs of structural deformation.

8.4.3 Load–Deflection Response

Figure 8.15 shows the load–deflection curves in group PD. Before the cracking load, all the load–deflection curves of specimens were basically coincident. This indicates that the beams have the same initial bending stiffness, and the corrosion of the prestressing strands has little effect on initial bending stiffness. After concrete cracking, the load–deflection curves of the beams are quite different, and the stiffness of the beams after cracking shows different variation laws with the different corrosion losses.

For the beams PD3 and PD4 with a corrosion loss of less than 10%, the flexural stiffness after cracking gradually decreases with the increase of the load, which is very close to the control beam PD8. This indicates that slight corrosion of strands has little effect on the flexural stiffness of beams after concrete cracking. For other heavily corroded beams, the flexural stiffness after cracking degrades very rapidly, especially for beam PD1, whose flexural stiffness directly degrades from a higher

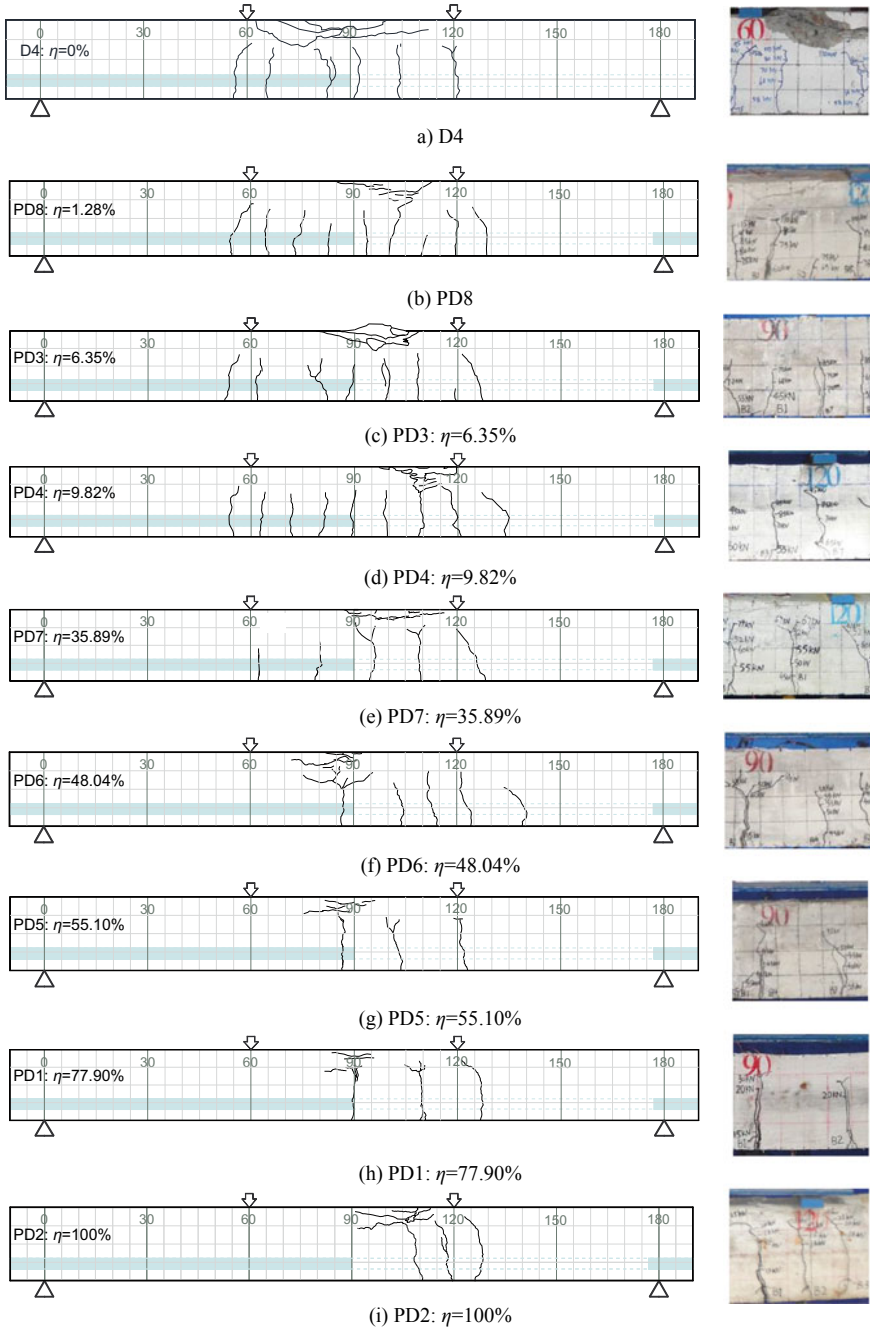


Fig. 8.13 Crack pattern in group PD

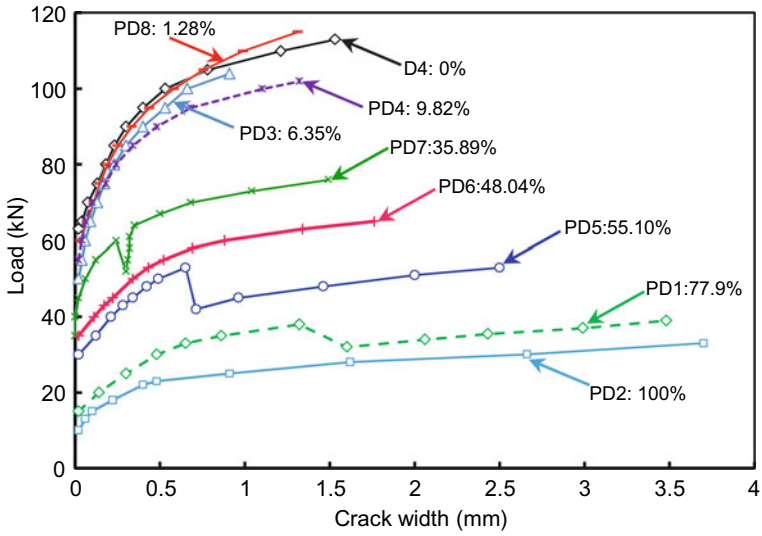


Fig. 8.14 Load-crack development in group PD

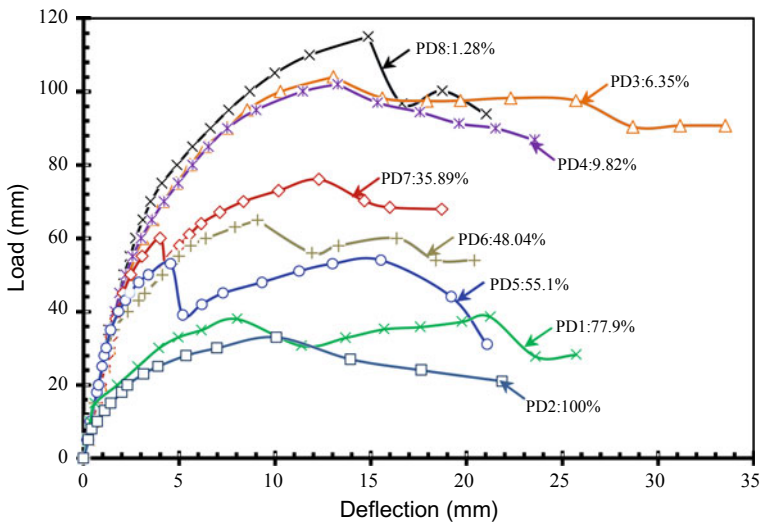


Fig. 8.15 Load-deflection curves in group PD

value before cracking to a smaller value after cracking. The severe corrosion of strands leads to a rapid decrease in the stiffness of concrete beams after cracking. In addition, for the heavily corroded test beam, the fracture of the strand wires during loading can cause a sudden decline in its load-deflection curve.

8.4.4 Failure Mode and Ultimate Strength

The failure modes of PD group changed gradually with the increase of corrosion loss. For PD8, PD3, and PD4 with a corrosion loss of less than 10%, the damage is caused by the concrete crushing in the compression zone. For other heavily corroded beams (>10%), the failures were the wire rupture accompanied with a sharp sound, and a sudden decrease of bearing capacity. Then, the main cracks deeply propagate into the compressive zone and the height of compressive concrete is reduced (see Fig. 8.13). Finally, the heavily corroded beams failed like reinforcement concrete beams as concrete crushing. In summary, the beam failure modes change from the concrete crushing to the rupture of corroded wires as the increase of strand corrosion levels.

The deflection ductility factor is employed to further investigate the ductility of beams. The load–deflection curve of PD group is slightly different from that of B group due to the corrosion. The load–deflection curve of each beam has no obvious yielding state. Some study have pointed out that the deflection at 0.75 times of ultimate strength can be used as the yield deformation [19]. The mid-deflection at ultimate state (Δ_u) and that at yielding state (Δ_y) and their ductility factors of specimens are given in Table 8.7.

Table 8.7 shows the ultimate strengths of beams in the group PD. The ultimate strength of the control beam PD8 is 115 kN. The ultimate strengths of lightly corroded beams PD3 and PD4 are 105 kN and 102 kN, respectively, which are 9.6% and 11.3% lower than the control beam, respectively. For the severely corroded beams PD7, PD6, PD5, and PD1, the ultimate strengths were 76kN, 65kN, 53kN, and 38kN, respectively, which are 33.9%, 43.5%, 53.0%, and 67.0% lower than the control beam, respectively. For the PD2 with 100% of corrosion loss, its ultimate strength is reduced by 71.3%. Therefore, it can be concluded that the severe corrosion causes the remarkable decrease of the ultimate strength of beams. Figure 8.16 shows the relationship between the ratio of the ultimate strength of other beams and the control beam as a function of corrosion loss.

As Fig. 8.16 shows, the ultimate strength gradually decreases with the increase of strand corrosion loss. The ultimate strength ratio of corroded beams to control beam can be expressed as follows

Table 8.7 Summary of group PD

No.	PD8	PD3	PD4	PD7	PD6	PD5	PD1	PD2
Corrosion loss ρ (%)	1.28	6.35	9.82	35.89	48.04	55.10	77.90	100.00
Ultimate load (kN)	115	105	102	76	65	53	38	33
Δ_y (mm)	5.93	5.29	5.17	5.01	3.88	1.63	3.60	3.79
Δ_u (mm)	14.86	13.06	13.28	12.28	9.08	3.38	8.03	10.06
u	2.51	2.47	2.57	2.45	2.34	2.08	2.23	2.65

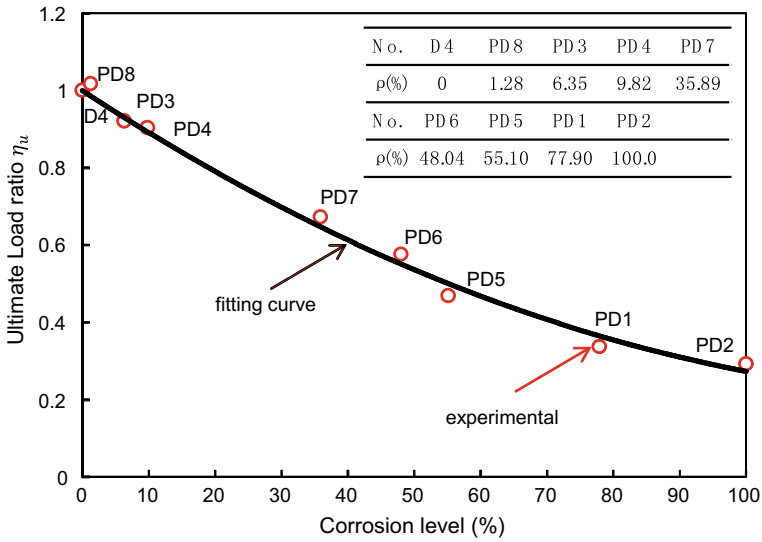


Fig. 8.16 Ultimate strengths of group PD

$$\eta_u = 0.4487\rho^2 - 1.1762\rho + 1 \tag{8.2}$$

The ultimate strength ratio roughly follows the distributional pattern of the quadratic parabola curve, and its correlation coefficient R^2 with the parabola fitting is 0.9929.

8.5 Effect of Strand Corrosion in Full Grouting on Flexural Behaviors

Prestressing strand in full grouting would corrode under the adverse erosive environment. In this section, the effect of strand corrosion under full grouting on the flexural performance of PT beams is investigated. Group PE consists of 7 beams with the same grouting form as D1. Figure 8.4a shows the specific grouting conditions.

8.5.1 Corrosion of Prestressed Concrete Beams

Figure 8.17 shows a schematic diagram of the accelerated corrosion system of group PE. A corrosion groove nearly the same length as the beam was installed on the beam. The 5% saline solution connects the elements into a current loop. Other designs of the corrosion device are consistent with the previous batch of tests.

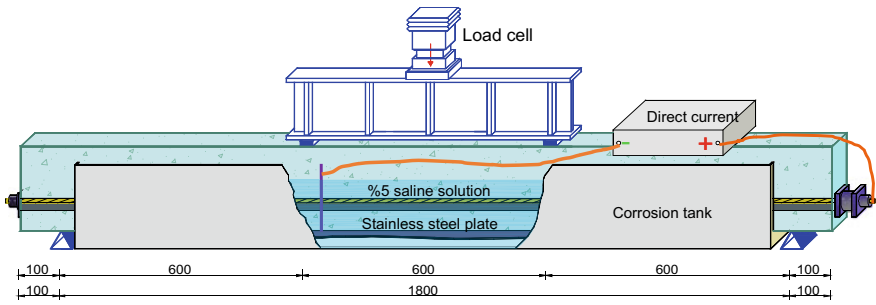


Fig. 8.17 Accelerated corrosion system and loading–unloading test set-up (Unit: mm)

The specimens were soaked in the saline solution for 3 days before the accelerated corrosion. The corrosion current is stable at about 0.4 A, and the current density is $180 \mu\text{A}/\text{cm}^2$. Table 8.8 lists the corrosion time of group PE.

After the accelerated corrosion, the corrosion-induced cracking of the beams was investigated. Longitudinal cracks appear at the bottom and two sides of the beam. The cracks are usually surrounded by a brown rust stain. The crack diagram of the slightly corroded beam PE5 is shown in Fig. 8.18, and the crack morphology of the other corroded beams is similar.

The width of corrosion-induced cracks was measured every 10 cm length using the portable microscope. The corrosion-induced crack width of beams in group PE is shown in Fig. 8.19. These cracks expanded as the corrosion loss of strand increases. The width of corrosion-induced cracks on the bottom of the test beam is greater than

Table 8.8 Corrosion time and corrosion loss of group PE

Beam No.	D1	PE5	PE6	PE7	PE2	PE3	PE1	PE4
Corrosion time (<i>d</i>)	0	10	15	20	25	30	35	40
Corrosion loss η (%)	0	12.1	19.5	27.0	46.0	61.7	73.7	84.7

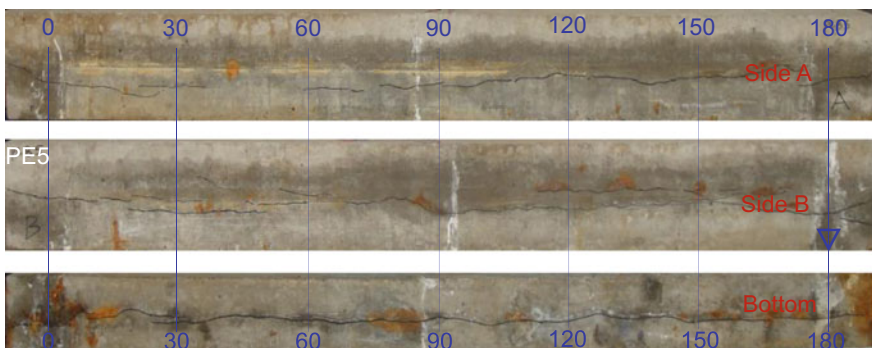


Fig. 8.18 Corrosion-induced cracks in beam PE5

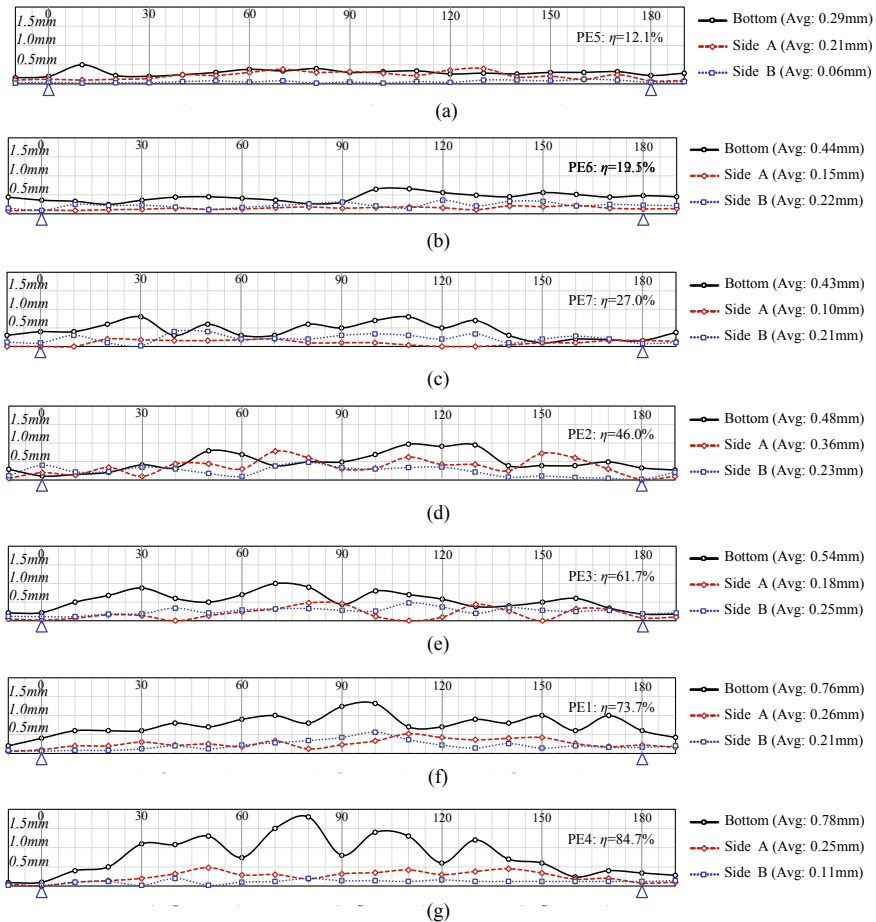


Fig. 8.19 Corrosion-induced crack widths: a PE5; b PE6; c PE7; d PE2; e PE3; f PE1; g PE4

that on both sides. In addition, for specimens PE5 and PE6 with low corrosion loss, the crack width distribution along the longitudinal direction is relatively uniform, but becomes uneven as the corrosion loss of strand increases.

8.5.2 Cracking Patterns at the Ultimate State

Figure 8.20 shows the crack distribution of the PE group at the ultimate state. The influence of strand corrosion on the cracking of beams depends on corrosion levels. For the slightly corroded beams PE5, PE6, and PE7 ($0 < \rho < 27.0\%$), the number and spacing of cracks are like the control beam D1, as shown in Fig. 8.20b–d. The cracks

are evenly distributed in the entire flexural region. The cracks depth is approximately equal. When the corrosion loss of strand was greater than 27.0%, the crack number reduces and the distribution becomes irregular, as shown in Fig. 8.20e–h. The depths of cracks are very uneven. Some cracks extend up into the concrete compression zone. This situation can easily lead to the formation of main cracks, which are harmful for the flexural behavior of concrete beams.

The change of the bond properties between corroded strand and concrete is the main reason that affects the crack distribution of the beam. The effect of bond performance on the development of cracks in concrete beams is shown in Fig. 8.21. It is usually assumed that the tensile strain of the strand and concrete varies linearly within the stress transfer region around the crack [13]. For slightly corroded beams, the cracking decreases slightly the strain energy of tensioned concrete in view of the effective bond performance. Thus, a short transmission length is enough to transmit the tension strain of concrete, as shown in Fig. 8.21. The residual tension strain of concrete is very large after the cracking. A minor deformation increment of beams can lead to the new cracking with a short spacing.

For the severely corroded beams, the bond between concrete and strand is seriously degraded. Therefore, the appearance of cracks usually leads to a large loss of concrete strain energy. After the cracks appear, a longer transmission length is required to transmit the tension strain of the concrete. The tension strain of concrete grows slowly along the transmission length, and the residual tension strain of concrete after cracking is small. The new cracks must therefore undergo considerable structural deformation and have a large spacing. During this process, the original crack will widen and continue upward, resulting in a reduction in the compression zone height of the concrete beam.

8.5.3 Load–Deflection Response

The load–deflection curves of the group PE are shown in Fig. 8.22. Before cracking, the load–deflection curves of the beams are similar, except for beam PE4. This is because the beam PE4 has already cracked during the loading–loading test. It can be seen that the test beam has the same initial flexural stiffness and the strand corrosion has little effect on it. After cracking, the baseline beam B1 has the greatest flexural stiffness compared to other corroded beams. Corrosion of the strand leads to a degradation of the flexural stiffness after cracking. For beams with the corrosion loss less than 27.0%, the stiffness degradation is not significant. As the corrosion loss further increases, the post-cracking stiffness of beam will be severely degraded. Additionally, for severely corroded beams, strand wire breakage during loading can cause abrupt jumps in their load–deflection curves, as shown in Fig. 8.22.

The stiffness of beams is mainly determined by the cross-section of uncracked concrete. Before cracking, the concrete sections of beams are intact and valid, so their initial flexural stiffness is approximately equal. After cracking, the crack expansion speed of the slightly corroded beam is slow, and the neutral axis position of the beam

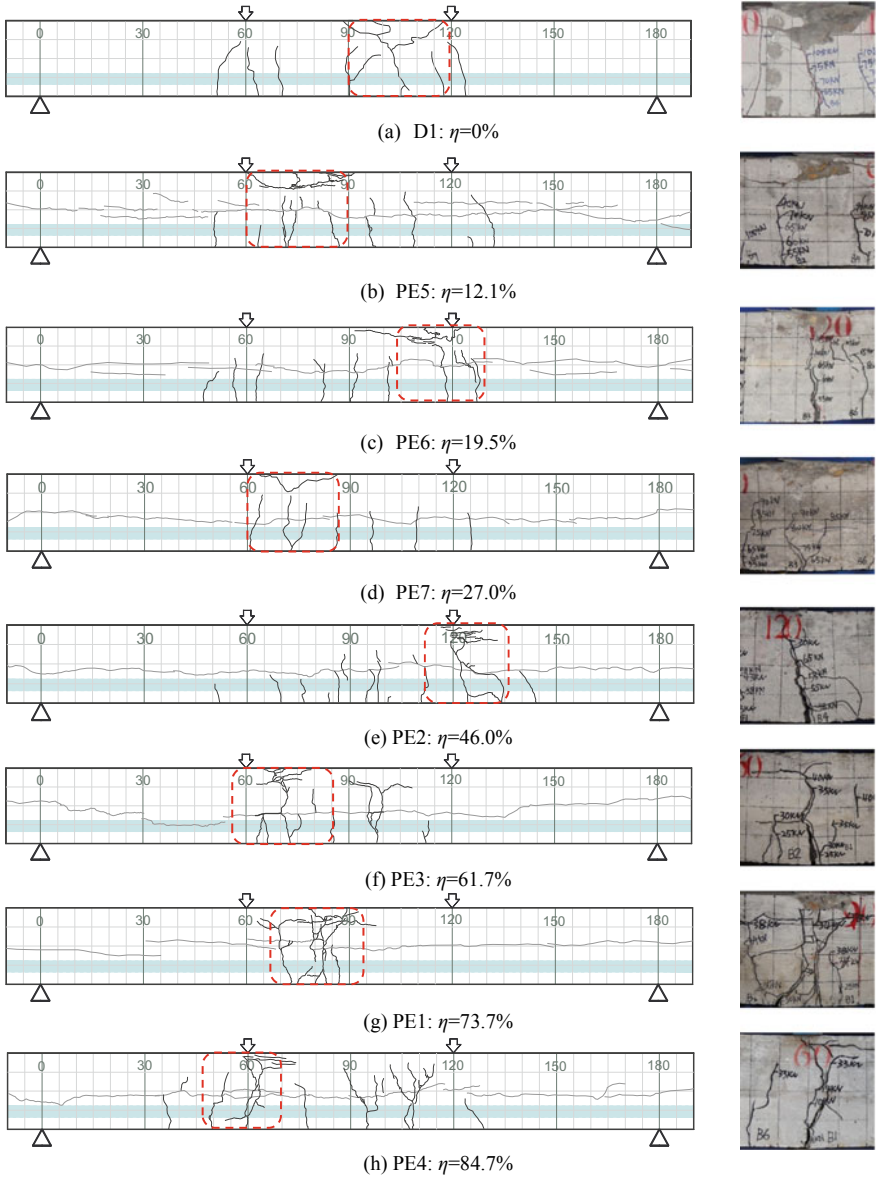


Fig. 8.20 Patterns of the flexural crack and corrosion-induced cracks: **a** D1; **b** PE5; **c** PE6; **d** PE7; **e** PE2; **f** PE3; **g** PE1; **h** PE4

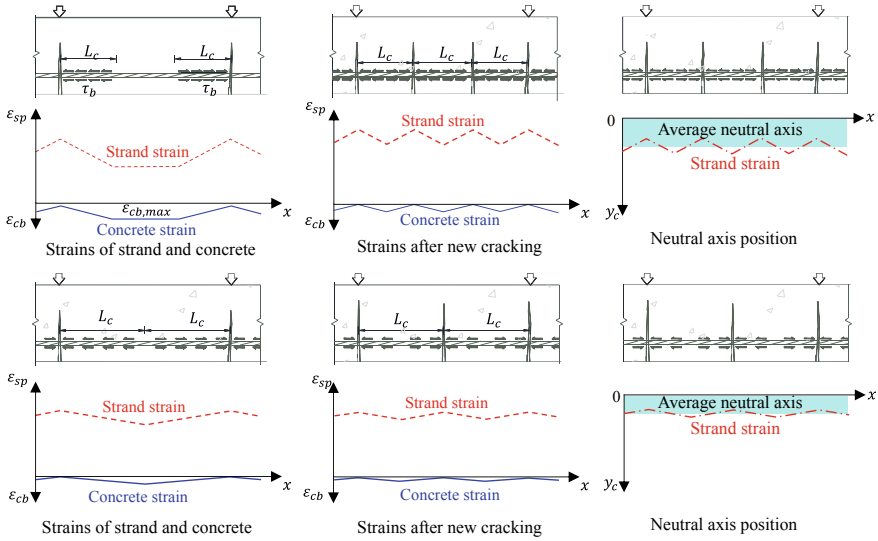


Fig. 8.21 Beam cracking affected by bond degradation: **a** slightly corroded beams; **b** severely corroded beams

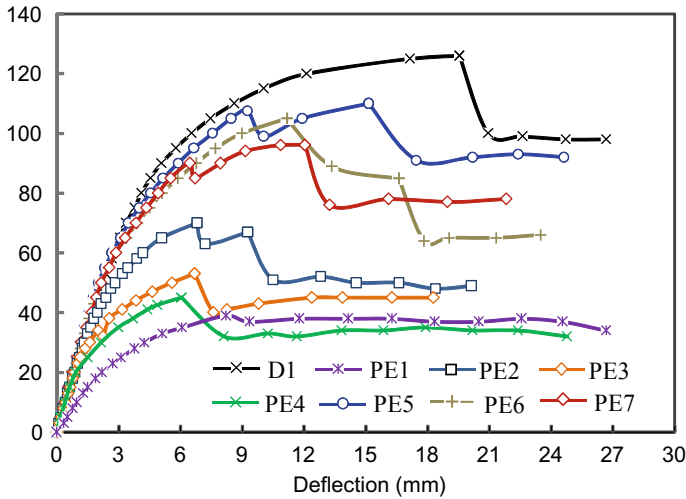


Fig. 8.22 Load–deflection curves

section is higher. At this time, the stiffness degradation of the concrete is relatively slow. When the corrosion is serious, the prestress loss is large, the restraint effect of prestress on the crack development is weakened. The crack expands rapidly, and the neutral axis position of the beam section is low, and the beam stiffness decreases obviously.

8.5.4 Failure Mode and Ultimate Strength

The failure mode of the PE group changes gradually with the increase of the corrosion loss. The control section of the specimen when it is damaged is shown in Fig. 8.20. The failure of control beam D1 was firstly the yielding of strands and followed by the crushing of concrete in the compression zone. The failure modes of the corroded beams are all slightly different compared to the control beams. The final failure mode of the corroded beam is slightly different due to the different corrosion losses. Slightly corroded beams PE5 and PE7 were damaged due to concrete crushing. Beams PE6 had concrete crushed at the same time as the wire fracture damage. The failure of beams PE2, PE3, PE1, and PE4 is caused by the wire fracture and the concrete compressive strain is small at this time. With the increase of the corrosion degree, the failure modes of specimens gradually change from concrete crushing to wire fracture. The structural failure mode changes from ductile failure to brittle failure.

The load–deflection curves of the PE group are like those of the PCB group. Neither of them has a significant yield phase. Therefore, the deflection at 0.75 times of ultimate strength continues is used as the yield deflection (Park 1989). Table 8.9 lists the ultimate deformation, yield deformation and deflection ductility factor for group PE. The ductility coefficient of the uncorroded control beam is larger than that of the other corroded beams. This shows that the strand corrosion will lead to the degradation of the ductility of concrete beams, as shown in Fig. 8.23, where CC represents the concrete crushing and WR represents the wire rupture.

The failure modes of beams also have a great influence on its ductility. The beam damaged by concrete crushing is significantly more ductile than that damaged by wire fracture. The wire fracture significantly reduced the ductility of the beam. PE6 has less corrosion loss than PE7, but its ductility factor is much less than PE7. This is because the final failure mode of PE6 is the wire fracture and concrete crushing at the same time, whereas the failure mode of PE7 is due to the concrete crushing. In addition, for the slightly and modestly corroded beams, the effect of wire fracture on ductility is stronger than its effect on the degradation of ultimate strength. For example, corrosion caused a 33.4% reduction in the deflection ductility factor of beam PE6, but only a 16.7% reduction in ultimate strength.

The ultimate strength of the beams in group PE is listed in Table 8.9. The ultimate bending strength of the control beam D1 is 126kN. Compared with the control beam

Table 8.9 Ductility coefficient of PE group

Beams No.	D1	PE5	PE6	PE7	PE2	PE3	PE1	PE4
Corrosion loss (%)	0	12.1	19.5	27.0	46.0	61.7	73.7	84.7
Ultimate load (kN)	126	110	105	96	70	53	45	39
Yield deformation (mm)	5.8	4.9	5.0	4.1	3.2	2.9	2.8	4.3
Ultimate deformation (mm)	19.6	15.1	11.2	12.1	6.8	6.7	6.1	8.2
Ductility coefficient	3.4	3.1	2.3	3.0	2.1	2.3	2.2	1.9

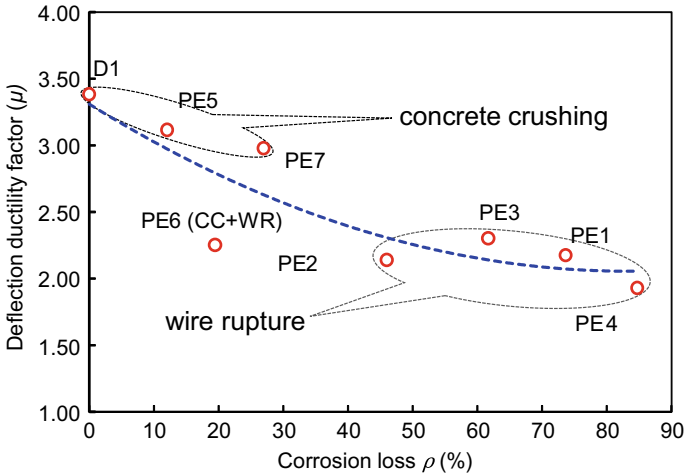


Fig. 8.23 Deflection ductility factors of specimens

D1, the ultimate bending strengths of the slightly corroded beams PE5, PE6, and PE7 are reduced by 12.7%, 16.7%, and 23.8%, respectively. For the severely corroded beams PE2, PE3, PE1, and PE4, 46.0%, 61.7%, 73.7%, and 84.7% corrosion loss result in a 44.4%, 57.9%, 64.3%, and 69.0% decrease in ultimate strength, respectively. The strand corrosion has a great influence on the degradation of the ultimate bending strength.

The degradation of flexural strength of corroded beams is mainly caused by several factors: area loss of the corroded strand, material degradation, and the bond deterioration between the corroded strand and the concrete. In the calculation of flexural strength, the influence of the area loss and material degradation can be considered through the corrosion loss of strand and the constitutive relationship model of the corroded material. However, there is no effective method to consider the effect of bond degradation on the flexural strength of concrete beams. This section will analyze the effect of bond degradation on flexural strength. First, the flexural strength of the beam is calculated based on the plan section assumption. During the calculation, the effect of area loss and material degradation of corroded strand was considered. Then, the effect of corrosion-induced bond degradation was analyzed by comparing the experimental and calculated values of flexural strength.

The conventional strain-compatibility method based on the plan section assumption consists of the following steps: (1) calculate the prestress in strand and concrete after strand corrosion; (2) assume an arbitrary loading state and calculate the corresponding moment; (3) assume the concrete strains at the extreme top and bottom fibers of the beams; (4) calculate the strains in strands, tension bars, hanger bars and concrete based on the linear strain distribution; (5) calculate the stresses and forces in strands, tension bars, hanger bars and concrete; (6) revise the assumed concrete strains and repeat the steps (3) to (6), the strains can be solved until the calculated

forces satisfy the equilibrium equations; (7) increase the applied load and repeat the step (2) to (7), the ultimate strength can be obtained until the strain of concrete, strand and reinforcing bars exceed their ultimate values.

Table 8.10 gives the theoretical values of the ultimate flexure strength for the group PE. Figure 8.24 also shows the relationship between the ratio of the ultimate strength of each beam and the control beam as a function of corrosion loss.

As Fig. 8.24 shows, the ultimate strength ratios decrease with increasing corrosion loss. The theoretical ultimate strength ratios and the experimental ultimate strength ratios can be expressed as follows

$$\eta_u = \begin{cases} -0.0338\rho^2 - 0.7348\rho + 1 & \text{(theoretical)} \\ 0.2447\rho^2 - 1.0453\rho + 1 & \text{(experimental)} \end{cases} \quad (8.3)$$

The theoretical and experimental ultimate strength ratios roughly follow the distribution law of the quadratic parabola, and the correlation coefficients R^2 of their fitting with the parabola are 0.999 and 0.994, respectively.

The calculated value of the uncorroded control beam D1 is closer to the experimental value. For other beams that were corroded, the calculated values are slightly

Table 8.10 Comparison of flexural load capacity of group PE

No.	D1	PE5	PE6	PE7	PE2	PE3	PE1	PE4
Corrosion loss ρ (%)	0	12.1	19.5	27.0	46.0	61.7	73.7	84.7
Ultimate strength (kN)	126	110	105	96	70	53	45	39
Theoretical strength (kN)	125	113	107	100	82	67	55	44
Compatibility coefficient	1	0.95	0.78	0.67	0.61	0.56	0.55	0.53

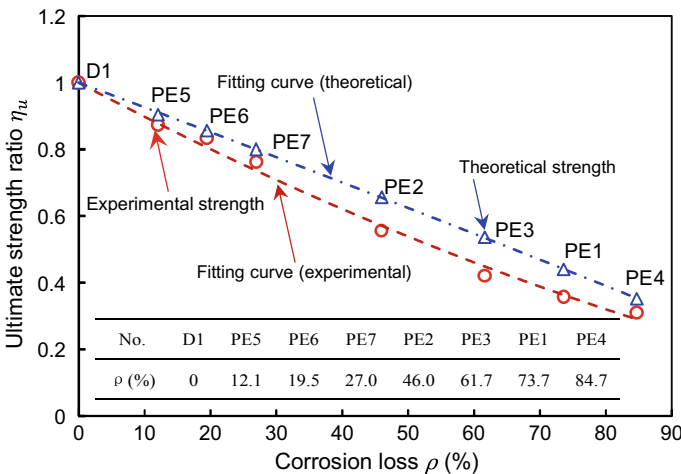


Fig. 8.24 Ultimate strength ratios of specimens

greater than the experimental values when the corrosion loss is low. As the corrosion loss increases, the degree of difference becomes progressively greater. When the corrosion loss exceeds 27.0%, the calculated strengths are approximately 20% greater than the experimental value. As mentioned earlier, the area loss and material deterioration of corroded strand have been considered in the calculation model. Therefore, the deviation between the experimental and calculated strengths can be mainly due to the strain compatibility. When the corrosion loss exceeds 27.0%, the incompatible strain between the corroded strand and concrete has a remarkable influence on the degradation of ultimate strength. Thus, the strain compatibility should be considered when predicting the ultimate strength of the corroded beams.

Corrosion-induced bond degradation results in uncoordinated deformation between strand and concrete, which in turn affects the flexural strength. This section proposes a compatibility coefficient to quantify the incompatible strain between the concrete and the corroded strand. The compatibility coefficient is defined as the ratio of the actual value of the strand to its calculated value under the ultimate state, which is expressed as

$$\Omega = \frac{\varepsilon_{p,a}}{\varepsilon_{p,c}}, \tag{8.4}$$

where Ω is the compatibility coefficient at the ultimate state; $\varepsilon_{p,a}$ is the actual strain of strand under the loading state; $\varepsilon_{p,c}$ is the strand strain calculated by the conventional strain-compatibility analysis, which is the total value of the ε_{pe} and $\Delta\varepsilon_{pc}$; ε_{pe} is the effective prestress in strand; $\Delta\varepsilon_{pc}$ is the strain increment of concrete at the strand position, which is determined by the plane section assumption. Figure 8.25 shows the strain relationship between the strand, reinforcement, and concrete under the influence of bond degradation.

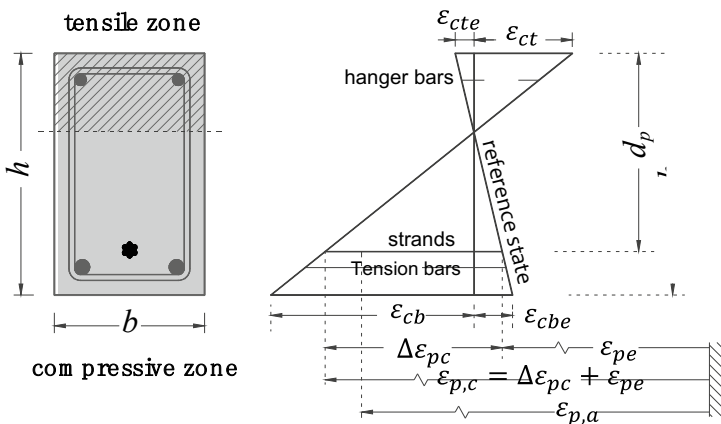


Fig. 8.25 Strains in beam sections

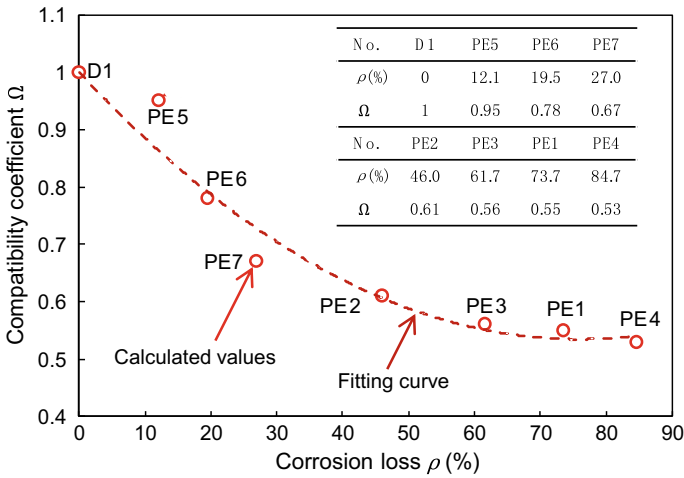


Fig. 8.26 Compatibility coefficient

This study calculates the compatibility coefficient of corroded beams by the trial-and-error principle. First, the compatibility coefficient is assumed. Next, the strand strain is corrected by the previous calculation method. Then, the modified strand strain is used to calculate the flexural strength. If the calculated value of the flexural strength is equal to the experimental value, then the assumed compatibility coefficient is feasible. Otherwise, a new assumption and recalculation are required. The compatibility coefficients for group PE are given in Table 8.10, and their relationship curve with corrosion loss is also shown in Fig. 8.26.

As Fig. 8.26 shows, the compatibility coefficient for corroded beams decreases with the increase of strand corrosion loss. The compatibility coefficient roughly follows the distribution law of the quadratic parabola, and the correlation coefficient R^2 of its fitting with the parabola is 0.9523. The compatibility coefficient can be expressed as follows:

$$\Omega = 0.8099\rho^2 - 1.2271\rho + 1. \tag{8.5}$$

The compatibility coefficient of this article provides an effective way that can consider the effects of corroded and bonding degeneration when calculating the bending capacity. Through this coefficient, the traditional calculation method based on the plane section assumption is convenient for the bearing capacity of bonding degradation structure. When calculating, first calculate the strand strain according to the plane section assumption, and then use the compatibility coefficient to modify the strand strain, and finally calculate the bear capacity through the corrected strand strain.

8.6 Conclusions

1. The cracking load degradation has almost a linear relationship with increasing strand corrosion levels. Slight corrosion of strand has little effects on the crack distribution and propagation. The severe corrosion decreases cracks and leads to the premature formation of main cracks.
2. The strand corrosion in ungrouted duct leads to pretension loss and decreases the cracking load of beams. The different strand corrosion levels have different effects on cracks. For the relatively modest corrosion loss (<10%), the number of cracks increases and the crack spacing decreases, and the beams have the similar load-crack width behavior. While as strand corrosion further increases, the number of crack decreases and crack spacing increases, and the main crack propagates fast in the beams.
3. The effects of the strand corrosion in ungrouted duct on the load-deflection behavior, the ultimate strength, and the failure modes of beams also depend on the corrosion levels. For the relatively modest corrosion loss (<10%), the strand corrosion has slight effects on the flexural performance and failure modes. While the severe strand corrosion causes significant degradation of the post-cracking stiffness and the ultimate strength and different failure modes of beams.
4. Strand corrosion decreases the ultimate strength of beams. For example, 19.5% of the corrosion loss decreases about 16.7% of the ultimate strength of beams in the present test. The incompatible strain between strand and concrete caused by slight corrosion of strand is negligible. With increasing the corrosion loss, the incompatible strain becomes significant and degrades obviously the flexural strength of beams. In the present test, the compatible strain decreases about 20% of the flexural strength as strand corrosion loss exceeds 27.0%.
5. With increasing the corrosion loss, the failure modes of beams changes from concrete crushing to strand rupture and decrease sharply the ductility of beams. For the slightly and modestly corroded beams, the wire rupture during the test degrades more significantly the ductility than the ultimate strength of beams.

References

1. O. Abraham, P. Cote, Impact-echo thickness frequency profiles for detection of voids in tendon ducts. *ACI Struct. J.* **99**(3), 239–247 (2002)
2. J. Bastien, J. Dugat, E. Prat, Cement grout containing precipitated silica and superplasticizers for post-tensioning. *ACI Mater. J.* **94**(4), 291–295 (1997)
3. M.S. Darmawan, M.G. Stewart, Spatial time-dependent reliability analysis of corroding pretensioned prestressed concrete bridge girders. *Struct. Saf.* **29**(1), 16–31 (2007)
4. P. Gardoni, R.G. Pillai, M.B.D. Hueste, K. Reinschmidt, D. Trejo, Probabilistic capacity models for corroding posttensioning strands calibrated using laboratory results. *J. Eng. Mech.* **135**(9), 906–916 (2009)
5. B. Hansen, Tendon failure raises questions about grout in posttensioned bridges. *Civ. Eng.* **77**(11), 17–18 (2007)

6. K.A. Harries, Structural testing of prestressed concrete girders from the Lake View Drive Bridge. *J. Bridg. Eng.* **14**(2), 78–92 (2009)
7. F.M. Li, Y.S. Yuan, Experimental study on bending property of prestressed concrete beams with corroded steel strands. *J. Build. Struct.* **31**(2), 78–84 (2010) (in Chinese)
8. H. Minh, H. Mutsuyoshi, K. Niitani, Influence of grouting condition on crack and load-carrying capacity of post-tensioned concrete beam due to chloride-induced corrosion. *Constr. Build. Mater.* **21**(7), 1568–1575 (2007)
9. H. Minh, H. Mutsuyoshi, H. Taniguchi, K. Niitani, Chloride-induced corrosion in insufficiently grouted posttensioned concrete beams. *J. Mater. Civ. Eng.* **20**(1), 85–91 (2008)
10. Z. Rinaldi, S. Imperatore, C. Valente, Experimental evaluation of the flexural behavior of corroded P/C beams. *Constr. Build. Mater.* **24**(11), 2267–2278 (2010)
11. A.J. Schokker, J.E. Breen, M.E. Kreger, Simulated field testing of high-performance grouts for post-tensioning. *J. Bridg. Eng.* **7**(2), 127–133 (2002)
12. M. Schupack, PT grout: bleed water voids. *Concr. Int.* **26**(8), 69–77 (2004)
13. N.A. Vu, A. Castel, R. François, Response of post-tensioned concrete beams with unbonded tendons including serviceability and ultimate state. *Eng. Struct.* **32**(2), 556–569 (2010)
14. Z.F. Wang, X.Y. Zhou, B.F. Yan, Y.F. Xiao, Grout quality testing in prestressed ducts with impact-echo method. *J. Vib. Shock* **28**(1), 166–169 (2009) (in Chinese)
15. F. Yu, J.Q. Jia, Y.P. Son, Experimental research on fatigue behavior of prestressed concrete beams with corroded steel strands. *Buil. Struct.* **42**, 1 (2012) (in Chinese)
16. Y.H. Zeng, Q.H. Huang, X.L. Gu, W.P. Zhang, Experimental study on bending behavior of corroded post-tensioned concrete beams, in *Earth and Space 2010: Engineering, Science, Construction, and Operations in Challenging Environments* (2010), pp. 3521–3528
17. X.Y. Zhou, Z.F. Wang, B.F. Yan, Nondestructive testing method of grouting quality for prestressed pipe. *China J. Highway Transport* **24**(6), 64–71 (2011) (in Chinese)
18. E.Y. Zhu, C. Liu, L. He, H.W. Zhang, N. Xie, Stress performance analysis on corroded prestressed concrete beam. *China Saf. Sci. J.* **16**(2), 136–140 (2006) (in Chinese)
19. R. Park, Evaluation of ductility of structures and structural assemblages from laboratory testing. *Bulletin of the new Zealand society for earthquake engineering* **22**(3), 155–166 (1989)

Open Access This chapter is licensed under the terms of the Creative Commons Attribution 4.0 International License (<http://creativecommons.org/licenses/by/4.0/>), which permits use, sharing, adaptation, distribution and reproduction in any medium or format, as long as you give appropriate credit to the original author(s) and the source, provide a link to the Creative Commons license and indicate if changes were made.

The images or other third party material in this chapter are included in the chapter's Creative Commons license, unless indicated otherwise in a credit line to the material. If material is not included in the chapter's Creative Commons license and your intended use is not permitted by statutory regulation or exceeds the permitted use, you will need to obtain permission directly from the copyright holder.



Chapter 9

Bearing Capacity Prediction of Corroded PT Beams Incorporating Grouting Defects and Bond Degradation



9.1 Introduction

Grouting is a critical program in the manufacture prestressed concrete (PC) beams, which can avoid the effect of environment erosion and improve the bearing capacity of PC beams. Some adverse voids can be caused by the poor construction, water diversion evaporation, and retention of air pockets in the grouting duct [25, 26]. Grouting problems can be discovered in PC beams used for long time [19, 23, 28, 31].

The bond degradation is also detrimental to the bearing capacity of PC beams. It can cause corroded strands to slip out of the surrounding concrete, causing incompatible strains and reducing the bending capacity of PC beams. [12]. More is worse, the bond degradation could lead to prestress loss and cause the anchorage problem of prestressing strands, which could cause the early failure of PC beams [24].

The prediction of the bearing capacity of PC beams under corrosion is noted by experts [7, 20]. The bond performance of prestressed tendons and concrete in the defective grouting area is deteriorated, and the coordination is degraded. The strain deformation of beams no longer satisfies the plane section assumption, but it can be determined by the overall deformation of the entire defective grouting section [14]. Some scholars have studied the calculation of flexural performance of unbonded structural members by some finite element calculation methods and established the calculation model of strain and stress increment of unbonded prestressed tendon considering the applied force [1, 14, 29].

The calculation of defective grouting is more complex than that of uncoordinated structural parts, which is also affected by the different types, positions, and lengths of defective grouting. Cavell et al. [8] calculated the bearing capacity of members considering the effects of local non-grouting, and the corrosion fracture of prestressed tendons. However, the analytical model merely considers the case of corroded prestressed tendons, but the effect of performance degradation of corroded prestressed tendons is not considered. There is not still a calculation method of structural deformation considering local grouting defects and corrosion.

The strand corrosion is the key factor for the degradation of structural performance in concrete. Strand corrosion can cause reduction in the section zone of strand, concrete cover cracking and bond degradation, and the deterioration of mechanical properties of materials. These factors will weaken the bearing capacity of concrete beams. Furthermore, corrosion in PC beams often causes the brittle failure without warnings under high stress state, which is more dangerous than reinforced concrete (RC) members.

As the corrosion loss increases, the failure mode of the specimen changes from bending failure to shear failure [4, 9, 32]. Compared to the researches on the flexural strength of corroded RC beams, few researches focus on the bearing strength of PC beams under corrosion. Some experimental researches have researched the influence of corrosion on cracking, stiffness, ductility, ultimate strength, and failure mode of PC members [8]. It was found that the corrosion loss can reduce the number of bending cracks and increase the crack distance, and decrease the ultimate force [5]. When the corrosion loss reached 20%, the bearing capacity decreased by 67% [6]. Some investigations also studied the bearing capacity of pretensioned members in aging concrete bridges, such as twenty-eight 25-years old concrete panels [16] and two concrete girders serviced at least 45 years [15]. These girders were loaded to study the degradation of flexural behavior, which point out that the strand corrosion can reduce the ultimate capacity of strand and the ductility of strand, and the failure mode will also be changed.

The flexural capacity of RC beams after corrosion should be accurately predicted, which is important for making maintenance and reinforcement decisions. Currently, however, the existing prediction theories consider bond degradation by means of empirical factors [1, 18, 27]. These empirical factors [1, 18, 27] were derived from experimental results, therefore, the effectiveness of these factors is limited. The bond behavior loss between the corroded reinforcement and concrete is considered to predict the flexural capacity of beams by Eyre and Nokhasteh [34] and Cairns and Zhao [35]. Bhargava et al. [4] discussed the ultimate capacity caused by the bond failure of strand at the mid-span of specimens. El Maaddawy et al. [36] have researched the reinforcement strain between the two bending cracks for the prediction of flexural capacity considering the bond degradation effects, while the analytical model ignores the slip of reinforcements in the different condition of cracks.

Corrosion can reduce the sectional zone of strand, degrade bond strength, induce concrete cracking and deteriorate the material property, which can further decrease the bearing capacity of PC beams. The combined effects of these factors should be reasonably considered in the bending capacity prediction model. How to reasonably consider the effect of the above elements on the bearing capacity of PC beams considering corrosion still needs to investigate further.

This chapter is organized as follows. An analytical model is developed to predict the flexural capacity of locally ungrouted PT beams at first. Next, a model is built to assessment the flexural capability of PT beams considering corrosion-induced bond degradation. Finally, the conclusions are discussed.

9.2 Analytical Model for Flexural Capacity of PT Beams

9.2.1 Simplified Calculation Method

For locally ungrouted PC beams, an analytical model was employed to assessment the residual flexural capacity of PC beams with local grouting. Incompatible strains, the strand zone loss, and material degradation due to corrosion were considered in the analytical model. A new method is developed to predict local rigidity degradation for asymmetric deformation of beams.

The ungrouted duct is the unbonded zone. Within the unbonded zone, the strain of strand is incompatible with the strain of the concrete, but the total elongation of the strand in the ungrouted zone should be equivalent to the elongation of the corresponding concrete. Based on this law, the strain of strand in the ungrouted duct can be obtained from the calculations mentioned below.

To simplify the calculation of strain, fully grouted and ungrouted ducts can be considered as completely fully bonded and unbonded zones, respectively. In the bonded zone, local slipped between the strand and the concrete was not considered. Next, the PC structure is separated into some segments, as shown in Fig. 9.1. The fully grouted segments are numbered from 1 to e , f to m , and n to g . The ungrouted segments are numbered from e to f and m to n . These arbitrary segments in fully grouted and ungrouted zones are denoted by i and j , respectively.

The stress-strain distribution in the segment i considering the applied force, numbered as $n \sim m$, is shown in Fig. 9.2. Combing the above theories, the strain increment ($\Delta\varepsilon_{pc,i}$) of concrete at the strand location can be computed as

$$\Delta\varepsilon_{pc,i} = (\varepsilon_{cb,i} - \varepsilon_{cbe,i}) + \frac{d_p}{h} [(\varepsilon_{ct,i} - \varepsilon_{cte,i}) - (\varepsilon_{cb,i} - \varepsilon_{cbe,i})], \quad (9.1)$$

where $\varepsilon_{ct,i}$ and $\varepsilon_{cb,i}$ are the strains of concrete at the top and bottom fibers, respectively; $\varepsilon_{cte,i}$ and $\varepsilon_{cbe,i}$ are the compressive strains of concrete at the top and bottom fibers, respectively; h is the beam height; d_p is the distance from the top fiber of concrete to the centroid of strand.

The elongation of the strand in the ungrouted duct is equivalent to the total elongation in the corresponding concrete, which is calculated as

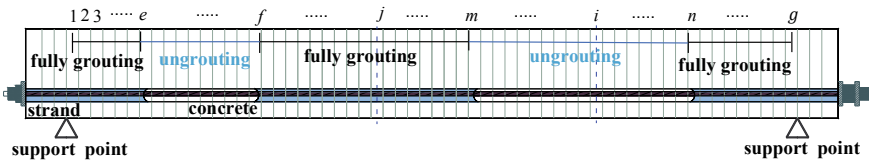


Fig. 9.1 Segment division of beams

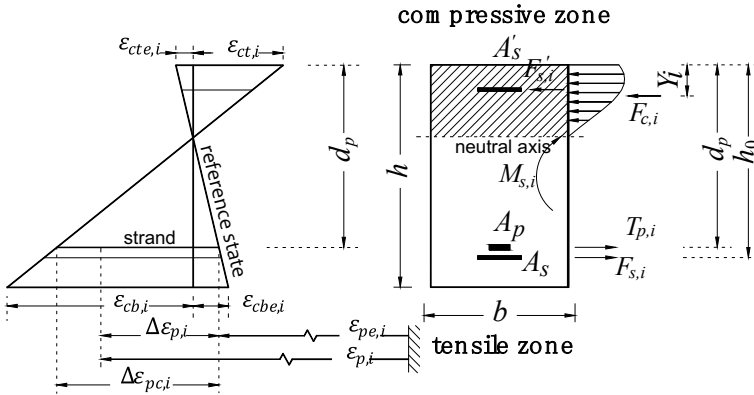


Fig. 9.2 Stress–strain distribution

$$\Delta L_w = \Delta L_c = \sum_{i=n}^m \Delta \varepsilon_{pc,i} l_{w,i}, \quad (9.2)$$

where ΔL_w and ΔL_c are the total elongation of the strand and corresponding concrete in the ungrouted duct, respectively; $l_{w,i}$ is the length in the arbitrary segment i ; n and m are the first and last segment in the ungrouted duct.

In the ungrouted zones, the friction between the strand and the concrete is usually ignored. Next, the average strain increment of strand in any ungrouted segment i ($\Delta \varepsilon_{p,i}$) can be expressed as

$$\Delta \varepsilon_{p,i} = \frac{\Delta L_w}{L_w}, \quad (9.3)$$

where L_w is the total length in the ungrouted duct.

At any segment j in the fully grouted zone $m \sim e$, it is usually assumed that the strand is well integrated with the concrete. The strain increment of the strand ($\Delta \varepsilon_{p,j}$) is equivalent to the strain increment of the corresponding concrete, which is calculated as

$$\Delta \varepsilon_{p,j} = (\varepsilon_{cb,j} - \varepsilon_{cbe,j}) + \frac{d_p}{h} [(\varepsilon_{ct,j} - \varepsilon_{cte,j}) - (\varepsilon_{cb,j} - \varepsilon_{cbe,j})], \quad (9.4)$$

where $\varepsilon_{ct,j}$ and $\varepsilon_{cb,j}$ are the concrete strains at the extreme top and bottom fibers, respectively; $\varepsilon_{cte,j}$ and $\varepsilon_{cbe,j}$ are the precompressive strains of concrete at the extreme top and bottom fibers, respectively.

The effective prestrain of strand will be induced by improving the strain rate, the strain of the strand ($\varepsilon_{p,k}$) in any segment k is calculated as

$$\varepsilon_{p,k} = \Delta \varepsilon_{p,k} + \varepsilon_{pe,k}, \quad (9.5)$$

where k is the number of any section, $k = i$ in the ungrouted zone, and $k = j$ in the fully grouted zone; $\varepsilon_{p,k}$ is the strain of the strand; $\Delta\varepsilon_{p,k}$ is the strain increment of the strand; $\varepsilon_{pe,k}$ is the effective prestrain of the strand.

The tensile force of the strand under the applied load is associated with its cross-sectional zone, the strain of the strand, and intrinsic structural laws. The proposed constitutive law can be used for tensile testing of corroded strands. Furthermore, the maximum corrosion loss can usually be used to measure the remaining cross-sectional zone of the strand at the equivalent force of strand in the ungrouted zone. Next, the tension force of strand in any segment k is calculated as

$$T_{p,k} = \sigma(\varepsilon_{p,k}\rho)A_p(1 - \rho), \tag{9.6}$$

where $T_{p,k}$ is the tension force of strand; $\sigma(\varepsilon_{p,k}\rho)$ is the stress of strand, which is associated with the strain of strand and the corrosion loss of strand which can be calculated by Eq. (9.1); $\varepsilon_{p,k}$ is the strain of the strand; A_p is the initial zone of the strand.

Based on the above-mentioned sectional assumption, the strain of longitudinal bars and hanger bars in the cross-sectional k can be computed as

$$\varepsilon_{s,k} = \varepsilon_{ct,k} + \frac{\varepsilon_{cb,k} - \varepsilon_{ct,k}}{h}h_0 \tag{9.7}$$

$$\varepsilon'_{s,k} = \varepsilon_{ct,k} + \frac{\varepsilon_{cb,k} - \varepsilon_{ct,k}}{h}a'_s, \tag{9.8}$$

where $\varepsilon_{s,k}$ and $\varepsilon'_{s,k}$ are the strains of longitudinal bars and hanger bars, respectively; h_0 and a'_s are the distances from the extreme top fiber of concrete to the centroids of longitudinal bars and hanger bars, respectively.

The elastic–plastic model can be employed to assessment the stress–strain relationship of steel bar. The force of longitudinal bars ($F_{s,k}$) and the force of hanger bars ($F'_{s,k}$) can be computed as

$$F_{s,k} = A_s E_s \varepsilon_{s,k} \leq f_{sy} A_s \tag{9.9}$$

$$F'_{s,k} = A'_s E'_s \varepsilon'_{s,k} \leq f'_{sy} A'_s, \tag{9.10}$$

where A_s, E_s, f_{sy} are the segment zone, elastic modulus, yield strength of longitudinal bars, and A'_s, E'_s, f'_{sy} are the segment zone, elastic modulus, yield strength of hanger bars, respectively.

In this study, the nonlinear composition method of concrete proposed by Zhang et al. [33] was used. The concrete composition law ignores the concrete tension, which can be expressed as

$$f_c = \begin{cases} f'_c [2(\varepsilon/\varepsilon_0) - (\varepsilon/\varepsilon_0)^2], & \varepsilon \geq 0 \\ 0, & \varepsilon < 0 \end{cases}, \quad (9.11)$$

where f'_c is the specified compressive strength of concrete, and ε_0 is the corresponding strain of the steel strand.

Combining the ultimate stress of the fibers at the bottom of the concrete with the ultimate stress of the fibers at the top of the concrete is an effective method to calculate the compression force of the concrete, and it can be expressed as

$$F_{c,k} = \int_0^h f_c b dy, \quad (9.12)$$

where $F_{c,k}$ is the compression force of the concrete; b is the width of the beam.

$$Y_k = \frac{\int_0^h f_c b y dy}{F_{c,k}}, \quad (9.13)$$

where Y_k is the distance from the centroid of the concrete compression force to the extreme top fiber of the concrete compression.

For the given force condition, the applied bending moment is known in each segment. In any segment k , the total forces of the strand, hanger bars, longitudinal bars, and concrete is equivalent to be a constant of zero. Moreover, the total moment of each segment is equivalent to the applied moment in the force condition. The moment of bending, the force of strand, the force of concrete, the force of longitudinal bar, and the force of hanger bar should satisfy the below calculation equations

$$F_{c,k} + F'_{s,k} + F_{s,k} + T_{p,k} = 0 \quad (9.14)$$

$$M_{s,k} = F_{c,k}(d_p - Y_k) + F'_{s,k}(d_p - a'_s) + F_{s,k}(h - d_p - a_s), \quad (9.15)$$

where $M_{s,k}$ is the bending moment; a_s is the distance from the extreme bottom fiber of concrete to the centroid of longitudinal reinforcement bars.

9.2.2 Calculation Procedure

Resolving the ungrouted segment is not easy as it is determined by the total elongation of the concrete in the ungrouted zone. Therefore, a method of iterative is proposed to resolve the segment as per the following instructions. For fully grouted segments, the variables are independent of each other, and the strain of the concrete in Eqs. (9.14) and (9.15) can be resolved quickly by the plane section assumption. First, the

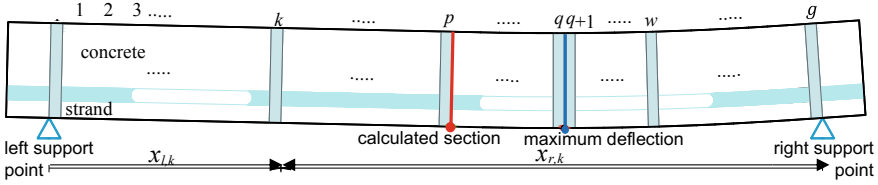


Fig. 9.3 Description of deflection prediction of specimens

flexural moment of the concrete ($M_{s,k}$) can be calculated for the applied force (P), and the tension in each duct segment within the ungrouted zone ($T_{p,k}$) is assumed to be similar. Then, the concrete strains ($\epsilon_{ct,k}$ and $\epsilon_{cb,k}$) can be calculated by using the above calculation equations (Eqs. 9.14 and 9.15). According to this above criterion, the strand force ($T'_{p,k}$) can be computed by Eqs. 9.1–9.6. Revising $T_{p,k}$ and repeating the procedure until $T_{p,k}$ is equivalent to $T'_{p,k}$. The corresponding of the strain of concrete, the force of strand, the force of longitudinal reinforcements, the force of hanger reinforcements, and the force of the concrete can be derived from the plane section assumption.

The cross-sectional curvature is a feasible way to tackle the deflection of PC beams. The existing models have been proposed to calculate the bearing capacity by cross-sectional curvature [16]. These works mainly study the symmetric deflection of the structure. The deformation of locally ungrouted beams considering corrosion is shown in Fig. 9.3. Therefore, the proposed model is suitable to assessment the deflection of ungrouted beams.

This paper presents a two-step method for predicting the asymmetric deformation of corroded beams. First, the trial-and-error method is used to determine the maximum deformation and its location. Second, combining the section curvature is an effective method to assessment the deformation of the other section.

According to the strain distribution of the cross-section of beams in Fig. 9.2, the cross-section of curvature at any segment k is calculated as

$$\phi_k = \frac{(\epsilon_{cb,k} - \epsilon_{cbe,k}) - (\epsilon_{ct,k} - \epsilon_{cte,k})}{h}, \tag{9.16}$$

where ϕ_k is the sectional curvature; $\epsilon_{cte,k}$ and $\epsilon_{cbe,k}$ are the precompressive strains of concrete at the extreme top and bottom fibers, respective

It can be assumed that the maximum deformation location occurs at segment q (see Fig. 9.3), which can be computed as

$$\Delta_{\max,ql} = \sum_{k=1}^q \phi_k l_{w,k} x_{l,k} \tag{9.17}$$

$$\Delta_{\max,qr} = \sum_{k=q+1}^g \phi_k l_{w,k} x_{r,k}, \tag{9.18}$$

where $\Delta_{\max,ql}$ and $\Delta_{\max,qr}$ are the maximum deflections calculated from the left and right support points, respectively; $x_{l,k}$ and $x_{r,k}$ are the distances from left and right support points to segment k , respectively; $l_{w,k}$ is the length of segment k ; g is the segment number.

If q is the segment of the true maximum deflection, both deformations can be obtained by Eqs. (9.17) and (9.18), which must be equal. Otherwise, this relationship is invalid. According to the trial difference method, the maximum deformation of any segment can be computed by the above-mentioned law. First, the maximum deformation in any segment can be considered as a constant. Next, the deformations can be obtained by using the two formulas mentioned above. The above two calculated maximum deflections are calibrated and the segment is corrected until the maximum deflection in the left support points and the maximum deflection in the right support points to be equal. The maximum deformation can be expressed as

$$\Delta_{\max,q} = \Delta_{\max,ql} = \Delta_{\max,qr}, \quad (9.19)$$

where $\Delta_{\max,q}$ is the maximum deformation of beams.

After the above calculation steps described, the maximum deflection and the position can be calculated. Then, the deformation of the segment p (see Fig. 9.3) can be expressed as

$$\Delta_p = \Delta_{\max,q} - \sum_{k=p}^q \phi_k l_{w,k} X_{p,k}, \quad (9.20)$$

where Δ_p is the deflection at segment p ; $X_{p,k}$ is the distance from the segment p to the segment k .

If the calculation starts from a smaller loading condition, which can be corrected with the increase of the given loading. The strains in the concrete, the forces in the strand, the force of longitudinal beam, the force of the concrete as well as the deflection of the deformed segment can be obtained from the overall bending response of the beam. The ultimate state of PC beams can be computed as the following two conditions. For example, when (1) the concrete strain at the top fiber ($\varepsilon_{ct,\max}$) exceeds the ultimate compressive strain (ε_{cu}); or (2) the strand strain ($\varepsilon_{p,\max}$) reaches the ultimate strain (ε_{pu}). The calculation procedure is shown in Fig. 9.4.

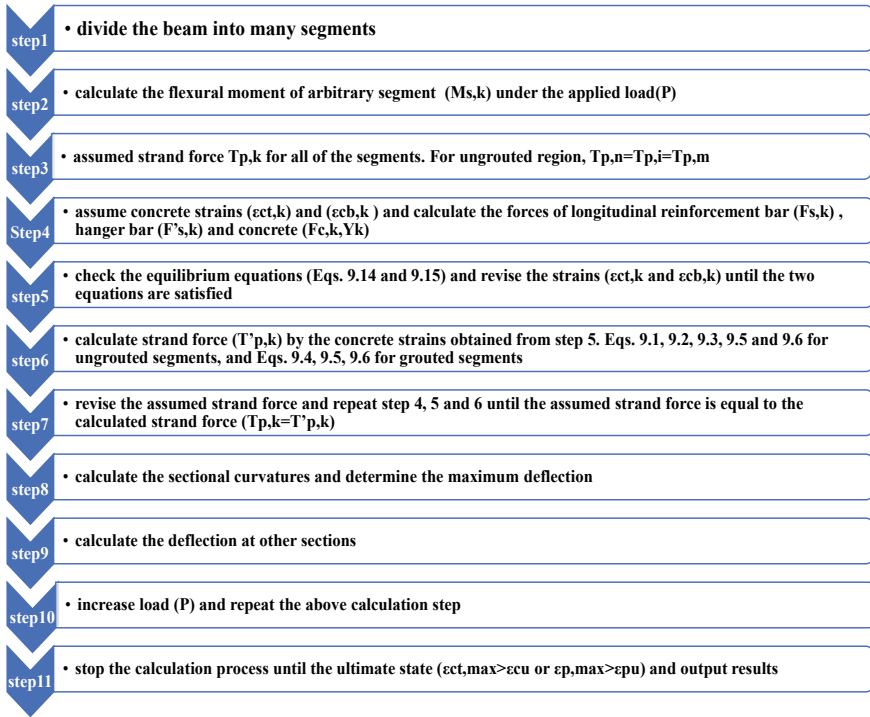


Fig. 9.4 Calculation procedure of flexural capacity of PC beams

9.3 Model Validation

The proposed model can effectively assess the flexural performance of the test beam. The beams are segmented into 200 segments with 9 mm length each. The initial force can be set to be a constant of 1 kN and loaded with an increase of 1kN per step. The ultimate compressive strain of concrete (ϵ_{cu}) can be taken as a constant of 0.0035. The stress–strain relationship of corroded strands can usually be decided by the proposed constitutive law in Eq. (9.1). The yield of the initial strain and the final strain was 0.0094 and 0.028, respectively.

The results show that the prediction of the models is in good consistent with the experimental results for PC beams. The experimental errors in the prediction of ultimate deformation are due to uncertainty in the evaluation of corrosion loss of the strand and material degradation. As described above, for PC beams with severe corrosion, the ultimate strain of the strand could usually be taken to keep it constant.

Figure 9.5 shows the load–deformation curves of PC beams under the similar corrosion loss. Because of the existing condition, the four beams (PD1, PD4, PD7, PD8) can be selected by the following comparisons. The experimental and predicted rotation angles are shown in Fig. 9.6. The theoretical rotation angles in the ungrouted

end and the fully grouted end are in well accordance with the experimental rotation angle in the ungrouted end and the fully grouted zone.

Figure 9.7 shows the prediction of compressive stress in concrete for four beams considering the ultimate force state. For comparison purposes, the figure also shows the existing cracking pattern. The ungrouted end has a different stress distribution as compared with the fully grouted end. The compressive stress at the fully grouted end is less than the compressive stress at the ungrouted end, and the pressure zone depth is greater than the compressive stress at the ungrouted end. These differences will become significant with the increase of corrosion losses. This phenomenon is in good agreement with cracking patterns. These cracks at the ungrouted end extend deeper into the pressure region than the cracks at the fully grouted end.

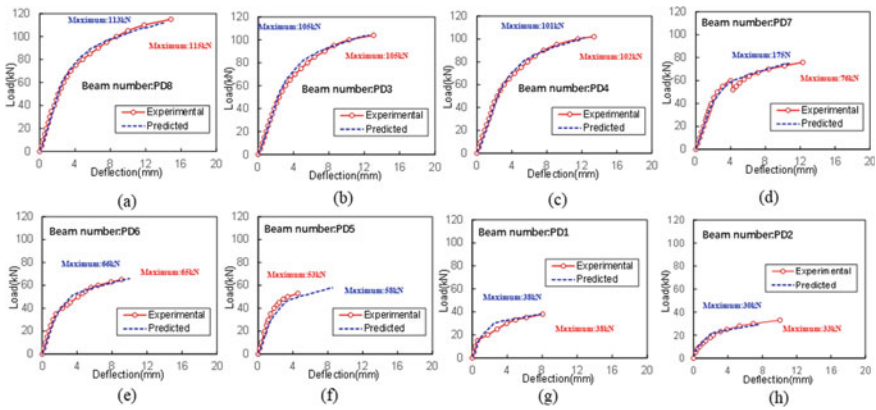


Fig. 9.5 Difference condition of load–deformation response: a PD8; b PD3; c PD4; d PD7; e PD6; f PD5; g PD1; h PD2

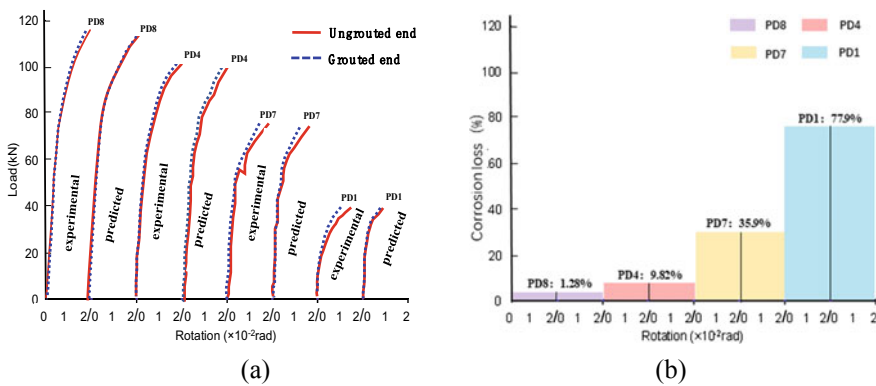


Fig. 9.6 Experimental and predicted load-rotation angle curves: a Load; b Corrosion loss

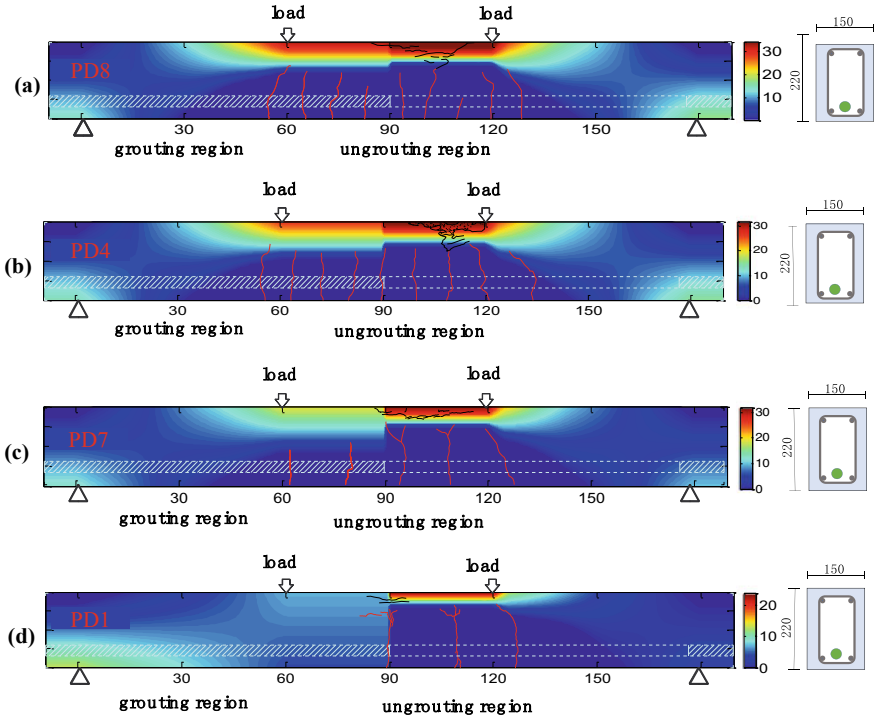


Fig. 9.7 Prediction of concrete stresses and crack patterns: a PD8; b PD4; c PD7; d PD1

Through the above-mentioned comparisons, the developed stress distribution model can reasonably predict the stress distribution of the material.

Table 9.1 gives the experimental and predicted ultimate strengths of specimens. The ultimate strength prediction error in the experimental beams is less than 5%. The prediction error can be obtained by three aspects: variability of material properties, experimental error, and the error of model. Overall, the proposed model can reasonably assess the degradation of bending performance of beams after corrosion. The asymmetric deformation of the PC structure is computed considering the distribution of the stress and ultimate strength of specimens.

Table 9.1 Experimental data and verification results

Beams	PD8	PD3	PD4	PD7	PD6	PD5	PD1	PD2
Experimental (kN)	115	105	102	76	65	53	38	33
Predicted (kN)	113	105	101	75	66	58	38	30
Error (%)	-2	0	-1	-1	+1	+5	0	-3

9.4 Quantification of Corrosion-Induced Uncoordinated Deformation in Bond–Slip Zone

9.4.1 Quantification Principle of Bond–Slip Zone

The bond stress between strand and concrete is related to the associated slip value. Adhesion action is an effective way to provide the initial bond stress before bond–slip zone. As the slip increases, the adhesion stress can be supplied by frictional and gear forces. The friction force and gear force will increase until the excessive slip shows that the concrete gear has been sheared off. Then, the longitudinal friction force can provide the bond force only, but the value is small. Thus, the effective bond force between the strand and concrete can be primarily supplied by the bond force and gear force before over bonding slips, and the corresponding zone is named as effective bond region. On the other hand, the bond force after the excessive slip is named as the residual bond force which is supplied by the small friction force between strand and concrete, and its region is called as the slip region.

Figure 9.8 shows the changes of effective bond force in the longitudinal direction with the increase of the applied force. The adhesive force will increase with the increase of the applied force (F_p). In the effective bond zone, the corresponding slip value is small. The effective bond region starts to move when the force of the strand (F_p) exceeds the total of effective bond force and prestressed force of the tendon ($F_{eb} + F_{pe}$). An increase in the slip zone area results in an increase in residual adhesion force. The effective bond zone is moved until the total of the effective bond force, the residual bond force, and the prestressed force of the tendon ($F_{eb} + F_{pe} + F_{rb}$) is equivalent to the force of the strand (F_p). The above-mentioned theories can be used to define the extent of slip region in aging PC beams.

The corrosion loss of strand and F_p can determine the range of slip region, which can be found specifically in Fig. 9.9. The bond between prestressed strand and concrete in uncorroded and slightly corroded PC beams is better than that in PC beams with severe corrosion. Throughout the entire loading procedure, the total of effective bond force and prestressed force ($F_{eb} + F_{pe}$) exceeds the maximum tensile

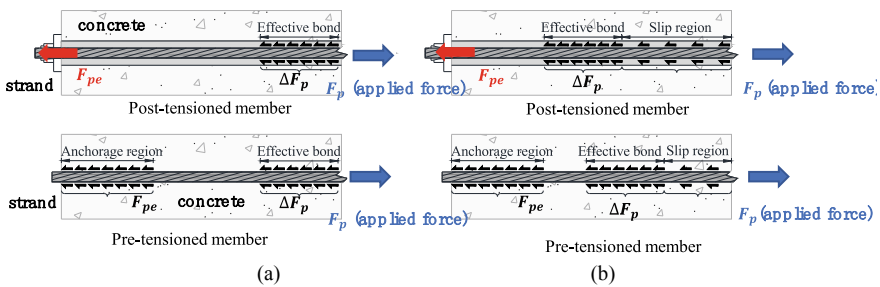


Fig. 9.8 Different shifting condition of bond force: a before shifting; b after shifting

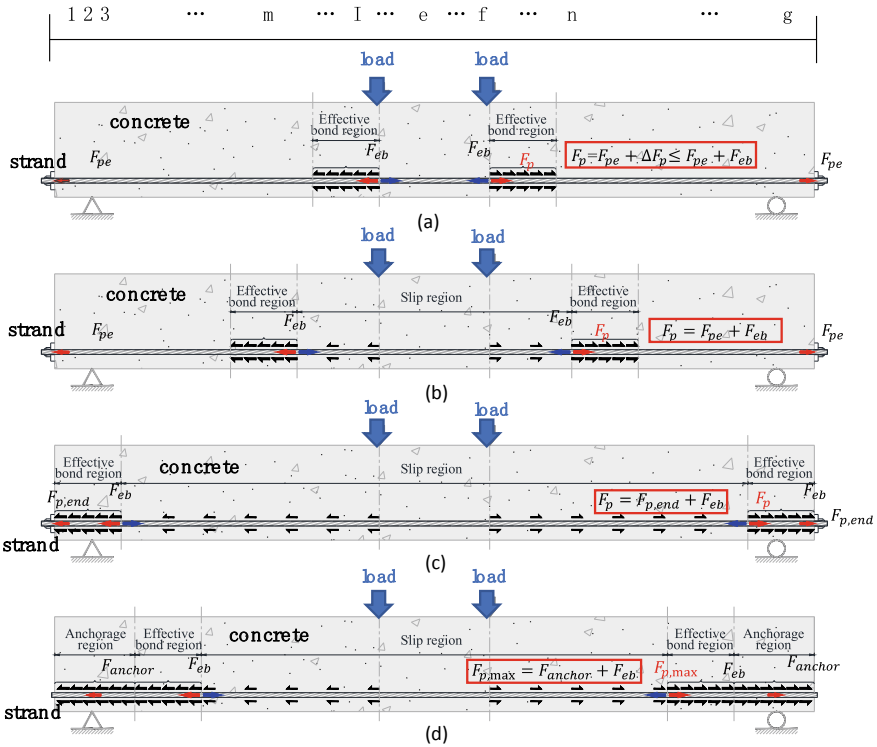


Fig. 9.9 Determination of the bond-slip region

force (F_p). The effective bond zone remains unchanged without excessive slip, which can be shown without bond-slip in Fig. 9.9a. The strains in the strand and concrete are determined by the plane section assumption. With the force increases, the tension force in the strand (F_p) may be greater than the sum of effective bond force and prestressed load ($F_{eb} + F_{pe}$). In Fig. 9.9b, the effective bond zone moves toward the beam end. This movement decreases the tension in the prestressed steel, but increases the overall bond force, and it is stopped until the tension of the strand is equivalent to the effective bond force. Next, the range of the slip region is determined according to the above-mentioned theory. The strains in the strand and concrete within the slip zone satisfy the condition that the total elongation of the strand is equivalent to the elongation of the corresponding concrete in the slip zone, but it does not obey the plane section assumption. The strains in the strand and concrete can be evaluated according to the above-mentioned theory, which is shown in details in the next segment.

It points out that the effective bond zone can move toward the beam end as the applied force increases, as shown in Fig. 9.9c. Under this condition, the post-tensioned segments in the slip regions were varied from the pretensioned segments in the slip regions. The pretensioned strand conveys the bond force directly to the

surrounding concrete, which is stopped until the bond length exceeds a length from the end beam. When the effective bond zone moves to the end of the PC beam, the post-tensioned of the strand continues to be anchored in the beam segment. As a result, the extent of the slip zone can be determined by subtracting the two lengths in the effective zone from the total length of the member. The tension force near the effective bond zone of the strand increases as the force increases, and the strain on the strand and the concrete can also be obtained from their equivalent total elongation of the slip zone. And, the corresponding force of the strand should be named as the bearing capacity in the beam. For pretensioned prestressed members, the strand anchorage would fail instantly when the effective bond zone moves to the PC beams end [5, 21, 22], as shown in Fig. 9.9d.

9.4.2 A Quantitative Method for Uncoordinated Deformation

As mentioned before, the solution of deflection response of the beam relies on the applied force (F_p) and corrosion loss. The uncorroded, slightly corroded, and severely corroded beams will not slip in a small provided force. According to these conditions, the method of plane section assumption will be used to calculate its flexural response. For the severely corroded beams in a very large force condition, which it will occur in the excessive slip. The slip zone can be decided before it is discussed. In this condition, the strand strains and the concrete strains will not obey the plane section assumption, but the total strand elongation is equivalent to the corresponding concrete in the slip zone. The flexural response of PC beams under corrosion can be obtained from the next section by the above-mentioned theories.

To optimize the flexural response of the calculation process, the beam is divided into several any segments to obtain the total elongations of the strand and concrete, and it can be shown in Fig. 9.10. These segments are numbered from 1 to g . The slip zone length is set to L_s , and these segments within the slip zone are marked from m to n . The cross-segments of the entire bending zone can be numbered from e to f . The cross-sectional length is defined as $l_{s,i}$. The average values of the cross-sections are used to express the strain–stress relationships in the arbitrary segment.

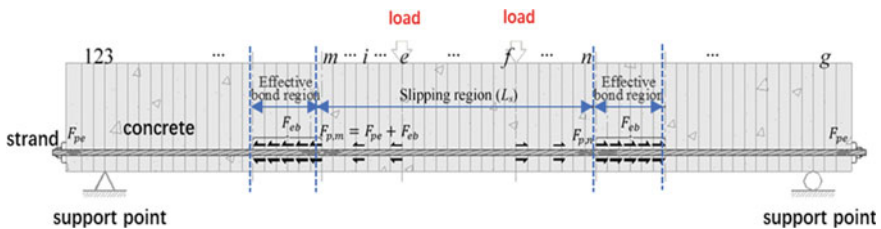


Fig. 9.10 Segment division of specimens

Zhang et al. [3] proposed the constitutive law for strand with the difference of the corrosion losses of PC beams, and it is employed to characterize the mechanical properties of the strand. All strands can be assumed to have the equivalent stress–strain curve before it has yielded. Then, the stress–strain curve will be changed with the increase of corrosion loss. When the strand corrosion loss is smaller than the critical value (η_c), the strand can enter the stiffening phase. When the corrosion loss is less than the critical value, the ultimate strains of them decreases linearly with the corrosion loss increases. The further corroded strand fails instantly after it has yielded.

According to the experimental results, the corrosion loss (η_c) was adopted as the value of 11%. The principal structure law for the strand considering the difference of corrosion losses, which is described as follows:

$$f_p = \left\{ \begin{array}{ll} E_p \varepsilon, & \varepsilon \leq \varepsilon_{py} \\ f_{py} + E_{pp}(\varepsilon - \varepsilon_{py}), & \varepsilon_{py} < \varepsilon \leq \varepsilon_{pu} - \frac{\eta}{\eta_c}(\varepsilon_{pu} - \varepsilon_{py}) \quad \eta \leq \eta_c \\ E_p \varepsilon, & \varepsilon \leq \varepsilon_{py} \quad \eta > \eta_c \end{array} \right\}, \quad (9.21)$$

where f_p and ε are the stress of strand and the strain of strand, respectively; E_p , E_{pp} , ε_{py} , ε_{pu} are the modulus of the elastic value, the modulus of hardening value, the strain of the yielding, and the ultimate strain, respectively; f_{py} is the yield strength of uncorroded strand.

The stress–strain relationship of concrete under compression can be characterized by a parabolic relationship [11], which can be calculated as follows:

$$f_c(\varepsilon_c) = f'_c \left[\frac{2\varepsilon_c}{\varepsilon_{c0}} - \left(\frac{\varepsilon_c}{\varepsilon_{c0}} \right)^2 \right], \quad (9.22)$$

where f'_c is the specified compressive strength of concrete and ε_{c0} is the corresponding strain in concrete.

The stress–strain relationship for the steel can be idealized as a linear elastic–plastic, considering strain hardening as a constant of 1% after it has yielded [33], which is expressed as follows

$$f_s(\varepsilon_s) = \left\{ \begin{array}{ll} \varepsilon_s E_s & \varepsilon_s \leq \varepsilon_{sy} \\ f_{sy} + E_{sp}(\varepsilon_s - \varepsilon_{sy}) & \varepsilon_s > \varepsilon_{sy} \end{array} \right\}, \quad (9.23)$$

where E_s , f_{sy} and ε_{sy} are the modulus of the elastic, the strength of the yield and yield strain of the strand, respectively; E_{sp} is hardening modulus of the strand.

For a given force condition, the slip zone can be identified as the effective adhesive force is equivalent to the tension increment near the effective bond–slip zone. In m or n segment, the increment of strand tension force should be equivalent to the effective adhesive force (F_{eb}). For the segment of m , the corresponding value is defined as

$$F_{p,m} = F_{pe} + \Delta F_{p,m} = F_{pe} + F_{eb}, \quad (9.24)$$

where $F_{p,m}$ is the strand tension force of segment m near the effective adhesive region; F_{pe} is the effective prestressed tension force, and $\Delta F_{p,m}$ is the increment tension force of segment m .

The strand tension force of any segment i in the slip zone is computed as

$$F_{p,i} = \begin{cases} F_{p,m} + L_p R(\eta) \tau_f l_{im} & m \leq i < e \\ F_{p,m} + L_p R(\eta) \tau_f l_{em} & e \leq i < f \\ F_{p,m} + L_p R(\eta) \tau_f (l_{nm} - l_{im}) & f \leq i < n \end{cases}, \quad (9.25)$$

where $F_{p,i}$ is the strand tension force of any segment i ; l_{im} is the distance from segment i to segment m ; l_{em} is the distance from segment e to segment m , and l_{nm} is the distance from segment n to segment m .

According to the proposed constitutive law of strand given in Eq. (9.21), the strand strain in any segment i is defined as follows:

$$\varepsilon_{p,i} = \begin{cases} \frac{F_{p,i}}{(1-\eta)A_p E_p} & F_{p,i} \leq (1-\eta)A_p f_{py} \\ \varepsilon_{py} + \frac{F_{p,i}}{(1-\eta)A_p E_{pp}} - \frac{f_{py}}{E_{pp}} & F_{p,i} > (1-\eta)A_p f_{py} \end{cases}, \quad (9.26)$$

where $\varepsilon_{p,i}$ is strand strain in segment i ; A_p is the segment zone of strand before corrosion.

The sum of the strand elongation in the slip zone, including the sum of the two effective adhesive zones and the elongation of the strand in all slip segments, and it can be calculated as follows

$$\Delta L_p = 2s_3 + \sum_{i=m}^n [l_{s,i} (\varepsilon_{p,i} - \varepsilon_{pe,i})], \quad (9.27)$$

where ΔL_p is the total elongation of the steel strand within the slip zone; $\varepsilon_{pe,i}$ is the prestrain of the strand; s_3 is the slip distance considering a relatively small value within the effective bond zone, as shown in Fig. 9.10. The value of s_3 is decreased by the increase of the corrosion, which is ignored in the current research [10].

All parts of the bending moment ($M_{s,i}$) can be quickly obtained with a given force condition. The tension force of the strand ($F_{p,i}$) in each segment is calculated by Eq. (9.25). Next, the strains of the concrete at the extreme top fiber and the bottom fiber ($\varepsilon_{ct,i}$ and $\varepsilon_{cb,i}$) in each segment can be obtained according to the equilibrium equation as the following mentioned content.

It is assumed that the steel reinforcement is not corroded in this study. At this point, the strains of both reinforcement and concrete are in accordance with the plane section assumption, which is shown in Fig. 9.11. The strains in the longitudinal bars and the hanger bars can be calculated as follows:

$$\varepsilon_{s,i} = \varepsilon_{ct,i} + \frac{\varepsilon_{cb,i} - \varepsilon_{ct,i}}{h} h_0 \quad (9.28)$$

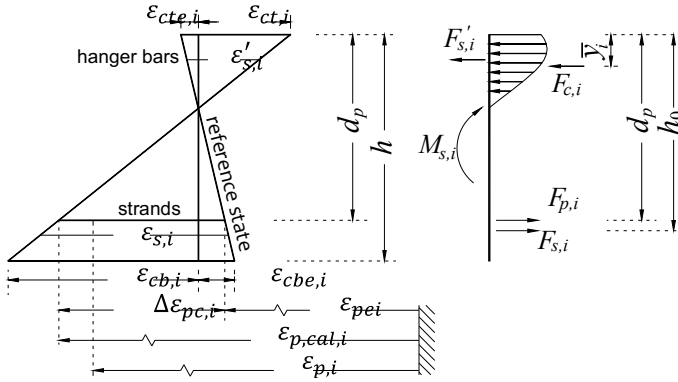


Fig. 9.11 Strain and stress distribution

$$\epsilon'_{s,i} = \epsilon_{ct,i} + \frac{\epsilon_{cb,i} - \epsilon_{ct,i}}{h} a'_s, \tag{9.29}$$

where $\epsilon_{s,i}$ is the strain in longitudinal bars and $\epsilon'_{s,i}$ is the hanger bars, respectively; h is the height of the segment; h_0 is the distances from the center of longitudinal bars to the extreme top fiber of beams; and a'_s is the center of hanger bars to the extreme top fiber of beams.

The force in the longitudinal bars and the hanger bars is calculated as follows

$$F_{s,i} = A_s f_s(\epsilon_{s,i}) \tag{9.30}$$

$$F'_{s,i} = A'_s f_s(\epsilon'_{s,i}), \tag{9.31}$$

where $F_{s,i}$ is the force of longitudinal bars and $F'_{s,i}$ is the force of hanger bars; A_s is the segment zones of longitudinal bars and A'_s is the segment zones of hanger bars; $f_s(\epsilon_{s,i})$ is the stress of longitudinal bars and $f_s(\epsilon'_{s,i})$ is the stress of hanger bars. The above-mentioned parameters can be decided by the related strains according to the constitutive law given in Eq. (9.23).

The compression force in the concrete is obtained by integrating the ultimate stress from 0 to h , which can be calculated as the following formula

$$F_{c,i} = \int_0^h f_c(\epsilon_c) b dy \tag{9.32}$$

$$\bar{y}_i = \frac{\int_0^h f_c(\epsilon_c) b y dy}{F_{c,i}}, \tag{9.33}$$

where $F_{c,i}$ is the compression force of concrete; $f_c(\varepsilon_c)$ is the concrete stress; b is the beam width; y is the distance from the extreme top fiber of concrete to the any segment of the height; \bar{y}_i is the distance from the extreme top fiber to the centroid of concrete equivalent-stress-block.

The forces of the reinforcement, prestressing strands, bending moments, and concrete can meet the following mentioned equilibrium equations in all segments. The strains of concrete at the extreme top fiber ($\varepsilon_{ct,i}$) and the bottom fiber ($\varepsilon_{cb,i}$) in each segment are expressed as follows:

$$F_{p,i} + F_{s,i} + F'_s + F_{c,i} = 0 \quad (9.34)$$

$$F_{s,i}(h_0 - d_p) + F'_{s,i}(d_p - a'_s) + F_{c,i}(d_p - \bar{y}_i) = M_{s,i}, \quad (9.35)$$

where d_p is the distance from the center of the prestressed strand to the extreme top fiber of PC beams.

According to the above-mentioned theories, the increment of the strain in concrete at the position of the strand is calculated as follows:

$$\Delta\varepsilon_{pc,i} = (\varepsilon_{cb,i} - \varepsilon_{cbe,i}) + \frac{d_p}{h} [(\varepsilon_{ct,i} - \varepsilon_{cte,i}) - (\varepsilon_{cb,i} - \varepsilon_{cbe,i})], \quad (9.36)$$

where $\Delta\varepsilon_{pc,i}$ is the strain increment of concrete at the position of the steel strand; $\varepsilon_{cte,i}$ and $\varepsilon_{cbe,i}$ are the prestrains in concrete at the extreme top fiber and the bottom fiber, respectively.

The sum of the elongation in concrete at the position of the steel strand is obtained as follows

$$\Delta L_{pc} = \sum_{i=m}^n l_{s,i} \Delta\varepsilon_{pc,i}, \quad (9.37)$$

where ΔL_{pc} is the sum of the elongation in concrete at the position of the strand.

Before the sum of the elongation of prestressed strand is equivalent to the sum of the corresponding elongation in concrete, and it can be expressed as

$$\Delta L_p = \Delta L_{pc} \quad (9.38)$$

If the above-mentioned strand elongation is not equivalent to the corresponding concrete elongation, the hypothetical length in the slip zone (L_s) could be corrected and the calculation process could be corrected by Eq. (9.37). The strains, stresses, and forces of concrete, reinforcement bars, and prestressed strands can be obtained at the given force condition. As the increase of the given force, the strains of concrete or prestressed strands exceed the corresponding values of the permissible is a crucial way to determine the flexural strength of beams.

9.5 Bearing Capacity Assessment Considering Bond Degradation

9.5.1 Bonding Degradation Model

In the current research, Wang et al. [30] proposed the proposed constitutive law to assess the bond–slip relationship between concrete and strands with corrosion. The proposed constitutive law considering the local bond characteristics is proposed to solve the problem of deformed bar by CEB Model Code [3], and it has been verified to be suitable for the concrete embedded strand [30]. As shown in Fig. 9.12, the bonded transfer zone can be divided into three different zones: the nonlinear zone will continue to increase until the maximum value of the adhesive stress, the linear decreasing region, and the linear invariant region, which can be calculated as follows:

$$\tau = \begin{cases} \tau_{max}(s/s_2)^\alpha & 0 \leq s \leq s_2 \\ \tau_{max} - (\tau_{max} - \tau_f)\left(\frac{s-s_2}{s_3-s_2}\right) & s_2 \leq s \leq s_3 \\ \tau_f & s_3 \leq s \end{cases} \quad (9.39)$$

where τ_{max} is the maximum value of the adhesive stress, and it is denoted as $1.25\sqrt{f_{ck}}$ in the good bond condition or denoted as $2.5\sqrt{f_{ck}}$ in other bond conditions; f_{ck} is the standard compressive stress of concrete; τ_f is the stress defined as $0.4\tau_{max}$ considering residual friction; α is defined as a constant of 0.4; for the corresponding slip zone, s_2 is the maximum bond stress and s_3 is the residual friction stress.

In the current study, an equivalent bi-uniform bond stress model is proposed to simplify the above-mentioned calculation process. The bond stresses are obtained by equating the energy dissipation before the excessive slip and are defined as a constant, which is an equivalent dissipation of energy along the length of strand to satisfy the requirement of the non-uniform distribution, as shown in Fig. 9.12. The

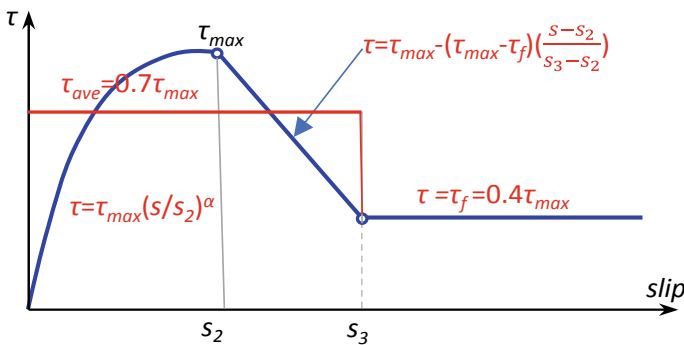


Fig. 9.12 Bond stress-slip at the strand–concrete interface

equivalent mean adhesive stress (τ_{ave}) is computed as follows:

$$\tau_{ave} = \frac{\int_0^{s_2} \left[\tau_{max} \left(\frac{s}{s_2} \right)^\alpha \right] ds + \int_{s_2}^{s_3} \left[\tau_{max} - (\tau_{max} - \tau_f) \left(\frac{s-s_2}{s_3-s_2} \right) \right] ds}{s_3} \tag{9.40}$$

By substituting these parameters into Eq. (9.40), the equivalent mean adhesive stress (τ_{ave}) is probably computed as:

$$\tau_{ave} = \frac{s_2}{(\alpha + 1)s_3} \tau_{max} + \frac{s_3 - s_2}{2s_3} (\tau_{max} + \tau_f) \approx 0.7\tau_{max} \tag{9.41}$$

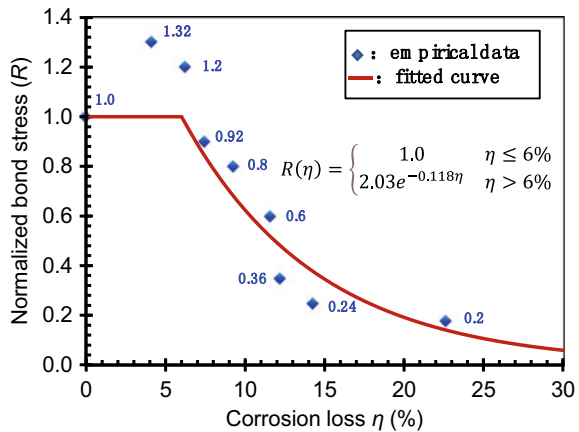
The increase of strand corrosion loss will reduce the bond strength and cause the early transfer of the effective bond force at a small given force condition. In the current study, Wang et al. [30] have studied the model to assess the degradation of the adhesive stress after the corrosion of the strand. The maximum bond stress is reduced after normalization, and it can be considered as a function of the strand considering corrosion loss, as shown in Fig. 9.13. When the corrosion of strand is lower than 6%, the maximum bond stress of strand will keep a constant. When the corrosion loss exceeds a constant of 6%, the bond stress is exponentially decreased. The function can be expressed as:

$$R(\eta) = \begin{cases} 1.0 & \eta \leq 6\% \\ 2.03e^{-0.118\eta} & \eta > 6\% \end{cases} \tag{9.42}$$

where $R(\eta)$ is the maximum bond stress after normalization; η is the corrosion loss of the strand.

The excessive slip normally appears after the strand has yielded. According to ACI 318 [13], the increment of effective bonded length under the strand tension can be expressed as

Fig. 9.13 Normalized bond stress and corrosion loss



$$l_{eb} = \frac{f_{py} - f_{pe}}{7} d_p, \quad (9.43)$$

where l_{eb} is the length in the effective bond zone; f_{py} is the yield strength of the strand; f_{pe} is the effective stress of the strand; d_p is the diameter of stranded wire.

The effective bond force in the strand under corrosion is computed as

$$F_{eb} = 0.7R(\eta)\tau_{max}L_p l_{eb}, \quad (9.44)$$

where F_{eb} is the effective bond force of the strand; L_p is the circumference of the strand.

9.5.2 Calculation of Bearing Capacity

For post-tensioned members with poor anchorage or pretensioned members, the bearing capacity is decided by the different of anchorage failure in the strand. Figure 9.14 shows the calculation process of the bearing capacity as the following mentioned content.

Stage I: calculate the parameter effective bonding force and divide the plane element.

Effective cohesive force (F_{eb}) and effective bond length (l_{eb}) between strand and concrete are calculated. Calculate the maximum length of the corrosion bond–slip zone ($L_{s,max}$), which is about the beam length minus twice the effective bond length. Then, the maximum bond–slip zone is divided into plane elements.

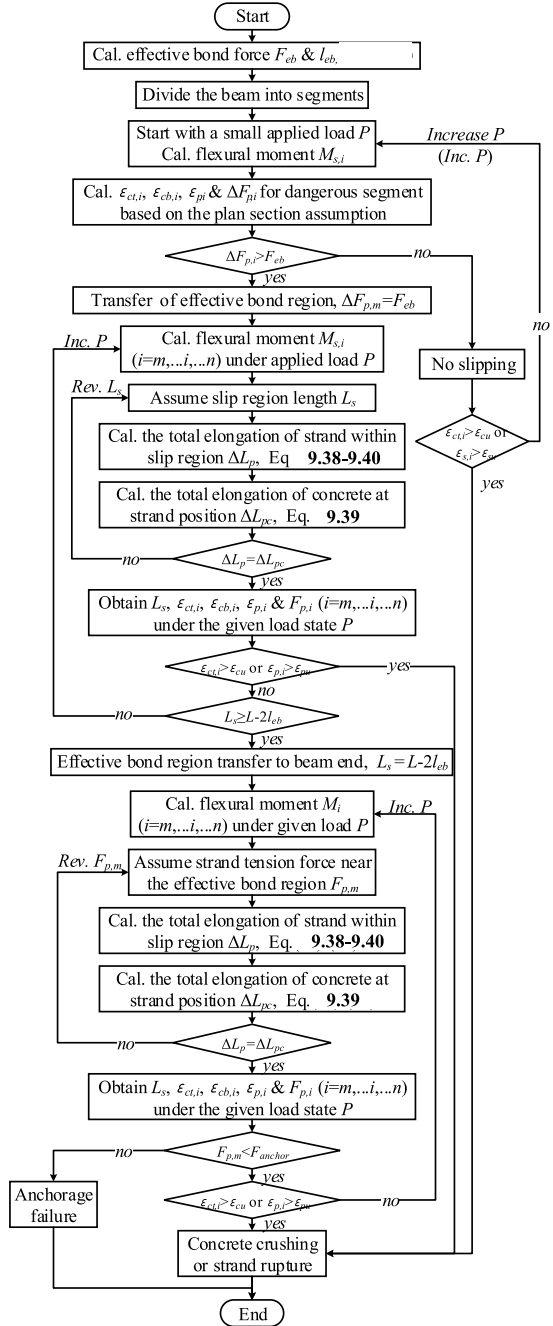
Stage II: analysis and calculation before effective bond zone slip.

Given a smaller calculated force (P), calculate the bending moment value ($M_{s,i}$) of each element. At this time, the force value is small and the concrete beam does not slip. Therefore, the maximum concrete strain, strand strains, and tensile force are calculated according to the plane section assumption. The strand tension will increase with the increase of the calculated load. When it exceeds the sum of the effective bonding force and the effective pretension of the strand ($F_{pe} + F_{eb}$), proceed to the next step of calculation. Otherwise, continue to increase the force and repeat this step. During the calculation, check whether the tensile strain of strands and the compressive strain of the concrete exceed their allowable values, and then determine their flexural capacity.

Stage III: analysis and calculation in the slip process of effective bonding zone.

At this time, the tensile force of the strand near the effective bonding segment is known ($F_{p,m} = F_{pe} + F_{eb}$), but the length of the bonding slip segment (L_s) is unknown. Therefore, first, assuming the length of the bond–slip segment (L_s) for the strand, calculate the corresponding stress deformation and the corresponding total elongation in the bond–slip segment according to formulas (9.25–9.27) (ΔL_p); then, calculate the concrete strain of each unit and the total elongation of concrete in the bond–slip segment according to formula (9.28–9.37) (ΔL_c). If the calculated

Fig. 9.14 Flowchart of the calculation procedure



total elongation of strand considering the effective bonding segment (ΔL_p) is not equivalent to the calculated total elongation of concrete (ΔL_c), the length in the bond–slip segment (L_c) needs to be assumed again and calculated again until it is equivalent. The value of L_c will increase with the increase of the calculated force. Once it exceeds its maximum length ($L_{S,max}$), proceed to the next step of calculation, otherwise continue to increase the force and repeat this step. During the calculation, check whether the tensile strain of strand and the compressive strain of concrete exceed their allowable values, and then determine their flexural capacity.

Stage IV: analysis and calculation when the effective bonding zone slides to the end.

At this time, the length of bond–slip segment of concrete beam is known ($L_s = L_{s,max}$). However, the tensile force ($F_{p,m}$) of the strand near the effective bonding segment is unknown. Therefore, first, assuming the tensile force ($F_{p,m}$) of the strand at the end, calculate the corresponding stress deformation in the bonding slip segment and the corresponding total elongation according to formula (9.25–9.27) (ΔL_p); then, calculate the concrete strain of each unit and the total elongation of concrete in the bond–slip section according to formula (9.28–9.37) (ΔL_c). If the calculated total elongation of the strand in the effective bonding segment (ΔL_p) is not equal to total elongation of concrete (ΔL_c), it is necessary to re-assume the tensile force ($F_{p,m}$) of the end strand and recalculate until it is equal. The tensile force ($F_{p,m}$) of the steel strand will increase at the beam end with the increase of calculated force. Once the total effective bonding force and the anchorage force at the end of the reinforcement ($F_{eb} + F_{p,end}$) are smaller than $F_{p,m}$, the anchorage failure of the test piece occurs. Otherwise, continue to increase the force and repeat this step. During the calculation, check whether the tensile strain of strand and the compressive strain of concrete exceed their allowable values to determine their flexural capacity.

9.5.3 Model Verification

Eight post-tensioned PC beams were employed to verify the feasibility of models. The size of the beam was 150 mm × 220 mm × 2000 mm. The bottom of the beam was anchored by two 8 mm common reinforcement bars. The top of the beam was anchored by 8 mm stirrups with 90 mm spacing, and two 12 mm deformed bars. The bottom and top of beams were prestressed with a 15.2 mm seven-wire strand considering the initial prestressing of 1395 MPa and casted in the 32 mm concrete pipe. The duct was grouted after the prestressed strand has occurred. Acceleration corrosion of the prestressed strand under different time can cause the different corrosion loss. A third point loading test was performed on the beam to study its flexural strength, which is shown in Fig. 9.15.

The yield strength and ultimate strength were adopted as 1830 MPa and 1910 MPa for prestressed strand, 235 MPa and 310 MPa for the 8 mm plain bars, 335 MPa and 425 MPa for the 12 mm deform bars, respectively. The elasticity modulus of the prestressed strand was adopted as 195 GPa, and the mild steel bars were adopted as

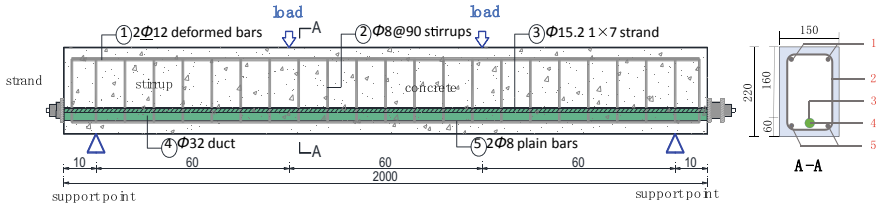


Fig. 9.15 Beam details (Unit: mm)

210 GPa. The strength (f_c), corrosion loss of the strand (η), and the bearing strength of each PC beams under experimental condition (M_{exp}) can be found in Table 9.2.

The flexural strength of tested beams can be decided by the above-mentioned model. The corroded beam is segmented into 200 segments with the length of 10 mm. With a given load of 1kN, each step is calculated in 1 kN increments. The entire shear-flexure span of the effective bond zone could be decided by the above-mentioned calculation method, and the effective bond zone would be displaced during the loading process. According to the above-mentioned condition, the maximum bond stress can be adopted as the large value of $2.5 \sqrt{f_{ck}}$, and the length of the effective bond zone is corrected to a small value according to the strand transmission length of calculation method proposed by ACI 318 [13], which can be calculated as:

$$l_{eb} = \frac{f_{py} - f_{pc}}{21} d_p. \tag{9.45}$$

The predicted flexural strengths ($M_{cal,p}$) are shown in Fig. 9.16 and listed in Table 9.1. The prediction of the bearing capacity of beams by the above-mentioned method is a good match with test results, the maximum prediction error is taken as about 15%. The above-mentioned model can provide an effective method to reasonably predict the bearing capacity in corroded PC beams. A simplified theory that considers only the zone loss of the strand and material deterioration is presented in

Table 9.2 Corresponding parameter values of beams

Beam No.	f_c (MPa)	η (%)	M_{exp} (kN m)	$M_{cal,s}$ (kNm)	$M_{cal,s}/M_{exp}$	Ω_u	$M_{cal,p}$ (kN m)	$M_{cal,p}/M_{exp}$
PE0	34.1	0	37.8	37.5	0.99	1.0	37.5	0.99
PE5	32.4	12.1	33.0	33.9	1.03	1.0	33.9	1.03
PE6	32.4	19.5	31.5	32.1	1.02	0.79	30.9	0.98
PE7	34.3	27.0	28.8	30	1.04	0.74	29.1	1.01
PE2	33.7	46.0	21.0	24.6	1.17	0.68	22.2	1.06
PE3	33.7	61.7	15.9	20.1	1.26	0.66	18.3	1.15
PE1	33.7	73.7	13.5	16.5	1.22	0.67	14.7	1.09
PE4	33.7	84.7	11.7	13.2	1.13	0.66	12.0	1.03

Fig. 9.16 Comparison of test and predicted flexural capacity

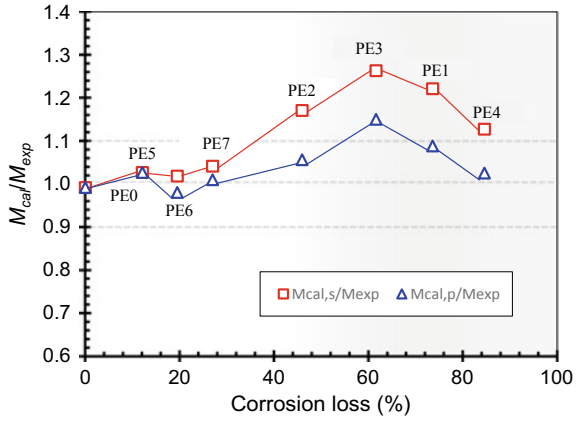


Table 9.2, which predicts the flexural capacity ($M_{cal,s}$). The error in the simplified theory slowly becomes larger due to the incompatible strain induced by the bond degradation between the corroded strand and concrete, and the value of the error has an important influence for the bearing capacity of the PC structure as the corrosion loss increases. And, the above-mentioned model gives a crucial method to calculate the incompatible strain of the PC structure. The coordination factor of beams under different force procedures is shown in Fig. 9.16.

9.5.4 Effect of Corrosion on Uncoordinated Deformation

As the above-mentioned theory, the bond degradation caused by the corrosion will lead to incompatible strains between strand and concrete, which have an impact on the bearing capacity. For this condition, a compatibility factor value is employed to assess the incompatible strain in these beams. And, the proposed model is employed to calculate the influence of the increase of corrosion loss on the incompatible strain.

Figure 9.12 schematically shows the strains in the strand, concrete, and reinforcement bars at a given force. The compatibility coefficient can be decided by the following mentioned calculation formula and it is employed to calculate the corresponding value as

$$\Omega = \frac{\varepsilon_p}{\varepsilon_{p,cal}}, \tag{9.46}$$

where Ω is the compatibility coefficient; ε_p is the strain of the strand at mid-span position of the PC structure; $\varepsilon_{p,cal} = \varepsilon_{pe} + \Delta\varepsilon_{pc}$ is the corresponding calculated strain of the steel strand according to the plane section assumption method; ε_{pe} is the effective prestress in the strand; $\Delta\varepsilon_{pc}$ is the strain increment in the strand position of concrete.

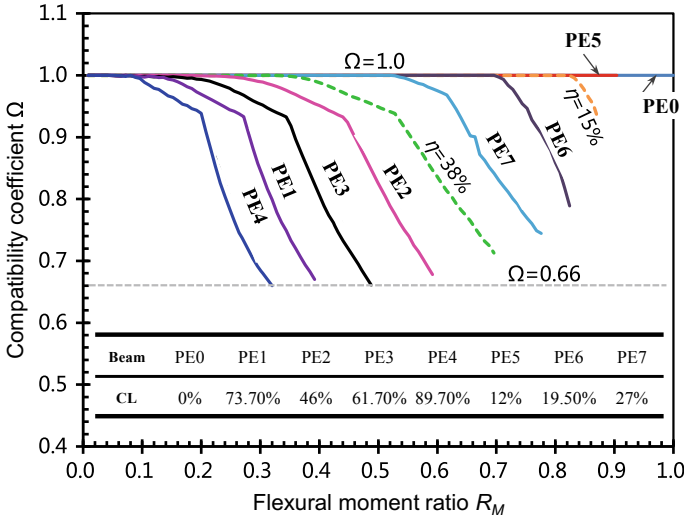


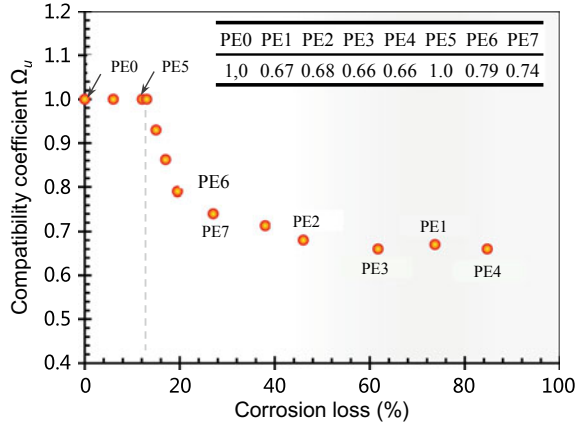
Fig. 9.17 Different compatibility coefficient of corroded PC beams (CL: Corrosion loss)

The coordination factor of each beam during loading processes was calculated using this model. Figure 9.17 shows the calculated compatibility factors of all tested PC beams. The compatibility factors for the beam with 15 and 38% corrosion loss can also be shown in Fig. 9.17. The compatibility factors can be determined by the corrosion loss increases, and the force rate increases. For the uncorroded structure PE0 and lightly corroded structure PE5, no slip will occur due to the effective bond. The compatibility factors can usually be taken as a constant of 1.0 throughout the entire loading process. It shows that corrosion loss less than 13%, and the value of it can hardly have an impact on the corresponding incompatible strain.

As the force increases, the compatibility coefficient decreases in the further corroded beam. The more serious corrosion of PC beams, the earlier the coordination coefficient will decrease under the condition of small force. The compatibility coefficient of mildly corroded beams PE6 and PE7 will be decreased under a large given force condition. The beam fails more slowly with the decrease of the compatibility coefficient. For beams with severe corrosion, the coordination coefficient will be reduced in the small loading condition, but these PC beams are slow to destroy and essentially reach the equivalent coordination coefficient value.

The ultimate coordination coefficient is defined as the coordination factor of beams under the ultimate condition, which is an effective method to assess the bearing capacity as shown in Fig. 9.18 and listed in Table 9.2. The ultimate compatibility coefficient will remain a constant of 1.0 until the corrosion loss of the PC beam is more than 13%. Next, the ultimate compatibility coefficient decreases rapidly to be a small constant. Then, the ultimate coordination coefficient can be kept a constant of the small value for the further corrosion of the beam.

Fig. 9.18 Ultimate compatibility coefficient in PC structures under corrosion



The prediction of ultimate compatibility coefficient and the variation of the compatibility coefficient has a good match with the reduction of the bond capacity occurs. For slightly corroded beams and the uncorroded beams, the slip and coordination strain will not happen during the loading test process in which the condition of adhesive capacity can be defined as the best bonding capacity. The corresponding compatibility factor is usually kept as a constant of 1.0. For the modestly corrosion of PC beams, the strand starts the condition of slippage until the tension force exceeds the effective bond force, resulting in a reduced coordination factor. These beams are subject to failure under the movement procedure that occurs in the effective bond zone. The difference in the slip region leads to a decrease of ultimate compatibility coefficient in corroded PC beams. For beams with severe corrosion, the effective bond zone tends to shift quickly to the end of the PC beam with the poorer adhesive capacity. The above-mentioned method can accurately assess the degradation of the effective bond and reasonably predict the bearing capacity.

9.6 Conclusions

1. Corrosion can reduce the ultimate strain of the strand, leading to the brittle damage of the strand. Corrosion has a slight impact on the modulus of elasticity and yield strength of strand. Corrosion can reduce the ultimate capacity and change the failure mode of PC beams.
2. An analytical model for the residual bearing capacity of corroded PC beams is proposed in the present study. The model can consider the incompatible strain caused by bond deterioration and the different failure modes.
3. The accuracy of the prediction model of corroded PC beams anchored by straight, hooked, and welded bars is verified through experimental study. The proposed model can effectively quantify the bond deterioration caused by corrosion, and

can reasonably predict the flexural capacity and the failure mode of corroded PC beams.

4. The bond degradation causes an incompatible strain. When the corrosion loss is lower than 13%, it has a slight impact on the corresponding incompatible strain. As the applied force increases, further corrosion rapidly reduces the coordination coefficient to a small value.

References

1. A.K. Azad, S. Ahmad, S.A.J.A.M.J. Azher, Residual strength of corrosion-damaged reinforced concrete beams, **104**(1), 40 (2007)
2. A.J.M.O.C.R. Baker, A plastic theory of design for ordinary reinforced and prestressed concrete including moment re-distribution in continuous members. **1**(2), 57–66 (1949)
3. B. Belletti, C. Damoni, J.A. den Uijl, M.A. Hendriks, J.C. Walraven, Shear resistance evaluation of prestressed concrete bridge beams: fib Model Code 2010 guidelines for level IV approximations. *Struct. Concr.* **14**(3), 242–249 (2013)
4. K. Bhargava, A. Ghosh, Y. Mori, S.J.N.E. Ramanujam, Design, Corrosion-induced bond strength degradation in reinforced concrete—Analytical and empirical models. **237**(11), 1140–1157 (2007)
5. L.A. Caro, J.R. Martí-Vargas, P.J.E.S. Serna, Prestress losses evaluation in prestressed concrete prismatic specimens. **48**, 704–715 (2013)
6. A. Castel, D. Coronelli, N.A. Vu, R.J.J.O.S.E. François, Structural response of corroded, unbonded posttensioned beams. **137**(7), 761–771 (2011)
7. A. Castel, R. François, G. Arliguie, Mechanical behaviour of corroded reinforced concrete beams—Part 2: bond and notch effects. *Mater. Struct.* **33**(9), 545–551 (2000)
8. D. Cavell, P.J.C. Waldron, Structures, A residual strength model for deteriorating post-tensioned concrete bridges. **79**(4), 361–373 (2001)
9. L. Chung, J.-H.J. Kim, S.-T.J.C. Yi, C. Composites, Bond strength prediction for reinforced concrete members with highly corroded reinforcing bars. **30**(7), 603–611 (2008)
10. M.P. Collins, D. Mitchell, Shear and torsion design of prestressed and non-prestressed concrete beams. *PCI J.* **25**(5), 32–100 (1980)
11. A. Committee, *Building Code Requirements for Structural Concrete (ACI 318-08) and Commentary* (American Concrete Institute, 2008)
12. M. Dekoster, F. Buyle-Bodin, O. Maurel, Y. Delmas, Modelling of the flexural behaviour of RC beams subjected to localised and uniform corrosion. *Eng. Struct.* **25**(10), 1333–1341 (2003)
13. S. El-Tawil, C. Ogunc, A. Okeil, M. Shahawy, Static and fatigue analyses of RC beams strengthened with CFRP laminates. *J. Compos. Constr.* **5**(4), 258–267 (2001)
14. M.H.J.A.S.J. Harajli, On the stress in unbonded tendons at ultimate: critical assessment and proposed changes. **103**(6), 803 (2006)
15. K.A.J.J.O.B.E. Harries, Structural testing of prestressed concrete girders from the Lake View Drive Bridge. **14**(2), 78–92 (2009)
16. C. Higgins, W.C. Farrow III., Tests of reinforced concrete beams with corrosion-damaged stirrups. *ACI Mater. J.* **103**(1), 133 (2006)
17. M. Kiviste, J.J.E.S. Miljan, Evaluation of residual flexural capacity of existing pre-cast prestressed concrete panels—A case study. **32**(10), 3377–3383 (2010)
18. C.Q. Li, J.J.M.O.C.R. Zheng, Propagation of reinforcement corrosion in concrete and its effects on structural deterioration. **57**(5), 261–271 (2005)
19. Q. Liu, P. Zhang, J. Zhao, Duct grouting investigation and research on mechanical properties of steel strand in PC continuous bridges. *Constr. Technol* **36**(2), 63–66 (2007)

20. P.S. Mangat, M.S. Elgarf, Flexural strength of concrete beams with corroding reinforcement. *Struct. J.* **96**(1), 149–158 (1999)
21. J.R. Martí-Vargas, P. Serna, J. Navarro-Gregori, J. Bonet, Effects of concrete composition on transmission length of prestressing strands. *Constr. Build. Mater.* **27**(1), 350–356 (2012)
22. J.R. Martí-Vargas, L. Caro, P. Serna, Experimental technique for measuring the long-term transfer length in prestressed concrete. *Strain* **49**(2), 125–134 (2013)
23. R. Powers, Corrosion evaluation of post-tensioned tendons on the nils channel bridge. (FDOT, Gainesville, FL, 1999)
24. Z. Rinaldi, S. Imperatore, C. Valente, Experimental evaluation of the flexural behavior of corroded P/C beams. *Constr. Build. Mater.* **24**(11), 2267–2278 (2010)
25. A.J. Schokker, J.E. Breen, M.E. Kreger, Grouts for bonded post-tensioning in corrosive environments. *Mater. J.* **98**(4), 296–305 (2001)
26. M. Schupack, PT grout: bleed water voids. *Concr. Int.* **26**(8), 69–77 (2004)
27. A.A. Torres-Acosta, S. Navarro-Gutierrez, J.J.E.S. Terán-Guillén, Residual flexure capacity of corroded reinforced concrete beams. **29**(6), 1145–1152 (2007)
28. F.D.O. Transportation, Sunshine skyway bridge post-tensioned tendons investigation (Parsons Brinckerhoff Quade and Douglas Tallahassee, FL, 2001)
29. N.A.Vu, A. Castel, R.J.E.S. François, Response of post-tensioned concrete beams with unbonded tendons including serviceability and ultimate state. **32**(2), 556–569 (2010)
30. L. Wang, X. Zhang, J. Zhang, J. Yi, Y. Liu, Simplified model for corrosion-induced bond degradation between steel strand and concrete. *J. Mater. Civ. Eng.* **29**(4), 04016257 (2017)
31. W.-Q. Wu, X.-G. Chen, B. Li, Q.-H. Xie, Investigation of construction quality evaluating indices in PC continuous box-girder. *J. Architect. Civil Eng.* **3** (2009)
32. Y.-Z. Wu, H.-L. Lv, S.-C. Zhou, Z.-N.J.C. Fang, B. Materials, Degradation model of bond performance between deteriorated concrete and corroded deformed steel bars. **119**, 89–95 (2016)
33. X. Zhang, L. Wang, J. Zhang, Y. Liu, Corrosion-induced flexural behavior degradation of locally ungrouted post-tensioned concrete beams. *Constr. Build. Mater.* **134**, 7–17 (2017)
34. J.R. Eyre, M.A. Nokhasteh, Strength assessment of corrosion damaged reinforced concrete slabs and beams. *Proceedings of the Institution of Civil Engineers-Structures and Buildings* **94**(2): 197–203 (1992)
35. J. Cairns, Z. Zhao, Behaviour of concrete beams with exposed reinforcement. *Proceedings of the institution of civil engineers-structures and buildings* **99**(2): 141–154 (1993)
36. T.E. Maaddawy, K. Soudki, T. Topper, Analytical model to predict nonlinear flexural behavior of corroded reinforced concrete beams. *ACI structural journal* **102**(4): 550 (2005)

Open Access This chapter is licensed under the terms of the Creative Commons Attribution 4.0 International License (<http://creativecommons.org/licenses/by/4.0/>), which permits use, sharing, adaptation, distribution and reproduction in any medium or format, as long as you give appropriate credit to the original author(s) and the source, provide a link to the Creative Commons license and indicate if changes were made.

The images or other third party material in this chapter are included in the chapter's Creative Commons license, unless indicated otherwise in a credit line to the material. If material is not included in the chapter's Creative Commons license and your intended use is not permitted by statutory regulation or exceeds the permitted use, you will need to obtain permission directly from the copyright holder.

